Carlos Filipe Cidre João

Mestre em Engenharia Biomédica

Inverted Colloidal Crystal Scaffolds

New Substitutes for Bone Tissue Engineering

Dissertação para obtenção do Grau de Doutor em

Ciência e Engenharia de Materiais

Orientador: Doutor João Paulo Miranda Ribeiro Borges,
Professor Auxiliar,
Faculdade de Ciências e Tecnologia
Universidade Nova de Lisboa

Co-orientador: Doutor Jorge Alexandre Monteiro Carvalho Silva,
Professor Auxiliar,
Faculdade de Ciências e Tecnologia
Universidade Nova de Lisboa

Júri

Presidente:	Prof. Doutor Rodrigo Ferrão de Paiva Martins
Arguentes:	Prof. Doutor João Filipe Colardelle da Luz Mano
	Prof. Doutor Pedro Lopes Granja
Vogais:	Prof. Doutora Maria Helena Mendes Gil
	Prof. Doutor João Paulo Miranda Ribeiro Borges
	Prof. Doutora Patrícia Almeida Carvalho
	Prof. Doutora Joana Dória Vaz Pinto

FACULDADE DE CIÊNCIAS E TECNOLOGIA
UNIVERSIDADE NOVA DE LISBOA

Dezembro, 2016

NOVA University of Lisbon

Faculty of Sciences and Technology

Inverted Colloidal Crystal Scaffolds

New Substitutes for Bone Tissue Engineering

Carlos Filipe Cidre João

supervised by

Prof. João Paulo Miranda Ribeiro Borges, PhD

Prof. Jorge Alexandre Monteiro Carvalho Silva, PhD

December 2016

Inverted Colloidal Crystal Scaffolds
New Substitutes for Bone Tissue Engineering

Este documento foi gerado utilizando o processador (pdf)LaTeX, com base no template "unlthesis" [1] desenvolvido no Dep. Informática da FCT-NOVA [2].
[1] https://github.com/joaomlourenco/unlthesis [2] http://www.di.fct.unl.pt

To my grandmother

Wherever you are I know that you are proud
Your engineer is becoming a doctor

Do not go where the path may lead
Go instead where there is no path
and leave a trail
Ralph Waldo Emerson

Acknowledgements

This work was funded by FEDER funds through the COMPETE 2020 Program and National Funds through FCT - Portuguese Foundation for Science and Technology - under the project number POCI-01-0145-FEDER-007688 ref: UID/CTM/50025. Carlos F. C. João acknowledges FCT for his PhD scholarship ref: SFRH/BD/80860/2011, the Faculty of Sciences and Technology (FCT/UNL), the Materials Science Department (DCM-FCT/UNL), CENIMAT/i3N and the Soft and Biofunctional Materials Group (SBMG) for providing their research facilities and hosting the Doctoral Program in Materials Science and Engineering.

"I would like to express my gratitude to a great number of persons that have contributed to this amazing journey.

First of all, I would like to thank my supervisores, Prof. João Paulo Borges and Prof. Jorge Carvalho Silva, for giving me the opportunity to pursuit this dream. They have provided the challenge, scientific knowledge, motivation, comprehension and help that any PhD student would wish for and which definitely contributed to my professional and personal growth as a researcher and a man. But most of all, I would like to thank both for their friendship and brotherhood. Even if I have not been able to fulfill all my scientific goals, this working period was already greatly accomplished by considering us as friends for life.

My acknowledgments to Prof. Rodrigo Martins, Prof. Elvira Fortunato, Prof. Maria Helena Godinho and Prof. Maria Teresa Cidade for giving me the great opportunity to integrate the DCM, CENIMAT/i3N and the SBMG, where I had the chance to contact with top experts in diverse knowledge fields and present the scientific output achieved during this PhD.

I am particularly grateful for all people who have directly or indirectly collaborated with me in various stages of this work. Special thanks to Prof. Maria Helena Godinho, Prof. Alexandre Velhinho, Dr. Coro Echeverria, MSc Teresa Kullberg, MSc Rute Almeida and MSc Joana Vasconcelos, who have contributed enormously to the success of this thesis. Thank to all current and former members of the SBMG group, who have welcomed me so well, particularly Augusta Gonçalves for being the heart and soul of the Polymers Lab. Thanks to Dr. Coro Echeverria and Dr. Ana Baptista who have been the beacon that always guided me in the best direction.

Thanks to Dr. Susete Fernandes, Dr. Paula Soares, Dr. João Canejo and MSc Ana Almeida for all support, scientific knowledge, exchange of experiences and friendship. I also thank Dr. Pedro Almeida, Dr. Marta Corvo, Dr. Daniela Gomes, Dr. Ana Pimentel, MSc Alexandra Gonçalves and MSc Sónia Pereira for all their contributions in the characterization measurements.

I want to thank all my friends who accompanied and encouraged me during this period. Thanks to Paulo Quental, Filipa Matias, Ricardo Francisco, Rita Dinis, Ana Pedrosa, Rui Lopes, Tiago Pires, Alexandre Dias, João Vicente and Miguel Martins. They reminded me that while the work takes up most of our time, it is only a small part of life. Their friendship is the most important part and I am sincerely grateful for having them.

Finally, thank you to my beloved family for all unconditional love and support. To my parents who have worked very hard and have done huge sacrifices to provide me all necessary conditions and opportunities to chase my dreams. They were the first to encourage me to take this path and so this PhD is dedicated to them. A special thanks to my dear Sandra Gonçalves for being my life partner. Her friendship, patience, affection and comfort made all the diference. Maybe love can not do a PhD but certainly helps and I am sure that without her by my side I would never have done it."

Abstract

Bone is a highly organised and specialised connective tissue with natural ability to self-heal and regain functionality. This capacity is, however, exposed to a great number of threats that can critically damage bone's health and trigger the need for bone substitutes.

The present thesis aimed at the production of new bone scaffolds for tissue regeneration using the Inverted Colloidal Crystal (ICC) structure as model system. ICCs are 3D structures, resultant from Colloidal Crystals (CC) inverse replication, that exhibit uniform pore size, interconnected network and whose architectural design enhances the cellular environment and vascular ingrowth.

Reported here is the use of organic (chitosan/chitin nanowhiskers) and inorganic (hydroxyapatite) building materials to develop scaffolds comprising ceramic, polymeric and composite matrices. Firstly, polystyrene microspheres are produced by simple microfluidic, assembled in hexagonal close packed CC and then used as templates for all scaffolds production. Ceramic based ICCs were developed using an hydroxyapatite sol-gel system and sintering route that allowed simultaneous template calcination and matrix formation. Polymeric based ICCs were subjected to hydrolytic degradation after being produced with different molecular weight chitosans in order to understand polymer influence on the scaffolds structural stability. Considering bone´s composite nature, ICCs were constructed using hydroxyapatite nanorods suspended in chitosan solutions. Also, structures whose materials have an imprinted liquid crystalline organization provided by chitin nanowhiskers were developed inspired by bone collagen arrangement that contributes to the tissue hierarchical architecture.

The morphological, biological and mechanical evaluation of such scaffolds contributes to establish the path for the development of new ICC based products with potential to complement or replace the currently clinically used bone substitutes and in that way constitute valuable solutions for bone tissue regeneration.

Keywords: Bone Tissue Engineering; Inverted Colloidal Crystals; Scaffolds; Chitosan; Hydroxyapatite; Chitin Nanowhiskers; Liquid Crystals.

Resumo

O osso é um tecido conjuntivo altamente organizado e especializado, com capacidade natural para se curar e recuperar a funcionalidade. No entanto, esta capacidade está exposta a um grande número de riscos que podem danificar irreversivelmente a saúde óssea, criando a necessidade de uso de substitutos ósseos.

A presente tese teve como objetivo a produção de novos substitutos ósseos sintéticos para regeneração de tecido tendo como base as Réplicas Inversas de Cristais Coloidais (RICC). As RICC são estruturas 3D, resultantes da reprodução negativa de Cristais Coloidais (CC), que possuem uma rede interconectada de poros de tamanho uniforme, cuja construção arquitectónica contribui para um melhor ambiente celular e penetração de vasos sanguíneos.

Nesta tese é reportado o uso de materiais orgânicos (quitosano/nanofibrilas de quitina) e inorgânicos (hidroxiapatite) no desenvolvimento de estruturas poliméricas, cerâmicas e compósitas. Primeiro, microesferas de poliestireno foram produzidas por microfluidica, empacotadas em geometrias hexagonais de CC e posteriormente usadas como moldes para toda a linha de desenvolvimento dos substitutos. RICCs com matrizes cerâmicas foram desenvolvidas utilizando um sistema sol-gel de hidroxiapatite e um programa de sinterização que simultaneamente permitiu a calcinação do molde e a formação da matriz. RICCs poliméricas foram sujeitas a degradação hidrolítica após terem sido produzidas com quitosanos de diferentes pesos moleculares, de forma a avaliar a influência do polímero na estabilidade estrutural das réplicas. Considerando a natureza compósita do osso, foram construídas RICCs a partir de suspensões de nanorods de hidroxiapatite em soluções de quitosano. Inspirados na organização do colagénio nos ossos, que contribui para a arquitectura hierárquica deste tecido, são ainda apresentadas estruturas cujos materiais evidenciam uma organização proveniente de fases líquidas cristalinas de nanofibrilas de quitina.

A caracterização morfológica, biológica e mecânica das estruturas produzidas abre o caminho do desenvolvimento de novos produtos com base em RICC, com potencial para complementar ou substituir os substitutos ósseos clinicamente usados, e que desta forma se constituem como soluções valiosas para a regeneração do tecido ósseo.

Palavras-chave: Engenharia de Tecido Ósseo; Réplicas Inversas de Cristais Coloidais; Estruturas Porosas 3D; Quitosano; Hidroxiapatite; Nanofibrilas de Quitina; Cristais Líquidos.

Contents

List of Figures

List of Tables

Acronyms

β-**TCP** β-Tricalcium phosphate.

α-**TCP** α-Tricalcium phosphate.

σ_{cr} Crushing compressive strength.

C_a Cappilary number.

E Elastic modulus.

W_e Webber number.

X_c crystallinity degree.

t cristal size.

CC Colloidal Crystal.

CI Crystallinity index.

CP Continuous phase.

CPs calcium phosphates.

CS chitosan.

CTNW chitin nanowhiskers.

DA acetylation degree.

DCM dichloromethane.

DD deacetylation degree.

DP Discontinuous phase.

DSC Differential scanning calorimetry.

FTIR Fourier transform infrared spectroscopy.

HAp hydroxyapatite.

hcp hexagonal close packed.

ICC Inverted Colloidal Crystal.

LC liquid crystalline.

MW molecular weight.

PCL polycaprolactone.

POM polarized optical microscopy.

PS polystyrene.

PVAc poly(vinylacetate).

SD standard deviation.

SEM scanning electron microscopy.

TEM transmission electron microscopy.

TG thermogravimetry.

XRD X-ray diffraction.

CHAPTER 1

MOTIVATION

In this chapter the motivation that drove the author in the research and development leading to this PhD thesis is presented. First, the inspiring study object - bone - is briefly presented in order to perceive its formidable complexity. Secondly, the risks and complications associated with human bone trauma and/or diseases will be addressed along with their key statistics and the diversity of the current solutions. Finally a new type of solution - Inverted Colloidal Crystal (ICC) - is suggested and the stages describing how to achieve it are presented and framed into thesis chapters.

1.1 Bone

Bone is a highly organized and specialized connective tissue. It is the main constituent of the skeletal system (213 bones in adults, excluding the sesamoid bones) (Figure 1.1) and the harder, stronger and more rigid tissue in the human body. It is responsible for major key actions such as structural support of the body, allows movement and locomotion, protects internal organs, serve as mineral, growth factor and cytokines reservoir, includes the marrow for blood cells production, regulates blood acid-base balance and is the source of multiple progenitor cell [1]. Bone functionality is directly linked to internal organization, so in the next sections a closer look at tissue architecture and composition will be given.

1.1.1 Bone Architecture

Bone results from an hierarchical construction of platforms from the nano to micro and macro scales that involves cells, growth factors, proteins and ceramics. The analysis of bone at different scales reveals an entire world of biological complexity that has intrincated and regulated interaction mechanisms [2]. Starting at the human scale and based

on their **shape** and **morphology**, bones can be either classified as:

Long bones or tubular bones, which are weight-bearing, have articular surfaces at their ends, and are confined to the limbs, as they primarily act as levers (e.g. humerus and femur);

Short bones or cuboidal bones, which have many articulating surfaces for the transmission of loads as well as articulation (e.g. carpal and tarsal bones);

Flatbones which are formed from two thick layers, separated by a layer of spongy-like bone, and are usually curved structures and provide protection and points of attachment for tendons and ligaments (e.g. scapula, sternum, pelvis).

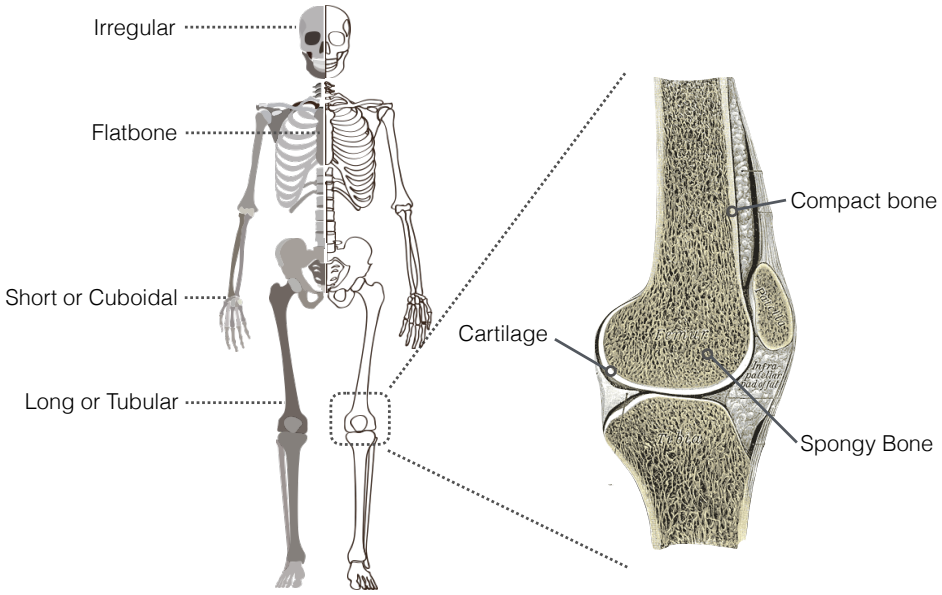

Figure 1.1: Human skeleton: bones morphology and bone macrostructural level. Stock images available at freepick.com.

A fourth type includes the irregular shaped bones that do not fit in the above three or might be combinations of them, e.g. the skull, vertebrae, maxilla, ribs and sesamoid bones [3]. Looking at the **macrostructural level** we can classify bone in two classes: **trabecular** or **cortical**. The *cortical* or *compact bone* represents approximately 80% of the skeletal mass. It is a solid mass that is filled with organic ground substance and inorganic salts and forms the outer wall of bones, supplying supportive and protective functions to the skeleton. The *trabecular* or *cancellous bone* can be found in the inner part of bone and represents approximately 20% of the bone mass. Also known as spongy bone, it is light, porous and typically exists in the form of interconnected plates and rods (trabeculae), which vary in amount in different bones. In the enclosed spaces, trabecular bone is filled with blood vessels and marrow. Depending on skeletal sites, bones can be

composed of cortical and trabecular parts in different ratios. While vertebras present 25:75 cortical/trabecular ratio, the femur is composed of 50:50 and 95:5 at the femoral head and in the radial diaphysis, respectively [1].

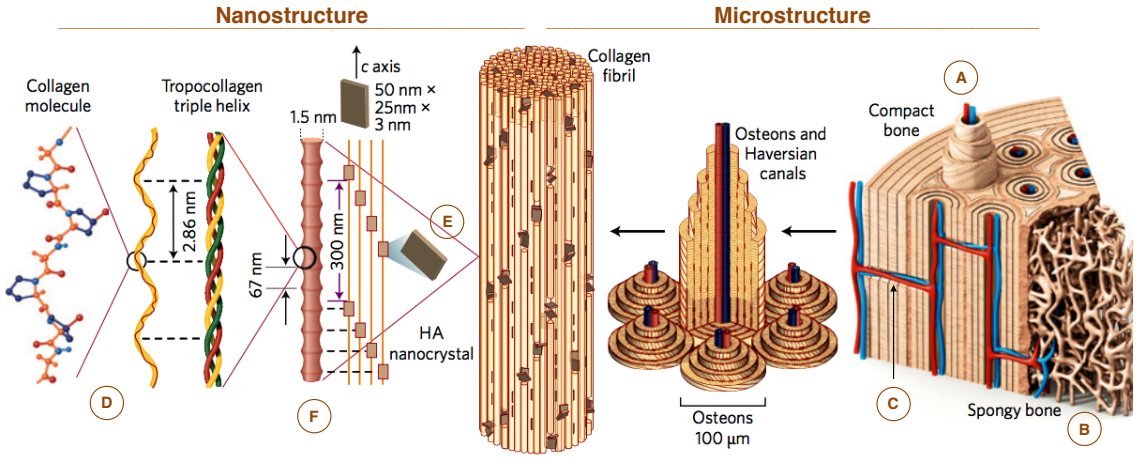

Figure 1.2: Bone hierarchical structure at the nanostructural and microstructural level: A) Haversian system; B) trabecula; C) Volkmann's canal; D) collagen; E) hydroxyapatite crystal and F) collagen fibril. Adapted with permission from Wegst et al. [4] copyright ©Nature Materials 2014.

The **microstructural level** is formed by the **Haversian system** (in cortical bone) and the **trabecula** (in spongy bone). The cortical bone base unit, the *osteon* or *Haversian system* (Figure 1.2 A), is a structural junction of concentric bone layers composed by an inner longitudinal canal (Haversian canal) and surronding concentric lamellae of fibers and ceramics. The Haversian canal contains small blood vessels allowing blood supply to osteocytes. Osteons are characteristic of mature bone and are formed preferentially along the long axis of bone. The morphology of these osteons gives bone a plywood aspect. The space between adjacent osteons is filled with interstitial lamellae and the vascular communication between consecutive osteons is achieved by the existence of perpendicular vessels called Volkmann's canals (Figure 1.2 C) [5]. The trabeculae (Figure 1.2 B) is cancellous bone base unit and it is arranged in a orderly pattern giving a honeycombed aspect to the inner bone. Trabeculae are aligned along lines of stress, providing structural support and flexibility with less weight when comparing with cortical bone.

Another important tissue is located within the cortical and cancellous bone cavities. The bone **marrow** is the organ of haemotopoiesis and very important in the first stages of bone formation at birth, being confined after maturation to specific bones like the vertebral collum and the proximal end of long bones. The marrow is yellow and composed of fat cells and few marrow cells in long bones and is red and composed of connective tissue, blood vessels and more marrow cells in flat and short bones [3].

At the **nanostructural level** bone is a composite of **organic** and **mineral** compounds that together constitute the bone extracellular matrix (ECM). The organic phase of bone

matrix represents 30% to 40% of bone dry weight and is composed approximately by 90% of *type I collagen* (Figure 1.2 D) and 10% of proteins like osteocalcin (promotes mineralization and bone formation), osteonectin (regulates calcium and organizes mineral in matrix) and osteopontin (cell-binding protein). The mineral phase of the ECM ranges from 30% to 98% dry weight depending on the site, but the majority of bones present 60% to 70% mineral dry weight formed by carbonate-substituted *hydroxyapatite* crystals (Figure 1.2 E) that can also incorporate citrate, magnesium, fluoride and strontium into the lattice or onto the surface. Bone hydroxyapatite (HAp) is poorly crystalline being more soluble than geologic hydroxyapatite ($Ca_{10}(PO_4)_6(OH)_2$), which facilitates body mineral homeostasis and bone remodeling during its life cycle. [1, 6].

Finally, at the **cell level**, bone has 3 major cell components: **osteoblasts**, **osteoclasts** and **osteocytes**.

Osteoblasts - Descend from the differentiation of osteogenic cells in the periosteum (tissue that covers the outer surface of the bone) and in the endosteum of the marrow cavity. Responsible for the synthesis and mineralization in initial bone formation and later bone remodeling, they produce the enzymes alkaline phosphatase and collagenase, growth factors, osteocalcin and collagen.

Osteoclasts - Large multinucleated cells responsible for the dissolution and absorption of bone. Osteoclasts are formed by the fusion of many cells derived from circulating monocytes in the blood. Osteoclasts may have as many as 200 nuclei, although most have only 5 to 20. Osteoclasts produce a number of enzymes like cathepsin K (degrades type I collagen and other noncollageneous proteins).

Osteocytes - The smallest cells in bone are found in the lacunae, which are contained in the calcified matrix. Osteocytes derive from osteoblasts and consist in osteoblasts surrounded by their secreted products. The osteocyte participates in calcium homeostasis [5].

1.1.2 Bone as a Liquid Crystalline based Composite Tissue

As seen previously, bone is a highly hierarchical structure and a composite tissue of organic and mineral matter. The formation of this composite is a complex process of protein, hormone, growth factor and cell interactions. Bone production starts with the deposition of an organic network of collagen fibrils which are calcified by the build-up of calcium phosphate. HAp crystals appear as flat nanoplates that nucleate within and around collagen, and dispose themselves alongside the organic fibrils axis (Figure 1.2 F) [7].

In osteons, groups of collagen fibrils run parallel to each other in consecutive lamellae, with a 90º change of orientation between each lamellae. The complex order in compact bone is directly related to the three-dimensional assembly of the collagen fibrils that influence the deposition of the mineral phase and the mechanical properties of the tissue.

By microscopic observation of the collagen orientation in bone, two coexisting models have been proposed: *orthogonal plywood* and *twistted plywood* (Figure 1.3)[8].

The first model translates the classical description of the two principal orientation of collagen fibrils, described in the literature by the bright and dark stripes observed in polarized light microscopy. The bright and dark stripes are related to the angular shift of fibrils lower than 90º (bright) and larger than 90º (dark), that allow or not the passage of light.

The twisted plywood model describes small and regular angular shifts, giving the impression of an existing continuous stratification. Different orientated plates are observed in each 180º shifts. The existence of both models at the same osteon has been described, as consequence of mechanical constraints. Compression and tension stimuli modulate the fibrillar arrangement and are responsible for the collagen network disposition.

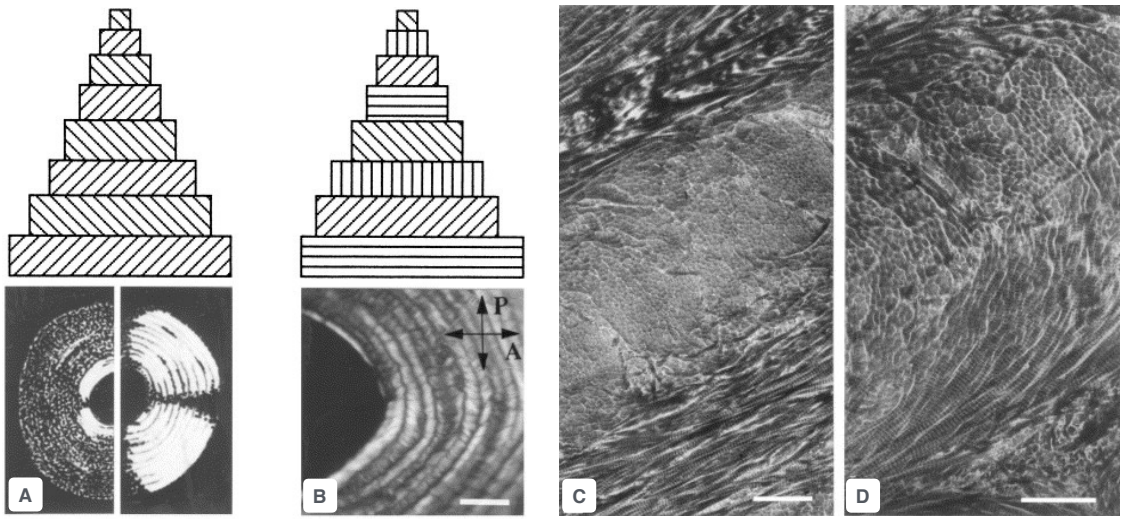

Figure 1.3: Collagen orientation models in single osteons (A,B) and in ultra-thin sections of osteons (C,D): Orthogonal plywood model (A, C) and twisted plywood model (B, D). Bar lengths: B = 5 μm; C and D = 0.1 μm. Adapted with permission from Giraud-Guille et al. [9] copyright ©Elsevier 2003.

An analogy between liquid crystalline (LC) geometries and the organic network of bone has been proposed due to the collagen long-range order. Collagen fibrils distribution is similar to that of molecules in cholesteric liquid crystals. In these mesophases molecules are organized in layers. In each layer the molecules are in average aligned in a direction given by the director $\vec{n}$, and this director rotates periodically along the long axis of the structure, like in a helix. The period of the rotation (the distance over which a full 360º rotation is completed) is know as the pitch, p, of the cholesteric. Several authors have been able to reproduce the liquid crystalline fingerprint-like texture in acidic collagen systems, suggesting that molecular interactions at liquid crystalline state are responsible for fibril assembly and collagen network architecture in bone [9, 10]. Although the tissue imprinted liquid crystalline organization has not yet been understood, there is an

increased belief that collagen molecules are created by specific cells like fibroblasts and osteoblasts, segregated into the ECM space in a dense state and then escape from cellular control to self-assemble in local liquid crystalline domains that give rise to long highly ordered tissues [11].

1.1.3 Bone Mechanical Properties

Bone physical properties are intrinsically linked with bone morphology, architecture and chemical composition. On the one hand, collagen fibrils are responsible for high elasticity, little compressive strength and considerable intrinsic tensile strength. On the other hand, the mineral content is responsible for hardness, rigidity and compressive strength of bone. Bone brings together the combination of properties of both mineral and organic in an unique composite material. The dispersion of rigid and brittle ceramics in an elastic collagen matrix decreases the propagation of stress failure throughout the brittle material and allows a closer approach to the theoretical limiting strength of single crystals [5].

As seen previously, bone can be subdivided in cortical and trabecular. Cortical bone exhibits anisotropic mechanical properties. Its Elastic modulus (E) varies from longitudinal to transverse - 17.4 to 9.6 GPa - and when bending or shearing - 14.8 to 3.51 GPa. Cancellous human bone elastic modulus has been difficult to be determined since different values are obtained depending on which plate is studied, resulting in 20 to 40% values variation. Some researchers have used the combination of micro-CT scans and finite-element computation to determine the elastic modulus, reaching values like 5.7 ± 1.6 GPa and 6.6 ± 1.1 GPa. Although different values have been reported, it is commonly accepted that cancellous bone is 20-30% less stiff than cortical bone tissue. This difference is explained not by mineralization but by the different collagen fibrils organization in both tissues [12].

Variation of the mineral/organic contents occurs depending on bone type and location. This ratio variation influences bone mechanical properties: more mineral leads to more brittle material, less mineral leads to higher flexibility. Also, bone elastic modulus is directly dependent on the load rate applied. Bones have different behavior during rapid or slow deformation which suggests the existence of viscous flow during deformation [5].

1.1.4 Bone Remodeling/Repairing System

Bone is dynamically maintained throughout life by a "self-regeneration program" that includes different complex events with the participation of cells and stimulating agents. In skeleton formation, repair and maintenance, a combination of intramembranous and endochondral ossification occurs, which is dependent on the mechanical environment involved.

Intramembranous bone formation is the process of ossification that forms the bulk of the cortical bone shell. Membranous bones appear from condensates of loose mesenchymal tissue that contain osteogenic cells. The first small mass of bone with its irregular

shape is called a spicule and the interconnection of consecutive spicules, promoted by osteoblasts, gives rise to the primary cancellous bone. At the trabecula surface and between voids, osteoblasts start to build primary osteons (Haversian systems) that are posteriorly replaced by secondary osteons. After sufficient bone mass has been produced, osteoclasts begin the remodelling phase allowing bone to achieve the most optimal shape and density. This process defines the formation of dense bone at the cortex (compact bone) or woven bone in the inner part (cancellous bone).

Endochondral bone formation is the mechanism of ossification that forms the bulk of cancellous bone. It starts with cartilage formation as mesenchymal cells condense and differentiate in an avascular environment into chondroblasts that produce cartilage matrix. This matrix constitutes the model of the future formed bone. After cells maturation and growth, the matrix calcifies. Chondrocytes stop secreting collagen and begin secreting an enzyme - alkaline phosphatase - essencial for mineral deposition. Following the calcification process, the cartilage matrix is invaded by capillaries and osteogenic cells that start the ossification process. Osteoblasts appose woven bone in the calcified cartilage and produce the primary spongiosa. Later, the spongiosa is replaced either by bone marrow or by lamellar trabeculae, forming the adult cancellous bone [12, 13].

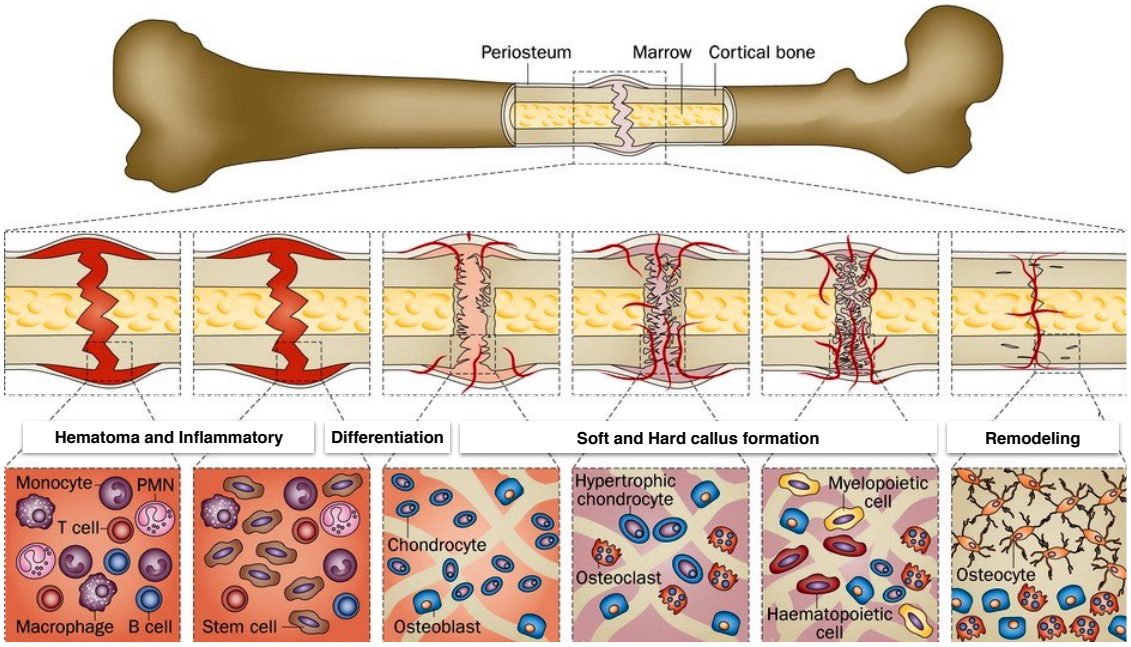

Figure 1.4: Representation of the fracture healing steps: A) Hematoma formation; B) inflammatory response. Arrival of mesenchymal cells; C) Formation of callus after endosteal and periosteal reaction; D) Callus remodeling. Adapted from Einhorn et al. [14] copyright ©Nature Reviews Rheumatology 2014.

The fracture healing process is a physiological process that involves biological factors and mechanical principles. It aims at rapid stabilization of broken bone parts with little

commitment to anatomy. In this process, intramembranous and endochondral ossification similar to the bone formation during osteogenesis, occurs. A sequence of stages are present during the process: *hematoma and inflammatory phase*, *proliferation and differentiation phase*, *soft and hard callus formation* and *remodelling phase* (Figure 1.4).

When a fracture happens, the hematoma event begins with bone and surrounding soft tissues bleeding. The microvascular disruption leads to hypoxia and causes bone necrosis. After, blood clots form around the bone extremities and within the medulla, providing a natural template for callus formation. This event triggers an inflammatory response (24 hours to 7days) with the release of cytokines (inflammatory mediators) followed by increased blood flow, vessel permeability and cell migration (anabolic phase). Bone debris are resorbed by osteoclasts and the increased blood flow and vascular proliferation supplies stem cells and signalling molecules.

The mechanical environment and biological signs cause the differentiation of mesenchymal stem cells into osteogenic cells. The repair phase follows with initial stabilization by chondroid cartilaginous matrix (containing proteoglycans and type II collagen) that is replaced by osteoid matrix (type I collagen), during 3 to 4 weeks - soft callus formation. The ossified cartilage is then replaced by woven bone, developing a more solid and resistant bone. Soft callus formation is followed by intramembranous ossifications at the distal and proximal ends of fractures, forming the hard callus. After the first month of repairing, the remodelling phase starts. The spongy bone is replaced with lamellar bone by osteoclasts resorption of the hard callus and lamellar deposition by osteoblasts. The new bone is reshaped in the final and best achievable bone morphology with its normal microstructure and material properties reestablished [15].

1.2 Background

As seen above, bone has the natural ability to self-heal and regain its structural and functional activity. However this capacity is exposed to a great number of threats that can critically affect the performance and irreversibly damage bone health. Disorders like osteoporosis, arthritis and diseases such as obesity, diabetes and cancer can cause extensive injuries to orthopedic tissues.

In the United States 1.5 million people suffer a fracture due to bone disease every year and this problem almost exponentially increases with demography. In 50 years old individuals, 39.7% of women and 13.1% of men have hip, vertebra or forearm fractures and by 2020 it is expected that nearly 14 million cases of osteoporosis and 47 million cases of low bone mass in risk of developing fractures will occur [16]. According to the World Health Organization, in the European Union in 2010 the number of fractures reached approximately 620.000 hip fractures, 520.000 vertebral fractures and 560.000 forearm fractures for a total of 3.5 million cases with an expected increase of 28% to 4.5 million cases in 2025. Also, 22 million women and 5.5 million men between 50 and 84 years of

age are estimated to have osteoporosis and this value will rise to 33.9 million in 2025 (23%)[17].

These conditions can lead to critical defects in the skeleton requiring surgery to replace or restore the missing bone volume and many times requiring the use of *Bone Graft Materials* (BGM) to allow bone regeneration. BGM have their application in augmenting/enhancing the healing of fractures and fusions, malunion/nonunion applications and in filling defects or voids resulting from bone loss due to trauma or diseases [18]. BGM solutions which are applied at considerable amounts in 20% of the arthroplasty, 19% in trauma and 12% in foot/hand cases [19], can be used in various physical forms (e.g. powders, granules, blocks, scaffolds, injectables, pastes) and are classified in four segments: *autografts*, *allografts*, *xenografts* and *synthetics*.

Autografts - Autologous bone graft, which means bone taken from the patients own body, normally from the iliac crest due to its accessibility and comparatively abundant bone volume. It is a font of osteogenic cells and osteoinductive factors capable of promoting bone healing and regeneration. Although it presents excellent biocompatibility, its use is restricted due to limited amount, size and shape availability and to donor site morbidity [20].

Allografts - Grafts collected from cadavers. Readily available, osteoconductive, relatively inexpensive. Has some risks with the possibility of viral diseases transmission like HIV [3]. Fresh allografts are rarely used due to risks of donor recipient infection and host immune response of host [21]. Processing of allograft tissue decreases disease transmission risk but also reduces biological and mechanical properties of the graft [22].

Xenografts - Grafts collected from other species. Normally bone with bovine origin is used to fill defects. Nowadays, xenografts are considered unsuitable for transplantation due to problems like risk of disease, virus transmission, infection and toxicity associated with sterilization [21].

Synthetics - In this category are considered all the applications developed in the Biomaterials and Tissue Engineering fields. The Synthetic BGM group is composed in its majority by 3D structures made with biodegradable and bioresorbable materials. Ceramics like HAp and β-Tricalcium phosphate (β-TCP), polymers like collagen, polycaprolactone (PCL), chitosan (CS), polylactide acid (PLLA) and metals like titanium and aluminum have been applied in a great variety of products. Since the architecture of the 3D structure plays an important role as physical support and as a vehicle for osteoinductive molecules and osteogenic cells, a major investment in the development of scaffold manufacturing techniques have been made with already good results.

Autologous bone grafts (autografts) remain the gold standard procedure to critical-sized bone defects but the adoption of synthetic solutions has been growing consistently [23]. In surgeries like craniofacial and dentoalveolar, bone grafts are frequently harvested from the skull tabula externa and from the jaw respectively, although iliac creast harvesting remains the most common donor site [24]. Autografts are not the ideal solution since the complication rate is as high as 39% and may include donor site morbidity, pain, paresthesia, prolonged hospitalization and rehabilitation, increased risk of deep infection, hematoma, inflammation and cosmetic deformity [21, 25, 26]. Xenografts and allografts are generally associated with potential viral infections, low osteogenicity and high resorption rate when compared with autologous bone. These factors have contributed to the increase of the demand for synthetic solutions with better performance than autografts and has prompted the scientific community to use the knowledge on biomaterials and tissue engineering fields to develop new grafts.

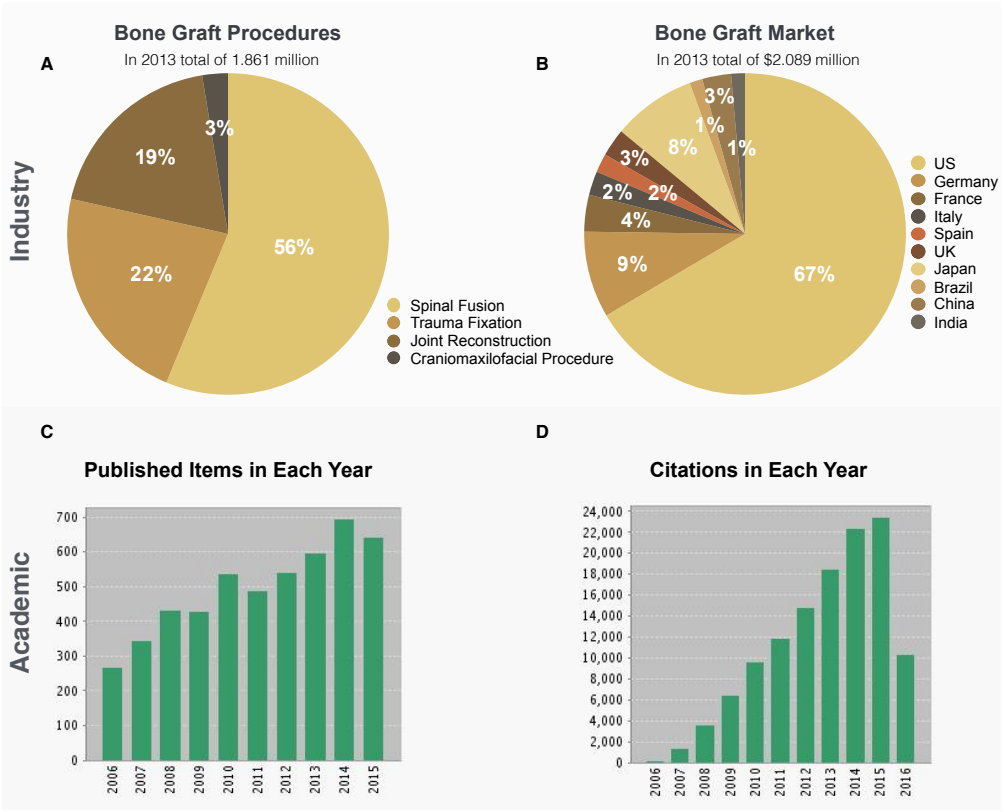

Figure 1.5: Graphic representation of bone grafts in: Industry - procedures (A) and market (B) in 2013 (Source: GlobalData Plc. 2016); Academic - papers (C) and citations (D) in the last 10 years (Source: Web of Science™2016. Keywords: scaffolds, bone tissue engineering, materials science, engineering).

In fact the academic interest on this subject has been growing in the last 10 years and the number of works related to scaffolds for bone tissue engineering applications have nearly reached a maximum of 700 papers in 2014 and 23.000 citations in 2015 (Figure 1.5 C and D). The industry is strongly betting in the development of new solutions for the

agressive BGM market and although the main solutions rely in 100% orthophospate based products, the combination between ceramics and polymers emerge with emphasis on the research of materials *bio* character either by profiteering from their intrinsic properties and/or with the incorporation of proteins and growth factors [27].

In 2013 a total of 1.861 million procedures involving bone grafting were performed worldwide from which 1.047 million were spinal fusion, 414 million of trauma fixation, 352 million of joint reconstruction and 48 million of craniomaxilofacial procedures. The BGM market (Figure 1.5 - B) represents 55% of the *Orthobiologics* segment (repair, replacement and regeneration solutions for musculosketal structures) and it has reflected a total revenue of U.S. $2.089.5 million in the 10 major markets including United States, France, Germany, Italy, Spain, United Kingdom, Japan, Brazil, China and India [28, 29]. This market is expected to growth into a total of U.S. $2.708.7 million by 2020 due to the increase of the number of affected people, a tendency primarily being driven by the incidence of arthritis, increasingly elderly population, rising incidence of road accidents, higher obesity rates and increasing participation in sports related activities.

1.3 Mission

One of the current challenges of orthopedic surgery is the regaining of bone volume lost due to trauma, cancer surgery or congenital disorders. The number of affected people is increasing and the existing solutions don't fulfill all requirements to correctly address this problem. Since the architectural design is extremely important to develop synthetic solutions that can allow good cellular distribution, mass transport conditions, nutrients and metabolites diffusion and vascular ingrowth, the search for the ideal scaffold is still underway.

The work reported in this thesis envisages the production of new bone scaffolds for tissue regeneration using the *Inverted Colloidal Crystal* (ICC) structure as model system. Benefiting from the superior capabilities of ICC structure, HAp and chitosan/chitin were applied as inorganic and organic building materials for the development of matrices with osteoconductive properties. With this approach the author hopes to offer valuable solutions that can trigger interest in the development of further ICC based products capable of complementing or substituting the gold standard solution and that away improve patients life quality around the world.

1.4 Thesis Outline

To accomplish the production of new ICC scaffolds for bone regeneration, a set of major objectives were defined, framed into main topics and described as chapters in this thesis.

Chapter 1 - Motivation

Establishment of the background and the motivation that led to this PhD thesis

elaboration.

Chapter 2 - An Overview of Inverted Colloidal Crystal Systems for Tissue Engineering
Literature review on ICC technology development, highlighting their main applications in the biomedical and tissue engineering fields.

Chapter 3 - The Colloidal Crystal Template
The third chapter reports the development of the starting unit in ICC construction that serve as base for all scaffolds reported in this thesis.

Chapter 4 - Hydroxyapatite Inverted Colloidal Crystal Scaffolds
The chapter reports the production of completely ceramic ICCs with a simple method of simultaneous sphere removal/matrix production and based on hydroxyapatite sol-gel synthesis.

Chapter 5 - Chitosan Inverted Colloidal Crystal Scaffolds
In this chapter the influence of chitosan molecular weight in ICC biodegradability and structural performance is examined.

Chapter 6 - Composite Chitosan/Hydroxyapatite Inverted Colloidal Crystal Scaffolds
The production of composite ICCs and their mechanical and biological properties are discussed.

Chapter 7 - Structures with Imprinted Liquid Crystalline Architecture
Inspired by collagen and chitin liquid crystalline based hierarchical structures observed in bones and arthropods exoskeleton respectively, this work reports: *Part 1*- the capturing and transferring of chitin nanowhiskers' chiral nematic order into a polymeric matrix; *Part 2* - the production of ICC scaffolds with imprinted liquid crystalline matrix.

Chapter 8 - Conclusion and Future Perspectives
The final chapter gathers the thesis main achievements and unlocks the path for future development in ICC based products for bone tissue engineering applications.

References

[1] B. Clarke. "Normal bone anatomy and physiology." In: *Clinical Journal of the American Society of Nephrology* 3 Suppl 3 (Nov. 2008), S131–S139. DOI: 10.2215/CJN.04151206. URL: http://eutils.ncbi.nlm.nih.gov/entrez/eutils/elink.fcgi?dbfrom=pubmed&id=18988698&retmode=ref&cmd=prlinks.

[2] J. E. Fonseca. "Bone Biology: from macrostructure to gene expression". In: *Medicographia* 34.2 (2012), pp. 142–148. URL: http://www.medicographia.com/category/medicographia-nÂř111/.

[3] A. Nather, ed. *Bone Grafts and Bone Substitutes: Basic Science and Clinical Applications*. English. World Scientific Publishing Company, Sept. 2005. ISBN: 9812560890. URL: http://0-www.ovid.com.innopac.lsuhsc.edu/site/catalog/Book/8660.pdf.

[4] U. G. K. Wegst, H. Bai, E. Saiz, A. P. Tomsia, and R. O. Ritchie. "Bioinspired structural materials." In: *Nature materials* 14.1 (Jan. 2015), pp. 23–36. DOI: 10.1038/nmat4089. URL: http://adsabs.harvard.edu/cgi-bin/nph-data_query?bibcode=2015NatMa..14...23W&link_type=EJOURNAL.

[5] K. Rogers. *Bone and Muscle*. English. Structure, Force, and Motion. The Rosen Publishing Group, 2010. ISBN: 9781615301010. URL: http://books.google.pt/books?id=wDIjRrMdlBgC&printsec=frontcover&dq=intitle:Bone+and+Muscle&hl=&cd=1&source=gbs_api.

[6] A. L. Boskey. "Bone composition: relationship to bone fragility and antiosteoporotic drug effects." English. In: *BoneKEy reports* 2 (2013), pp. 447–447. DOI: 10.1038/bonekey.2013.181. URL: http://www.nature.com/doifinder/10.1038/bonekey.2013.181.

[7] M. M. G. Guille, G. Mosser, C. Helary, and D. Eglin. "Bone matrix like assemblies of collagen: From liquid crystals to gels and biomimetic materials". In: *Micron* 36.7 (Jan. 2005), pp. 602–608. DOI: 10.1016/j.micron.2005.07.005. URL: http://linkinghub.elsevier.com/retrieve/pii/S0968432805001101.

[8] M. M. Giraud-Guille. "Twisted plywood architecture of collagen fibrils in human compact bone osteons." English. In: *Calcified tissue international* 42.3 (Mar. 1988), pp. 167–180. URL: http://eutils.ncbi.nlm.nih.gov/entrez/eutils/elink.fcgi?dbfrom=pubmed&id=3130165&retmode=ref&cmd=prlinks.

[9] M.-M. Giraud-Guille, L. Besseau, and R. Martin. "Liquid crystalline assemblies of collagen in bone and in vitro systems." English. In: *Journal of Biomechanics* 36.10 (Sept. 2003), pp. 1571–1579. URL: http://eutils.ncbi.nlm.nih.gov/entrez/eutils/elink.fcgi?dbfrom=pubmed&id=14499304&retmode=ref&cmd=prlinks.

[10] M.-M. Giraud-Guille, E. Belamie, and G. Mosser. "Organic and mineral networks in carapaces, bones and biomimetic materials". English. In: *Comptes Rendus Palevol* 3.6-7 (Oct. 2004), pp. 503–513. DOI: 10.1016/j.crpv.2004.07.004. URL: http://linkinghub.elsevier.com/retrieve/pii/S1631068304001289.

[11] E Belamie, G Mosser, F Gobeaux, and M. M. Giraud-Guille. "Possible transient liquid crystal phase during the laying out of connective tissues: α-chitin and collagen as models". In: *Journal of Physics: Condensed Matter* 18.13 (Mar. 2006), S115–S129. DOI: 10.1088/0953-8984/18/13/S08. URL: http://stacks.iop.org/0953-8984/18/i=13/a=S08?key=crossref.a0b2707d2393b2c24479b3a4754c1f32.

[12] S. C. Cowin, ed. *Bone Mechanics Handbook, Second Edition*. English. 2nd ed. Informa Healthcare, Mar. 2001. ISBN: 0849391172. URL: http://scholar.google.com/scholar?q=related:ZENkK4LUWTsJ:scholar.google.com/&hl=en&num=30&as_sdt=0,5.

[13] C. van Blitterswijk, P. Thomsen, J. Hubbell, R. Cancedda, J. D. de Bruijn, A. Lindahl, J. Sohier, and D. F. Williams. *Tissue Engineering (Academic Press Series in Biomedical Engineering)*. English. 1st ed. Academic Press, Apr. 2008. ISBN: 0123708699. URL: http://books.google.com/books?id=AN9s2p9ZzgoC&pg=PR11&dq=Tissue+Engineering+Langer&hl=&cd=7&source=gbs_api.

[14] T. A. Einhorn and L. C. Gerstenfeld. "Fracture healing: mechanisms and interventions." In: *Nature Reviews: Rheumatology* 11.1 (Jan. 2015), pp. 45–54. DOI: 10.1038/nrrheum.2014.164. URL: http://www.nature.com/doifinder/10.1038/nrrheum.2014.164.

[15] J. M. Féron. "An Architect´s dream: a self-repairing structure". In: *Medicographia* 34.2 (), pp. 185–190.

[16] Office of the Surgeon General (US). "Bone Health and Osteoporosis: A Report of the Surgeon General". English. In: (2004). URL: http://eutils.ncbi.nlm.nih.gov/entrez/eutils/elink.fcgi?dbfrom=pubmed&id=20945569&retmode=ref&cmd=prlinks.

[17] E Hernlund, A Svedbom, M Ivergård, J Compston, C Cooper, J Stenmark, E. V. McCloskey, B Jönsson, and J. A. Kanis. "Osteoporosis in the European Union: medical management, epidemiology and economic burden". In: *Archives of Osteoporosis* 8.1 (2013), pp. 1–115. DOI: 10.1007/s11657-013-0136-1. URL: http://dx.doi.org/10.1007/s11657-013-0136-1.

[18] Orthoworld Inc. *The Orthopaedic Industry Annual Report 2009-2010*. Tech. rep. Chagrin Falls. URL: http://www.orthoworld.com.

[19] M. P. G. Bostrom and D. A. Seigerman. "The Clinical Use of Allografts, Demineralized Bone Matrices, Synthetic Bone Graft Substitutes and Osteoinductive Growth Factors: A Survey Study". English. In: *HSS Journal* 1.1 (Sept. 2005), pp. 9–18. DOI: 10.1007/s11420-005-0111-5. URL: http://link.springer.com/10.1007/s11420-005-0111-5.

[20] A. J. Salgado, O. P. Coutinho, and R. L. Reis. "Bone Tissue Engineering: State of the Art and Future Trends". English. In: *Macromolecular Bioscience* 4.8 (Aug. 2004), pp. 743–765. DOI: 10.1002/mabi.200400026. URL: http://doi.wiley.com/10.1002/mabi.200400026.

[21] J. R. Porter, T. T. Ruckh, and K. C. Popat. "Bone tissue engineering: A review in bone biomimetics and drug delivery strategies". English. In: *Biotechnology Progress* (2009), NA–NA. DOI: 10.1002/btpr.246. URL: http://doi.wiley.com/10.1002/btpr.246.

[22] P. V. Giannoudis, H. Dinopoulos, and E. Tsiridis. "Bone substitutes: an update." English. In: *Injury* 36 Suppl 3 (Nov. 2005), S20–7. DOI: 10.1016/j.injury.2005.07.029. URL: http://eutils.ncbi.nlm.nih.gov/entrez/eutils/elink.fcgi?dbfrom=pubmed&id=16188545&retmode=ref&cmd=prlinks.

[23] A. Kinaci, V. Neuhaus, and D. C. Ring. "Trends in Bone Graft Use in the United States". English. In: *Orthopedics* 37.9 (Sept. 2014), e783–e788. DOI: 10.3928/01477447-20140825-54. URL: http://www.healio.com/doiresolver?doi=10.3928/01477447-20140825-54.

[24] H Schaaf, S Lendeckel, H. P. Howaldt, and P Streckbein. "Donor site morbidity after bone harvesting from the anterior iliac crest". In: *YMOE* 109.1 (Jan. 2010), pp. 52–58. DOI: 10.1016/j.tripleo.2009.08.023. URL: http://dx.doi.org/10.1016/j.tripleo.2009.08.023.

[25] A. E. Freeland and J. P. Rehm. "Autogenous bone grafting for fractures of the hand." English. In: *Techniques in hand & upper extremity surgery* 8.2 (June 2004), pp. 78–86. DOI: 10.1097/01.bth.0000129885.85827.ea. URL: http://content.wkhealth.com/linkback/openurl?sid=WKPTLP:landingpage&an=00130911-200406000-00004.

[26] R. Dimitriou, G. I. Mataliotakis, A. G. Angoules, N. K. Kanakaris, and P. V. Giannoudis. "Complications following autologous bone graft harvesting from the iliac crest and using the RIA: A systematic review". In: *Injury* 42 (Sept. 2011), S3–S15. DOI: 10.1016/j.injury.2011.06.015. URL: http://dx.doi.org/10.1016/j.injury.2011.06.015.

[27] S. V. Dorozhkin. *Calcium Orthophosphates*. English. Applications in Nature, Biology, and Medicine. CRC Press, June 2012. ISBN: 9814316628. URL: http://books.google.pt/books?id=VouONZJhBE4C&printsec=frontcover&dq=intitle:Calcium+Orthophosphates+applications+in+nature&hl=&cd=1&source=gbs_api.

[28] G. Research. *Orthobiologics Market to 2016 - Alternatives to Surgery and Superior Outcomes are Driving Wider Adoption of Orthobiologics*. Tech. rep. URL: http://www.marketresearch.com/GBI-Research-v3759/Orthobiologics-Alternatives-Surgery-Superior-Outcomes-6501704/.

[29] GlobalData. *Bone Grafts and Substitutes - Global Analysis and Market Forecast*. Tech. rep. GDME0192MAR. GlobalData, Jan. 2014. URL: http://store.globaldata.com/market-reports/Medical-Devices/MediPoint-Bone-Grafts-and-Substitutes-Global-Analysis-and-Market-Forecasts#.VwebjWNszBI.

Chapter 2

An Overview of Inverted Colloidal Crystals Systems for Tissue Engineering

Scaffolding is at the heart of tissue engineering but the number of techniques available for turning biomaterials into scaffolds displaying the features required for a tissue engineering application is somewhat limited. ICC are inverse replicas of an ordered array of monodisperse colloidal particles, which organize themselves in packed long-range crystals. The literature on ICC systems has grown enormously in the past 20 years, driven by the need to find organized macroporous structures. Although replicating the structure of a packed Colloidal Crystal (CC) into solid structures has produced a wide range of advanced materials (e.g., photonic crystals, catalysts, and membranes) only in recent years have ICCs been evaluated as devices for medical/pharmaceutical and tissue engineering applications. The geometry, size, pore density, and interconnectivity are features of the scaffold that strongly affect the cell environment with consequences on cell adhesion, proliferation, and differentiation. ICC scaffolds are highly geometrically ordered structures with increased porosity and connectivity, which enhances oxygen and nutrient diffusion, providing optimum cellular development. In comparison to other types of scaffolds, ICCs have three major unique features: the isotropic three-dimensional environment, comprising highly uniform and size-controllable pores, and the presence of windows connecting adjacent pores. Thus far, this is the only technique that guarantees these features with a long-range order, between a few nanometers and thousands of micrometers. In this review, we present the current development status of ICC scaffolds for tissue engineering applications[1].

[1] The work described in this chapter is based on the publication: C. F. C. João, J. M. Vasconcelos, J. C. Silva, and J. P. Borges. "An Overview of Inverted Colloidal Crystal Systems for Tissue Engineering". In: Tissue Engineering Part B: Reviews 20.5 (Oct. 2014), pp. 437–454 [1].

2.1 Introduction

Tissue engineering aims at developing new solutions for tissue repair and regeneration based on biological substitutes [2]. The scaffold-based tissue engineering (TE) concept involves the use of designed constructs that may contain a specific population of cells and/or bioactive molecules to promote the recovery of form and function in affected tissues and organs [3–5]. To engineer a living tissue with a specific function, a matrix material (natural or synthetic) plays a critical role in allowing the appropriate cell distribution and in guiding tissue regeneration in three dimensions. The scaffold acts as a synthetic extracellular matrix that cells interact with, before forming a new tissue. The structural features of tissue engineering scaffolds affect cell response and must be engineered to support cell adhesion, proliferation, migration, and, possibly, differentiation. Therefore, to develop a scaffold, the architectural design concerning the spatial cellular distribution, mass transport conditions, nutrient and metabolite diffusion, and tissue function are very important [6–8]. In this way, a scaffold ought to meet several generic requirements:

1. The material used for fabricating the scaffold must be biocompatible and biodegradable and allow cell adhesion and migration;
2. The scaffold must contain a network of pores, and preferably in the form of a three-dimensional (3D) interconnected architecture;
3. The scaffold should have proper mechanical properties to suit the specific application and temporarily offer structural support until new tissue has formed;
4. The scaffold degradation rate should be adjustable to match the tissue regeneration rate;
5. The scaffold should be resorbed once it has served its purpose of providing template for regenerating tissue.

To achieve a well-defined scaffold, a number of fabrication technologies have been applied to process biodegradable and bioresorbable materials into 3D polymeric or composite scaffolds of high porosity and surface area [3–5, 9]. Techniques, such as porogen leaching[10], phase separation [7, 11], gas foaming [12, 13], emulsion freeze drying [14], electrospinning [15–17], 3D printing [18],extrusion [19, 20], selective laser sintering [21] solid free-form fabrication and rapid prototyping [22] have been suggested as capable of producing 3D structures for tissue growth. The literature [5] reports the known methods of producing tissue-engineered constructs, with extensive descriptions about the particularities of those methods, their potential and limitations. Notwithstanding the great advances that have been made in scaffolding, the majority of the methods fail in one or more specifications of what a scaffold should be. Irregular pore sizes and pore distribution, irregular structure and shape, lack of a well-defined third dimension, poor

connectivity, and lack of mechanical strength are pointed out as recurring problems [4, 23, 24].

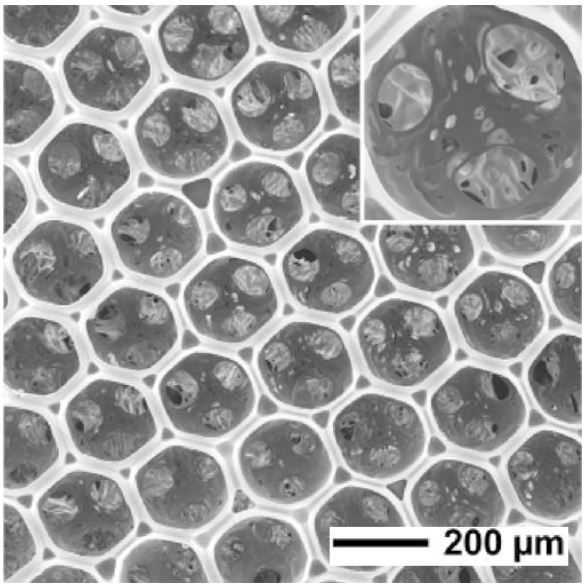

Figure 2.1: SEM image of a poly(lactic-co-glycolic acid) (PLGA) inverted colloidal crystal (ICC) scaffold. Inset: Example of the high organization achieved in a scaffold with ICC architecture. Adapted with permission from Choi et al. [25] copyright ©2010 American Chemical Society.

In an effort to solve these problems, several groups have suggested the use of the inverse opal, or inverted colloidal crystal, structure as an ideal system, which presents a high degree of organization with the most uniform pore size and regular 3D interconnectivity [26]. In ICC scaffolds, thanks to the hexagonal close packed (hcp) geometry created by microspheres self-assembly, each spherical cavity is connected with up to 12 nearest-neighbor cavities, allowing efficient cell migration and nutrient and oxygen diffusion in all directions. Since the uniform size and connection between pores are reported to interpret a vital function in cell culture because they are responsible for adhesion, migration, and cell distribution and also for the exchange of nutrients and metabolite wastes, ICC scaffolds (Figure 2.1) seem to be the best approach so far, capable of producing a structure with the best results in cell growth and tissue regeneration. In this chapter the methods of ICC scaffold production are reviewed, including the most used techniques for colloidal crystals production, the hexagonal close packing of microspheres, and ICC scaffold assembly. We also address the applications of ICCs to tissue engineering reported in the literature.

2.2 ICC scaffold

Many artificial structures have been synthesized based on CCs. Here, we review the approach that consists in assembling CCs in order to serve as templates, whose voids

are infiltrated by material that solidifies there. The original colloidal particles are then removed, leaving behind a material with pores that preserve a long-ranged periodic structure. Although replicating the structure of packed CCs is a method widely used, for example, in novel photonic materials, only in 2001 was this first reported as a promising scaffold for biomedical applications. Peter X. Ma created 3D PLLA and PLGA scaffolds with paraffin spheres as template [27]. Even using nonuniform spheres with different sizes, these researchers achieved to construct a primitive ICC scaffold with high degree of interconnectivity and porosity. They also realized the influence of annealing temperature and time on the openings between pores.

In 2004, Ratner's group described the use of sphere-templated scaffolds to understand scaffold vascular in-growth and they found that the degree of vessel formation is highly dependent on the pores' size [28]. In the same year, Kotov et al. proved that ICCs could be used as 3D cell culture scaffolds. Using an hexagonal crystal lattice of polystyrene (PS) spheres and infiltrating it with a sol-gel formulation containing sodium silicate, they demonstrated that this type of scaffold was useful for cell–cell and cell–matrix interaction investigation during tissue generation following culture of human bone marrow cells [29]. Afterward, a number of works that focus on biomedical and tissue-engineered applications emerged. In general, the fabrication of ICC scaffolds includes three major steps [30]:

1. Production of uniform microspheres;
2. Fabrication of an hcp lattice;
3. Development of an inverse opal structure.

In the following sections we focus in more detail on these three steps.

2.2.1 Microspheres

Colloidal particles are used in many industries, such as the food, ink, paint, coating, paper, cosmetics, photographic films, printing, coating, drug delivery, and rheological fluid industry[31]. Colloidal systems can be obtained with particles with a diameter between a few nanometers and hundreds of micrometers [32]. Artificial opals (CCs) denote an optical band gap that has been under extensive study aimed at lasing media, 3D information storage, optical computing and switches, sensors, and catalysts. In medicine and biology, the application of CCs is being dominated by biosensors made from latex or silica spheres [26]. Other uses have been reported, such as drug carriers, blood flow indicators, cell culture carriers, particles for phagocytosis assays, and heterogeneous immunoassays [33]. PS colloids were successfully used for protein adsorption and slide agglutination, silica CCs were used for DNA/RNA adsorption and covalent attachment, and polymethylmethacrylate CCs were used for passive agglutination and CS microspheres for oral delivery of insulin [34].

In this review we focus on polymer microspheres (also referred to as beads) since they are the main source for ICC scaffold production in tissue engineering. Polymer microspheres can be prepared using a wide variety of methods: solvent-in-emulsion evaporation, phase separation, coacervation, spray drying, crosslinking/gelation, hot melting, grinding, electrospraying, and polymerization (emulsion, suspension, dispersion, and precipitation) [35, 36]. For polymerization techniques the starting material is unsaturated monomer molecules, which, upon chain-growth polymerization, will form the beads. For all the other techniques described hereafter the starting material is the polymer already.

Precipitation: Precipitation polymerization is a stabilizer or surfactant-free method that allows the synthesis of spheres with sizes in the range 0.1–100μm. The initial reaction mixture is homogeneous but the polymerization medium is a precipitant for the resulting polymer. No surfactant is required to stabilize the particles. It involves two steps: nucleation of the monomers followed by growth of the nuclei. Monodisperse microspheres have been produced with a standard deviation (SD)< 5% [37–41].

Dispersion: In general, dispersion polymerization involves the polymerization of monomer or comonomers dissolved in a solution with initiator and dispersant. These reactions start with a homogeneous phase and then phase separation occurs. Monodisperse particles are formed by the precipitation of the polymer, with diameters in the range 0.1–15μm and reported SD <5%. Parameters like type and concentration of the stabilizer, initiator and monomer, and solvent concentration, play important roles in producing microspheres with different diameters[42–47].

Emulsion: There are two types of emulsion polymerization: oil-in-water and water-in-oil emulsions. Oil-in-water emulsions are the most common and can be performed with water-insoluble monomers involving polymerization in the presence of an emulsifier and by the aid of a water-soluble initiator. Emulsion usually refers to a liquid dispersion with a broad distribution of particle diameters: 50–500μm for conventional emulsion and miniemulsion and 10–100μm for microemulsion. Particle size distributions commonly have SDs between 4% and 11% [48–52].

Suspension: Suspension is a polymerization process that involves a monomer or a mixture of monomers dispersed by strong mechanical agitation into droplets suspended in a liquid phase with the use of a stabilizer. Polydisperse monomer droplets (SD higher than 20%) are directly converted into polymer particles of approximately the same size and with a high degree of conversion. This method is widely used to produce polyvinyl chloride, styrene, and poly(styrene-acrylo-nitrile) spheres. The interfacial tension, the degree of agitation, and the design of the stirrer system govern the dispersion of monomer droplets, typically in the range of 10μm –5 mm [53–57].

Spray drying: This technique is widely used to produce powders, granules, and drug excipients. In the spray-drying method a polymer is dissolved in a suitable solvent and a spray dryer is used to disperse small droplets into a hot drying medium, where a stream of flowing gas solidifies them. Different particle sizes (generally in the 1–500 μm size range) can be obtained with narrow size distribution (SD < 2%) by modifying several parameters, such as concentration of the polymer, solution flow rate, spraying rate, and drying temperature [58–61].

Electrospraying: Electrospraying is a method similar to classical electrospinning. The difference between both methods relies in polymer concentration, with a critical value defining where one process stops and the other begins. During electrospraying, the polymer jet that emerges from the Taylor cone that forms at the tip of a charged needle breaks into droplets due to the lack of polymer chain entanglement. As the drops travel toward the collector, the solvent evaporates and solid particles are formed. A wide variety of spheres with diameters ranging from a few nanometers up to hundreds of micrometers, and SDs between 5% and 20%, have been reported [62–66].

Hot melting: Widely used in the industry for tube, pipe, granule, wire, and film productions. It has been also applied in pharmaceutical field to prepare sustained-release tablets and transdermal drug delivery systems. This technique often employs polymers with low melting point. The polymers are heated into the molten phase and then dispersed in a suitable dispersion medium and slowly cooled and fabricated into microsphere format. Microspheres with a SD between 1% and 5% have been reported[67–70].

Crosslinking/gelation: Sol–gel or gelation methods are used for fine-particle production. The gelation method uses a polymeric solution, starting from a sol state (colloidal solution) that evolves into a gel state (particles), which is extruded and submerged in a coagulation solution, which acts as a crosslinking agent of the polymer. Polydisperse spheres with diameters between 2 μm and 1 mm (SD higher than 10%) can be produced with this method [71–75].

Microfluidic: Recently, microfabrication using microfluidic methods has been reported to synthesize monodisperse microparticles. By generating highly monodisperse emulsion droplets, easily controlled with the combination of driving pressures of two immiscible fluids and geometry of microchannels, microspheres with < 5% diameter standard deviation can be obtained at a high throughput [31, 76–80].

Coacervation:There are two types of coacervation methods that can produce a broad range of polymer particles (from 500 nm to 2 mm): simple and complex. Simple coacervation is caused by changing the solvent composition or the solution temperature and complex coacervation is induced by ion complexes between polyelectrolytes and natural polymers, such as chitosan/poly(ethylene glycol) (PEG)–alginate.

Particle diameter SD can vary from 2% to 20% [81–85].

2.2.2 Packaging and Annealing

Packing of nano or microspheres results in organized structures (opalescent structures or artificial opals) that have singular properties useful in a variety of applications in optics, as photonic crystals, as solid-phase supports in catalysis, or as chemical sensors [86].

During particle aggregation, repulsive and attractive forces influence their self-organization. Spheres are packed into stable and low-energy systems, governed by the balance of force interactions: van der Waals dispersion forces, hard-core repulsion, Coulomb interaction, and hydrodynamic coupling [87]. The balance between competition and cooperation between these interactions gives rise to a variety of occurrences, including colloidal crystallization, gel formation, glass formation, and other collective responses to external forces and fields [88].

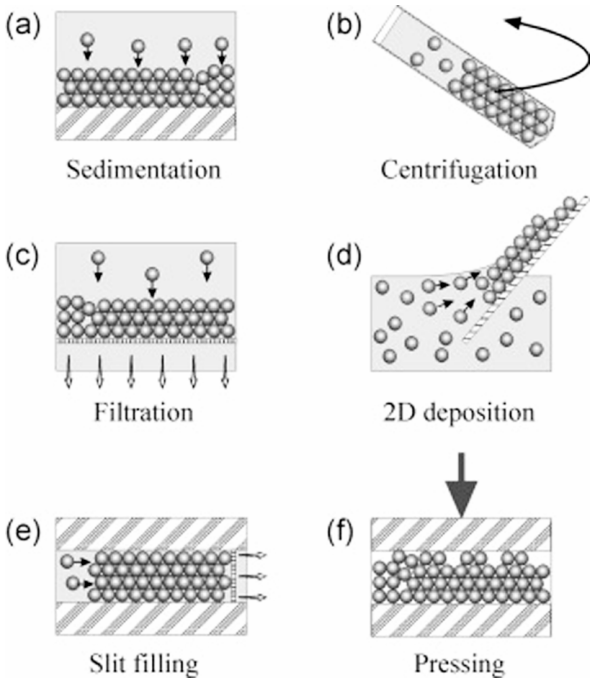

Figure 2.2: Methods used for colloidal crystal (CC) template assembling: (a) sedimentation, (b) centrifugation, (c) filtration, (d) 2D deposition, (e) slit filling, (f) pressing. Adapted from Velev et al. [89] copyright ©2010 with permission from Elsevier.

The relative importance of these interactions can be controlled by changing parameters, like sphere diameter, chemical composition, bulk structure, crystallinity, and surface functional groups. Structures formed by organized spheres are produced by a fundamental mechanism called self-assembly that requires particles with narrow size and shape distributions. By definition, self-assembly is the autonomous organization of components into patterns or structures without human intervention. In a system undergoing a self-assembly process, there is a flow of molecules until equilibrium is reached. In the

transition to the ordered state, microspheres tend to organize into the thermodynamically stable forms, face-centered cubic (fcc) and hcp structures[90]. If we are attempting a self-assembly in solution via Brownian motion, then the assembly process will depend on both the frequency of random particle impact and the size and orientation of the colliding particles. As the particle size increases, the Brownian driving force becomes weak. For large microspheres (> 10 μm), Brownian forces are insufficient to promote ordering and external fields or geometric confinements are needed to induce self-assembly. In Figure 2.2 we illustrate the most frequently used methods to assemble colloidal particles into organized structures. Along the years, procedures such as gravity sedimentation, centrifugation, vertical disposition, template deposition, electrophoresis, patterning, and controlled drying have been successfully used in microsphere assembly. Parameters such as temperature, air pressure, solvent, humidity, and the contact angle, are crucial to control the morphology and to improve the quality of assembled structures.

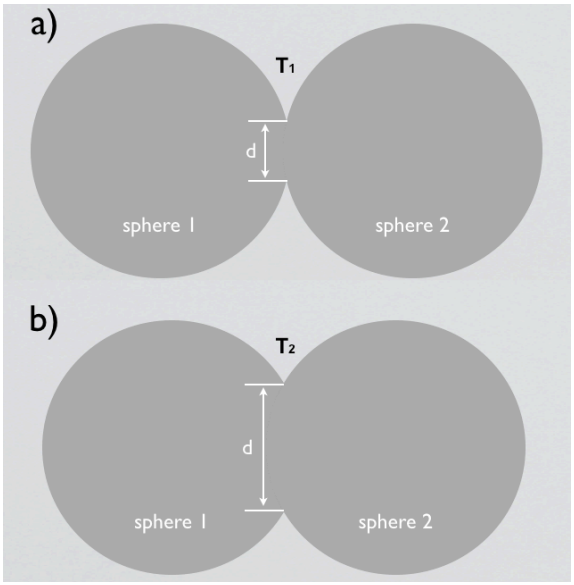

Figure 2.3: Schematics of the result of annealing microspheres at different temperatures: (a) annealing at temperature T1, (b) annealing at temperature T2, where T2 > T1. Reprinted with permission from João et al. [1] copyright ©2014 Mary Ann Liebert, Inc.

In CC construction, the term annealing is used to describe the heat treatment used to create bridges between consecutive spheres and turning the assembled structure into a linked solid construct. The major factor that influences the annealing process is the crystallinity of the polymer used to produce the spheres. Amorphous polymers, like PS, that soften above the glass-transition temperature allow an easier production of the bridges between the spheres allowing an easier production of the solid construct. On the other hand, if a crystalline polymer is used, then the annealing must be performed close to the melting point. In this case special care has to be taken to avoid complete fusion of the spheres and the formation of a solid film instead of a 3D solid based on the packing

of the spheres. This treatment is also responsible for the diameter of the interconnected pores (Figure 2.3). With the increase of the annealing temperature, the bridges become wider, resulting in ICC scaffolds with interconnected pores of higher diameter [91].

2.2.3 Construction

After assembling the CCs, we are two steps away from obtaining an ICC; these steps are biomaterial impregnation and bead removal. Applying a biocompatible polymer or composite in the form of a gel, solution, or even after melting fills the interstices between packed microspheres. Solidification of the structure between the microspheres can be achieved by, among other methods, polymerization, sol-gel hydrolysis of a liquid precursor, electrochemical deposition, infiltration followed by solvent evaporation, and crosslinking. Lastly, the beads are removed from the matrix (e.g., by dissolution) and the porous structure is obtained. This structure is the negative replica of the original CC (Figure 2.4) [89].

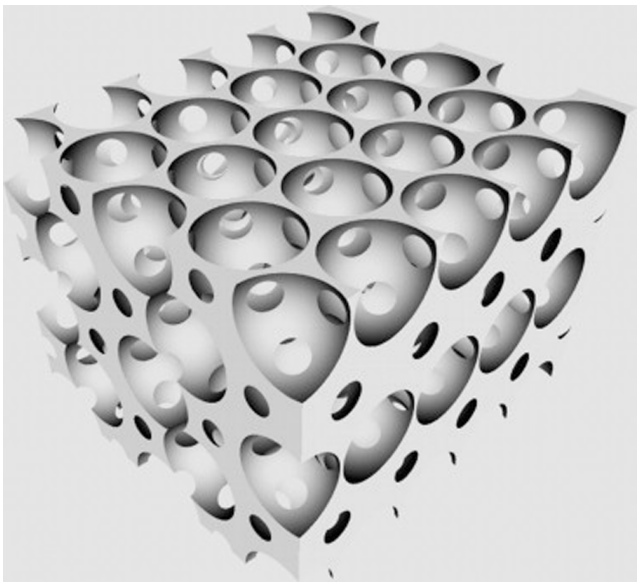

Figure 2.4: Schematic illustration of a CC negative replica (ICC scaffold). Reprinted from Takagi et al.[92] copyright ©2010 with permission from Elsevier.

The hcp geometry guarantees interconnectivity between all spherical cavities and a maximum theoretical porosity of 74% [93]. Using bone tissue engineering as an example, the high porosity of the scaffolds produced by traditional techniques (where porosities often approach 95% to ensure complete pore interconnectivity) denies sufficient mechanical strength to support the load of the body until bone regeneration is complete. In ICC scaffolding, the high interconnectivity with a lower porosity (comparing with disordered structures) leads to stiffer structures than predicted for bulk materials [93].

2.3 ICC scaffolds for Tissue Engineering

As previously stated, only in 2001 was the ICC scaffold first reported for tissue engineering purposes. Here we describe the publications in this field since then.

2004

Marshall et al.[28] extended their sphere-templating method to design degradable scaffolds for soft tissue engineering. They used polymethyl methacrylate (PMMA) beads with different sizes (20±5μm, 35±5μm, 50±5μm, 70±5μm, 90±5μm, and 160 ±15 μm) to form various fused-bead templates. They used these templates to create ICC scaffolds with a new degradable version of poly(2-hydroxyethyl methacrylate) (pHEMA). These scaffolds were implanted under the skin of mice for 4 weeks and after retrieval were evaluated histologically. They concluded that the number of blood vessels inside the pores increased as the pore size decreased, reaching a maximum at an optimum pore size of 35 μm.

Kotov et al. [29] experiences with CCs brought inverse replicas of spheres to another level. Using hexagonal crystal lattices of PS spheres they infiltrated them with a sol-gel formulation of Na_2SiO_3 and produced ICC scaffolds from this material. They found some advantages in this method: 1) easy control of pore dimension by changing sphere's diameter; 2) uniform spherical voids provide a uniform environment for cell evolution; 3) the ordered structure could be used in computer modeling of nutrient, metabolism and cell migration within the scaffold. After testing the scaffold biocompatibility with the incubation of HEP G2 (human hepatocellular carcinoma) and HS-5 (human bone marrow) cells, the authors observed cell behavior and distribution in four scaffolds with micropores of 10, 75, 90 and 165 μm. Higher cell density was observed on 75 μm scaffolds with cells forming closely associated colonies of 10-15 elements. Differences between element numbers in colonies of the two cell types were also observed in scaffolds with the same cavity size.

2005

Stachowiak et al.[93] reported a method to prepare soft hydrogels with interconnected pores at moderate void fractions, maintaining compressive stiffness comparable to native tissue. Using cross-linked poly(ethylene glycol) (PEG) solution to perfuse a CC template by centrifugation followed by photopolymerization, these researchers produced scaffolds with 78% porosity. The scaffolds were found to combine excellent interconnectivity with stiffness 10-1000 times greater than that predicted for disordered structures. Mechanical properties of PEG ICC scaffolds were evaluated and remained suitable for mimicking soft tissues. Cell attachment and migration was also observed after seeding fibroblasts on the scaffold.

Zhang et al. [26] produced a hydrogel matrix using a template of 104 μm poly(methyl methacrylate) spheres. The resulting ICC scaffold, with 97 μm spherical cavities, showed

higher swelling ratios and faster swelling equilibrium than the bulk material, combined with desirable mechanical and optical properties that can facilitate tissue regeneration while allowing continuous high-resolution optical monitoring of cell proliferation and cell-cell interaction within the scaffold. HEP G2 and HS-5 cells were seeded in the scaffold and thanks to the high optical transparency of this scaffold the monitoring of the growth and cell migration was possible. The results demonstrated that the scaffold has the ability to facilitate the infiltration of cells that remain viable deep within the scaffold, up to a depth of 250 μm observable by confocal microscopy.

Still in 2005, Shanbhag et al. contributed with two works about diffusion and cell distribution profiles in scaffolds with Inverted Colloidal Crystal geometry. In the first report [94] , these researchers used Brownian dynamics and Monte Carlo simulations to model the effective nutrient diffusivity. They found that nutrient diffusivity in ICC scaffolds was 30% (300 $\mu m^2 s^{-1}$) of free solution diffusivity and the characteristic distance travelled by a point particle was about 40 μm in 1 second. These measurements did not take into consideration the possible additional retardation that could arise from blocked intercavity pores by cell aggregation nor the adsorption of nutrients by scaffold walls. In real conditions, cells affect the concentration gradient of the nutrients by consuming them.

In the second work [95] a computational model was developed for explaining and predicting cell distribution considering effects like competitive product inhibition and cell-contact inhibition to describe the scaffold-cell interaction. First, stromal cells were seeded on ICC scaffolds constructed as reported before on previous works regarding sol-gel bioactive glasses with 3D ordered macroporous structures[96]. Cell growth and migration was observed after three weeks of seeding, registering stromal cells grow into fully packed monolayer on the surface of the scaffold but only 2-3 layers of spherical cavities within the scaffold. A computer model was developed and computational suggested a very good correlation between experimental and theoretical data. Like *in vitro* tests, the computational modeling showed that the ingrowth of adherent cells was identical, for both static and dynamic cell cultures, to the respective SEM observations indicating that the higly regular structure of ICC scaffolds is adapted for cell growth modeling. This approach presents as useful for tissue growth optimization in ICC scaffolds and other ordered 3D cell suports, taking into account the transport restrictions.

Liu et al.[97] managed to produce CC templates by a floating self-assembly technique using polystyrene (PS) particles (10-240μm) and ethylene glycol as a solvent. In the floating self-assembly of colloidal crystals, the density of the solvent ethylene glycol plays an important role since its density (1.11 g/mL) is higher than that of PS (1.05 g/mL), which leads to the floating of polystyrene microspheres.

Slow evaporation of the solvent induces microsphere assembly into a solvent-free 3D hexagonal crystal lattice structure. Infiltrating a Na2SiO3 solution via capillary force into the template interstitials, the resulting ICC scaffold was used as cell scaffold for HEP G2

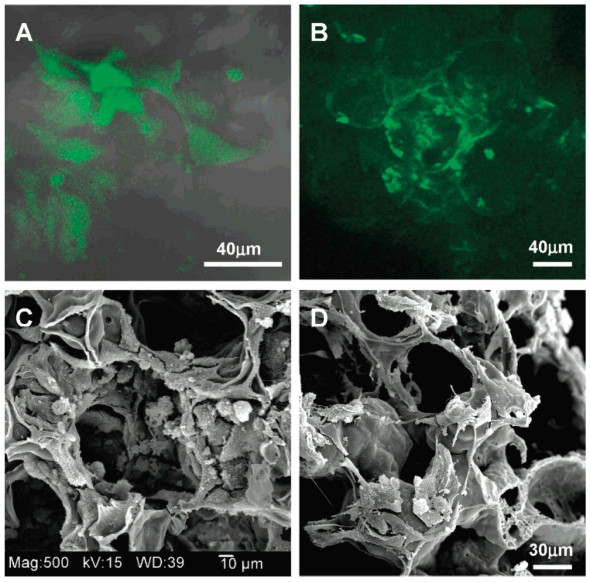

Figure 2.5: Confocal microscopy and SEM images of 80μm scaffolds after incubation with a cell culture for 8 days: (A) confocal, HEP G2 cells, (B) confocal HS-5 cells, (C) SEM, HEP G2 cells, (D) SEM, HS-5 cells. Reprinted with permission from from Liu et al.[97] copyright ©2005 American Chemical Society.

and HS 5 cell cultures (Figure 2.5).

2006

Lee et al.[98] presented a new form of ICC scaffold development. Based on layer-by-layer assembly with clay nanoparticles/poly (diallyldimethylammonium chloride) (PDDA), they introduced adherent and non-adherent cells in the scaffold and simulated the non-adherent cells migration. After PS microsphere assembly and heating at 120°C for softening of the bead's surface, a poly(acryl amide) hydrogel was used to infiltrate the template by centrifugation. To the hydrogel precursor solution, a cross-linker and a fluorescent monomer were also added. The surfaces of the ICC hydrogel scaffold were coated with sequential layer-by-layer (LBL) deposition of positively charged PDDA enhancing cell adhesion because acrylamide polymer chains of the hydrogel matrices do not have cell adhesion receptors. Human thymic epithelial cells and human premyeloblast monocytes were seeded on the scaffolds. Confocal microscopy images showed the diffusion of many monocytes while some remained entrapped inside the pores. While epithelial cells densely covered the scaffold exterior, monocytes travelled deeper within the scaffold. Modeling through simplified Brownian dynamics revealed that cells were effectively trapped in the spherical chambers and entrapped suspension cells spent a significant fraction of time in the vicinity of the ICC chamber wall or the epithelial coating in co-cultures. Lee et. al. concluded that the proposed ICC scaffold structure generates super and cellular scale microenvironment for intense cell contacts with other cells or matrix and that the addition of signaling molecules and membrane bound receptors is possible through

the layer-by-layer method used.

Yi et al.[99] communicated the crosslinking of polydimethylsiloxane prepolymer under controlled rheological conditions to produce a two-dimensional (2D) microring interconnected honeycomb structure using colloidal templates. Bacterium *Serratia marcescens* was patterned on the microstructure and the results demonstrated that the 2D scaffold had higher induced packing density of bacteria compared to the case of using non-patterned flat polydimethylsiloxane susbstrate. The honeycomb structure evidenced the potential application for microbioanalytical devices, micro-fluidics and bio-micro-electromechanical systems.

2007

Bryant et al.[100] produced novel photopatterned hydrogel scaffolds based on sphere templates. Briefly, PMMA microspheres were annealed at 140°C during 19h to form a CC template. The CC template was infiltrated with pHEMA and inverse photomasks (200, 300, 400, and 500μm channel spaces) were applied with the objective of producing patterned hydrogels. Following infiltration of the polymer, initiation light was allowed to pass through the photomask with different intensities. After sphere removal, patterned and porous hydrogels were obtained (62±6 μm and 147±15 μm pore size). To increase cell adhesion, collagen type I was immobilized on the scaffold surfaces. Mouse skeletal myoblasts (C2C12) were seeded on the scaffold to assess the potential for tissue engineering applications. Histology analysis revealed that patterned pHEMA ICCs with collagen I evidenced cell elongation, spreading, and dispersion along the scaffold, when compared with scaffolds not containing collagen. Three-dimensional digital volumetric imaging also showed that myoblasts appeared to form a network of fibrillar structures in the void spaces and also the cells/fibrillar structures were aligned circumferentially along the channel walls.

Liu and Wang [101] developed a cell scaffold with luminescence-based oxygen sensing capability offering the possibility of 3D mapping of oxygen level during cell growth. Using PMMA microspheres to construct a close-packed bead template (50-150 μm), inverse colloidal crystal scaffolds were obtained by photo-polymerization of poly(2-hydroxyethyl methacrylate) (pHEMA) and poly(methacryloyloxy) ethyltrimethylammonium chloride (pMEATAC), and were consecutively LBL coated with tris(4,7-diphenyl-1,10-phenanthroline) ruthenium chloride (Ru(dpp)3). Human bone marrow stromal cells HS 5 were seeded on the scaffolds to observe oxygen level variation within the scaffold due to oxygen consumption by the cells. Since the fluorescence emission of Ru(dpp)3 can be dynamically quenched by oxygen, measurement of emission intensity allows monitoring of local oxygen level. Fluorescence quenching is related to the frequency of collisions between oxygen and Ru(dpp)3 molecules, which is a function of concentration, pressure and temperature of oxygen in the medium. An enhanced Ru(dpp)3 emission occurred in cell rich areas within the scaffold although the local concentration of oxygen could not be quantified by photoluminescence due to shifting of baseline emission.

Also in 2007, Liu et al. [102] worked on an aqueous photo-polymerization towards the fabrication of different polymer hydrogel 3D ICC scaffolds presenting different physical and chemical properties. Noncrosslinked PMMA beads with uniform (104 μm) and non-uniform size (100± 20 μm) where used for colloidal crystal templating. Various polymers were used like polyacrylamide (pAAM), pHEMA and poly(2-hydroxyethyl acrylate) (pHEA), and also polymer mixtures like pAAM-pHEMA, pHEMA-pMAETAC and pHEA-pMEATAC. HS 5 cells were again cultured on the six different scaffold types for biocompatibility testing. All the scaffolds supported cell cultures but the polymer blend scaffolds with positively charged components (pHEMA-pMEATAC and pHEA-pMEATAC) were found to have improved cell adhesion and proliferation. These scaffolds were proposed as having great potential for accelerating in-vitro cell culture and in-vivo tissue regeneration.

Stachowiak [103, 104] developed and tested macroporous poly(ethylene glycol) (PEG) hydrogel scaffolds as platforms for lymphoid tissue models for the study of immune cell migration and immunotherapy. Inspired by the idea of engineering lymphoid tissue at disease sites (e.g. tumors) for boosting insufficient native immunity, Stachowiak applied the method of colloidal crystal templating to materials and length scales appropriate for soft tissues. After ICC construction, T lymphocytes were seeded and biological tests were performed. Migratory responses were tested looking for T cell motility as a base for the promotion of efficient immune responses. Results pointed to the need of polymer blend scaffolds structure to attain *in vivo*-like cell migration. A modified ICC scaffold was developed, with the porous PEG hydrogel providing mechanical stability and the ability to deliver proteins of interest, while an infused fibrillar collagen gel supported intra-scaffold migration of loaded T lymphocytes and dendritic cells.

2008

Addressing the need of bone tissue engineering for scaffolds with high porosity, high interconnectivity and sufficient mechanical strength, Cuddihy and Kotov [91] introduced in 2008 a biodegradable PLGA ICC scaffolds based on soda lime colloidal particles assembly (Figure 2.6) . Following colloidal crystal assembly, a range of annealing temperatures (660 ºC and 690 ºC for 100 μm spheres, 690ºC and 720ºC for 200 and 300 μm spheres) was used to adjust the stability of the colloidal templates. Then, they were submerged in a solution of 85:15 PLGA in methylene chloride, allowing time for solution infiltration. The removal of colloidal crystals was possible through the application of an hydrofluoric acid/hydrochloric acid cycle followed by a washing stage with phosphate buffered saline (PBS) for ICC scaffold pH stabilization at 7.4.

Measurement of interconnecting channel diameter for different annealing temperatures revealed that channels diameter increases with temperature. Mechanical properties were evaluated through compressive tests and the results showed that with increase of cavity diameter the compressive modulus of ICCs decreases. For biocompatibility testing,

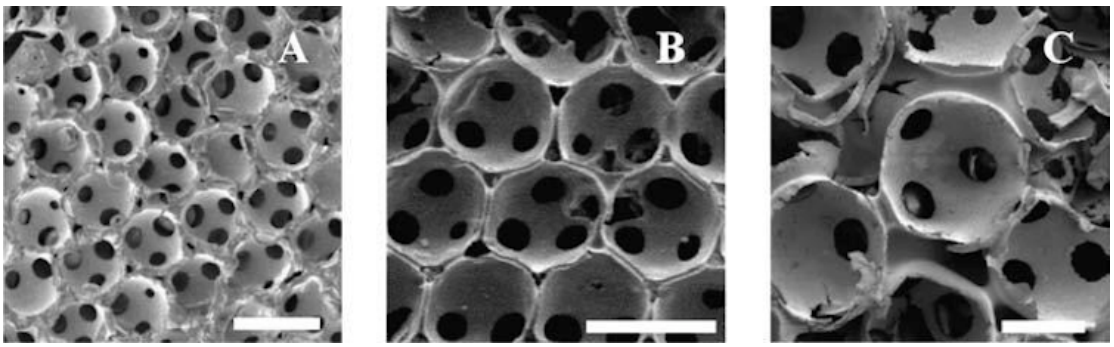

Figure 2.6: SEM images of PLGA ICC scaffolds: A) 100 μm; B) 200 μm; C) 300 μm. Scale bar=200 μm. Reprinted with permission from Cuddihy and Kotov [91]copyright ©2008 Mary Ann Liebert, Inc.

human fetal osteoblasts (hFOB) were introduced in the scaffolds. Microscopy observations indicated that larger pore sizes (>100 μm) could increase cell growth and bone formation.

2009

Nichols et al. [105] worked on *in vitro* artificial bone marrow based on a three-dimensional scaffold with Inverted Colloidal Crystal geometry mimicking the structural topology of bone marrow matrix. These researchers found in ICC scaffolds a way to obtain a suitable 3D matrix with sufficiently large surface area for cell attachment, high porosity for cell migration and transport of nutrients and the possibility of modifying its surface to control cell-to-cell contacts. By applying LBL technique (as mentioned in (95)) they coated a polyacrylamide hydrogel ICC scaffold with sequential layers of negative and positive charges of clay platelets and PDDA solution, respectively. For ICC scaffold production, PS beads with a diameter of 110 μm were used, originating cavities with the same dimension and interconnecting channels of 10-20 μm. To analyze the capability of the scaffold to mimic bone marrow stroma, human bone marrow stromal cells were seeded on scaffolds and cultured for 3 days to allow the formation of a support cell layer on the scaffold surface prior to the addition of CD34+ hematopoietic stem cells (HSCs). Stromal cells were also seeded on 2D plates to establish the importance of the 3D geometry. After observing confocal microscopy images, the authors concluded that cells in ICC scaffolds formed more actin-rich cell processes and demonstrated substantially more CD34+ proliferation than plate cultures. The scaffold was also able to support B-lymphocyte differentiation since B cell development involves a series of stages where close 3D contact between bone marrow stroma and the developing B cell is critical. To confirm the *in vitro* results, the bone marrow construct was used to perform *in vivo* tests by implantation of matrices containing human CD34+ cells onto the back of severe combined immunodeficiency (SCID) mice with subsequent generation of human immune cells. This work demonstrated that the organized structure of the ICC scaffold

provided the essential environment (similar to *in vivo* bone marrow environment during hematopoiesis and B lymphopoiesis) to support proliferation of CD34+ HSCs cells and B lymphocyte differentiation with production of functional B cells.

Choi et al. [30] described a technique for fabricating chitosan Inverse Opal scaffolds by using polycaprolactone (PCL) microspheres template. CS, a nontoxic, anti-microbial, biocompatible and biodegradable co-polymer is a widely used material (e.g electrospinning , wet-spinning, microfluidics) but in this article it was used for the first time as matrix material in ICC scaffolds. Using the principles of emulsion, Choi and his co-workers produced PCL microspheres of (147,7 ± 1,4) μm based on the methods described on a well-know work for preparation of uniform microspheres using a simple fluidic device [31]. Microspheres dispersed in water were self-assembled by sedimentation and after solvent evaporation the colloidal crystal lattice was heated for microsphere annealing. By capillary force a solution of chitosan was infiltrated through the lattice under vacuum suction. After freeze-drying of the chitosan solution, the structure was submerged in dichloromethane (DCM) for PCL removal, originating the ICC chitosan scaffold (Figure 2.7).

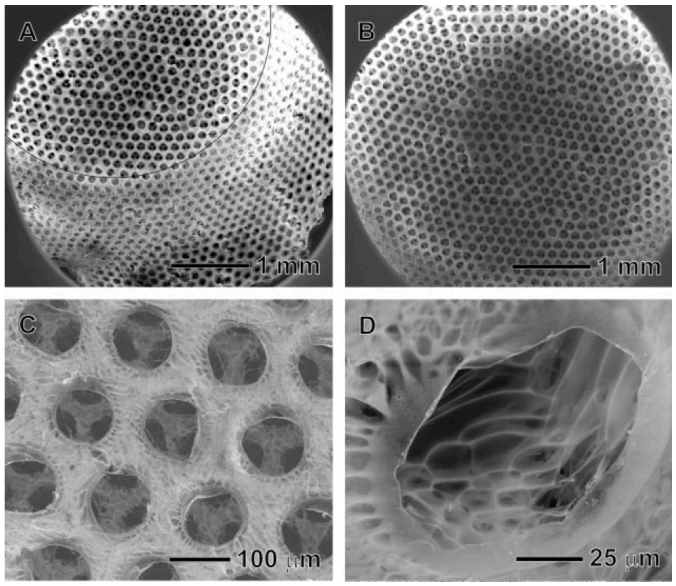

Figure 2.7: SEM images of chitosan ICC scaffold. A) side view, B) top view, C) a magnified view of the top surface, and D) a magnified view of the side wall in a pore. Reprinted with permission from Choi et al.[30] copyright ©2009 John Wiley and Sons.

Mechanical and biological evaluations were performed on this scaffold. Tensile strength of the porous chitosan scaffold was in the range of 30-60 kPa and confocal microscopy images showed that after 14 days the cells fully spread and proliferated throughout the scaffold while the pores maintained their spherical structure.

Lee et al. [106, 107] focused on the production of a tool for systematic evaluation of the dependence of many cellular processes on cell cluster diameter, and for that they managed to engineer liver tissue spheroids within ICC scaffolds. Once again, pAAM hydrogel

was chosen (hydrogel transparency is an advantage for observing cell cultures within the scaffold) as matrix for the scaffold, and, by using monodisperse glass beads, different cavity size scaffolds were constructed (50, 100, 140, 170 and 200 μm) to check pore diameter effect on multicellular spheroid formation. Cultures of HEP G2 cells were seeded on the scaffold (Figure 2.8) and the initial cell seeding profile and 3D cell aggregation process were characterized. Typically, spheroid diameters reached approximately 77% of pore diameter or 50% of pore volume, but when ICC pore diameter was above 170 μm effects like nutrient delivery to the inner cells influenced more than space restriction and spheroid diameter became less dependent on cavity size. Different developmental stages of 46.5–152 μm spheroids from HepG2 hepatocytes with vivid morphological similarities to liver tissue (bile canaliculi) were observed. Also verified were albumin production and cytochrome P450 activity.

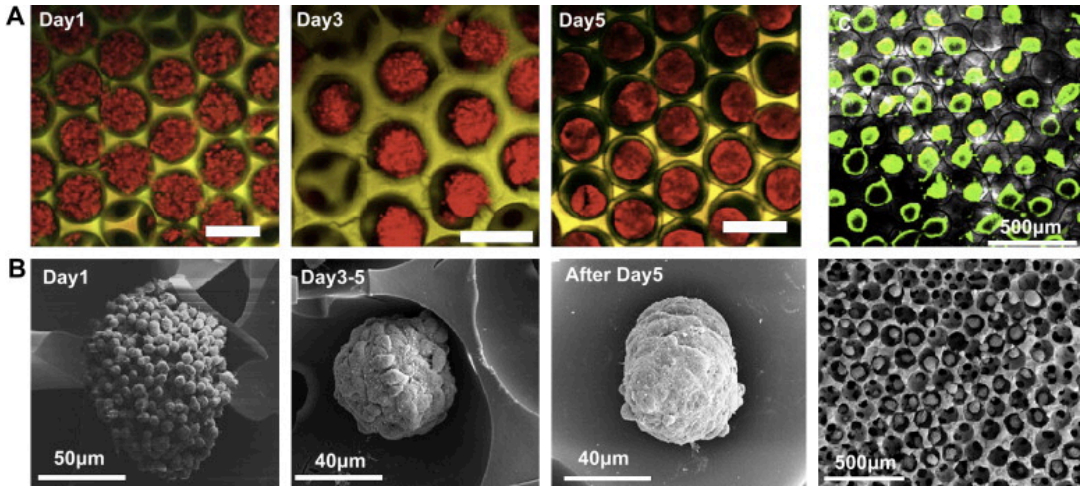

Figure 2.8: Characterization of the spheroid formation process. (A) Three-dimensionally reconstructed confocal images of HepG2 spheroid formation in hydrogel ICC scaffolds on Day 1, Day 3 and Day 5 culture (Scale bar is 200 μm). (B) Confocal images of live–dead stained spheroids cultured for 5 days overlapped with transmission microscope image. Green indicates live cells and red indicates dead cells. Most cells show green color. (C) SEM images of different stages of spheroids and large scale image of mature spheroids in an ICC scaffold. Individual cells aggregate and the surface morphology gradually changes. Reprinted from Lee et al. [106]copyright ©2009 with permission from Elsevier.

Diffusion processes and cellular aggregation affect metabolic activity which contributes to the level of dependence of liver functions in HepG2 spheroids in ICC scaffolds. The hydrogel scaffolds studied made the formation of uniform spheroids with a narrow size distribution possible. The researchers also concluded that liver-specific function was demonstrated to be dependent on spheroid size.

Lee and Kotov [108] also reported in 2009 the development of ICC scaffolds with surface modification with the addition of notch ligands by the LBL technique. They investigated the effectiveness of 3D ICC topography and the bioactivity of LBL immobilized

delta-like1 (DL-1) notch ligands in ex vivo T-lymphocyte development of HSC. Polyacrylamide hydrogel ICC scaffolds with 110 μm pores and 25-30 μm interconnecting channel size were produced and coated with clay/PDDA followed by DL-1 notch ligand. In order to verify T-cell differentiation of HSCs the investigators characterized the progression of differential stage-specific surface marker expression under confocal microscopy. By analyzing the culture images, they concluded that the system was able to support self-renewal or maintenance of undifferentiated population of HSCs. Although the scaffold demonstrated being useful to create *in vitro* HSC niches, isolating a large amount of cells from the ICC culture presented some difficulties due to strong cellular adhesion to the coated surfaces. Effective cell harvesting methods have to be investigated.

2010

Takagi et al. [92] developed β-tricalcium phosphate (β-TCP) ICC scaffolds by ceramic slip casting using a CC template of polyethylene microspheres. Knowing that the annealing of microspheres directly determines the size of interconnecting pores (interparticle neck size), a thermal study was performed in the range 95ºC - 105ºC to optimize the annealing temperature. Microsphere assembly was done by confining the spheres in a pyramidal form and inducing an fcc structure by vibration and gravitational force. For the scaffold matrix material, a β-TCP slurry was prepared by dispersing β-TCP micro powders in water containing polyvinyl alcohol as a binder and polyester acrylate copolymer as a dispersant, and applying ultrasonication. By immersing the pyramidal CC template in the ceramic slurry, ICC scaffolds were obtained with the infiltration of the slurry into the interstices of the template followed by a drying and sintering processes for slurry solidification and sphere removal. The resulting bioceramic scaffold showed an ordered pore structure with high porosity and high pore interconnection.

In 2010, Choi et al. [25]published a work on ICC scaffolds aimed at validating the importance of uniformity in pore size and structure for scaffolds used in tissue engineering. They fabricated two scaffold types: uniform pore (ICC) and nonuniform pore. The ICC structure was constructed using gelatin micro-spheres and PLGA matrix. Mouse fibroblasts (NIH/3T3; ATCC CRL-1658) were seeded on the scaffolds for cell distribution experiments. Scaffold properties were evaluated by macromolecule diffusion, fibroblast spatial distribution, and preosteoblast differentiation analysis. Results showed a superior performance of ICC scaffolds due to the uniform pore size, homogeneous environment, and high interconnectivity resulting in higher diffusion rate, uniform cell distribution, and homogeneous differentiation. It was also found that secretion pattern of cells could be regulated by varying the pore size of the scaffolds. This work has produced compelling evidence that ICC scaffolds provide better microenvironment for cells in comparison to other nonuniform size and structure scaffolds.

Choi et al [109] fabricated PLGA and hydroxyapatite (HAp) Inverse Opal scaffolds for bone tissue engineering. Using CC templates of gelatin microspheres with diameters of 225,8 ± 2,4 μm, they produced porous scaffolds (with 75% porosity and 213 ± 4,4 μm pore

size) with three different formulations: PLGA, PLGA/HAp and apatite (Ap)-coated PLGA/HAp. Biological tests were performed with the seeding of preosteoblasts MC3T3-E1 in the different scaffolds and forward micro-CT volume analysis and SEM image evaluation. The spatial distribution of mineral from the differentiated preosteoblasts in the scaffolds (osteoinductivity) showed that cells in the Ap-coated scaffold tend so secrete more mineral than those in the PLGA and PLGA/Hap scaffolds. These results reveal that the uniform pore structure and favorable surface could facilitate the uniform secretion of extracellular matrix by cells throughout the scaffold, and Ap-coated PLGA/HAp scaffolds provided the best environment (mechanical properties, osteoinductivity and spatial distribution of mineral) among the three scaffolds.

Kuo and Tsai [110] researched chitin/chitosan ICC scaffolds for diarthrodial cartilage regeneration. Uniform nutrient supply over a construct is essential during the regeneration of cartilage. With the objective of developing such a structure, different CC templates were obtained by the assembly of PS spheres (160 μm) in three solvents: acetone, ethylene glycol and ethanol. Comparison between the templates revealed that the assembly of spheres in pure ethanol results in more regular colloidal crystal arrays. For the matrix material the authors used chitin gels and chitosan gels, both mixed with 2% genipin. Using a vacuum pump, chitin/chitosan gel was infiltrated into the arrays and then dried at 40ºC for 24h. Following these steps, the template was immersed in tetrahydrofuran for microsphere dissolution, resulting in ICC matrices. Porosity of approximately 84% was obtained with gel concentration below 2,5% in scaffolds obtained after using pure ethanol as solvent. Bovine knee chondrocytes (BKC) seeded on the scaffolds showed cellular viability above 92%. BKCs secrete glucosaminoglycans and type II collagen, both on the periphery and the interior of the ICC structure, indicating phenotypic preservation and metabolic activity of the chondrocytes.

Da Silva et al. [111] presented tissue-mimicking ICC scaffolds with tunable mechanical properties and large flat seeding surfaces, adapted for cell migration studies. The ICC scaffolds, with 150 μm pore diameter, were prepared using a poly(acrylamide) (PAA) hydrogel matrix. Cells from the NB4 cell line (used as *in vitro* model for acute promyelocytic leukaemia, APL) were seeded on the structure to study scaffold adequacy for migration assays. In conjunction with confocal microscopy, these scaffolds were used to study the importance of cell compliance on invasive potential. APL cells were differentiated with all-trans retinoic acid (ATRA) and treated with paclitaxel. ATRA differentiation enabled cell motility throughout the scaffold structure but was reduced by additional paclitaxel treatment. These results confirm previous studies on the use of scaffolds for investigating cell migration in a 3D model and added more information about the simulation of *in vivo* cell migration behavior of leukaemia cells through tissue.

Galperin et al. [112] applied the sphere-templating technique to produce hydrogel scaffolds. Poly(N-isopropylacrylamide) (pNIPAM) hydrogels with degradable units

within the polymer backbone and at the crosslinking sites were synthesized by photopolymerization of NIPAM with 2-methylene-1,3- dioxepane and polycaprolactone dimethacrylate. Based on these hydrogels, fully degradable sphere-templated scaffolds were prepared with the use of PMMA microspheres (35±1, 49±8, 81±8, and 188±26 μm). A study on the change of pore diameter as a function of temperature was performed that revealed that pores decreased in diameter when the temperature was raised from 25°C to 37°C. After NIH3T3 cells were sown on the scaffolds, SEM image observation demonstrated good cell adhesion (after 2 days of culture), uniform infiltration, and an elongated morphology after 7 days of culture, proving the thermosensitive pNIPAM scaffold ability to promote cell attachment and growth.

Madden et al. [113] also applied the sphere-template method to produce scaffolds for cardiac tissue engineering. Having in mind a strategy to address multicellular organization, integration into host myocardium, and the functional architecture of heart muscle, they developed scaffolds using a template with spheres surrounding fibers (45±150 μm diameter). The researchers managed to construct pHEMA-co-MAA hydrogel scaffolds with channels (25% of scaffold volume) and a porous network (75% of scaffold volume) of 60% porosity, also with modified surfaces to incorporate collagen. Human embryonic stem cell (ESC)–derived cardiomyocytes were seeded on the scaffolds and, after 2 weeks of proliferation, the cells reach adult heart densities. Acellular scaffolds (30–40μm) implanted in nude rat myocardium showed angiogenesis and reduced fibrotic response, at the same time that a shift in macrophage phenotype toward the M2 state was observed.

2011

In 2011, Silva et al also reported hydrogel ICC scaffolds as realistic cell migration assay substrates for drug screening applications by surveying the effects of cytoskeletal toxins that impact cell mechanics [114]. They constructed PAA ICC scaffolds, using PMMA colloidal crystal templates. Results showed that cell migration in 3D scaffolds is affected by different mechanisms comparing with 2D substrates. Different reactions to changes in the substrate stiffness or after exposure to cytoskeletal drugs occurred. Cells often actively deform their surroundings when squeezing through the scaffold channels, a constraint that does not occur in 2D. Drug tests with nocadazole and phalloidin resulted in different cell migration profiles. In nocadazole testing, significant decrease in migration was registered comparing with untreated controls, verifying the opposite effect on cells migrating on flat surfaces. In phalloidin treatment, whereas the migration depth apparently was not affected, the migration length on flat surfaces suffered a significant increase. Once again, 3D scaffolds like ICC scaffolds represent suitable assays to investigate the effect of drugs on cell migration in realistic environments instead of 2D models.

After their work one year before, in constructing scaffolds for cartilage regeneration, Kuo and Tsai [115] researched homogeneous chondrogenesis in heparinised ICC scaffolds. Colloidal crystal templates were prepared by floating PS microspheres (160 μm) in a medium containing ethylene glycol and inducing sphere self-assembling, followed by

temperature treatment for sphere annealing and structure consolidation. Heparin/chitin/chitosan gels were used to infiltrate the CC template. After gel drying, the spheres were removed by tetrahydrofuran washing, creating an ICC scaffold (82,3 ± 2,6% porosity). An increase in the weight percentage of heparin enhanced the viability of bovine knee chondrocytes (BKCs) in ICC matrices and promoted the production of BKCs, GAGs and collagen in ICC constructs. Staining of the cultured ICC constructs revealed minor differences in BKCs, GAGs and type II collagen between the peripheral and core regions. Therefore, the ordered pores in the heparinized ICC constructs could favour the chondrocyte culture to regenerate uniformly cartilaginous tissue.

Together with Chiu, Kuo also published a study on the effect of pore regularity on the preservation and neuronal differentiation of bone stromal cells (BMSC), using ICC scaffolds as physical structures for cell culture [116]. By infiltration of chitosan-gelatin gels into the interstices of self-assembled PS microsphere CC template, ICC scaffolds were obtained and afterwards modified by surface grafting with laminin-derived peptides (LDP). BMSCs were seeded and after 7 days their distribution was uniform within the structure compared with freeform scaffolds. ICC scaffolds could preserve 63% phenotypic BMSCs (freeform scaffolds: 56%) and thanks to the grafted LDP, adhesion cell efficiency was enhanced (70-75%) and produced NeuN-positive cells.

Yang et al. [117] studied the capability of peptide-modified chitosan/gelatin ICC scaffolds seeded with bone marrow stromal cells on spinal cord injury (SCI) therapy. The constructs were applied to the treatment of SCI in the thoracic spine lesion of rats. When treated with peptide-modified ICC construct, neuronal survival was enhanced and the expression of glial fibrillary acidic protein and tumor necrosis factor reduced significantly, indicating the inhibition of the formation of glial scar tissue and inflammatory cytokine. Besides guiding BMSCs differentiation toward neuronal precursor cells at the wound site, the authors find that the ICC topography with the surface peptides could also enhance SCI treatment.

Orita et al. [118] developed a new strategy to control cell adhesion, morphology, and proliferation by culturing mouse osteoblast-like MC3T3-E1 cells on ICC scaffolds with ordered nanometer-sized pores (100, 300, 500, and 1000 nm). Two dimensional structures based on HAp, alumina and silica ICC films were prepared utilizing PS spheres as CC templates. Growth and diffusion of osteoblast-like MC3T3-E1 cells was significantly restricted by silica ICC films with 100 nm to 500 nm pore sizes, but for 1000 nm pore size, only a slight restriction (comparing to non-porous control films) on cell proliferation was observed. Better results were obtained for HAp ICC films, where the number of growing cells increased to approximately 20% above that obtained for non-porous HAp films. Actin stress fibers formation decreased in HAp, alumina and silica ICC films compared to non-porous films, although MC3T3-E1 cells exhibited higher multi directional spread and highly flattened morphology on nonporous films. Pore size and film material played an important role in morphology and cell proliferation control.

Underwood et al. [119] studied the effect of pore size and surface treatment on epidermal incorporation into percutaneous implanted sphere-templated porous biomaterials in mice. Cylindrical rods of pHEMA sphere-templated scaffolds (20, 40, and 60 μm pore size), with and without surface modifications, were implanted in mice. After 3, 7, and 14 days the implants and surrounding tissue were harvested. With the use of immune histochemistry for pankeratins and image analysis, the epithelia migration was investigated revealing tight contact between epidermis and biomaterial, without suggestion of open sinuses, in all scaffolds. Although surface treatment minimally influenced epidermis migration to the inferior of the scaffold, a decrease in the migration was registered in the 20μm scaffolds when comparing with 40 and 60μm. Epithelial integration occurred quickly and epidermis closed the sinus within 3 days, penetrating an average of 11% of the scaffold diameter.

2012

Fleckman et al. [120] conducted a study about the cutaneous responses to long-term percutaneously implanted rods surrounded by sphere-templated porous biomaterials. They constructed two types of rods: silicone and hollow tubes of pHEMA sphere-templated scaffold (36 μm pore size). These tubular scaffolds were implanted in mice for 14 days and 1, 3, and 6 months. By histochemical analysis of the implants and surrounding tissue, pHEMA/skin showed better morphology than silicone rods. The researchers also highlighted the keratinocyte migration in different directions through the sphere-templated scaffold: ventral and dorsal.

Zhang and Xia [121] fabricated alginate Inverse Opal scaffolds for the production of embryoid bodies (EB) with uniform and controllable sizes and later recovery after ICC disintegration. Using a fluidic device, PS microspheres were produced and cubic-close packed into lattices for template creation. Then, the CC template was infiltrated by an aqueous solution of alginate giving rise to an ICC alginate scaffold (Figure 2.9). EBs are aggregates of cells derived from ESCs. For EB production, a 4 step work was done: (1) seeding of ES cells into the pores of the scaffold; (2) proliferation of cells under the confinement of the pores; (3) disintegration of the scaffold with a PBS solution and (4) separation of EBs from the debris of the disintegrated scaffold. The alginate scaffold rehydrates when immersed in water to become a hydrogel system that may prevent the adhesion of seeded cells to the walls, promoting EB formation. Results demonstrated that ICC scaffolds could reach a maximum EB occupancy of 70%. By varying the culture time and/or using different pore sized scaffolds, different size EB could be obtained. EB conserved pluripotency (viability and undifferentiating state) and were able to differentiate into specific lineages (bone and neural) after appropriate stimulation.

Zhang et al. [122] reported the pore modification of an ICC structure with chitosan microstructures. Gelatin microspheres were assembled in a CC template for construction of a PLGA ICC scaffold. To functionalize the pores, a chitosan solution was infiltrated into the as-prepared ICC scaffold. After freeze-drying, chitosan randomly filled the void

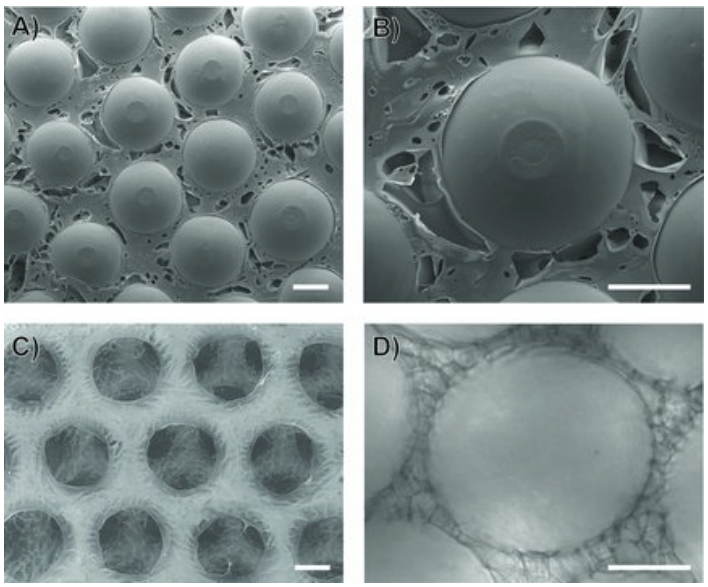

Figure 2.9: A), B) SEM images of a CC lattice of PS microspheres (250 μm) filled with alginate and then freeze-dried. C) SEM image of an alginate ICC after the polystyrene microspheres had been selectively removed. D) Optical microscopy of the alginate ICC scaffold after hydration. Scale bars: 100 μm. Reprinted with permission from Zhang and Xia[121] copyright ©2009 John Wiley and Sons.

space of a pore with a fibrous arrangement, creating a new 3D environment inside the ICC scaffold and efficiently reducing the distance between the opposite surfaces of a pore from hundreds of micrometers to a few tens of micrometers. MC3T3-E1 pre-osteoblasts were seeded in two types of construct for comparison: PLGA ICC scaffolds and PLGA-CS ICC scaffolds. In spite of PLGA constructs demonstrating higher seeding efficiency (due to large pore size), PLGA-CS constructs showed a higher number of cells after a few days of culture. Good interconnectivity between the pores could also be retained allowing cell migration within the scaffold.This method for functionalizing the pores appears as an efficient way of utilizing the entire pore void space.

The neovascularization of PLGA ICC scaffolds was investigated by Choi et al. [123] who fabricated scaffolds with 4 different pore sizes (79, 147, 224 and 312 μm in diameter) and studied the influence of pore size in neovascularization *in vivo* by implanting these scaffolds at the dorsal side of nude mice. Histological analyses revealed that scaffolds with pores bigger than 200 μm favored the formation of vascular networks with larger blood vessels at low densities and deep penetration depth whereas small pores (<200 μm) induced the formation of small vessels at high densities and poor penetration depth.

Kuo and Chung reported three studies on ICC scaffolds for applications in nervous regeneration. For that they developed alginate/poly(γ-glutamic acid) ICC scaffolds with

TATVHL [124] or CSRARKQAASIKVAVSADR [125] peptides on their surfaces. The objective of introducing these specific peptides into the scaffold surfaces was to favor neurothropic factor delivery, remyelination, functional synaptic replacement and axonal elongation, stimulating pluripotent stem cells (iPS) adhesion and differentiation into nervous cells. With these modifications they observed an accelerated expression of β III tubulin by iPS cells differentiation, favouring a generation of neuron-lineage cells.

2013

Following their previous works, Kuo and Lin constructed chitin-chitosan-gelatin ICC scaffolds for guided differentiation of iPS cells towards neurons [126]. They compared ICC and freeform constructs and concluded that although cell adhesion affinity was superior in freeform constructs, iPS viability was superior in ICC scaffolds. They also verified that β III tubulin-identified region was larger in ICC scaffolds than that founded in freeform constructs, proving faster differentiation toward neurons. The ICC geometry and the use of chitin-chitosan-gelatin materials have demonstrated their capability for biomedical applications in nervous tissue regeneration.

Long et al. [127]described a capillary-force-based method for seeding the human prostate cancer cell lines M12 and LNCaP C4-2 into sphere-templated pHEMA hydrogels. A capillary-force-based technique was used to seed cells within the ICC scaffold, which proved to enhance cell number and distribution in the 3D structure when comparing with static and centrifugation seeding. The researchers found a strong dependence of the seeding efficiency on the rounded cell diameter relative to the pore diameter and to the pore interconnection size. They concluded that sphere-templated pHEMA could be used as a 3D scaffold for prostate cancer cell culture and the polymeric scaffold system and the techniques developed in the studies could have further applications in tissue-engineered biomaterial-based cancer models.

Sharma et al. [128] developed 3D ordered macroporous polypyrrol (PPy) inverse opal thin films and tested their viability for controlled drug release.126 The PPy ICC was produced by electropolymerization of PPy through the interstitial voids of a PMMA CC template (sphere diameter average 430 nm). To test the scaffold as capable of drug-releasing structure, a model drug risperidone was loaded into the PPy ICCs, and entrapped by electropolymerization of a nonporous PPy overlayer. Due to the high interconnectivity, the drug penetrated easily through the structure by gravity and capillary action. The researchers demonstrated that the high-surface-area PPy inverse opal scaffolds exhibited enhanced drug-loading and releasing capabilities when compared with conventional nonporous PPy films. They also verified that PPy ICCs were redox active and when electrically stimulated, drug release profiles could be modified. They concluded that this type of ICCs can be important in drug-delivering implants since the drug release can be controlled by electrical stimulus application, according to patient's requirements.

Cai et al. [129] tested the combination of multiscale photo acoustic microscopy (PAM) and optical coherence tomography (OCT) on the quantification of neovascularization

in ICC scaffolds. They prepared PLGA ICCs with cuboid shape and subcutaneously implanted in nude mice ears. The combination of PAM with OCT allowed the observation of the scaffold/ tissue construct with down to 5 μm and up to 3 mm lateral resolution and penetration depth, respectively. By comparing ICCs with 80 and 200 μm pore sizes, PAM images revealed that normalized vessel areas of the 200 μm pore ICCs were 2– 3.5 times larger than 80 μm-pore ICCs. They concluded that PAM results correlated well with the traditional histology analyses, proving that PAM imaging could be very useful in evaluating thick scaffold/tissue constructs.

Galperin et al.[130] constructed an innovative bilayered scaffold for cartilage and bone tissue engineering. Using different layers of 38 μm and 200 μm PMMA microspheres, they produced a scaffold with pHEMA/hyaluronic acid (HAc) and pHEMA/HAp composites. HAc and HAp were introduced specifically to support regeneration of articular cartilage and subchondral bone. The integrated bilayered scaffold was cocultured with human mesenchymal stem cells (hMSCs) differentiated to chondrocytes and primary hMSCs, respectively. The results of the *in vitro* studies showed that the scaffold provided simultaneously a suitable environment for cell attachment, infiltration, proliferation, and differentiation of hMSCs to osteoblasts (for the designated bone layer) and retention of chondrocyte phenotype (for the designated cartilage layer).

After their previous work in 2010, Galperin et al.[131] reported a sphere-templated pNIPAM hydrogel scaffold obtained with the use of 48±6 μm PMMA spheres. Soft muscle cells (A-10) were seeded in the scaffolds and then warmed to 37°C entrapping cells in pores of $\simeq 40\mu$m diameter, a size described by the authors as optimal for angiogenesis and biointegration. After proceeding to degradability, hydrolytic degradation, cytocompatibility, and cell adhesion tests, the researchers concluded that due to the degradable nature, tunable molecular weight (MW), highly interconnected morphology, thermally controlled monodisperse pore size, and temperature-induced volume expansion–contraction, the pNIPAM-based scaffolds developed could be very useful for tissue engineering applications.

Zhang et al.[132] studied the influence of manufacturing conditions in the pore/window sizes and physical properties of PLGA ICC scaffolds. Studying the annealing of gelatin microspheres (190 μm), they concluded that varying the time of the procedure (3–5 h) did not influence the size of pore. Instead, increasing the annealing temperature (65°C, 80°C, and 100°C) showed to have a more immediate effect in increasing pore size (25, 43, and 66 mm). The capability of controlling the surface pore size was also investigated by increasing concentration (10, 18, 25, and 30 wt%) in the infiltration polymer (PLGA). At higher concentration, the pores became more sealed by the polymer. Cell migration assays were also performed in four types of ICC scaffolds with different pore sizes. The migration rate revealed that scaffolds with large windows allow a homogeneous migration throughout the scaffold, perpendicularly to its surface. Mechanical properties were also evaluated and the researchers concluded that with the increase of pore size (108, 190, and 330 μm) the compressive modulus decreased (412, 361, and 313

kPa, respectively).

Bhrany et al.[133] evaluated the performance of sphere-templated pHEMA scaffold (pore size 40μm) as subcutaneous implant by comparing with high-density porous polyethylene (HDPPE) (pore size 100 μm). After implantation in dorsal subcutis of mice for 4 and 9 weeks, histological examination of the implants was performed. Both implants supported cellular and collagen ingrowth with minimal inflammatory response. Neovascularization was identified by the appearance of blood vessels within the fibrous ingrowth of the HDPPE and within the cavities of the pHEMA scaffold. The difference registered between the two implants occurred in thinner collagen fibrils within the smaller pores of the pHEMA scaffold, suggesting that a less scar-type reaction occurred.

2014[2]

Zhang et al.[134] developed a new type of cell patch based on the ICC technology. With the objective of producing cell patches for healing injured tissue surfaces like epidermis and myocardium, they developed scaffolds with an hexagonal array of interconnected pores (SHAIPs). These SHAIPs constituted by monolayers of ICC scaffolds are fabricated with the use of gelatin CC templates and PLGA matrix. The researchers conducted *in vitro* cell cultures in the scaffolds and obtained skeletal myoblast patches 150-μm thick with capability of differentiating into myotubes. Also, *in vivo* tests revealed that ICC patches induced the formation of blood vessels at a density of 86 ± 14 per mm^2 and a blood vessel–to–tissue area ratio of 3.03% ± 0.48%, which proved the ability of SHAIPs to promote neovascularization *in vivo*.

Kim et al.[135] constructed an inverse opal hydrogel with potencial application as 3D cell co-culture system for biological processes like paracrine signaling in stem cell niches and/or cancer-stroma interactions. Alginate microbeads (500, 800 and 1500μm) were ionically crosslinked and used as template for infiltration with photocrosslinkable methacrylated gelatin solutions incorporating MSC cells. After being crosslinked, the impregnated structure was washed with cell-friendly ethylenediaminetetraacetic acid (EDTA) for sphere dissolution. The structure obtained revealed uniformly distributed MSCs within the matrix with perfect 3D pore interconnection and cell encapsulation. Later, human umbilical vein endothelial cells were also seeded at the scaffolds surface. Results revealed that the gelatin based ICCs were viable for both cells encapsulated within the hydrogel matrix and on the surface of macropores, which constitutes an advance for co-culture systems applications based on 3D structures.

Jiang et al.[136] fabricated an innovative enzyme-based ICC using horseradish peroxidase (HRP) as model enzime and bovine serum albumin (BSA) as proteic feeder. Starting from a PS microspheres template, HRP and BSA were filled into the voids of the template and further cross-linked with glutaraldehyde for 5h at 4^{o}C. The infiltrated structure was then treated with ethyl acetate, acetone or thetrahydrofuram in order to remove the

[2]The publication of this chapter included the work performed until the end of 2013[1]. Sections 2014, 2015 and 2016 have been introduced in the thesis in order to update the work reported in the literature.

spheres and it was found that ethyl acetate was the best choice for template removal without seriously affecting the enzymes and their activity (only 10% enzyme initial activity lost). The enzyme activity was also investigated and compared with free HRP as a function of pH and temperature and it was concluded that ICC geometry promoted greater enzimatic activity at higher pH and higher temperatures. The structure also exhibited enhanced performance as a biocatalyst in the removal of phenolic compounds from an H_2O_2 aqueous solution.

Cam et al.[137] tested the *in vitro* cell viability, spreading and proliferation and also the *in vivo* cell invasion in acrylate functionalized hyaluronic acid hydrogel ICCs. To construct the scaffold, PMMA microspheres (53-63μm) were packed in glass-bottom silicon wells and annealed with different methods: A) for 17 to 22h at 150ºC; B) introducing a mixture of ethanol and acetone to the packed spheres promoting a chemical annealing (1-2h) and C) Non-annealed. The hydrogel formation was achieved by Michael-type addition of acrylate functionalized HAc with bis-cysteine containing MMP peptide crosslinkers at neutral pH. The gel solutions were introduced in the templates by centrifugation later aged at 37ºC for 30 minutes. The final construct was achieved by dissolving the spheres in acetone solution for 48h. To test the bio performance, mouse bone marrow-derived mensenchymal cells were cultured in the ICCs that were also subcutaneous implanted in BALB/c mice for 14 days. The results revealed that there was no significant difference in *in vitro* or *in vivo* activity between the three type generated scaffolds and all ICCs were capable of promoting rapid cellular invasion and high blood vessel density with capilar formation. Moreover mechanical properties were higher for heat and chemical annealed ICCs and similar between these two. Chemical annealing proved to be a faster and easy method of ICC production without compromising the structure performance.

2015

Bin Zhang, Huan Wang et al. [138] produced a new multifunctional drug delivery system with monitoring ability based on pNIPAM ICC hydrogels. As system components, silica microspheres were applied as template, pNIPAM gel as matrix and encapsulated fluorescein isothiocyanate (FITC)-dextran as model drug. After ICC production the structure was loaded with a pregel solution containing the encapsulated drug. Taking advantage of pNIPAM thermoresponsive ability, the ICC was capable of shrinking and swelling under different temperatures, causing the release of encapsulated drugs from the particles. At the same time the spacing of the pores causes changes in the reflection peak of the structure. By analysis of the ICC hydrogel reflection spectra and reflection images during a dynamic temperature release process, the researchers established a monitoring profile and therefore the design of pNIPAM ICC systems with double capacity, release and monitoring.

Somo et al.[139] explored the influence of ICC pore interconnectivity on the optimization of vascular ingrowth. Since porosity and pore sizes have already received a lot of attention in ICC design, these investigators looked for the role of the communication

windows between consecutive pores in the promotion of growth factor mediated vascularization. PMMA microspheres of 112.0±6.5 μm were used to prepare CC templates that were annealed at different temperatures (160-175ºC; t=0-30h) in order to fuse consecutive spheres at different levels. PEG solutions were infiltrated in the templates and further photopolymerized with UV light. The interconnectivity level was established dividing the window size by the mean pore size to obtain normalized pore connectivity (NPC). After dissolving the templates, three different NPC sizes were obtained: 0.24, 0.29, 0.42. Mechanical evaluation of the hydrogels revealed an inverse relation between the elastic modulus and the interconnectivity, achieving a maximum of 1284±182 kPa for the minimum NPC of 0.24. On the contrary, *in vitro* growth factor release is faster for higher NPC and has a sustained release profile for 40 days. The vascular tissue invasion was studied *in vivo* by implanting the scaffolds subcutaneously in male Lewis rats. The histological results showed that after 3 weeks vascular tissue formed and occupied half volume of the lower NPC ICCs and the entire volume for higher NPC. A 20 μm difference between pore windows was enough to evidence greater tissue invasion due to easiness of cell penetration, oxygen diffusion an nutrient transportation that is important for new tissue formation.

Parke-Houben et al.[140] designed an artificial cornea application based on PEG and poly(acrylic acid) (PAA) ICCs. PS microspheres of 25, 50 and 100 μm were used to produce the templates that were infiltrated with PEG and photoinitiator solutions and further soaked in acrylic acid (AA) solutions ir order to produce PEG/PAA hydrogels. To enable cell attachment, the scaffolds surface was functionalized with extracellular matrix proteins by using EDC/NHS coupling chemistry. The ICCs bioactivity was tested with white rabbit corneal fibroblasts. All scaffolds allowed cells attachment but the 25 μm scaffolds did not allow cell penetration. Although with better results, the 50 and 100 μm scaffolds showed limited cell migration within the scaffold. Even so the ICCs produced in this work satisfied critical requirements of strength, optical clarity and permeability to nutrients that are essential for their feasibility as materials for cornea periphery regeneration.

Galperin et al.[141] reported the production of pHEMA, AA and fluorostyrene (FS) based scaffolds for antiobiotic realease in oftalmologic applications. To assemble the structures, the researchers infiltrated solutions of HEMA or HEMA combined with AA and/or FS in templates of PMMA microspheres (38 μm diameter). After photopolymerization with UV light, the hydrogel + template was washed with dichloromethane to allow spheres dissolution. The ICCs were then loaded with the drug norfloxacin via swelling method in drug-saturated solutions of acetone, ethanol, water and chloroform. After drug integration, the structures were freeze-dried and used for *in vitro* antibacterial activity study in order to infer the kinetic release of norfloxacin and its efficiency in bacteria growth inhibition (Figure 2.10). Scaffold evaluation highlighted the higher efficiency in drug loading by the AA based scaffolds and the quick drug release by the pHEMA based ICCs. The *in vitro* tests with *Staphylococcus epidermidis* and *Pseudomonas aeruginosa* revealed that pHEMA FS are the ICC type with better encapsulation and drug release for

an ideal antibacterial effect for 1 week of action.

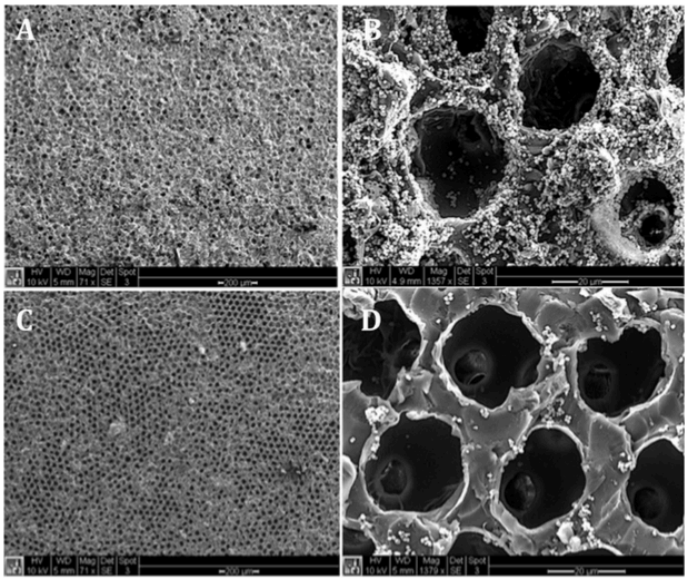

Figure 2.10: Representative SEM images of poly(HEMA-2.5FS) PTP inoculated with an S. epidermidis strain after 7 days in the flow cell. (A, B) Drug-free PTPs (controls); (C, D) drug-loaded scaffolds. Reprinted with permission from Galperin et al.[141] copyright ©2015 American Chemical Society John Wiley.

Myung Hee Kim et al.[142] studied the application of ICC for liver tissue engineering applications. Biofunctionalized PEG-DA ICCs were developed and the hepatic sheet formation at their surface was evaluated. First PS microspheres (140 μm) based colloidal crystals were infiltrated with prepolymer solutions of PEG-DA. To functionalize the PEG-DA hydrogel, chemically reactive acryloyl-PEG-NHS groups were added, and collagen was covalently attached using standard EDC/NHS chemistry. After UV light exposition the structures were washed with THF in order to remove spheres and give rise to the final ICC scaffold. To investigate the scaffolds function, human hepatocarcinoma cells (Huh-7.5) were seeded and evaluated by cell adhesion and proliferation tests. The incorporation of PEG-NHS groups at different concentrations allowed the controlled formation of uniform coatings of type I collagen. Since type I collagen is responsible for binding cell surface integrins and influence cell behavior, with this approach the researchers established an easy method to achieve a bioactive platform at ICC's surface, confirmed with the improved rates of cell viability. SEM morphologic evaluation revealed the cell spheroid formation at non-functionalized ICCs (PEGDA) and perfect cell sheet-like formation aligned within the scaffolds architecture for the other PEG-NHS ICCs.

2016

Based on the work reported in 2015, Huan Wang et al.[143] developed an ICC barcode for medical diagnostics by developing boronate affinity molecularly imprinted polymer (MIP) in ICCs structures. Once again, different silica microspheres were used as template

and infiltrated with MIP pregel solutions. Due to different size of the microspheres it was possible to obtain a set of ICCs exhibiting different light diffraction profiles and therefore different colors, being later used as barcodes. Boronate has the ability to bind glycoproteins and when this happens in the MIP ICCs, the polymer changes the swelling behavior causing changes in the diffraction spectra profile of the ICC structure. Since a readable red shift is perceptible in the diffraction peak of the barcode structures, this feature can be used for directly detecting and decoding of the biomolecules by the specificity and sensitivity of the MIP. Moreover the researchers tested this system by using different proteins like HRP, ribonuclease B (RNase B) and transferrin (TRF) as the imprinted molecules and obtained good ICC recognition to the specific target, showing the versatility of the ICC imprinted structure for multiple detection.

Li et al. [144] proposed an HA scaffold for bone tissue engineering using sugar spheres as templates. To prepare the templates, sucrose was melted and mechanically stirred in an oil bath to allow drop formation. After cooling, sugar spheres were recoiled and sieved within three different size ranges (500-600, 750-900, 1150-1350 μm). The spheres were then packed in a cylindrical mould and annealed at 60ºC for 0, 5 and 8 minutes. As material for impregnation an HA/chitin slurry was prepared using lithium chloride (LiCl) and dimehtylacetamide (DMAc) as dispersion medium. After washing the ensemble with water, the slurry converted into gel (by gelation of chitin) with simultaneous removal of the sugar spheres. The retrieved gel was then dried at 80ºC prior to a sintering process at 1200ºC for 2h. With this process the authors report a final structure with improved interconnectivity and uniform pore distribution when comparing with structures obtained with other porogen agents (NaCL or Sucrose particles).

2.4 Conclusions

ICCs have recently emerged as a novel class of scaffolds for tissue engineering. ICCs are a good alternative for scaffold production in tissue engineering since they can be manufactured easily and at a low cost. Moreover, they display three major features: 3D format, uniform pore network with controllable size, and high interconnectivity within the structure. These superior features, which are highly valued in TE, impart ICCs with significant advantages in comparison with other scaffolding techniques and make ICCs excellent at providing uniform cell distributions, transport of nutrients, oxygen, and metabolic wastes, and for creating a microenvironment for cell differentiation and metabolism. Given the superior capabilities of ICCs, we can conclude that their potential for advancing tissue engineering and regenerative medicine has not yet been fully realized.

References

[1] C. F. C. João, J. M. Vasconcelos, J. C. Silva, and J. P. Borges. "An Overview of Inverted Colloidal Crystal Systems for Tissue Engineering". English. In: *Tissue*

Engineering Part B: Reviews 20.5 (Oct. 2014), pp. 437–454. DOI: 10.1089/ten.teb.2013.0402. URL: http://online.liebertpub.com/doi/abs/10.1089/ten.teb.2013.0402.

[2] C. T. Laurencin and L. S. Nair. *Nanotechnology and Tissue Engineering*. English. The Scaffold. CRC Press, June 2008. ISBN: 9781420051834. URL: http://books.google.com/books?id=txlC7ujnlkUC&dq=Nanotechnology+and+Tissue+Engineering&hl=&cd=1&source=gbs_api.

[3] P. X. Ma. "Scaffolds for tissue fabrication 10.1016/S1369-7021(04)00233-0 : Materials Today | ScienceDirect.com". In: *Materials today* (2004). URL: http://www.sciencedirect.com/science/article/pii/S1369702104002330.

[4] C. Liu, Z. Xia, and J. T. Czernuszka. "Design and development of three-dimensional scaffolds for tissue engineering". English. In: *Chemical Engineering Research & Design* 85.7 (2007), pp. 1051–1064. DOI: 10.1205/cherd061915. URL: http://www.sciencedirect.com/science/article/pii/S0263876207731428.

[5] C. van Blitterswijk, P. Thomsen, J. Hubbell, R. Cancedda, J. D. de Bruijn, A. Lindahl, J. Sohier, and D. F. Williams. *Tissue Engineering (Academic Press Series in Biomedical Engineering)*. English. 1st ed. Academic Press, Apr. 2008. ISBN: 0123708699. URL: http://books.google.com/books?id=AN9s2p9ZzgoC&pg=PR11&dq=Tissue+Engineering+Langer&hl=&cd=7&source=gbs_api.

[6] R. R. Zhang and P. X. P. Ma. "Synthetic nano-fibrillar extracellular matrices with predesigned macroporous architectures." English. In: *Journal of Biomedical Materials Research* 52.2 (Nov. 2000), pp. 430–438. URL: http://deepblue.lib.umich.edu/handle/2027.42/34418.

[7] X. Liu and P. X. Ma. "Polymeric Scaffolds for Bone Tissue Engineering". English. In: *Annals of Biomedical Engineering* 32.3 (2004), pp. 477–486. DOI: 10.1023/B:ABME.0000017544.36001.8e. URL: http://journals.kluweronline.com/article.asp?PIPS=482175.

[8] I. O. Smith, X. H. Liu, L. A. Smith, and P. X. Ma. "Nanostructured polymer scaffolds for tissue engineering and regenerative medicine." English. In: *Wiley interdisciplinary reviews. Nanomedicine and nanobiotechnology* 1.2 (Feb. 2009), pp. 226–236. DOI: 10.1002/wnan.26. URL: http://eutils.ncbi.nlm.nih.gov/entrez/eutils/elink.fcgi?dbfrom=pubmed&id=20049793&retmode=ref&cmd=prlinks.

[9] J. Lee, M. J. Cuddihy, and N. A. Kotov. "Three-Dimensional Cell Culture Matrices: State of the Art". English. In: *Tissue Engineering Part B: Reviews* 14.1 (Mar. 2008), pp. 61–86. DOI: 10.1089/teb.2007.0150. URL: http://www.liebertonline.com/doi/abs/10.1089/teb.2007.0150.

[10] D. Hutmacher. "Scaffolds in tissue engineering bone and cartilage". In: *Biomaterials* 21.24 (2000), pp. 2529–2543. URL: http://www.sciencedirect.com/science/article/pii/S0142961200001216.

[11] Y. S. Nam and T. G. Park. "Porous biodegradable polymeric scaffolds prepared by thermally induced phase separation." English. In: *Journal of Biomedical Materials Research* 47.1 (Oct. 1999), pp. 8–17. URL: http://eutils.ncbi.nlm.nih.gov/entrez/eutils/elink.fcgi?dbfrom=pubmed&id=10400875&retmode=ref&cmd=prlinks.

[12] L. D. L. Harris, B. S. B. Kim, and D. J. D. Mooney. "Open pore biodegradable matrices formed with gas foaming." English. In: *Journal of Biomedical Materials Research* 42.3 (Dec. 1998), pp. 396–402. URL: http://eutils.ncbi.nlm.nih.gov/entrez/eutils/elink.fcgi?dbfrom=pubmed&id=9788501&retmode=ref&cmd=prlinks.

[13] J. J. Yoon and T. G. Park. "Degradation behaviors of biodegradable macroporous scaffolds prepared by gas foaming of effervescent salts." English. In: *Journal of Biomedical Materials Research* 55.3 (June 2001), pp. 401–408. URL: http://eutils.ncbi.nlm.nih.gov/entrez/eutils/elink.fcgi?dbfrom=pubmed&id=11255194&retmode=ref&cmd=prlinks.

[14] K Whang, T. K. Goldstick, and K. E. Healy. "A biodegradable polymer scaffold for delivery of osteotropic factors." English. In: *Biomaterials* 21.24 (Dec. 2000), pp. 2545–2551. URL: http://eutils.ncbi.nlm.nih.gov/entrez/eutils/elink.fcgi?dbfrom=pubmed&id=11071604&retmode=ref&cmd=prlinks.

[15] S. Agarwal, J. H. Wendorff, and A. Greiner. "Use of electrospinning technique for biomedical applications". English. In: *Polymer* 49.26 (2008), pp. 5603–5621. DOI: 10.1016/j.polymer.2008.09.014. URL: http://www.sciencedirect.com/science/article/pii/S0032386108007994.

[16] B. Chuenjitkuntaworn, P. Supaphol, P. Pavasant, and D. Damrongsri. "Electrospun poly(L-lactic acid)/hydroxyapatite composite fibrous scaffolds for bone tissue engineering". English. In: *Polymer international* 59.2 (2010), pp. 227–235. DOI: 10.1002/pi.2712. URL: http://links.isiglobalnet2.com/gateway/Gateway.cgi?GWVersion=2&SrcAuth=mekentosj&SrcApp=Papers&DestLinkType=FullRecord&DestApp=WOS&KeyUT=000273922300013.

[17] P. Q. Franco, C. F. C. João, J. C. Silva, and J. P. Borges. "Electrospun hydroxyapatite fibers from a simple sol–gel system". English. In: *Materials Letters* 67.1 (2011), pp. 233–236. DOI: 10.1016/j.matlet.2011.09.090. URL: http://links.isiglobalnet2.com/gateway/Gateway.cgi?GWVersion=2&SrcAuth=mekentosj&SrcApp=Papers&DestLinkType=FullRecord&DestApp=WOS&KeyUT=000298272200067.

[18] C. Lam, X. M. Mo, S. H. Teoh, and D. Hutmacher. "Scaffold development using 3D printing with a starch-based polymer". English. In: *Materials Science & Engineering C-Biomimetic and Supramolecular Systems*. Natl Univ Singapore Dept Orthoped Surg, Singapore 0511 Singapore. 2002, pp. 49–56. URL: http://www.sciencedirect.com/science/article/pii/S0928493102000127.

[19] G. Ciardelli, V. Chiono, C. Cristallini, N. Barbani, A. Ahluwalia, G. Vozzi, A. Previti, G. Tantussi, and P. Giusti. "Innovative tissue engineering structures through advanced manufacturing technologies." English. In: *Journal of materials science. Materials in medicine* 15.4 (Apr. 2004), pp. 305–310. URL: http://eutils.ncbi.nlm.nih.gov/entrez/eutils/elink.fcgi?dbfrom=pubmed&id=15332590&retmode=ref&cmd=prlinks.

[20] K El Tahlawy and S. Hudson. "Chitosan: Aspects of fiber spinnability". In: *Journal of Applied Polymer Science* 100.2 (2006), pp. 1162–1168. URL: http://onlinelibrary.wiley.com/doi/10.1002/app.23201/full.

[21] K. H. Tan, C. K. Chua, K. F. Leong, C. M. Cheah, P Cheang, M. S. Abu Bakar, and S. W. Cha. "Scaffold development using selective laser sintering of polyetheretherketone-hydroxyapatite biocomposite blends." English. In: *Biomaterials* 24.18 (Aug. 2003), pp. 3115–3123. DOI: 10.1016/S0142-9612(03)00131-5. URL: http://eutils.ncbi.nlm.nih.gov/entrez/eutils/elink.fcgi?dbfrom=pubmed&id=12895584&retmode=ref&cmd=prlinks.

[22] D. W. Hutmacher, M. Sittinger, and M. V. Risbud. "Scaffold-based tissue engineering: rationale for computer-aided design and solid free-form fabrication systems." English. In: *Trends in biotechnology* 22.7 (July 2004), pp. 354–362. DOI: 10.1016/j.tibtech.2004.05.005. URL: http://eutils.ncbi.nlm.nih.gov/entrez/eutils/elink.fcgi?dbfrom=pubmed&id=15245908&retmode=ref&cmd=prlinks.

[23] S Yang, K. F. Leong, Z Du, and C. K. Chua. "The design of scaffolds for use in tissue engineering. Part I. Traditional factors." English. In: *Tissue Engineering* 7.6 (Dec. 2001), pp. 679–689. DOI: 10.1089/107632701753337645. URL: http://eutils.ncbi.nlm.nih.gov/entrez/eutils/elink.fcgi?dbfrom=pubmed&id=11749726&retmode=ref&cmd=prlinks.

[24] S. Yang, K.-F. Leong, Z. Du, and C.-K. Chua. "The design of scaffolds for use in tissue engineering. Part II. Rapid prototyping techniques." English. In: *Tissue Engineering* 8.1 (Feb. 2002), pp. 1–11. DOI: 10.1089/107632702753503009. URL: http://eutils.ncbi.nlm.nih.gov/entrez/eutils/elink.fcgi?dbfrom=pubmed&id=11886649&retmode=ref&cmd=prlinks.

[25] S.-W. Choi, Y. Zhang, and Y. Xia. "Three-dimensional scaffolds for tissue engineering: the importance of uniformity in pore size and structure." English. In: *Langmuir : the ACS journal of surfaces and colloids* 26.24 (Dec. 2010), pp. 19001–

19006. DOI: 10.1021/la104206h. URL: http://eutils.ncbi.nlm.nih.gov/entrez/eutils/elink.fcgi?dbfrom=pubmed&id=21090781&retmode=ref&cmd=prlinks.

[26] Y. Zhang, S. Wang, M. Eghtedari, M. Motamedi, and N. Kotov. "Inverted-Colloidal-Crystal Hydrogel Matrices as Three-Dimensional Cell Scaffolds". English. In: *Advanced Functional Materials* 15.5 (May 2005), pp. 725–731. DOI: 10.1002/adfm.200400325. URL: http://doi.wiley.com/10.1002/adfm.200400325.

[27] P. X. Ma and J.-W. Choi. "Biodegradable Polymer Scaffolds with Well-Defined Interconnected Spherical Pore Network". English. In: *Tissue Engineering* 7.1 (Feb. 2001), pp. 23–33. DOI: 10.1089/107632701300003269. URL: http://www.liebertonline.com/doi/abs/10.1089/107632701300003269.

[28] A. J. MARSHALL, C. A. IRVIN, T. BARKER, E. H. SAGE, K. D. HAUCH, and B. D. Ratner. "Biomaterials with tightly controlled pore size that promote vascular in-growth". English. In: *Polymer Preprints, American Chemical Society, Division of Polymer Chemistry* 45.2 (2004), pp. 100–101. URL: http://cat.inist.fr/?aModele=afficheN&cpsidt=16007034.

[29] N. A. Kotov, Y. Liu, S. Wang, C. Cumming, M. Eghtedari, G. Vargas, M. Motamedi, J. Nichols, and J. Cortiella. "Inverted colloidal crystals as three-dimensional cell scaffolds." English. In: *Langmuir : the ACS journal of surfaces and colloids* 20.19 (Sept. 2004), pp. 7887–7892. DOI: 10.1021/la049958o. URL: http://eutils.ncbi.nlm.nih.gov/entrez/eutils/elink.fcgi?dbfrom=pubmed&id=15350047&retmode=ref&cmd=prlinks.

[30] S.-W. Choi, J. Xie, and Y. Xia. "Chitosan-Based Inverse Opals: Three-Dimensional Scaffolds with Uniform Pore Structures for Cell Culture." English. In: *Advanced materials (Deerfield Beach, Fla.)* 21.29 (Apr. 2009), pp. 2997–3001. DOI: 10.1002/adma.200803504. URL: http://eutils.ncbi.nlm.nih.gov/entrez/eutils/elink.fcgi?dbfrom=pubmed&id=19710950&retmode=ref&cmd=prlinks.

[31] S.-W. Choi, I. W. Cheong, J.-H. Kim, and Y. Xia. "Preparation of uniform microspheres using a simple fluidic device and their crystallization into close-packed lattices." English. In: *Small (Weinheim an der Bergstrasse, Germany)* 5.4 (Apr. 2009), pp. 454–459. DOI: 10.1002/smll.200801498. URL: http://eutils.ncbi.nlm.nih.gov/entrez/eutils/elink.fcgi?dbfrom=pubmed&id=19189332&retmode=ref&cmd=prlinks.

[32] Y. N. Xia, B Gates, Y. D. Yin, and Y Lu. "Monodispersed colloidal spheres: Old materials with new applications". English. In: *Advanced materials* 12.10 (2000), pp. 693–713. URL: http://www.unm.edu/~solgel/Course%20Stuff/Xia%20Adv%20Mater%202000.pdf.

[33] H Kawaguchi. "Functional polymer microspheres". In: *Progress in polymer Science* 25.8 (2000), pp. 1171–1210. URL: http://www.sciencedirect.com/science/article/pii/S0079670000000241.

[34] L. B. Bangs and M Merza. *Bangs: Microspheres, part 1: Selection, cleaning,... - Google Scholar*. IVD Technol. Mag, 1995. DOI: 10.1002/2013WR014345/full. URL: http://scholar.google.com/scholar?q=related:ECq6LcqpgPwJ:scholar.google.com/&hl=en&num=20&as_sdt=0,5.

[35] R Arshady. "In the name of particle formation". English. In: *Colloids and Surfaces a-Physicochemical and Engineering Aspects*. Univ London Imperial Coll Sci Technol & Med Dept Chem London SW7 2AY England. 1999, pp. 325–333. URL: http://links.isiglobalnet2.com/gateway/Gateway.cgi?GWVersion=2&SrcAuth=mekentosj&SrcApp=Papers&DestLinkType=FullRecord&DestApp=WOS&KeyUT=000081847100040.

[36] M. B. Oliveira and J. F. Mano. "Polymer-Based Microparticles in Tissue Engineering and Regenerative Medicine". English. In: *Biotechnology Progress* 27.4 (2011), pp. 897–912. DOI: 10.1002/btpr.618. URL: http://links.isiglobalnet2.com/gateway/Gateway.cgi?GWVersion=2&SrcAuth=mekentosj&SrcApp=Papers&DestLinkType=FullRecord&DestApp=WOS&KeyUT=000294107600001.

[37] F Bai, X Yang, Y Zhao, and W. Huang. "Synthesis of core–shell microspheres with active hydroxyl groups by two-stage precipitation polymerization". In: *Polymer international* 54.1 (2005), pp. 168–174. URL: http://onlinelibrary.wiley.com/doi/10.1002/pi.1670/full.

[38] F. Bai, B. Huang, X. Yang, and W. Huang. "Synthesis of monodisperse poly(methacrylic acid) microspheres by distillation-precipitation polymerization". English. In: *European Polymer Journal* 43.9 (2007), pp. 3923–3932. DOI: 10.1016/j.eurpolymj.2007.06.024. URL: http://www.sciencedirect.com/science/article/pii/S0014305707003564.

[39] Y Jin, M Jiang, Y Shi, Y Lin, Y Peng, K Dai, and B. Lu. "Narrowly dispersed molecularly imprinted microspheres prepared by a modified precipitation polymerization method". In: *Analytica chimica acta* 612.1 (2008), pp. 105–113. URL: http://www.sciencedirect.com/science/article/pii/S0003267008003036.

[40] Q. Yan, Y. Bai, Z. Meng, and W. Yang. "Precipitation polymerization in acetic acid: Synthesis of monodisperse cross-linked poly(divinylbenzene) microspheres". English. In: *Journal of Physical Chemistry B* 112.23 (2008), pp. 6914–6922. DOI: 10.1021/jp711324a. URL: http://pubs.acs.org/doi/abs/10.1021/jp711324a.

[41] M. M. Flake, P. K. Nguyen, R. A. Scott, L. R. Vandiver, R. K. Willits, and D. L. Elbert. "Poly(ethylene glycol) microparticles produced by precipitation polymerization in aqueous solution." English. In: *Biomacromolecules* 12.3 (Mar. 2011), pp. 844–850. DOI: 10.1021/bm1011695. URL: http://eutils.ncbi.nlm.nih.

gov/entrez/eutils/elink.fcgi?dbfrom=pubmed&id=21341681&retmode=ref&cmd=prlinks.

[42] Z.-S. Xu, Z.-W. Deng, X.-X. Hu, L. Li, and C.-F. Yi. "Monodisperse polystyrene microspheres prepared by dispersion polymerization with microwave irradiation". English. In: *Journal of Polymer Science Part A: Polymer Chemistry* 43.11 (2005), pp. 2368–2376. DOI: 10.1002/pola.20714. URL: http://doi.wiley.com/10.1002/pola.20714.

[43] S. Kawaguchi and K. Ito. "Dispersion polymerization". In: *Polymer Particles* (2005), pp. 299–328. URL: http://www.springerlink.com/index/e2kvt0y0.jhn3rjvq.pdf.

[44] J LEE, J HA, S CHOE, C LEE, and S SHIM. "Synthesis of highly monodisperse polystyrene microspheres via dispersion polymerization using an amphoteric initiator". English. In: *Journal of Colloid and Interface Science* 298.2 (June 2006), pp. 663–671. DOI: 10.1016/j.jcis.2006.01.001. URL: http://linkinghub.elsevier.com/retrieve/pii/S0021979706000075.

[45] M. Muranaka, Y. Kitamura, and H. Yoshizawa. "Preparation of biodegradable microspheres by anionic dispersion polymerization with PLA copolymeric dispersion stabilizer". English. In: *Colloid and Polymer Science* 285.13 (2007), pp. 1441–1448. DOI: 10.1007/s00396-007-1701-1. URL: http://links.isiglobalnet2.com/gateway/Gateway.cgi?GWVersion=2&SrcAuth=mekentosj&SrcApp=Papers&DestLinkType=FullRecord&DestApp=WOS&KeyUT=000249664100004.

[46] A. I. Abdelrahman, S. Dai, S. C. Thickett, O. Ornatsky, D. Bandura, V. Baranov, and M. A. Winnik. "Lanthanide-containing polymer microspheres by multiple-stage dispersion polymerization for highly multiplexed bioassays." English. In: *Journal of the American Chemical Society* 131.42 (Oct. 2009), pp. 15276–15283. DOI: 10.1021/ja9052009. URL: http://eutils.ncbi.nlm.nih.gov/entrez/eutils/elink.fcgi?dbfrom=pubmed&id=19807075&retmode=ref&cmd=prlinks.

[47] Q. Liu, Y. Li, S. Shen, Z. Zhou, B. Ou, and S. Tang. "Preparation of Monodisperse Cationic Microspheres by Dispersion Polymerization of Styrene and a Cation-Charged Monomer in the Absence of a Stabilizer". English. In: *Journal of Macromolecular Science Part a-Pure and Applied Chemistry* 48.7 (2011), pp. 518–525. DOI: 10.1080/10601325.2011.579810. URL: http://links.isiglobalnet2.com/gateway/Gateway.cgi?GWVersion=2&SrcAuth=mekentosj&SrcApp=Papers&DestLinkType=FullRecord&DestApp=WOS&KeyUT=000291273600003.

[48] C. D. Anderson and E. S. Daniels. *Emulsion Polymerisation And Latex Applications*. English. Smithers Rapra Technology, Apr. 2003. ISBN: 9781859573815. URL: http://books.google.com/books?hl=en&lr=&id=De9RUVtQ5TQC&oi=fnd&pg=PA3&dq=Emulsion+Polymerisation+and+Latex+Applications&ots=RUMjb7s08x&sig=Xj1nktGV38KujNLPEUtcj3NDMCQ.

[49] J. Sjoblom. *Encyclopedic Handbook of Emulsion Technology*. English. CRC Press, Mar. 2001. ISBN: 9780824704544. URL: http://books.google.pt/books?id=Q4wwWbQTivUC&printsec=frontcover&dq=Encyclopedic+handbook+of+emulsion+technology&hl=&cd=1&source=gbs_api.

[50] Y. He. "Synthesis of polyaniline/nano-CeO2 composite microspheres via a solid-stabilized emulsion route". English. In: *Materials chemistry and physics* 92.1 (July 2005), pp. 134–137. DOI: 10.1016/j.matchemphys.2005.01.033. URL: http://linkinghub.elsevier.com/retrieve/pii/S0254058405000532.

[51] Y. Gao, F.-d. Cui, Y. Guan, L. Yang, Y.-s. Wang, and L.-n. Zhang. "Preparation of roxithromycin-polymeric microspheres by the emulsion solvent diffusion method for taste masking". English. In: *International Journal of Pharmaceutics* 318.1-2 (Aug. 2006), pp. 62–69. DOI: 10.1016/j.ijpharm.2006.03.018. URL: http://linkinghub.elsevier.com/retrieve/pii/S0378517306002365.

[52] M Kalyanaraman, S. Retterer, T. McKnight, M. Ericson, S. Allman, J. Elkins, A. Palumbo, M Keller, and M. Doktycz. "Controlled microfluidic production of alginate beads for in situ encapsulation of microbes". In: *Biomedical Science & Engineering Conference, 2009. BSEC 2009. First Annual ORNL*. 2009, pp. 1–4. DOI: 10.1109/BSEC.2009.5090482. URL: http://ieeexplore.ieee.org/search/freesrchabstract.jsp?tp=&arnumber=5090482.

[53] K Tokuoka, M Senna, and H Kung. "Preparation of inorganic/polymeric composite microspheres by direct suspension polymerization". English. In: *Journal of Materials Science* 21.2 (Feb. 1986), pp. 493–496. DOI: 10.1007/BF01145513. URL: http://www.springerlink.com/index/10.1007/BF01145513.

[54] A. G. Mayes and K. Mosbach. "Molecularly Imprinted Polymer Beads: Suspension Polymerization Using a Liquid Perfluorocarbon as the Dispersing Phase". English. In: *Analytical Chemistry* 68.21 (Jan. 1996), pp. 3769–3774. DOI: 10.1021/ac960363a. URL: http://pubs.acs.org/doi/abs/10.1021/ac960363a.

[55] E. Vivaldo-Lima, P. E. Wood, A. E. Hamielec, and A. Penlidis. "An Updated Review on Suspension Polymerization". English. In: *Industrial & Engineering Chemistry Research* 36.4 (Apr. 1997), pp. 939–965. DOI: 10.1021/ie960361g. URL: http://pubs.acs.org/doi/abs/10.1021/ie960361g.

[56] S. R. S. Ting, T. L. U. Nguyen, and M. H. Stenzel. "One Pot Synthesis of Surface PEGylated Core-Shell Microparticles by Suspension Polymerization with Surface Enrichment of Biotin/Avidin Conjugation". English. In: *Macromolecular Bioscience* 9.3 (2009), pp. 211–220. DOI: 10.1002/mabi.200800161. URL: http://links.isiglobalnet2.com/gateway/Gateway.cgi?GWVersion=2&SrcAuth=mekentosj&SrcApp=Papers&DestLinkType=FullRecord&DestApp=WOS&KeyUT=000264420500001.

[57] M. S. Islam, J. H. Yeum, and A. K. Das. "Synthesis of poly(vinyl acetate-methyl methacrylate) copolymer microspheres using suspension polymerization." English. In: *Journal of Colloid and Interface Science* 368.1 (Feb. 2012), pp. 400–405. DOI: 10.1016/j.jcis.2011.11.002. URL: http://eutils.ncbi.nlm.nih.gov/entrez/eutils/elink.fcgi?dbfrom=pubmed&id=22137854&retmode=ref&cmd=prlinks.

[58] A CHAWLA, K. TAYLOR, J. NEWTON, and M. JOHNSON. "Production of Spray-Dried Salbutamol Sulfate for Use in Dry Powder Aerosol Formulation". English. In: *International Journal of Pharmaceutics* 108.3 (1994), pp. 233–240. URL: http://links.isiglobalnet2.com/gateway/Gateway.cgi?GWVersion=2&SrcAuth=mekentosj&SrcApp=Papers&DestLinkType=FullRecord&DestApp=WOS&KeyUT=A1994NY05700008.

[59] P He. "Chitosan microspheres prepared by spray drying". In: *International Journal of Pharmaceutics* 187.1 (Sept. 1999), pp. 53–65. DOI: 10.1016/S0378-5173(99)00125-8. URL: http://linkinghub.elsevier.com/retrieve/pii/S0378517399001258.

[60] M.-I. Ré. "Formulating Drug Delivery Systems by Spray Drying". English. In: *Drying Technology* 24.4 (May 2006), pp. 433–446. DOI: 10.1080/07373930600611.877. URL: www.tandfonline.com/doi/abs/10.1080/07373930600611877.

[61] K. Sollohub and K. Cal. "Spray drying technique: II. Current applications in pharmaceutical technology". English. In: *Journal of Pharmaceutical Sciences* (2009), n/a–n/a. DOI: 10.1002/jps.21963. URL: http://doi.wiley.com/10.1002/jps.21963.

[62] L REYDERMAN and S STAVCHANSKY. "Electrostatic Spraying and Its Use in Drug-Delivery - Cholesterol Microspheres". English. In: *International Journal of Pharmaceutics* 124.1 (1995), pp. 75–85. URL: http://www.sciencedirect.com/science/article/pii/037851739500078W.

[63] S.-H. S. Hong, J. H. J. Moon, J.-M. J. Lim, S.-H. S. Kim, and S.-M. S. Yang. "Fabrication of spherical colloidal crystals using electrospray." English. In: *Langmuir : the ACS journal of surfaces and colloids* 21.23 (Nov. 2005), pp. 10416–10421. DOI: 10.1021/la051266s. URL: http://eutils.ncbi.nlm.nih.gov/entrez/eutils/elink.fcgi?dbfrom=pubmed&id=16262301&retmode=ref&cmd=prlinks.

[64] S. Vlad, C. Ciobanu, M. Butnaru, D. Macocinschi, D. Filip, L. M. Gradinaru, and M. Mandru. "Preparation of Polyurethane Microspheres by Electrospray Technique". English. In: *Digest Journal of Nanomaterials and Biostructures* 6.2 (2011), pp. 643–652. URL: http://links.isiglobalnet2.com/gateway.

[65] Q. Zhang, Y. Zhang, Q. Wei, X. Wang, J. Liu, J. Yang, and C. Zhao. "Electrosprayed Porous Microspheres for the Removal of Endocrine Disruptors". English. In: *Journal of Applied Polymer Science* 120.5 (2011), pp. 2648–2653. DOI: 10.1002/app.33478. URL: http://onlinelibrary.wiley.com/doi/10.1002/app.33478/full.

[66] N. Bock, M. A. Woodruff, D. W. Hutmacher, and T. R. Dargaville. "Electrospraying, a Reproducible Method for Production of Polymeric Microspheres for Biomedical Applications". English. In: *Polymers* 3.1 (Mar. 2011), pp. 131–149. DOI: 10.3390/polym3010131. URL: http://www.mdpi.com/2073-4360/3/1/131/.

[67] W. J. Lin and C. C. Yu. "Comparison of protein loaded poly(epsilon-caprolactone) microparticles prepared by the hot-melt technique". English. In: *Journal of Microencapsulation* 18.5 (2001), pp. 585–592. URL: http://links.isiglobalnet2.com/gateway/Gateway.cgi?GWVersion=2&SrcAuth=mekentosj&SrcApp=Papers&DestLinkType=FullRecord&DestApp=WOS&KeyUT=000170240400004.

[68] C. R. Young, J. J. Koleng, and J. W. McGinity. "Production of spherical pellets by a hot-melt extrusion and spheronization process." English. In: *International Journal of Pharmaceutics* 242.1-2 (Aug. 2002), pp. 87–92. URL: http://eutils.ncbi.nlm.nih.gov/entrez/eutils/elink.fcgi?dbfrom=pubmed&id=12176229&retmode=ref&cmd=prlinks.

[69] W. J. Lin and W. W. Kang. "Comparison of chitosan and gelatin coated microparticles: prepared by hot-melt method". English. In: *Journal of Microencapsulation* 20.2 (2003), pp. 169–177. DOI: 10.1080/02652040210162559. URL: http://eutils.ncbi.nlm.nih.gov/entrez/eutils/elink.fcgi?dbfrom=pubmed&id=12554372&retmode=ref&cmd=prlinks.

[70] V. R. Sinha, K Bansal, R Kaushik, R Kumria, and A Trehan. "Poly-ϵ-caprolactone microspheres and nanospheres: an overview". In: *International Journal of Pharmaceutics* 278.1 (2004), pp. 1–23. URL: http://www.sciencedirect.com/science/article/pii/S0378517304001693.

[71] D Poncelet. "Production of alginate beads by emulsification/internal gelation." English. In: *Annals of the New York Academy of Sciences* 944 (Nov. 2001), pp. 74–82. URL: http://eutils.ncbi.nlm.nih.gov/entrez/eutils/elink.fcgi?dbfrom=pubmed&id=11797697&retmode=ref&cmd=prlinks.

[72] L. W. Chan, H. Y. Lee, and P. Heng. "Production of alginate microspheres by internal gelation using an emulsification method". English. In: *International Journal of Pharmaceutics*. Natl Univ Singapore, Fac Sci Dept Pharm S-117543 Singapore Singapore. 2002, pp. 259–262. URL: http://eutils.ncbi.nlm.nih.gov/entrez/eutils/elink.fcgi?dbfrom=pubmed&id=12176259&retmode=ref&cmd=prlinks.

[73] C. M. Silva, A. J. Ribeiro, I. V. Figueiredo, A. R. Goncalves, and F Veiga. "Alginate microspheres prepared by internal gelation: Development and effect on insulin stability". English. In: *International Journal of Pharmaceutics* 311 (2006), pp. 1–10. DOI: 10.1016/j.ijpharm.2005.10.050. URL: http://www.sciencedirect.com/science/article/pii/S0378517305008574.

[74] M. K. Das and D. P. Maurya. "Microencapsulation of water-soluble drug by emulsification-internal gelation technique". In: *Indian Journal of Pharmaceutical Education and Research* 43.1 (2009), pp. 28–38. URL: http://scholar.google.com/scholar?q=related:8LY9edhX4RMJ:scholar.google.com/&hl=en&num=20&as_sdt=0,5.

[75] B. V. Gangar, K Nagarajan, R. V. Krishnan, and A. B. Pandit. "Studies of internal gelation for the production of microspheres: sonication assisted gelation." English. In: *Ultrasonics sonochemistry* 18.1 (Jan. 2011), pp. 250–257. DOI: 10.1016/j.ultsonch.2010.05.015. URL: http://eutils.ncbi.nlm.nih.gov/entrez/eutils/elink.fcgi?dbfrom=pubmed&id=20638887&retmode=ref&cmd=prlinks.

[76] S. Takeuchi, P. Garstecki, D. Weibel, and G. Whitesides. "An Axisymmetric Flow-Focusing Microfluidic Device". In: *Advanced materials* 17.8 (2005), pp. 1067–1072. URL: http://onlinelibrary.wiley.com/doi/10.1002/adma.200401738/abstract.

[77] X. Gong, W. Wen, and P. Sheng. "Microfluidic Fabrication of Porous Polymer Microspheres: Dual Reactions in Single Droplets". English. In: *Langmuir : the ACS journal of surfaces and colloids* 25.12 (June 2009), pp. 7072–7077. DOI: 10.1021/la900120c. URL: http://pubs.acs.org/doi/abs/10.1021/la900120c.

[78] N. Prasad, J. Perumal, C.-H. Choi, C.-S. Lee, and D.-P. Kim. "Generation of Monodisperse Inorganic-Organic Janus Microspheres in a Microfluidic Device". English. In: *Advanced Functional Materials* 19.10 (May 2009), pp. 1656–1662. DOI: 10.1002/adfm.200801181. URL: http://doi.wiley.com/10.1002/adfm.200801181.

[79] H. Zhang, X.-J. Ju, R. Xie, C.-J. Cheng, P.-W. Ren, and L.-Y. Chu. "A microfluidic approach to fabricate monodisperse hollow or porous poly(HEMA-MMA) microspheres using single emulsions as templates". English. In: *Journal of Colloid and Interface Science* 336.1 (2009), pp. 235–243. DOI: 10.1016/j.jcis.2009.03.070. URL: http://www.sciencedirect.com/science/article/pii/S0021979709003932.

[80] L. Zhu, Y. Li, Q. Zhang, H. Wang, and M. Zhu. "Fabrication of monodisperse, large-sized, functional biopolymeric microspheres using a low-cost and facile microfluidic device". English. In: *Biomedical Microdevices* 12.1 (2010), pp. 169–177. DOI: 10.1007/s10544-009-9373-x. URL: http://links.isiglobalnet2.com/

gateway/Gateway.cgi?GWVersion=2&SrcAuth=mekentosj&SrcApp=Papers&DestLinkType=FullRecord&DestApp=WOS&KeyUT=000275195000020.

[81] A. K. Andrianov and J Chen. "ScienceDirect.com - Biomaterials - Preparation of hydrogel microspheres by coacervation of aqueous polyphosphazene solutions". In: *Biomaterials* (1998). URL: http://www.sciencedirect.com/science/article/pii/S0142961297002275.

[82] J Lazko, Y Popineau, and J Legrand. "Soy glycinin microcapsules by simple coacervation method." English. In: *Colloids and surfaces. B, Biointerfaces* 37.1-2 (Aug. 2004), pp. 1–8. DOI: 10.1016/j.colsurfb.2004.06.004. URL: http://eutils.ncbi.nlm.nih.gov/entrez/eutils/elink.fcgi?dbfrom=pubmed&id=15450301&retmode=ref&cmd=prlinks.

[83] W Dong and R Bodmeier. "Encapsulation of lipophilic drugs within enteric microparticles by a novel coacervation method." English. In: *International Journal of Pharmaceutics* 326.1-2 (Dec. 2006), pp. 128–138. DOI: 10.1016/j.ijpharm.2006.07.013. URL: http://eutils.ncbi.nlm.nih.gov/entrez/eutils/elink.fcgi?dbfrom=pubmed&id=16942845&retmode=ref&cmd=prlinks.

[84] F. Liu, L. Liu, X. Li, and Q. Zhang. "Preparation of chitosan-hyaluronate double-walled microspheres by emulsification-coacervation method". English. In: *Journal of Materials Science-Materials in Medicine*. Peking Union Med Coll Chinese Acad Med Sci Inst Biomed Engn Tianjin 300192 Peoples R China. 2007, pp. 2215–2224. DOI: 10.1007/s10856-007-3228-x. URL: http://eutils.ncbi.nlm.nih.gov/entrez/eutils/elink.fcgi?dbfrom=pubmed&id=17701294&retmode=ref&cmd=prlinks.

[85] S. K. Basu, K. Kavitha, and M. Rupeshkumar. "Evaluation of ketorolac tromethamine microspheres by chitosan/gelatin B complex coacervation." English. In: *Scientia pharmaceutica* 78.1 (2009), pp. 79–92. DOI: 10.3797/scipharm.0903-16. URL: http://eutils.ncbi.nlm.nih.gov/entrez/eutils/elink.fcgi?dbfrom=pubmed&id=21179371&retmode=ref&cmd=prlinks.

[86] N. V. Dziomkina, M. A. Hempenius, and G. J. Vancso. "Synthesis of cationic core-shell latex particles". English. In: *European Polymer Journal* 42.1 (2006), pp. 81–91. DOI: 10.1016/j.eurpolymj.2005.07.015. URL: http://links.isiglobalnet2.com/gateway/Gateway.cgi?GWVersion=2&SrcAuth=mekentosj&SrcApp=Papers&DestLinkType=FullRecord&DestApp=WOS&KeyUT=000234817700009.

[87] J. Zhang, Y. Li, X. Zhang, and B. Yang. "Colloidal self-assembly meets nanofabrication: from two-dimensional colloidal crystals to nanostructure arrays." English. In: *Advanced materials (Deerfield Beach, Fla.)* 22.38 (Oct. 2010), pp. 4249–4269. DOI: 10.1002/adma.201000755. URL: http://doi.wiley.com/10.1002/adma.201000755.

[88] D. Grier and S. Behrens. "Interactions in Colloidal Suspensions". In: *NATO Science Series*. Ed. by C. Holm, P. Kékicheff, and R. Podgornik. Springer Netherlands, 2001, pp. 87–116. DOI: 10.1007/978-94-010-0577-7_4. URL: http://dx.doi.org/10.1007/978-94-010-0577-7_4.

[89] O. D. Velev and A. M. Lenhoff. "Colloidal crystals as templates for porous materials". English. In: *Current Opinion in Colloid & Interface Science* 5 (2000), pp. 56–63. URL: http://www.sciencedirect.com/science/article/pii/S135902940000039X.

[90] P. Pusey, W. van Megen, P. Bartlett, B. Ackerson, J. Rarity, and S. Underwood. "Structure of crystals of hard colloidal spheres." English. In: *Physical review letters* 63.25 (Dec. 1989), pp. 2753–2756. URL: http://eutils.ncbi.nlm.nih.gov/entrez/eutils/elink.fcgi?dbfrom=pubmed&id=10040981&retmode=ref&cmd=prlinks.

[91] M. J. Cuddihy and N. A. Kotov. "Poly(lactic-co-glycolic acid) bone scaffolds with inverted colloidal crystal geometry." English. In: *Tissue engineering. Part A* 14.10 (Oct. 2008), pp. 1639–1649. DOI: 10.1089/ten.tea.2007.0142. URL: http://eutils.ncbi.nlm.nih.gov/entrez/eutils/elink.fcgi?dbfrom=pubmed&id=18491955&retmode=ref&cmd=prlinks.

[92] K. Takagi, T. Takahashi, K. Kikuchi, and A. Kawasaki. "Fabrication of bioceramic scaffolds with ordered pore structure by inverse replication of assembled particles". English. In: *Journal of the European Ceramic Society* 30.10 (2010), pp. 2049–2055. DOI: 10.1016/j.jeurceramsoc.2010.04.009. URL: http://www.sciencedirect.com/science/article/pii/S0955221910001603.

[93] A. Stachowiak, A. Bershteyn, E. Tzatzalos, and D. Irvine. "Bioactive Hydrogels with an Ordered Cellular Structure Combine Interconnected Macroporosity and Robust Mechanical Properties". In: 17 (2005), pp. 399–403. ISSN: 1521-4095. DOI: 10.1002/adma.200400507. URL: http://dx.doi.org/10.1002/adma.200400507.

[94] S Shanbhag, J. Lee, and N Kotov. "Diffusion in three-dimensionally ordered scaffolds with inverted colloidal crystal geometry". English. In: *Biomaterials* 26.27 (Sept. 2005), pp. 5581–5585. DOI: 10.1016/j.biomaterials.2005.01.059. URL: http://linkinghub.elsevier.com/retrieve/pii/S0142961205001092.

[95] S. Shanbhag, S. Wang, and N. A. Kotov. "Cell distribution profiles in three-dimensional scaffolds with inverted-colloidal-crystal geometry: modeling and experimental investigations." English. In: *Small (Weinheim an der Bergstrasse, Germany)* 1.12 (Dec. 2005), pp. 1208–1214. DOI: 10.1002/smll.200500191. URL: http://eutils.ncbi.nlm.nih.gov/entrez/eutils/elink.fcgi?dbfrom=pubmed&id=17193421&retmode=ref&cmd=prlinks.

[96] K. Zhang, H. Yan, D. C. Bell, A. Stein, and L. F. Francis. "Effects of materials parameters on mineralization and degradation of sol-gel bioactive glasses with 3D-ordered macroporous structures". In: 66A (2003), pp. 860–869. ISSN: 1552-4965. DOI: 10.1002/jbm.a.10093. URL: http://dx.doi.org/10.1002/jbm.a.10093.

[97] Y. Liu, S. Wang, J. Lee, and N. Kotov. "A floating self-assembly route to colloidal crystal templates for 3D cell scaffolds". In: *Chemistry of materials* 17.20 (2005), pp. 4918–4924. URL: http://pubs.acs.org/doi/abs/10.1021/cm048050g.

[98] J. Lee, S. Shanbhag, and N. A. Kotov. "Inverted colloidal crystals as three-dimensional microenvironments for cellular co-cultures". In: 16 (2006). ISSN: 0959-9428. DOI: 10.1039/B605797G. URL: http://dx.doi.org/10.1039/B605797G.

[99] D. Yi, M. Kim, L. Turner, K. Breuer, and D.-Y. Kim. "Colloid Lithography-Induced Polydimethylsiloxane Microstructures and their Application to Cell Patterning". In: 28 (2006), pp. 169–173. ISSN: 0141-5492. DOI: 10.1007/s10529-005-5331-8. URL: http://dx.doi.org/10.1007/s10529-005-5331-8.

[100] S. J. Bryant, J. L. Cuy, K. D. HAUCH, and B. D. Ratner. "Photo-patterning of porous hydrogels for tissue engineering". English. In: *Biomaterials* 28.19 (July 2007), pp. 2978–2986. DOI: 10.1016/j.biomaterials.2006.11.033. URL: http://linkinghub.elsevier.com/retrieve/pii/S0142961206010015.

[101] Y. Liu and S. Wang. "3D inverted opal hydrogel scaffolds with oxygen sensing capability". English. In: *Colloids and Surfaces B-Biointerfaces*. 1024S Innovation Way Stillwater OK 74074 USA. 2007, pp. 8–13. DOI: 10.1016/j.colsurfb.2006.08.014. URL: http://eutils.ncbi.nlm.nih.gov/entrez/eutils/elink.fcgi?dbfrom=pubmed&id=17005382&retmode=ref&cmd=prlinks.

[102] Y. Liu, S. Wang, J. Krouse, N. A. Kotov, M. Eghtedari, G. Vargas, and M. Motamedi. "Rapid aqueous photo-polymerization route to polymer and polymer-composite hydrogel 3D inverted colloidal crystal scaffolds." English. In: *Journal of biomedical materials research. Part A* 83.1 (Oct. 2007), pp. 1–9. DOI: 10.1002/jbm.a.31199. URL: http://eutils.ncbi.nlm.nih.gov/entrez/eutils/elink.fcgi?dbfrom=pubmed&id=17335022&retmode=ref&cmd=prlinks.

[103] D. Irvine and A. Stachowiak. "Inverse opal hydrogel scaffolds as lymphoid microenvironments for the study of immune cell migration and immunotherapy". In: (2007). URL: http://digitalcommons.unl.edu/civilengfacpub/26.

[104] A. N. Stachowiak and D. J. Irvine. "Inverse opal hydrogel-collagen composite scaffolds as a supportive microenvironment for immune cell migration." English. In: *Journal of biomedical materials research. Part A* 85.3 (June 2008), pp. 815–828. DOI: 10.1002/jbm.a.31661. URL: http://eutils.ncbi.nlm.nih.gov/entrez/eutils/elink.fcgi?dbfrom=pubmed&id=17937415&retmode=ref&cmd=prlinks.

[105] J. E. Nichols, J. Cortiella, J. Lee, J. A. Niles, M. Cuddihy, S. Wang, J. Bielitzki, A. Cantu, R. Mlcak, E. Valdivia, R. Yancy, M. L. McClure, and N. A. Kotov. "In vitro analog of human bone marrow from 3D scaffolds with biomimetic inverted colloidal crystal geometry." English. In: *Biomaterials* 30.6 (Feb. 2009), pp. 1071–1079. DOI: 10.1016/j.biomaterials.2008.10.041. URL: http://eutils.ncbi.nlm.nih.gov/entrez/eutils/elink.fcgi?dbfrom=pubmed&id=19042018&retmode=ref&cmd=prlinks.

[106] J. Lee, M. J. Cuddihy, G. M. Cater, and N. A. Kotov. "Engineering liver tissue spheroids with inverted colloidal crystal scaffolds". In: 30 (2009), pp. 4687–4694. ISSN: 0142-9612. URL: http://www.sciencedirect.com/science/article/pii/S0142961209005353.

[107] J. Lee, G. D. Lilly, R. C. Doty, P. Podsiadlo, and N. A. Kotov. "In vitro toxicity testing of nanoparticles in 3D cell culture." English. In: *Small (Weinheim an der Bergstrasse, Germany)* 5.10 (May 2009), pp. 1213–1221. DOI: 10.1002/smll.200801788. URL: http://eutils.ncbi.nlm.nih.gov/entrez/eutils/elink.fcgi?dbfrom=pubmed&id=19263430&retmode=ref&cmd=prlinks.

[108] J. Lee and N. A. Kotov. "Notch ligand presenting acellular 3D microenvironments for ex vivo human hematopoietic stem-cell culture made by layer-by-layer assembly." English. In: *Small (Weinheim an der Bergstrasse, Germany)* 5.9 (May 2009), pp. 1008–1013. DOI: 10.1002/smll.200801242. URL: http://eutils.ncbi.nlm.nih.gov/entrez/eutils/elink.fcgi?dbfrom=pubmed&id=19334013&retmode=ref&cmd=prlinks.

[109] S.-W. Choi, Y. Zhang, S. Thomopoulos, and Y. Xia. "In vitro mineralization by pre-osteoblasts in poly(DL-lactide-co-glycolide) inverse opal scaffolds reinforced with hydroxyapatite nanoparticles." English. In: *Langmuir : the ACS journal of surfaces and colloids* 26.14 (July 2010), pp. 12126–12131. DOI: 10.1021/la101519b. URL: http://eutils.ncbi.nlm.nih.gov/entrez/eutils/elink.fcgi?dbfrom=pubmed&id=20450216&retmode=ref&cmd=prlinks.

[110] Y.-C. Kuo and Y.-T. Tsai. "Inverted colloidal crystal scaffolds for uniform cartilage regeneration." English. In: *Biomacromolecules* 11.3 (Mar. 2010), pp. 731–739. DOI: 10.1021/bm901312x. URL: http://eutils.ncbi.nlm.nih.gov/entrez/eutils/elink.fcgi?dbfrom=pubmed&id=20158195&retmode=ref&cmd=prlinks.

[111] J. da Silva, F. Lautenschlager, E. Sivaniah, and J. R. Guck. "The cavity-to-cavity migration of leukaemic cells through 3D honey-combed hydrogels with adjustable internal dimension and stiffness." English. In: *Biomaterials* 31.8 (Mar. 2010), pp. 2201–2208. DOI: 10.1016/j.biomaterials.2009.11.105. URL: http://eutils.ncbi.nlm.nih.gov/entrez/eutils/elink.fcgi?dbfrom=pubmed&id=20015545&retmode=ref&cmd=prlinks.

[112] A. Galperin, T. J. Long, and B. D. Ratner. "Degradable, thermo-sensitive poly(N-isopropyl acrylamide)-based scaffolds with controlled porosity for tissue engineering applications." English. In: *Biomacromolecules* 11.10 (Oct. 2010), pp. 2583–2592. DOI: 10.1021/bm100521x. URL: http://pubs.acs.org/doi/abs/10.1021/bm100521x.

[113] L. R. Madden, D. J. Mortisen, E. M. Sussman, S. K. Dupras, J. A. Fugate, J. L. Cuy, K. D. HAUCH, M. A. Laflamme, C. E. Murry, and B. D. Ratner. "Proangiogenic scaffolds as functional templates for cardiac tissue engineering". In: *Proceedings of the National Academy of Sciences* 107.34 (2010), pp. 15211–15216. DOI: 10.1073/pnas.1006442107/-/DCSupplemental. URL: http://www.pnas.org/content/107/34/15211.short.

[114] J. da Silva, F. Lautenschlager, C.-H. R. Kuo, J. Guck, and E. Sivaniah. "3D inverted colloidal crystals in realistic cell migration assays for drug screening applications." English. In: *Integrative biology : quantitative biosciences from nano to macro* 3.12 (Dec. 2011), pp. 1202–1206. DOI: 10.1039/c1ib00065a. URL: http://eutils.ncbi.nlm.nih.gov/entrez/eutils/elink.fcgi?dbfrom=pubmed&id=22038190&retmode=ref&cmd=prlinks.

[115] Y.-C. Kuo and Y.-T. Tsai. "Heparin-conjugated scaffolds with pore structure of inverted colloidal crystals for cartilage regeneration." English. In: *Colloids and surfaces. B, Biointerfaces* 82.2 (Feb. 2011), pp. 616–623. DOI: 10.1016/j.colsurfb.2010.10.031. URL: http://eutils.ncbi.nlm.nih.gov/entrez/eutils/elink.fcgi?dbfrom=pubmed&id=21074384&retmode=ref&cmd=prlinks.

[116] Y.-C. Kuo and K.-H. Chiu. "Inverted colloidal crystal scaffolds with laminin-derived peptides for neuronal differentiation of bone marrow stromal cells." English. In: *Biomaterials* 32.3 (Jan. 2011), pp. 819–831. DOI: 10.1016/j.biom.2010.09.057. URL: http://eutils.ncbi.nlm.nih.gov/entrez/eutils/elink.fcgi?dbfrom=pubmed&id=20974492&retmode=ref&cmd=prlinks.

[117] J.-T. Yang, Y.-C. Kuo, and K.-H. Chiu. "Peptide-modified inverted colloidal crystal scaffolds with bone marrow stromal cells in the treatment for spinal cord injury." English. In: *Colloids and surfaces. B, Biointerfaces* 84.1 (May 2011), pp. 198–205. DOI: 10.1016/j.colsurfb.2010.12.034. URL: http://eutils.ncbi.nlm.nih.gov/entrez/eutils/elink.fcgi?dbfrom=pubmed&id=21251802&retmode=ref&cmd=prlinks.

[118] T. Orita, M. Tomita, and K. Kato. "Regulation of cellular responses to macroporous inorganic films prepared by the inverse-opal method." English. In: *Colloids and surfaces. B, Biointerfaces* 84.1 (May 2011), pp. 187–197. DOI: 10.1016/j.colsurfb.2010.12.032. URL: http://eutils.ncbi.nlm.nih.gov/entrez/eutils/elink.fcgi?dbfrom=pubmed&id=21273052&retmode=ref&cmd=prlinks.

[119] R. A. Underwood, M. L. Usui, G. Zhao, K. D. HAUCH, M. M. Takeno, B. D. Ratner, A. J. MARSHALL, X. Shi, J. E. Olerud, and P. Fleckman. "Quantifying the effect of pore size and surface treatment on epidermal incorporation into percutaneously implanted sphere-templated porous biomaterials in mice." English. In: *Journal of biomedical materials research. Part A* 98.4 (Sept. 2011), pp. 499–508. DOI: 10.1002/jbm.a.33125. URL: http://eutils.ncbi.nlm.nih.gov/entrez/eutils/elink.fcgi?dbfrom=pubmed&id=21681942&retmode=ref&cmd=prlinks.

[120] P. Fleckman, M. Usui, G. Zhao, R. Underwood, M. Maginness, A. Marshall, C. Glaister, B. Ratner, and J. Olerud. "Cutaneous and inflammatory response to long-term percutaneous implants of sphere-templated porous/solid poly(HEMA) and silicone in mice". English. In: *Journal of biomedical materials research. Part A* 100A.5 (Feb. 2012), pp. 1256–1268. DOI: 10.1002/jbm.a.34012. URL: http://doi.wiley.com/10.1002/jbm.a.34012.

[121] Y. Zhang. "Formation of Embryoid Bodies with Controlled Sizes and Maintained Pluripotency in Three-Dimensional Inverse Opal Scaffolds". In: *Advanced Functional Materials* (2012). URL: http://onlinelibrary.wiley.com/doi/10.1002/adfm.201101690/full.

[122] Y. Zhang, S.-W. Choi, and Y. Xia. "Modifying the pores of an inverse opal scaffold with chitosan microstructures for truly three-dimensional cell culture." English. In: *Macromolecular rapid communications* 33.4 (Feb. 2012), pp. 296–301. DOI: 10.1002/marc.201100695. URL: http://eutils.ncbi.nlm.nih.gov/entrez/eutils/elink.fcgi?dbfrom=pubmed&id=22231861&retmode=ref&cmd=prlinks.

[123] S.-W. Choi, Y. Zhang, M. R. MacEwan, and Y. Xia. "Neovascularization in Biodegradable Inverse Opal Scaffolds with Uniform and Precisely Controlled Pore Sizes - Choi - 2012 - Advanced Healthcare Materials - Wiley Online Library". English. In: *Advanced Healthcare Materials* 2.1 (Jan. 2013), pp. 145–154. DOI: 10.1002/adhm.201200106. URL: http://onlinelibrary.wiley.com/doi/10.1002/adhm.201200106/full.

[124] Y.-C. Y. Kuo and C.-Y. C. Chung. "TATVHL peptide-grafted alginate/poly(γ-glutamic acid) scaffolds with inverted colloidal crystal topology for neuronal differentiation of iPS cells." English. In: *Biomaterials* 33.35 (Dec. 2012), pp. 8955–8966. DOI: 10.1016/j.biomaterials.2012.08.073. URL: http://eutils.ncbi.nlm.nih.gov/entrez/eutils/elink.fcgi?dbfrom=pubmed&id=22998813&retmode=ref&cmd=prlinks.

[125] Y.-C. Kuo and C.-W. Chen. "Inverted colloidal crystal scaffolds with induced pluripotent stem cells for nerve tissue engineering." English. In: *Colloids and surfaces. B, Biointerfaces* 102C (Sept. 2012), pp. 789–794. DOI: 10.1016/j.colsurfb.

2012.09.013. URL: http://eutils.ncbi.nlm.nih.gov/entrez/eutils/elink.fcgi?dbfrom=pubmed&id=23107957&retmode=ref&cmd=prlinks.

[126] Y.-C. Kuo and C.-C. Lin. "Accelerated nerve regeneration using induced pluripotent stem cells in chitin-chitosan-gelatin scaffolds with inverted colloidal crystal geometry." English. In: *Colloids and surfaces. B, Biointerfaces* 103C (Nov. 2012), pp. 595–600. DOI: 10.1016/j.colsurfb.2012.11.001. URL: http://eutils.ncbi.nlm.nih.gov/entrez/eutils/elink.fcgi?dbfrom=pubmed&id=23261585&retmode=ref&cmd=prlinks.

[127] T. J. Long, M. Takeno, C. C. Sprenger, S. R. Plymate, and B. D. Ratner. "Capillary force seeding of sphere-templated hydrogels for tissue-engineered prostate cancer xenografts." English. In: *Tissue engineering. Part C, Methods* 19.9 (Sept. 2013), pp. 738–744. DOI: 10.1089/ten.TEC.2012.0388. URL: http://eutils.ncbi.nlm.nih.gov/entrez/eutils/elink.fcgi?dbfrom=pubmed&id=23373788&retmode=ref&cmd=prlinks.

[128] M. Sharma, G. I. N. Waterhouse, S. W. C. Loader, S. Garg, and D. Svirskis. "High surface area polypyrrole scaffolds for tunable drug delivery." English. In: *International Journal of Pharmaceutics* 443.1-2 (Feb. 2013), pp. 163–168. DOI: 10.1016/j.ijpharm.2013.01.006. URL: http://eutils.ncbi.nlm.nih.gov/entrez/eutils/elink.fcgi?dbfrom=pubmed&id=23318368&retmode=ref&cmd=prlinks.

[129] X. Cai, Y. Zhang, L. Li, S.-W. Choi, M. R. MacEwan, J. Yao, C. Kim, Y. Xia, and L. V. Wang. "Investigation of neovascularization in three-dimensional porous scaffolds in vivo by a combination of multiscale photoacoustic microscopy and optical coherence tomography." English. In: *Tissue engineering. Part C, Methods* 19.3 (Mar. 2013), pp. 196–204. DOI: 10.1089/ten.TEC.2012.0326. URL: http://online.liebertpub.com/doi/abs/10.1089/ten.tec.2012.0326.

[130] A. Galperin, R. A. Oldinski, S. J. Florczyk, J. D. Bryers, M. Zhang, and B. D. Ratner. "Integrated bi-layered scaffold for osteochondral tissue engineering." English. In: *Advanced Healthcare Materials* 2.6 (May 2013), pp. 872–883. DOI: 10.1002/adhm.201200345. URL: http://eutils.ncbi.nlm.nih.gov/entrez/eutils/elink.fcgi?dbfrom=pubmed&id=24352858&retmode=ref&cmd=prlinks.

[131] A. Galperin, T. J. Long, S. Garty, and B. D. Ratner. "Synthesis and fabrication of a degradable poly(N-isopropyl acrylamide) scaffold for tissue engineering applications." English. In: *Journal of biomedical materials research. Part A* 101.3 (Mar. 2013), pp. 775–786. DOI: 10.1002/jbm.a.34380. URL: http://eutils.ncbi.nlm.nih.gov/entrez/eutils/elink.fcgi?dbfrom=pubmed&id=22961921&retmode=ref&cmd=prlinks.

[132] Y. S. Zhang, K. P. Regan, and Y. Xia. "Controlling the pore sizes and related properties of inverse opal scaffolds for tissue engineering applications." English. In: *Macromolecular rapid communications* 34.6 (Mar. 2013), pp. 485–491. DOI: 10.1002/marc.201200740. URL: http://pubget.com/site/paper/23365045?institution=.

[133] A. D. Bhrany, C. A. IRVIN, K. Fujitani, Z. Liu, and B. D. Ratner. "Evaluation of a sphere-templated polymeric scaffold as a subcutaneous implant." English. In: *JAMA facial plastic surgery* 15.1 (Jan. 2013), pp. 29–33. DOI: 10.1001/2013.jamafacial.4. URL: http://eutils.ncbi.nlm.nih.gov/entrez/eutils/elink.fcgi?dbfrom=pubmed&id=23329269&retmode=ref&cmd=prlinks.

[134] Y. S. Zhang, J. Yao, L. V. Wang, and Y. Xia. "Fabrication of cell patches using biodegradable scaffolds with a hexagonal array of interconnected pores (SHAIPs)". English. In: 55.1 (Jan. 2014), pp. 445–452. DOI: 10.1016/j.polymer.2013.06.019. URL: http://www.sciencedirect.com/science/article/pii/S0032386113005557.

[135] J. Kim, S. A. Bencherif, W. A. Li, and D. J. Mooney. "Cell-Friendly Inverse Opal-Like Hydrogels for a Spatially Separated Co-Culture System". English. In: 35.18 (Aug. 2014), pp. 1578–1586. DOI: 10.1002/marc.201400278. URL: http://doi.wiley.com/10.1002/marc.201400278.

[136] Y. Jiang, C. Cui, Y. Huang, X. Zhang, and J. Gao. "Enzyme-based inverse opals: a facile and promising platform for fabrication of biocatalysts". English. In: *Chemical Communications* 50.41 (2014), pp. 5490–4. DOI: 10.1039/c4cc01721h. URL: http://xlink.rsc.org/?DOI=c4cc01721h.

[137] C. Cam and T. Segura. "Chemical sintering generates uniform porous hyaluronic acid hydrogels". In: *Acta Biomaterialia* 10.1 (Jan. 2014), pp. 205–213. DOI: 10.1016/j.actbio.2013.10.002. URL: http://dx.doi.org/10.1016/j.actbio.2013.10.002.

[138] B. Zhang, Y. Cheng, H. Wang, B. Ye, L. Shang, Y. Zhao, and Z. Gu. "Multifunctional inverse opal particles for drug delivery and monitoring." English. In: *Nanoscale* 7.24 (June 2015), pp. 10590–10594. DOI: 10.1039/c5nr02324f. URL: http://pubs.rsc.org/en/content/articlehtml/2015/nr/c5nr02324f.

[139] S. I. Somo, B. Akar, E. S. Bayrak, J. C. Larson, A. A. Appel, H. Mehdizadeh, A. Cinar, and E. M. Brey. "Pore Interconnectivity Influences Growth Factor-Mediated Vascularization in Sphere-Templated Hydrogels". English. In: *Tissue engineering. Part C, Methods* 21.8 (Aug. 2015), pp. 773–785. DOI: 10.1089/ten.tec.2014.0454. URL: http://online.liebertpub.com/doi/10.1089/ten.tec.2014.0454.

[140] R. Parke-Houben, C. H. Fox, L. L. Zheng, D. J. Waters, J. R. Cochran, C. N. Ta, and C. W. Frank. "Interpenetrating polymer network hydrogel scaffolds for artificial cornea periphery". English. In: *Journal of Materials Science* 26.2 (Feb. 2015), pp. 107–12. DOI: 10.1007/s10856-015-5442-2. URL: http://link.springer.com/10.1007/s10856-015-5442-2.

[141] A. Galperin, K. Smith, N. S. Geisler, J. D. Bryers, and B. D. Ratner. "Precision-Porous PolyHEMA-Based Scaffold as an Antibiotic-Releasing Insert for a Scleral Bandage". English. In: *ACS Biomaterials Science & Engineering* 1.7 (July 2015), pp. 593–600. DOI: 10.1021/acsbiomaterials.5b00133. URL: http://pubs.acs.org/doi/abs/10.1021/acsbiomaterials.5b00133.

[142] M. H. Kim, S. K. Kumar, H. Shirahama, J. Seo, J.-H. Lee, V. P. Zhdanov, and N.-J. Cho. "Biofunctionalized Hydrogel Microscaffolds Promote 3D Hepatic Sheet Morphology". English. In: *Macromolecular Bioscience* (Nov. 2015), n/a–n/a. DOI: 10.1002/mabi.201500338. URL: http://doi.wiley.com/10.1002/mabi.201500338.

[143] H. Wang, Q. Xu, L. Shang, J. Wang, F. Rong, Z. Gu, and Y. Zhao. "Boronate affinity molecularly imprinted inverse opal particles for multiple label-free bioassays." English. In: *Chemical Communications* 52.16 (Feb. 2016), pp. 3296–3299. DOI: 10.1039/c5cc09371f. URL: http://xlink.rsc.org/?DOI=C5CC09371F.

[144] J. Li, T. Xu, Q. Wang, J. Ren, K. Duan, Y. Mu, and J. Weng. "Integrating surface topography of stripe pattern on pore surface of 3-dimensional hydroxyapatiye scaffolds". In: *Materials Letters* 169.C (Apr. 2016), pp. 148–152. DOI: 10.1016/j.matlet.2016.01.076. URL: http://dx.doi.org/10.1016/j.matlet.2016.01.076.

Chapter 3

The Colloidal Crystal Template

Colloidal crystals (CC) are very important in ICC construction, namely in the control of pore sizes and related scaffold properties. This chapter focus on the development of uniform CC undergoing the production of monodisperse microspheres and their assembly into lattices. Based on a simple microfluidic device, the production of polymeric particles with uniform diameters in a wide range of sizes is reported. Furthermore methods for selection, packaging and annealing of PS microspheres with specific diameters for bone tissue engineering scaffolds are also described.

3.1 Introduction

Monodisperse polymeric microspheres have been obtained with a diverse set of methods (see section 2.2.1). Microfluidic, a miniaturization of emulsion technique, rises over the conventional methods allowing the production of particles with excellent control over the composition, surface, range size and size standard deviation (SD) [1]. Generally, two phases (Discontinuous phase (DP) and Continuous phase (CP)) containing two immiscible fluids are manipulated in channels with tens to thousands of micrometers. The fluids are brought into contact inside those channels leading to the creation of an emulsion droplet (oil-in-water or water-in-oil) that after solvent evaporation becomes a solid particle [2].

Different microfluidic systems have been proposed, optimizing the geometric scheme that governs the droplet break off and in that way generating particles with spheric, rod, disk, ellipsoid or even hollow and Janus-face shape [3]. Depending on process control parameters, the microfluidic system can either produce stable emulsions by working in *jetting mode* or in *dripping mode*. In the dripping mode, the emulsion is produced at phase contact in the inner orifice at slow production rate (Figure 3.1C) while in the jetting mode, capillary instability takes place and the emulsions are formed at certain distance from

the contact between fluids.

With jet stream instability, emulsion surface area is reduced by interfacial tension action, breaking the flow into small segments. Then the broke emulsion segments shrink in order to minimize the surface area leading to final spherical droplets. Controlling parameters like flow rate, solutions viscosity, interfacial tension and the inner diameter of the capillary tube, different size droplets can be obtained [4].

The formation of emulsions at the end of the inner tip is governed by the competition between the effect of viscous stress and the surface tension stress. This force relation can be determined by calculating the Cappilary number (C_a):

$$\mathrm{C_a} = \mu_\mathrm{c} v_\mathrm{c} / \gamma \tag{3.1}$$

where μ_c and v_c represents the CP viscosity and velocity. Also, the relation between the inertial force from the inner liquid relative to the interfacial tension can be referenced by the Webber number (W_e):

$$\mathrm{W_e} = \rho_\mathrm{d} \mathrm{d_{tip}} v_\mathrm{d}^2 / \gamma \tag{3.2}$$

where ρ_d, d_{tip} and v represent DP density, inside channel inner diameter and velocity, respectively . The interfacial tension is described by γ. When C_a and W_e are low they establish the dripping regime but when they are high the jetting regime dominates[5, 6].

As seen previously in section 2.2.2, colloidal crystal formation depends upon uniform microspheres packaging into an ordered structure. Since larger particles are considered (>10 μm), microspheres have to be confined in specific molds and helped by external methods in order to promote self-assembly into a thermodynamically stable cubic or hcp structure. Then, to stiffen the structure, the polymeric particles have to be subjected to thermal or chemical annealing, allowing necking between neighboring microspheres.

The thermal treatment is responsible for ICC interconnected pores size and CC voids availability for matrix formation. It is essential that a commitment between annealing temperature and pore design is established in order to allow the essential mechanical and biological properties for normal bone tissue development within the scaffold. [7, 8]. In that sense, amorphous polymers like PS and PCL are very useful since they can be softened above its glass transition temperature enabling a wide temperature range for the growth of bridges between particles and therefore allowing an easier production of the solid construct.

3.2 Experimental Section

3.2.1 Microspheres Production

To the production of homogeneous microspheres to use as scaffold template, a microfluidic apparatus (Figure 3.1) was developed based on the one reported by Choi et. al [5].

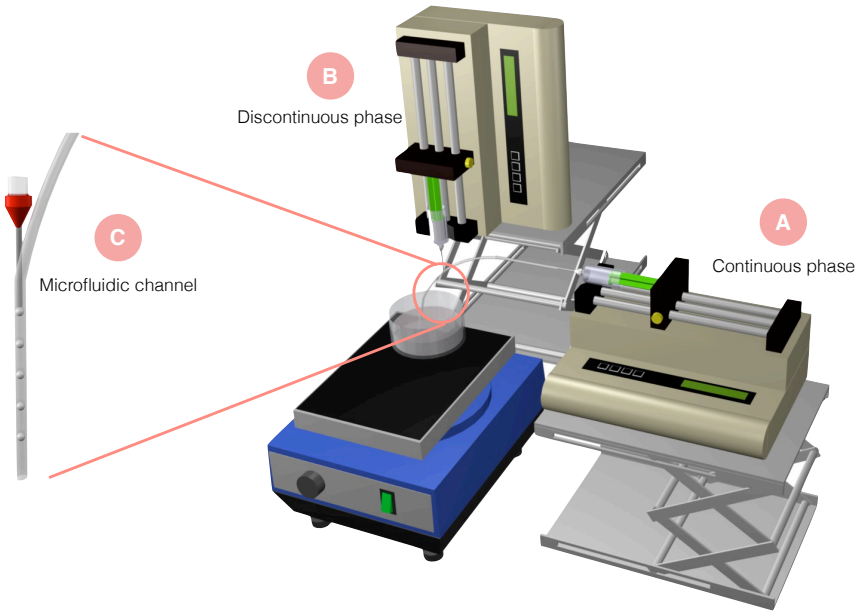

Figure 3.1: Schematic of the microfluidc system used to produce PS and PCL microspheres

The microfluidic system is constituted by 3 parts: A) the continuous phase, B) the discontinuous phase; and C) the microfluidic channel. Two infusion pumps (KDS-100-CE) are used to inject the solutions. The CP is a 2% to 5% (wt/wt) polyvinyl alcohol (PVA, M_w=9,500, Acros Organics) aqueous solution, contained in a syringe (B.Braun 20ml) with a 18G needle. For the DP, a solution of 5% (wt/wt) PS (Mn=350,000, Aldrich) or a 5% (wt/wt) PCL (Mn=70,000-90,000, Aldrich) in dichloromethane (Fluka) is supplied by a syringe with a 25G needle. The microfluidic channel, a PVC tube (1/16 inch), allows the communication between both phases . At the junction of the two phases, droplets are formed and collected at the end of the channel in a glass vessel. The collected droplets stay in the coagulation bath overnight, in an orbital shaker (bioSan OS 20) at 100 rpm, to allow drying by solvent evaporation, turning into solid spheres.

3.2.2 Colloidal Crystal Template Construction

To create the scaffold template, it was necessary to develop a mold (Figure 3.2) in order to confine and compact the microspheres into a singular structure. The mold was constructed with packed perforated teflon and aluminum rectangular layers with circular holes, forming 32 orifices (6 mm diameter; 4 mm depth) that enable the final CC cylindrical shape.

For CC assembly, fourty milligrams of PS microspheres (average diameter 261 ± 11 μm) are weighted (Mettler Toledo AG204) and introduced in each mold hole. Then, 150 μl of Ethanol (purity = 99,9%, Fisher Chemical) is added to the orifices. The mold is put inside an ultrasound bath (Bandelin Sonorex Super RK 510H) for 10 minutes and then in

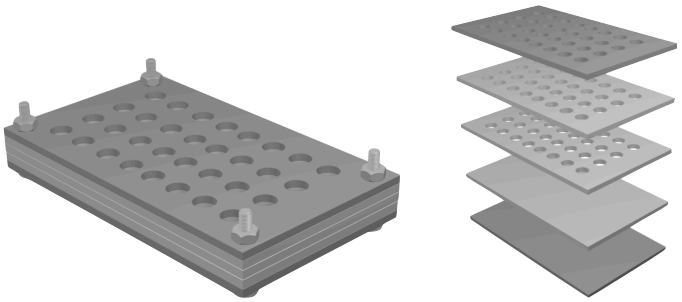

(a) Assembled mold (b) Open mold

Figure 3.2: Homemade mold used to produce the colloidal crystal template.

an orbital shaker (bioSan OS 20) for 1 hour to promote the microspheres self-assembly into a HCP structure. Afterwards, the mold is placed in an oven (Memmert) at 110ºC to 140 ºC for 4 hours to promote microspheres annealing. After cooling, the mold is unpacked and the CC samples are stored for later use.

3.2.3 Characterization

Microspheres and CC structures were morphologically characterized by optical microscopy, OM (Nikon Eclipse LV100) and Scanning Electron Microscopy, SEM (Zeiss Auriga). Spheres diameter was measured from SEM images with software Image J™(version 1.46e Wayne Rasband, National Institutes of Health, USA)[9]. Differential scanning calorimetry (DSC) and thermogravimetry (TG) was conducted on PS and PCL microspheres to evaluate the glass temperature transition (appendix A).

3.3 Results and Discussion

3.3.1 Policaprolactone and Polystyrenne Microspheres

The microfluidic device developed in this work allowed the production of polymeric spheres through oil-in-water micro emulsions. Different spheres were obtained concerning the variation of three main parameters: DP polymer and its concentration; DP flow rate and CP flow rate. In Figure 3.3, SEM images of PCL and PS microspheres are presented. As can be observed, although both type of spheres have similar dimensions, their surface is clearly different. PS spheres present smooth surfaces in contrast with more roughened PCL spheres that often present a raspberry-like morphology. Immediately after their production, swollen PCL and PS spheres show good regularity with smooth surface that after drying is lost in the case of PCL spheres. This difference can be attributed to the polymeric chains rearrangement during DCM evaporation that occurs homogeneously within the PS spheres whilst happens to be heterogeneous within the PCL spheres, conducting to rough zones formation. Another noticeable difference is

the presence of tiny orifices in PCL spheres that could be formed when DCM volatilizes during the non-uniform evaporation.

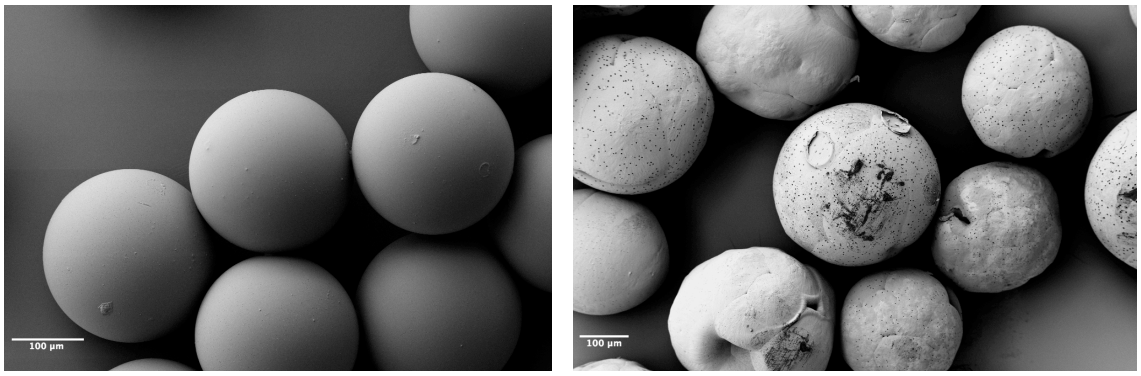

(a) (b)

Figure 3.3: SEM imagens of the microspheres produced using the microfluidic system: a) PS; b) PCL.

Microspheres size definition is very important for the design of final ICC structure porosity. The optimal scaffold pore size essential for successful bone tissue engineering has not been consensually determined in all the works reported in the literature, but usual results point out the 100 to 400 μm range as capable of promoting osteoblasts adhesion and proliferation [10, 11]. Nevertheless, macropores are not the only concern in the ICC architecture and connective pore windows between the main spherical pores must be correctly addressed in order to ensure cell migration throughout the scaffolds. Usually, the ICC's windows diameter corresponds to about 1/4 of the main pores diameter (depending also on the annealing conditions), so since its known that osteoblasts have about 10-30 nm in size and in order to avoid windows blockage by cells, spheres within the 200 to 300 μm range are desirable. In this work microfluidic parameteres were explored and final system operating settings were established in order to produce spheres in that range. All conditions used in this work respected the production of droplets in the microfluidic dripping-mode (see appendix A , section A.1).

In Figures 3.4, 3.5 and 3.6 the data of PCL and PS microspheres diameters measured with ImageJ™ is presented. From all the results it was possible to conclude that PCL and PS droplets formation mechanism follow similar rules and therefore general assumptions could be clearly established:

- Increasing CP flow rate causes microspheres size decrease;
- Increasing DP flow rate leads to microspheres size increase and production rate increase;
- Increasing CP polymer concentration leads to microspheres size decrease;
- Increasing DP polymer concentration contributes to microspheres size increase.

In Figure 3.4, PCL spheres diameters were determined varying CP flow rate and PCL concentration, maintaining DP flow rate at 3 mL/h and PVA concentration at 2%. With the increase of flow rate, droplets were created more frequently and with smaller diameters. This tendency was also verified by decreasing the DP polymer concentration, which conducted to the formation of droplets with less polymeric material that upon drying led to higher shrinking and therefore the formation of smaller spheres. DP polymer concentration of 5% was chosen since it was the minimum concentration needed to produce spheres with sizes that comply with the established criteria.

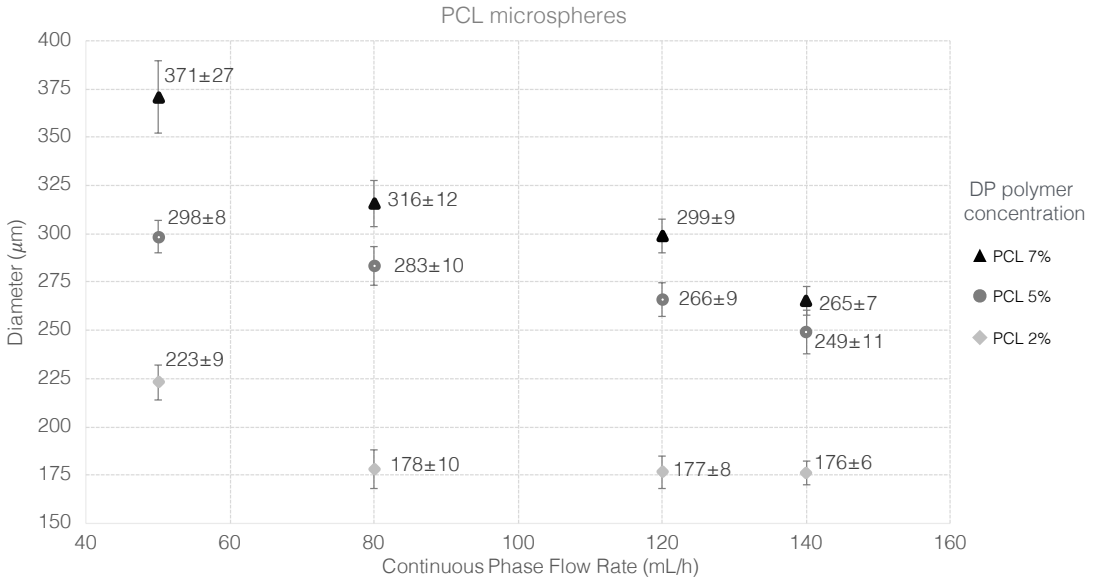

Figure 3.4: PCL microspheres diameter variation as a function of continuous phase flow rate for different DP polymer concentrations: light gray - PCL 2% wt/wt; dark gray - PCL 5% wt/wt; black - 7% wt/wt (Constants: DP flow rate = 3mL/h; PVA = 2% wt/wt).

In Figure 3.5, PS spheres diameters were studied varying CP flow rate and PVA concentration, maintaining DP flow rate at 3 mL/h and PS concentration at 5%. The increase of CP polymer concentration led to the increase of CP viscosity and higher influence of the surfactant effect over the PS droplet. For a 5% PVA solution, with the increase of CP flow rate, from 10 to 50 mL/h, the viscous shear stress effect becomes more intense and causes the quick sphere reduction from 317±15 μm to 165±17μm. For the 2% PVA solution that effect is reduced, sphere diameter transition is smoother, higher CP flow rate range is needed (from 50 to 140 mL/h) and a decrease from 317±12 μm to 210±4μm is observed. Sizes of PS microspheres produced using PVA 2% can be compared with PCL 5% microspheres sizes reported above in Figure 3.4. For CP flow rates of 50 to 140 mL/h, PS originates microspheres with similar or slightly smaller diameters which shows that PS and PCL droplet formation parameters are similar. However, PVA 2% revealed to be insufficient to allow the collection of isolated spheres and often after drying, PS spheres aggregated and could not be further used. In that sense, PVA 5%, having a higher surfactant effect, allowed handling of single spheres and therefore was chosen for PS

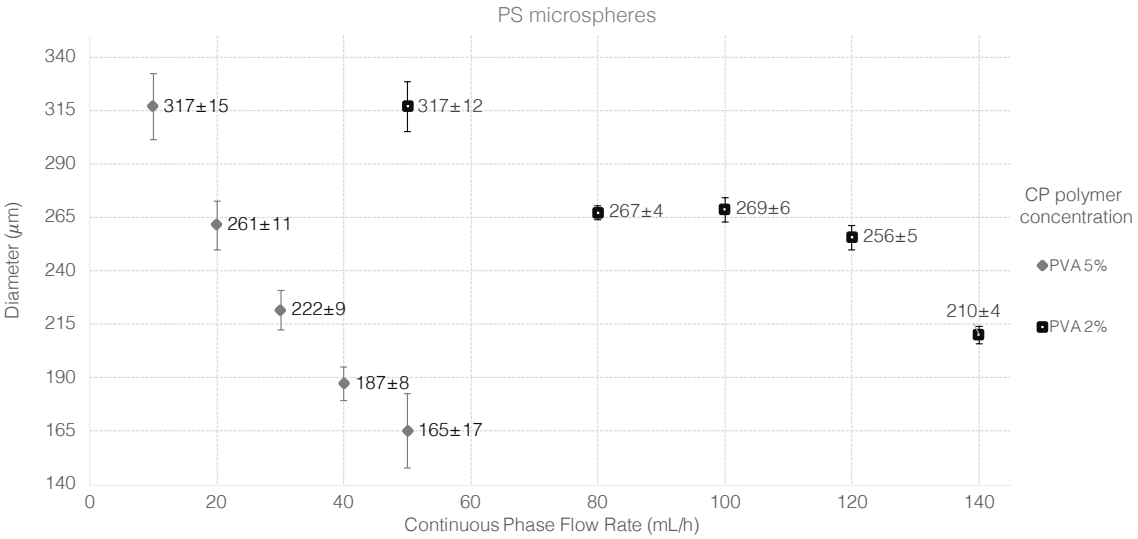

Figure 3.5: PS microspheres diameter variation as a function of continuous phase flow rate for different CP polymer concentration: dark gray - PVA 5% wt/wt; black - PVA 2% wt/wt (Constants: DP flow rate = 3mL/h; PS = 5% wt/wt).

microspheres production, contributing also for the reduction of CP solution volume since lower flow rates could be applied.

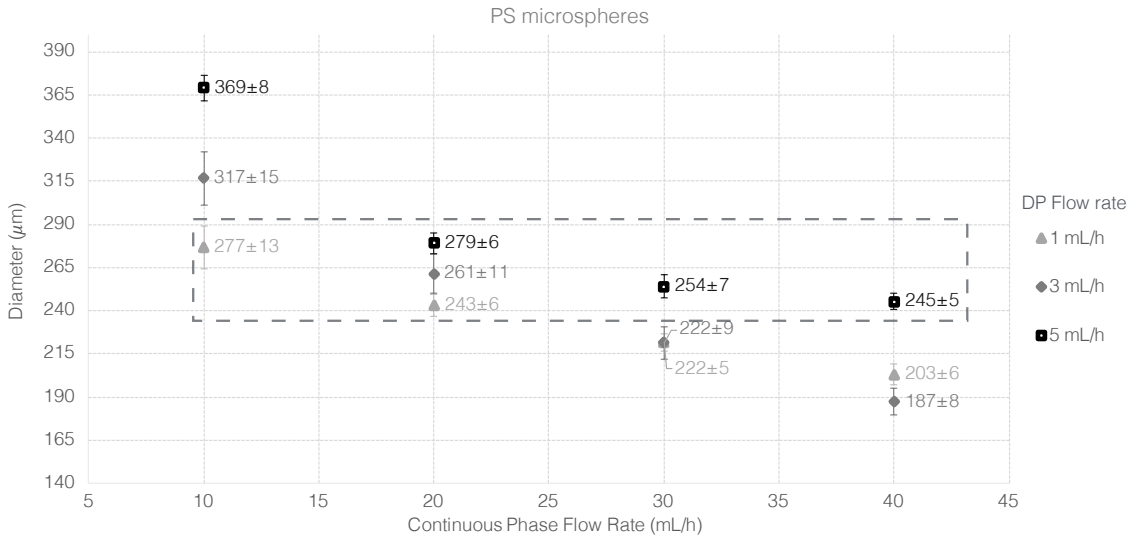

Figure 3.6: PS microspheres diameter variation as a function of continuous phase flow rate for different DP flow rates: light gray - 1mL/h; dark gray - 3mL/h; black - 5mL/h (Constants: PS = 5% wt/wt; PVA = 5% wt/wt).

Finally, Figure 3.6 shows the evolution of PS microspheres diameter by changing CP and DP flow rates. The increase of DP flow rate allows the production of bigger spheres whilst, as seen before, the increase of CP flow rate induces the formation of smaller spheres. Nevertheless, all DP flow rates chosen (1 to 5 mL/h) enabled the production of spheres that targeted the 200 to 300 μm size interval. From the results, a tighter

selection was made (rectangle with discontinuous line) and spheres within 245±3μm and 277±13μm were chosen since they enable a larger range of CP flow rates. Further system settings optimization towards the use of smaller solutions volume and the increase of spheres production rate resulted in the selection of spheres with 261±11μm diameter, corresponding to the microfluidic parameters:

- DP concentration: PS 5%
- DP flow rate: 3 mL/h
- CP concentration: PVA 5%
- CP flow rate: 20 mL/h

Moreover, the diferences in morphology justify the use of PS as main material for microspheres production since surface roughness of PCL microspheres can lead to the formation of defects in colloidal crystal structure, resulting in non-uniform pores in the ICC scaffold.

3.3.2 Polystyrenne Colloidal Crystal Template

Here, a simple method for the packaging and assembling of microspheres into HCP lattices is reported. Using the teflon mold (Figure 3.2), vibration and gravitational forces and ethanol as dispersion medium it was possible to ensure ordered packaging of spheres that self-assembled at the bottom of every hole. However, to obtain a single structure composed of thousands of spheres, it was necessary to introduce a thermal treatment - annealing - that allowed the partial fusion of the junctions between consecutive particles.

Being an amorphous polymer, PS does not have a specific melting point but instead softens gradually as temperature rises from the glass transition temperature, T_g, and above, increasing the freedom of movement of local segments of the polymeric chain. Analyzing the polymer thermal behavior through DSC-TG (Appendix A - FigureA.5), PS begins to soften sensibly at 97.2ºC. According to this T_g, annealing temperatures between 110ºC and 140ºC were selected to produce structurally stable colloidal crystal templates (Figure 3.7).

Bellow 115ºC, the temperatures were not sufficient to provide enough annealing between spheres and when manipulating the CC, the structure colapsed. It was found that 120ºC was the minimum temperature that could be used to obtain structural integrity for handling. By contrast, temperatures above 140ºC gave rise to excessive particle melting that could result in templates with insufficient space for matrix infiltration or final scaffolds with non-spherical macropores and/or oversized pore windows.

From all annealing temperatures, 130ºC is the one that allows structurally stable CCs with interconnected microspheres and enough open spaces for ICC's material infiltration. However, some irregularities were observed in the CC template which resulted in uneven

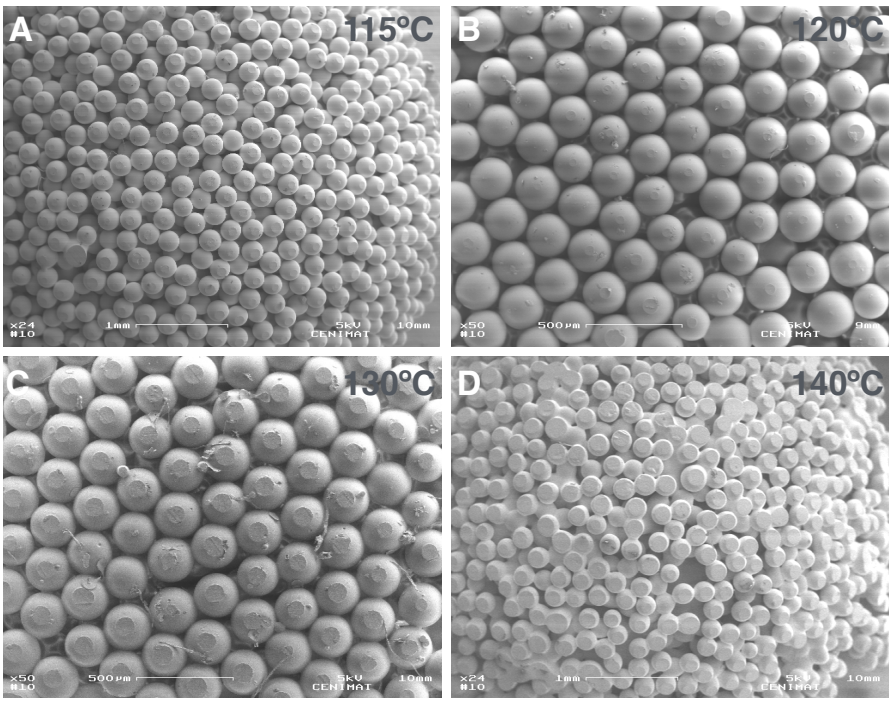

Figure 3.7: SEM images of the colloidal crystal templates annealed at different temperatures: A) 115ºC; B) 120ºC; C) 130ºC and D) 140ºC.

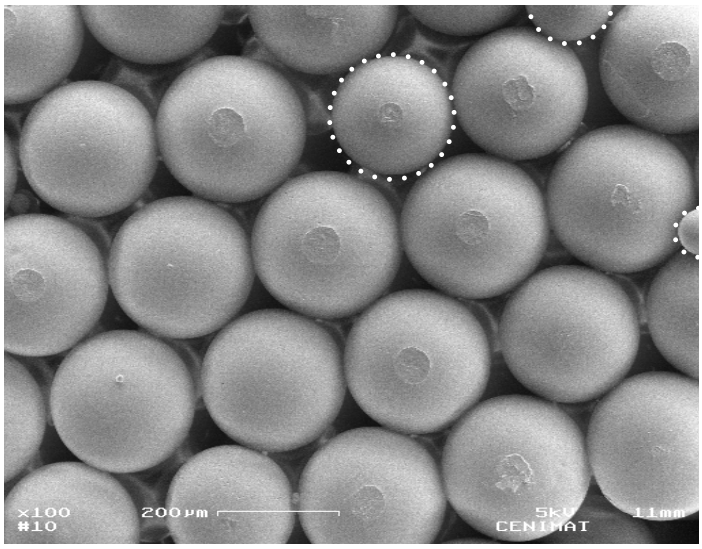

Figure 3.8: SEM images of the colloidal crystal template annealed at 130ºC with noticeable minor spheres that cause defects in the packed structure .

necking in some scaffold areas (Fig 3.8). The presence of larger or smaller than average spheres in the packaging stage can lead to the occurrence of local defects that propagate in the long-range system, destabilizing the uniformity and connectivity. Although our microfluidic device allowed the production of spheres with SD less than 5%, its normal that sometimes in a long production batch some very small and/or oversized spheres are

obtained due to minor microfluidic perturbation. To eliminate such defects, a sieving stage was created after collecting the spheres. Using sieves of 212, 250, 280 and 300 μm pore size, the spheres were screened and the 250-280μm range selected for the production of CC with acceptable uniformity (Fig 3.7C). If a more perfect arrangement is required, introducing narrow sieve ranges in the screening step will be sufficient to reduce or eliminate final structure defects.

3.4 Conclusions

A fluidic device based upon microcapillary tubes was developed to produce microspheres of uniform diameters (less than 5 % diameter variation). PS and PCL microspheres, whose diameters can vary in the range (150 - 400) μm, were obtained exhibiting smooth and rough surfaces, respectively. PS spheres were assembled in hcp lattices using a combination of agitation and solvent evaporation. The heat treatment at 130ºC was used to make the CC a cohesive structure by fusing the microspheres at their contact points. At this time PS colloidal crystals were obtained for further use as templates in ICC development.

References

[1] C. A. Serra and Z Chang. "Microfluidic-Assisted Synthesis of Polymer Particles". English. In: *Chemical Engineering & Technology* 31.8 (Aug. 2008), pp. 1099–1115. DOI: 10.1002/ceat.200800219. URL: http://doi.wiley.com/10.1002/ceat.200800219.

[2] P. Tabeling. *Introduction to Microfluidics*. English. Oxford University Press, May 2010. ISBN: 0199588163. URL: http://books.google.pt/books?id=wysKAwAAQBAJ&pg=PA21&dq=intitle:Introduction+to+Microfluidics&hl=&cd=1&source=gbs_api.

[3] M Kalyanaraman, S. Retterer, T. McKnight, M. Ericson, S. Allman, J. Elkins, A. Palumbo, M Keller, and M. Doktycz. "Controlled microfluidic production of alginate beads for in situ encapsulation of microbes". In: *Biomedical Science & Engineering Conference, 2009. BSEC 2009. First Annual ORNL*. 2009, pp. 1–4. DOI: 10.1109/BSEC.2009.5090482. URL: http://ieeexplore.ieee.org/search/freesrchabstract.jsp?tp=&arnumber=5090482.

[4] L. Zhu, Y. Li, Q. Zhang, H. Wang, and M. Zhu. "Fabrication of monodisperse, large-sized, functional biopolymeric microspheres using a low-cost and facile microfluidic device". English. In: *Biomedical Microdevices* 12.1 (2010), pp. 169–177. DOI: 10.1007/s10544-009-9373-x. URL: http://links.isiglobalnet2.com/gateway/Gateway.cgi?GWVersion=2&SrcAuth=mekentosj&SrcApp=Papers&DestLinkType=FullRecord&DestApp=WOS&KeyUT=000275195000020.

[5] S.-W. Choi, I. W. Cheong, J.-H. Kim, and Y. Xia. "Preparation of uniform microspheres using a simple fluidic device and their crystallization into close-packed lattices." English. In: *Small (Weinheim an der Bergstrasse, Germany)* 5.4 (Apr. 2009), pp. 454–459. DOI: 10.1002/smll.200801498. URL: http://eutils.ncbi.nlm.nih.gov/entrez/eutils/elink.fcgi?dbfrom=pubmed&id=19189332&retmode=ref&cmd=prlinks.

[6] C.-H. Choi, J.-H. Jung, T.-S. Hwang, and C.-S. Lee. "In Situ Microfluidic Synthesis of Monodisperse PEG Microspheres". English. In: *Macromolecular Research* 17.3 (2009), pp. 163–167. URL: http://www.springerlink.com/index/J6T444V2104V4157.pdf.

[7] S Shanbhag, J. Lee, and N Kotov. "Diffusion in three-dimensionally ordered scaffolds with inverted colloidal crystal geometry". English. In: *Biomaterials* 26.27 (Sept. 2005), pp. 5581–5585. DOI: 10.1016/j.biomaterials.2005.01.059. URL: http://linkinghub.elsevier.com/retrieve/pii/S0142961205001092.

[8] Y. S. Zhang, K. P. Regan, and Y. Xia. "Controlling the pore sizes and related properties of inverse opal scaffolds for tissue engineering applications." English. In: *Macromolecular rapid communications* 34.6 (Mar. 2013), pp. 485–491. DOI: 10.1002/marc.201200740. URL: http://pubget.com/site/paper/23365045?institution=.

[9] C. A. Schneider, W. S. Rasband, and K. W. Eliceiri. "NIH Image to ImageJ: 25 years of image analysis". In: *Nature Methods* 9.7 (June 2012), pp. 671–675. DOI: 10.1038/nmeth.2089. URL: http://www.nature.com/doifinder/10.1038/nmeth.2089.

[10] S.-W. Choi, J. Xie, and Y. Xia. "Chitosan-Based Inverse Opals: Three-Dimensional Scaffolds with Uniform Pore Structures for Cell Culture." English. In: *Advanced materials (Deerfield Beach, Fla.)* 21.29 (Apr. 2009), pp. 2997–3001. DOI: 10.1002/adma.200803504. URL: http://eutils.ncbi.nlm.nih.gov/entrez/eutils/elink.fcgi?dbfrom=pubmed&id=19710950&retmode=ref&cmd=prlinks.

[11] C. M. Murphy, M. G. Haugh, and F. J. O. Brien. "The effect of mean pore size on cell attachment, proliferation and migration in collagen-glycosaminoglycan scaffolds for bone tissue engineering". In: *Biomaterials* 31.3 (Jan. 2010), pp. 461–466. DOI: 10.1016/j.biomaterials.2009.09.063. URL: http://dx.doi.org/10.1016/j.biomaterials.2009.09.063.

Chapter 4

Hydroxyapatite Inverted Colloidal Crystal Scaffolds

Hydroxyapatite (HAp) scaffolds with uniform pore size and interconnected pore network were constructed based on the inverted colloidal crystal (ICC) geometry and a simple sol-gel formulation. Monodisperse polystyrene microspheres were self-assembled and annealed into a hexagonal close packed structure. HAp sol-gel was infiltrated in this template followed by thermal treatment for simultaneous HAp matrix sintering and polymeric colloidal crystal calcination. The resultant ICC scaffolds exhibit an ordered architecture that was able to offer a favourable environment for human osteoblasts adhesion and proliferation, an essential feature for bone ingrowth in tissue engineering applications [1].

4.1 Introduction

Bone tissue engineering requires the development of 3D scaffolds that provide the necessary support for cell adhesion, proliferation and differentiation, and whose architecture contributes to cell migration and regenerative activity through an adequate supply of oxygen and nutrients [2]. As biocompatible scaffolding materials, bioceramics namely calcium phosphates (CPs) and in particular hydroxyapatite (HAp) and β-Tricalcium phosphate (β-TCP), are frequently used due to their bone-bonding properties, bioactivity, noninflammatory and osteoinductive properties [3, 4].

Stoichiometric HAp, ie $Ca_{10}(PO_4)_6(OH)_2$, belongs to the apatite group and is an hexagonal isomorphic mineral with a Ca/P ratio of 1.67. HAp is susceptible to capture ions like Pb^{2+}, Cd^{2+}, Co^{2+}, Cu^{2+} and Fe^{2+} that can change its crystallinity, crystal network

[1] The work described in this chapter is based on the publication: C. F. C. João, R. Almeida, J. C. Silva, J. P. Borges. "A simple sol-gel route to the construction of hydroxyapatite inverted colloidal crystals for bone tissue engineering" in Material Letters 2016. http://dx.doi.org/10.1016/j.matlet.2016.09.030 [1].

Table 4.1: Examples of procedures for manufacturing HAp porous scaffolds. Adapted from [7].

Procedure	Porosity control	Pore size	Porosity	Compressive strength
		(μm)	(%)	(MPa)
HAp + ammonium methacrylate in PTFE mold, freeze-dried and sintered (1300ºC)	Slurry concentration and pore controled by physics of ice front formation	50-150 open unidirectional	>60 56 47	16 65 145
Polymer foams infiltrated with HAp powder, compressed and calcined (700-1300ºC)	Extent of compression, HA loading	100-200	n.d.	n.d.
Directly injectable nanocrystalline HAp, self hardens, mannitol as porogen	Controling of mannitol mass fraction in mixture	0-50% macroporous	65-82	2.2-4.2 flexural
Sponge impregnation, isotactic pressing, sintering (1250ºC, 1h) of HAp in simulated body fluid	n.d.	6% closed 60%open	66	23 ± 3.8
Thermoplastic negative porosity by Ink jet printing, slip casting process for HAp	Negative printing	n.d.	44	12.5 ± 4.6
Slurries of HAp prepared: gel-casting + polymer sponge technique, sintered (600ºC, 1h and 1350ºC, 2h)	Replicate of polymer sponge template	200-400	70-77	0.5-5
Slurry of HAp with polyoxyethylene - laurylether (crosslinked) and sintered (1200ºC, 3h)	Polymer interconnects cross-linking	200-500	77	2.25 (0 weeks) 4.92 (12 weeks) 11.2 (24 weeks)
Electrophoretic deposition of HAp, sintering (1200ºC, 2h).	Electrophoresis field	0.5-130	20	860

n.d.= non-defined

parameters, crystal dimensions, stability and solubility. When substituted with fluor, the physical, chemical and biological properties of HAp improve with the increase of crystallinity, increase of cristal size (t) and reinforcement of structural stability [5, 6].

Calcium and phosphorus are the most important minerals to be considered since both actively participate in the ionic equilibrium between the ceramic and the body fluid. Although biological HAp does not respect the 1.67 ratio and is slightly carbonated, the fact that stoichiometric HAp is constituted in its majority by Ca and P allows higher

Table 4.2: Examples of commercially available HAp based scaffolds.

Product	Composition	Pore size	Porosity	Compressive strength	Ref.
	(HAp%/β-TCP%)	(μm)	(%)	(MPa)	
Adbone®BCP	75/25	300-500	80	1-2	[8]
BF+®	60/40	200-500	60-80	n.d.	[9]
Ceraform®	65/35	150-400	60-85	n.d.	[10]
Graftys®BCP	60/40	>100	70	>10	[11]
Neobone®	75/25	200-500	60-80	>0.2	[12]
Reprobone™	60/40	200-800	83	>1.5	[13]
TCH®	75/25	200-500	60-80	>5	[14]

n.d.= non-defined

affinity with hard and soft tissues where those minerals dominate. HAp resemblance with bone ceramic phase and the ability to forme stable interfaces with living host tissue has been driving researchers to investigate HAp based applications and a huge set of procedures have already been reported as capable of originating porous HAp structures (Table 4.1).

Companies dedicated to healthcare, medical devices and tissue regeneration fields have also been exploring the HAp use (alone or in combination with other CPs) in the development of several products with capacity to promote bone regeneration. Table 4.2 presents a few examples of 3D scaffolds available as commercial products, usually referred to as bone grafts, from the companies Medbone, Ldr, Teknimed, Graftys, Ceramed, Ceramisys and Kasios. More information about the bone graft market can be found in section 1.2.

In this work, a simple method for the design of 3D HAp scaffolds exhibiting the ICC architecture is suggested. Combining a polymeric colloidal crystal (CC) template with a ceramic sol-gel route, the procedure for the development of scaffolds with high porosity and controllable pore network is presented, along with the morphological, chemical and *in-vitro* characterization of the resultant products.

4.2 Experimental Section

4.2.1 Hydroxyapatite Sol-Gel Preparation

For the fabrication of the ceramic precursor, HAp was produced using a simple sol-gel route adapted from the work reported by Franco et al. [15] for the production of HAp electrospun fibers. Briefly, solutions containing calcium nitrate 4-hydrate ($Ca(NO_3)_2.4H_2O$, Panreac) and phosphorous pentoxide (P_2O_5, Sigma-Aldrich) precursors in ethanol were mixed together in a Ca/P molar ratio of 1.67. A translucent gel with low viscosity was obtained after stirring this mixture for 5h and ageing it for 24h, both at ambient temperature. Posteriorly, a binder composed of 25 wt% poly(vinylacetate) (PVAc)($(C_4H_6O_2)_n$, Acros Organics, $M_w \simeq 100{,}000$) (PVAc) in acetone was added to the gel at a gel:binder 98:2 weight ratio in order to hold the ceramic structure together and reduce the amount

of structural defects after HAp gel drying.

4.2.2 Colloidal Crystal Construction

Homogeneous polystyrene (PS) microspheres with diameters of (261 ± 11) μm were obtained using a microfluidic apparatus built according to Choi et al.[16]. The PS microspheres were self-assembled into a hexagonal close packed (hcp) structure in a cylindrical mould under orbital agitation. Subsequently, the microspheres were heated at 130°C for 4 hours to promote annealing between adjacent microspheres. A solid structure CC was obtained after mold removal (see chapter 3).

4.2.3 Ceramic ICC Scaffold Production

The CC was infiltrated with the HAp + binder gel mixture by introducing the template into the solution and forcing its infiltration under vacuum. The binder consisted of a 25 wt/wt% PVAc solution in acetone. The impregnated template was placed in a muffle oven (Select-Horn Electric Muffle Furnace) and subjected to 4 temperature stages, comprehending drying (at 75°C), template removal (450°C and 550°C) and sintering (600°C, 800°C or 1100°C):

1. 75°C for 20h at a heating rate 1°C/min;
2. 450°C at a rate of 2°C/min and held for 2h;
3. 550°C at a rate of 2°C/min and held for 2h;
4. 600°C or 800°C or 1100°C for 2h for sintering, with a heating rate of 10°C/min.

Low heating rates were used to ensure that ICC's internal shape was not destroyed. The slow heat-up rate from ambient temperature prevented bloating from evaporation that could originate cracks in the structure. A schematic representation of ICC production is shown in Figure 4.1.

4.2.4 Characterization

The ICC scaffold was characterized by SEM for morphological assessment, Archimedes method for porosity evaluation, X-ray diffraction (XRD) for calcium phosphate phase composition, crystal size and crystallinity calculation, compression tests for mechanical properties evaluation, Fourier transform infrared spectroscopy (FTIR) for chemical analysis and *in vitro* culture and fluorescence microscopy of human osteoblasts for cell adhesion and proliferation (Appendix A, section A.2.3).

Morphological characterization of the polymeric CC's and the ceramic ICC was performed using a Zeiss (model DSM 962) scanning electron microscope (SEM). All samples

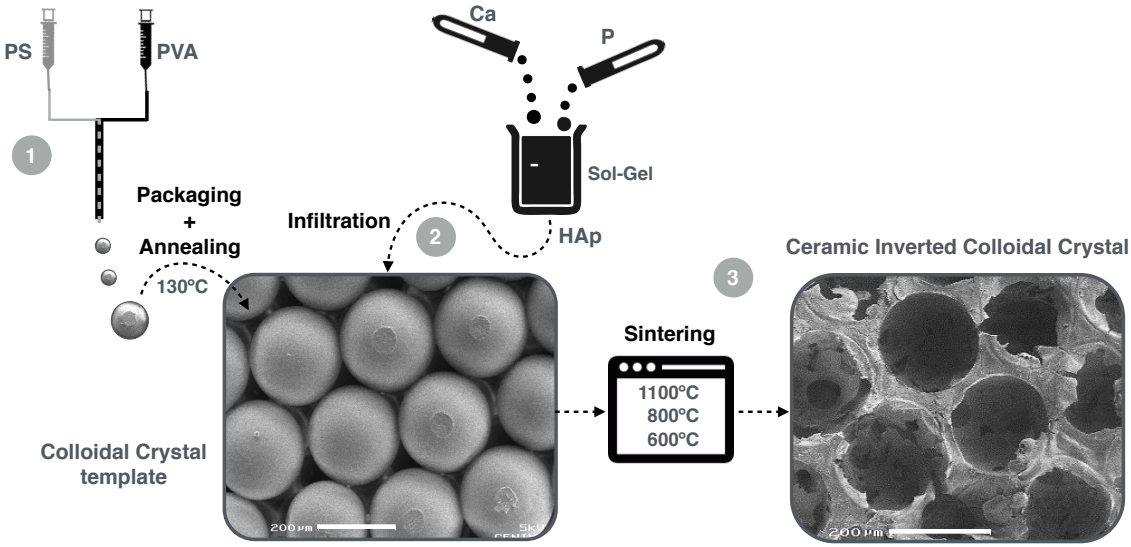

Figure 4.1: Production of HAp ICC scaffolds: 1) Microspheres and colloidal crystal template construction; 2) Sol-gel synthesis and template infiltration by vacuum; 3) ICC production in a single step of spheres calcination and ceramic matrix formation.

were sputter-coated with gold before SEM observation. Microspheres and cells were observed with optical microscopes, Olympus Microscope Digital Camera DP73 and Nikon Inverted Microscope Eclipse Ti-S, respectively.

Uniaxial mechanical properties of the ICC scaffolds were evaluated through compressive tests with a Rheometric Scientific (Minimat Firmware 3.1) system equipped with 20 N load cell. At least 10 samples of each composition were compressed at a rate of 0.5 mm/min, in a dry state (45% relative humidity) at room temperature (23 ºC) and the compressive modulus was determined as the slope of the linear portion of the stress-strain curve.

Scaffolds porosity was measured following the Archimedes method proposed by Unosson et al. [17].

Glass transition and melting temperatures of PS and PVAc were evaluated by DSC and TG (Appendix A, section A.2.2).

The phase composition and crystallinity of HAp was analyzed by XRD using CuKα radiation generated at 45 kV and 40 mA, in the range of $20°<2\theta<60°$, in a X'Pert PRO (PANAlytical) X-ray diffractometer. The obtained peaks were compared with JCPDS cards: #09-0169(β-TCP), #09-0348 (α-TCP), #09-0432(HAp) and #37-1497 (CaO). The t was calculated from XRD patterns using the Scherrer equation 4.1 [18]:

$$t = \frac{0.9\lambda}{\beta \cos\theta_B} \tag{4.1}$$

where λ represent the X-ray wavelength, β the width at the half of the maximum diffraction peak, θ_B the maximum peak respective Bragg angle. The crystallinity degree (X_c),

corresponding to the fraction of crystalline phase present in the analyzed sample, was calculated following the method of Landi et al. [19]:

$$X_c \approx 1 - \frac{V_{112/300}}{I_{300}} \tag{4.2}$$

where I_{300} is the intensity of (300) reflection and $V_{112/300}$ is the intensity of the hollow between (112) and (300) reflections, which completely disappears in non-crystalline samples.

Chemical bonding analysis of the different sintered samples was carried by FTIR using a Thermo Scientific (model Nicolet 6700) spectrometer.

4.3 Results and Discussion

4.3.1 Ceramic ICC Scaffold

Fabrication of the ceramic ICC implied a single-step procedure of sphere removal and sintering, composed of 4 temperature stages. Gel drying occurs during the first stage with the loss of solvent and physically adsorbed water leading to a solid structure able to maintain its shape. In stage 2, the temperature above PS and PVAc glass transitions (Figures A.4 and A.5) caused the PS template softening. Above 250°C, pyrolysis of the dried gel molecular network began. Pyrolysis created tiny "holes" in the skeletal network that contributed to pore volume and surface area increase with no associated shrinkage. At the hold temperature the pyrolysis of organics was complete and HAp crystallization began. At stage 3, the PS template was completely calcined. The ICC became a porous structure composed by an assembly of ceramic particles.

The thermal treatment's last stage ensured the sintering, during which the majority of the densification and microstructure development took place. The plateau temperature was chosen to ensure that crystalline HAp was present (Figure A.6). At the lower temperatures (600°C and 800°C) the densification was not effective. At the higher temperature (1100°C), the ICC's present a fully interconnected structure with 80 vol.% porosity and pore sizes of (196 ± 13)μm (Figure 4.2A). The scaffolds also present sub-micrometer porosity and roughness on their surface (Figure 4.2C).

4.3.2 Matrix Characterization

In order to characterize the ceramic matrix that composes the ICC scaffolds, XRD and FTIR analysis were conducted for the samples sintered at different temperatures (Figure4.3). From the diffractograms it is possible to infer that temperature plays an important role on the formation of crystalline hydroxyapatite. As the sintering temperature is increased from 600°C to 1100°C, several of the HAp peaks become more distinct and narrower which suggests an increase in crystallinity. Crystal size growth is verified from (25 ± 3) nm to (47 ± 5) nm and (62 ± 3) nm for T=600°C, 800°C and 1100°C, respectively.

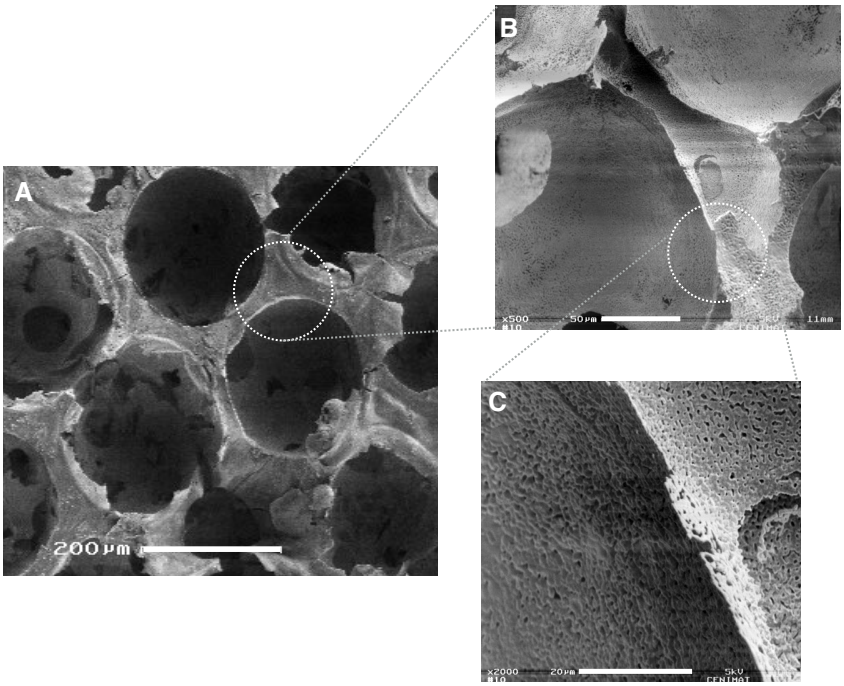

Figure 4.2: SEM images of the HAp ICC scaffold showing its macroporosity (A), pore walls (B) and microporosity (C).

Moreover, the crystallinity degree augments from 31% to 51% and 98% for the same temperature range.

Using stoichiometric hydroxyapatite it should be possible to sinter, without phase purity problems, at temperatures up to 1300°C [20]. However, a minor misbalance in the calcium/phosphorus ratio (from the standard molar ratio of 1.67) can lead to the appearance of additional crystalline phases during heat treatment. It can be seen that β-TCP (β-$Ca_3(PO_4)_2$) appeared at all the sintering temperatures. As the temperature rises to 1100°C a fraction of β-TCP phase transforms into α-Tricalcium phosphate (α-TCP) (α-$Ca_3(PO_4)_2$). The phase was observed after sintering at 800°C and above. This data indicates that in this experiment, as the sintering temperature increased, HAp partly decomposed into β-TCP/α-TCP and CaO, following the reaction proposed by Fahti et al. [21]:

$$Ca_{10}(PO_4)_6(OH)_2 \rightleftharpoons 3Ca_3(PO_4)_2 + CaO + H_2O \tag{4.3}$$

These calcium phosphates have different solubilities (HAp being the least soluble) [20], which in the case of ICC matrix biphasic composition can influence the scaffold dissolution/bioresorption rate in *in vivo* applications.

In Figure 4.3B the FTIR spectra of HAp ICC's sintered at different temperatures is presented. The most characteristic chemical groups in a HAp FTIR spectra are PO_4^-, OH^- and CO_3^{2-}. The first indication of the formation of HAp is in the form of broad band centered at about 1000 - 1100 cm^{-1}. The bands at 960 - 965 cm^{-1} and at 560 - 601 cm^{-1}

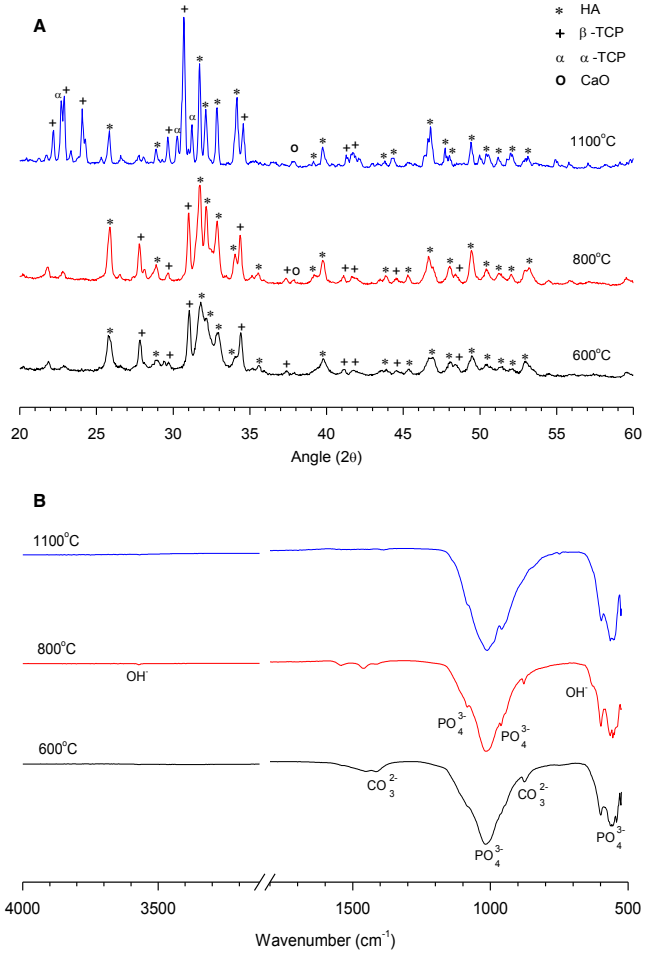

Figure 4.3: Difractograms (A) and FTIR spectra (B) of HAp ICCs sintered at 600°C, 800°C and 1000°C. The diffractograms show the increase of crystallinity of the ceramic but also the evolution of the composition towards a HAp/β-TCP biphasic ceramic with increasing sintering temperature.

correspond to the symmetric P-O stretching vibration of the PO_4^{3-} ion [22]. CO_3^{2-} group forms a weak peak at 877 cm^{-1} and a wider band between 1459 and 1546 cm^{-1} that suggest the presence of a type A carbonated hydroxyapatite (hydroxyl ions are replaced by carbonate ions) [21]. At 1100 °C the vibrational assignment of CO_3^{2-} is absent from the FTIR spectra evidencing that carbonate substitution no longer exists. The bands assigned to the stretching modes of hydroxyl groups of HAp (3571 cm^{-1} and 632 cm^{-1}) can also be observed in the spectra [22].

4.3.3 Mechanical Properties Evaluation

The mechanical properties of HAp ICC scaffolds sintered at three different temperatures were evaluated through compression tests (Figure 4.4). Compressive strength of ceramic porous scaffolds depends on various factors. Macrostructure (architecture of pores) and the microstructure (for instance, the presence of cracks within the structure walls), have

a strong influence on the mechanical behavior of the ceramic porous material.

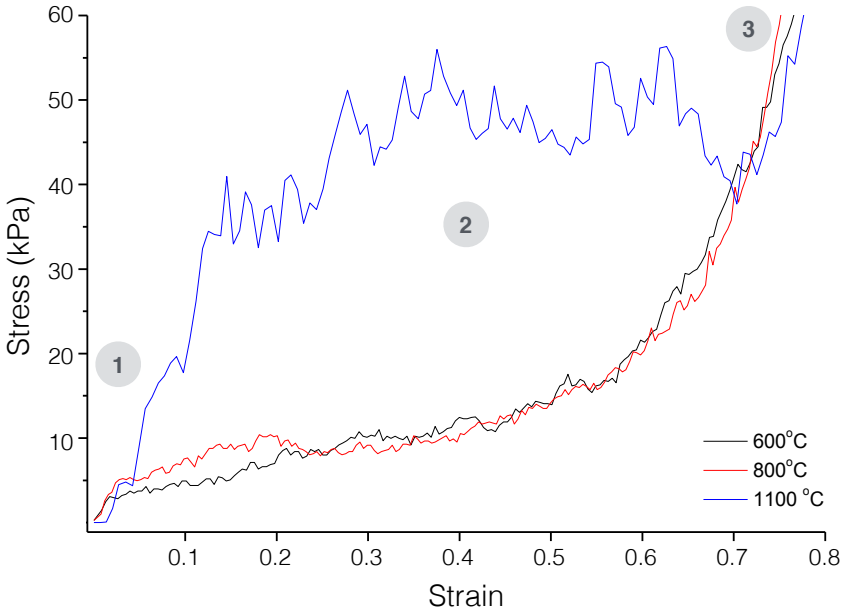

Figure 4.4: Typical stress/strain curves obtained from the compression tests of HAp ICC scaffolds sintered at 600ºC, 800ºC and 1100ºC. 1 - Elastic region; 2 - Plastic region; 3 - Densification

The stress-strain curves show the typical behavior of a foam-like structure with honeycomb architecture reported by Gibson and Ashby [23]. Three regions are shown corresponding to different deformation mechanisms: 1) linear elasticity; 2) plateau of roughly constant stress; 3) densification region. Stress oscillations in those regions are characteristic of brittle materials which is the case of ceramics like HAp.

When the compressive loading begins, the cell walls bend and the material exhibit pseudo elastic behavior (region 1). Here, there is a linear elastic deformation and E can be determined from the strain-stress curve slope. Then, when a critical strain is reached (yield point), the cells collapse by brittle fracture (region 2). This collapse will proceed under nearly constant load to a relatively high strain level. The limit state of compressive stress that leads to failure by brittle crushing (Crushing compressive strength (σ_{cr})) and characterizes the plateau region, is considered coincident with the ultimate compressive strength and the yield point in brittle materials. At high strains (region 3), the cells collapse is finished and with further deformation, the cell walls begin to touch with each other, closing up the structure and leading to densification, which causes the fast stiffness increase visible by the almost exponencial increase of the stress/strain curve [23].

As can be seen from Figure 4.4, sintering temperature has a significant influence in the scaffolds mechanical properties. From the linear region of the stress-strain curves, the elastic modulus of (171 ± 12) kPa, (227 ± 34) kPa and (747 ± 130) kPa for 600ºC, 800ºC and 1100ºC ICC scaffolds were determined. There is also a noticeable increase of the plateau region compressive strength with σ_{cr} of 3 to 10 kPa in the lower temperature

sintered ICCs to 35-45 KPa in 1100ºC ICCs. Taking into account that macropore design and organization (macrostructure) obeys the ICC geometry in all cases, the increase of temperature causes the augmentation of cell walls relative density (microstructure) which results in higher resistance to pore wall bending and collapsing. Thus, the ICC would exhibit higher E and higher plateau stress with temperature increase.

However, the compressive strength observed in the highest temperature sintered ICC is still low when compared with the available commercial products. This is a symptom that ICC structure has lack of material within the pore walls which may be explained by the use of low concentration of HAp precursors and/or by the sol-gel process itself. After CC infiltration with the HAp gel and during the heating process first stage, the scaffolds walls are formed by expansion of the gel. The expansion is able to generate a HAp network with entrapped air bubbles, giving rise to a foam-like morphology. Although the surface seems completely dense, walls interior might be composed of voids that provoke the existence of non-continuous medium and therefore explain the low mechanical properties. Considering this phenomenon, the HAp ICC scaffolds manufacturing procedure has large room for improvement and possible alternative solutions might consist in using HAp precursors with increasing concentration towards higher material content inside the scaffold walls and/or modifying the heating process first stage by increasing its duration and reducing the heating rate in order to reduce the air-bubble formation.

4.3.4 Biocompatibility Evaluation

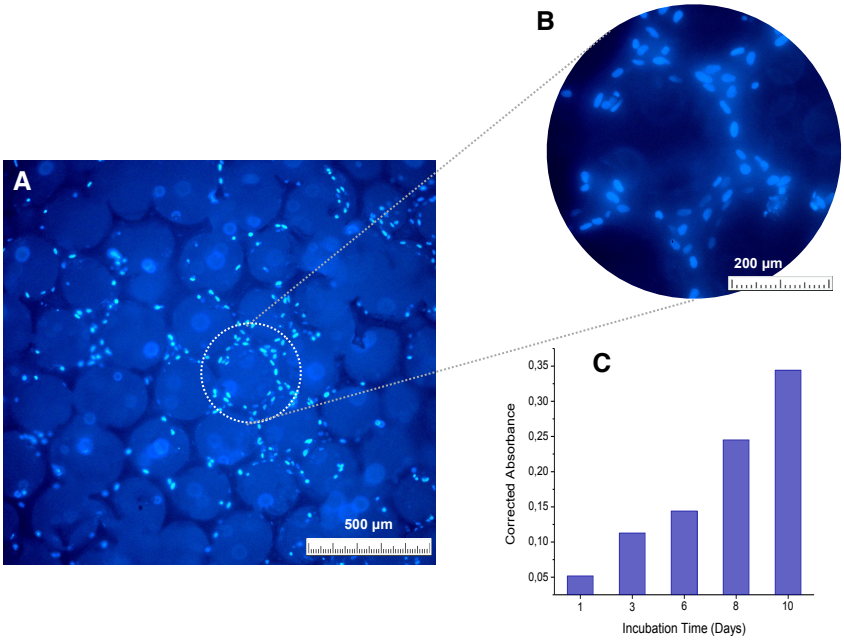

Figure 4.5: Fluorescente microscopy images of human osteoblasts (SaOs-2) on the HAp ICC (A and B); C - Proliferation assay with corrected absorbance.

After mechanical properties assessment, the ICC scaffolds with the highest elastic

modulus were also biologically evaluated and *In vitro* tested with human osteosarcoma cells SaOs2. One day after cell seeding, osteoblasts showed (56 ± 7)% of adhesion. Osteoblast adhesion onto the ICC surface is a necessary step before proliferation and further differentiation. Throughout the 10 days of culture, an increase in the resazurin test absorbance values was observed, corresponding to a proportional increase of the cell number (Figure 4.5C). This shows that the samples were able to promote cellular proliferation. Fluorescence microscopy confirmed that osteoblasts were able to attach, proliferate and inhabit the scaffolds. The abundance of stained cells (bright spots corresponding to cell's nucleus) indicates a good viability (Figure 4.5A and B).

4.4 Conclusions

Ceramic porous scaffolds with ICC geometry were successfully produced based on a simple sol-gel route. The fabricated scaffold composed of HAp/β-TCP showed an ordered pore structure that inversely replicated the microspheres' template, exhibiting macropores sizes of 196 μm in diameter and a porosity of about 80 vol.%. Osteoblasts ability to attach and proliferate within the scaffold reveals a favorable environment for bone ingrowth. Thus, the structures designed present interesting features that upon further development can lead to new products for bone tissue regeneration.

References

[1] C. F. C. João, R. Almeida, J. Silva, and J. Borges. "A simple sol-gel route to the construction of hydroxyapatite inverted colloidal crystals for bone tissue engineering". In: *Materials Letters* (). DOI: 10.1016/j.matlet.2016.09.030. URL: http://www.sciencedirect.com/science/article/pii/S0167577X16314987.

[2] D. Hutmacher. "Scaffolds in tissue engineering bone and cartilage". In: *Biomaterials* 21.24 (2000), pp. 2529–2543. URL: http://www.sciencedirect.com/science/article/pii/S0142961200001216.

[3] S. V. Dorozhkin. "Bioceramics based on calcium orthophosphates (Review)". English. In: *Glass and Ceramics* 64.11-12 (Nov. 2007), pp. 442–447. DOI: 10.1007/s10717-007-0109-1. URL: http://link.springer.com/10.1007/s10717-007-0109-1.

[4] L. L. Hench. "Bioceramics". In: *Journal of the American Ceramic Society* 81.7 (1998), pp. 1705–1728. DOI: 10.1111/j.1151-2916.1998.tb02540.x. URL: http://dx.doi.org/10.1111/j.1151-2916.1998.tb02540.x.

[5] D Shi. *Introduction to biomaterials*. 2006. URL: http://www.worldscientific.com/doi/pdf/10.1142/9789812700858_fmatter.

[6] T. S. Araujo and J. Santos-Filho. *Hidroxiapatita Pura E Dopada com Cr3+:* Portuguese. Santos-Filho & T.S.Araujo. ISBN: 8590901319. URL: http://books.google.pt/books?id=-Seg-hhEl_YC&pg=PA3&dq=intitle:Hidroxiapatita+Pura+E+Dopada+com+Cr3&hl=&cd=1&source=gbs_api.

[7] S. V. Dorozhkin. *Calcium Orthophosphates*. English. Applications in Nature, Biology, and Medicine. CRC Press, June 2012. ISBN: 9814316628. URL: http://books.google.pt/books?id=VouONZJhBE4C&printsec=frontcover&dq=intitle:Calcium+Orthophosphates+applications+in+nature&hl=&cd=1&source=gbs_api.

[8] Medbone. *Adbone TCP*. (Accessed 16 Ago 2016). URL: http://www.medbone.eu/en/products/orthopedic/adbone-bcp.html.

[9] LDR. *BF+ Calcium Phosphate Ceramic*. (Accessed 16 Ago 2016). URL: https://fr.ldr.com/english/Products/BoneSubstitute.

[10] Teknimed. *Ceraform*. (Accessed 16 Ago 2016). URL: http://www.teknimed.com/products-portfolio/products/spine/bone-substitutes/ceraform/.

[11] Graftys. *Graftys Products*. (Accessed 16 Ago 2016). URL: http://www.graftys.com/injectable-ceramic-products/.

[12] Ceramed. *Neobone*. (Accessed 16 Ago 2016). URL: http://ceramed.pt/pdf/neobone_ortho.pdf.

[13] Ceramisys. *Bone Graft Substitute Clinical Performance*. (Accessed 16 Ago 2016). URL: http://www.ceramisys.com/bone_graft_substitutes_properties.html.

[14] Kasios. *TCH*. (Accessed 16 Ago 2016). URL: http://www.kasios.com/doc-pdf/TCH-gb.pdf.

[15] P. Q. Franco, C. F. C. João, J. C. Silva, and J. P. Borges. "Electrospun hydroxyapatite fibers from a simple sol–gel system". English. In: *Materials Letters* 67.1 (2011), pp. 233–236. DOI: 10.1016/j.matlet.2011.09.090. URL: http://links.isiglobalnet2.com/gateway/Gateway.cgi?GWVersion=2&SrcAuth=mekentosj&SrcApp=Papers&DestLinkType=FullRecord&DestApp=WOS&KeyUT=000298272200067.

[16] S.-W. Choi, I. W. Cheong, J.-H. Kim, and Y. Xia. "Preparation of uniform microspheres using a simple fluidic device and their crystallization into close-packed lattices." English. In: *Small (Weinheim an der Bergstrasse, Germany)* 5.4 (Apr. 2009), pp. 454–459. DOI: 10.1002/smll.200801498. URL: http://eutils.ncbi.nlm.nih.gov/entrez/eutils/elink.fcgi?dbfrom=pubmed&id=19189332&retmode=ref&cmd=prlinks.

[17] J. E. Unosson, C. Persson, and H. Engqvist. "An evaluation of methods to determine the porosity of calcium phosphate cements". English. In: *Journal of Biomedical Materials Research Part B-Applied Biomaterials* 103.1 (Jan. 2015), pp. 62–71. DOI: 10.1002/jbm.b.33173. URL: http://doi.wiley.com/10.1002/jbm.b.33173.

[18] B. D. Cullity and S. R. Stock. *Elements of X-ray diffraction; 3rd ed.* Upper Saddle River, NJ: Pearson, 2001. URL: http://cds.cern.ch/record/821266.

[19] E Landi, A Tampieri, G Celotti, and S Sprio. "Densification behaviour and mechanisms of synthetic hydroxyapatites". English. In: *Journal of the European Ceramic Society* 20.14-15 (Dec. 2000), pp. 2377–2387. DOI: 10.1016/S0955-2219(00)00154-0. URL: http://linkinghub.elsevier.com/retrieve/pii/S0955221900001540.

[20] B. D. Ratner, A. S. Hoffman, F. J. Schoen, and J. E. Lemons. *Biomaterials Science*. English. An Introduction to Materials in Medicine. Academic Press, Dec. 2012. ISBN: 008087780X. URL: http://books.google.pt/books?id=8hBq-dLLaxwC&printsec=frontcover&dq=intitle:Biomaterials+Science+An+Introduction+to+Materials+in+Medicine&hl=&cd=1&source=gbs_api.

[21] M. H. Fathi and A Hanifi. "Evaluation and characterization of nanostructure hydroxyapatite powder prepared by simple sol-gel method". English. In: *Materials Letters* 61.18 (July 2007), pp. 3978–3983. DOI: 10.1016/j.matlet.2007.01.028. URL: http://linkinghub.elsevier.com/retrieve/pii/S0167577X0700016X.

[22] M. H. Fathi, A Hanifi, and V Mortazavi. "Preparation and bioactivity evaluation of bone-like hydroxyapatite nanopowder". English. In: *Journal of Materials Processing Technology* 202.1-3 (2008), pp. 536–542. DOI: 10.1016/j.jmatprotec.2007.10.004. URL: http://linkinghub.elsevier.com/retrieve/pii/S0924013607009090.

[23] L. J. Gibson and M. F. Ashby. *Cellular Solids*. English. Structure and Properties. Cambridge University Press, July 1999. ISBN: 9780521499118. URL: http://books.google.pt/books?id=IySUr5sn4N8C&printsec=frontcover&dq=intitle:Cellular+Solids&hl=&cd=1&source=gbs_api.

Chapter 5

Chitosan Inverted Colloidal Crystal Scaffolds

Chitosan with three different molecular weights (538±48, 229±45 and 13±3 kDa) was used to develop biodegradable Inverted Colloidal Crystal (ICC) scaffolds with uniform pore size and interconnected pore network. Mass loss and mechanical properties were analyzed after hydrolytic degradation in order to understand the influence of molecular weight on structural and mechanical degradation of chitosan ICC structures. Results show that medium molecular weight chitosan (229±45 kDa) retains ICC structure and mechanical properties for an extended period (4 weeks) and is therefore the preferred one for the production of ICC for soft tissue engineering[1].

5.1 Introduction

Chitosan (CS) is a well-known polysaccharide used in biomedical, pharmaceutical and other industrial applications. It is a linear semicrystalline polymer with an orthorhombic unit cell that contains two antiparallel polymer chains of β-(1→4)-linked d-glucosamine and N-acetyl-d-glucosamine (Figure 5.1) [1, 2]. CS is chitin´s copolymer (the second most widely distributed polymer in the world) and is commercially obtained mainly by the deacetylation of chitin from crustaceans' shells obtained from food wastes. Depending on the chemical treatment performed, different deacetylation degree (DD) and MW chitosans can be originated, with strong influence on crystallinity, solubility and degradation of the final product. Usually DD and MW ranges from 50% to 95% and 300 to 1000 kDa, respectively[3].

[1] The work described in this chapter is based on the publication: C.F.C. João, A.T. Kullberg, J.C.Silva, J.P.Borges. "Chitosan Inverted Colloidal Crystal Scaffolds: Influence of the Molecular Weight on Structural Stability". Materials Letters 2016 (submitted/under revision).

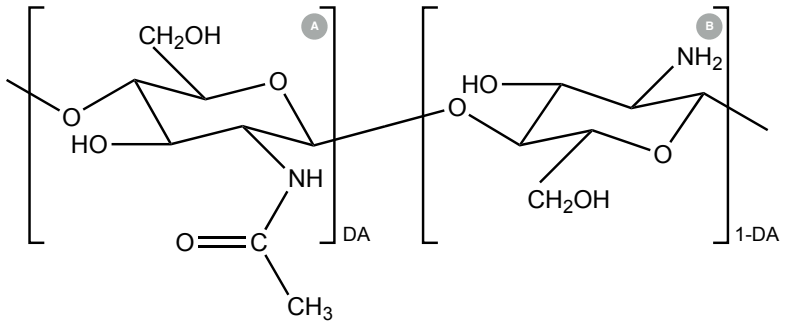

Figure 5.1: Schematic representation of the chitosan/chitin molecule: A) N-acetyl-glucosamine unit; B) N-glucosamine unit. Chitin obtained when DA > 50%. Chitosan obtained when 1-DA > 50%.

This polymer is a polyelectrolyte with reactive functional groups, gel-forming capability and high adsorption capacity. It is insoluble in neutral and basic solutons but its amine groups allow the formation of water-solube salts in both organic and inorganic acids. The reactive side groups (primary amines and secondary hydroxil groups) allow chemical modification and functionalization that make CS tremendously useful. The inclusion of amino acids, peptides, growth factors and medical drugs accredits extended attributes that can make the difference in health care related applications [2, 3].

CS is biocompatible, biodegradable, promotes hemostatic activity, accelerates healing and is able to overpower bacterial and fungal growth. These properties sustain CS as a particularly powerful material to be used in wound dressings, surgical sutures and more recently as bone and cartilage scaffold material since it is also capable of supporting osteoblasts activity towards the formation of mineralized tissue [4–6].

Usually, high molecular weight chitosan is chosen as material for biomedical applications. However, it presents a major drawback related to the difficulty in the processing of high viscosity solutions. Overcoming this difficulty involves the use of lower molecular weight CS which can originate products with completely different features. Changing chitosan MW strongly influences characteristics like crystallinity, Young's modulus and antimicrobial activity [7]. In particular, lower MWs can have a huge impact on structures' integrity during a tissue engineering application where they are exposed to multiple degradation agents like enzymes and macrophages.

The use of CS as scaffold material for bone, cartilage, tendon and ligament, skin, liver and nerve applications, has been growing supported by a variety of manufacturing methods that offer the construction of porous structures that provide cell attachment, ingrowth and osteogenesis[3, 8]. The techniques most used involving CS are freeze-drying, biomineralization, precipitation, particle aggregation, electrospinning, wet-spinning and gelation [9, 10]. However, as seen earlier in chapter 2, those technologies commonly convey the recurrent scaffold problems (irregular pore sizes, shapes, structures and poor

connectivity [11]). On the contrary, ICC have been evidenced by generating highly geometrically organized macroporous structures able to provide optimum cellular development. Also, the use of CS in the production of ICC scaffolds for cartilage and bone-marrow based applications has already been explored with promising results [12].

Nonetheless, ICC scaffolds' performance regarding structural stability during degradation has not yet been described. Moreover, the degradation process may also be influenced by the morphology and geometry of the final structure, and in that sense degradation studies are still needed. This work reports the use of different molecular weight CS to construct ICC scaffolds as well as the influence of molecular weight on the scaffolds degradation and on its mechanical properties.

5.2 Experimental Section

5.2.1 Chitosan Depolymerization

Chitosan samples with different molecular weights were obtained via the depolymerization of commercial chitosan (M_w=500,000, DD=75-85%, Cognis S) defined here as high MW CS (CSH), by the method described by Mao et al. [13]. Glacial acetic acid (CH_3COOH, 99.7%, Panreac) was diluted to 1% using distilled water and applied as solvent for all chitosan solutions. Sodium nitrite ($NaNO_2$, Sigma-Aldrich) was used as depolymerizing agent and sodium hydroxide ($NaOH$, max 0.0002K, Merck) was employed to stop the reaction and precipitate chitosan.

To produce CS with different MW, $NaNO_2$ was added to 1% (wt/wt) original CS (CSH) in acetic acid aqueous solution, at the $NaNO_2$:CS ratios: 1:15, 1:20, 1:25, 1:33.3, 1:50, 1:100 and 1:200. After 1h of mechanical stirring, 4M NaOH was added dropwise to the solutions until pH=9 was reached. Then, the samples were washed with ultrapure water (Millipore Elix Advante 3 purifcation system) and centrifuged (Heraues Multiguge X1R Thermo Schientific) three to four times for 15 minutes periods at 12,000 rpm. The resultant pellets were then freeze-dried (-40ºC, 24h), manual grinded with porcelain pestle and mortar until powder form, and stored for later use.

CS with low (CSL) and medium (CSM) MW were obtained from CSM by chemical depolymerization using 1:15 and 1:100 $NaNO_2$:CS ratios.

5.2.2 Chitosan ICC Scaffolds Production

In Figure 5.2 the schematic of ICC scaffold production is presented. To obtain monodisperse PS microspheres, a microfluidic apparatus was developed based on the one reported by Choi et. al [14] as described in Figure 5.2-1. For ICCs manufacturing, the spheres produced (see section 3.3.2) are close packed into lattices (Figure 5.2-2) and infiltrated with CS solutions under vacuum.

The first chitosan ICCs were produced using 2% acetic acid solutions where CSH was dissolved in concentrations ranging from 2% to 5% (all concentrations in wt/wt %).

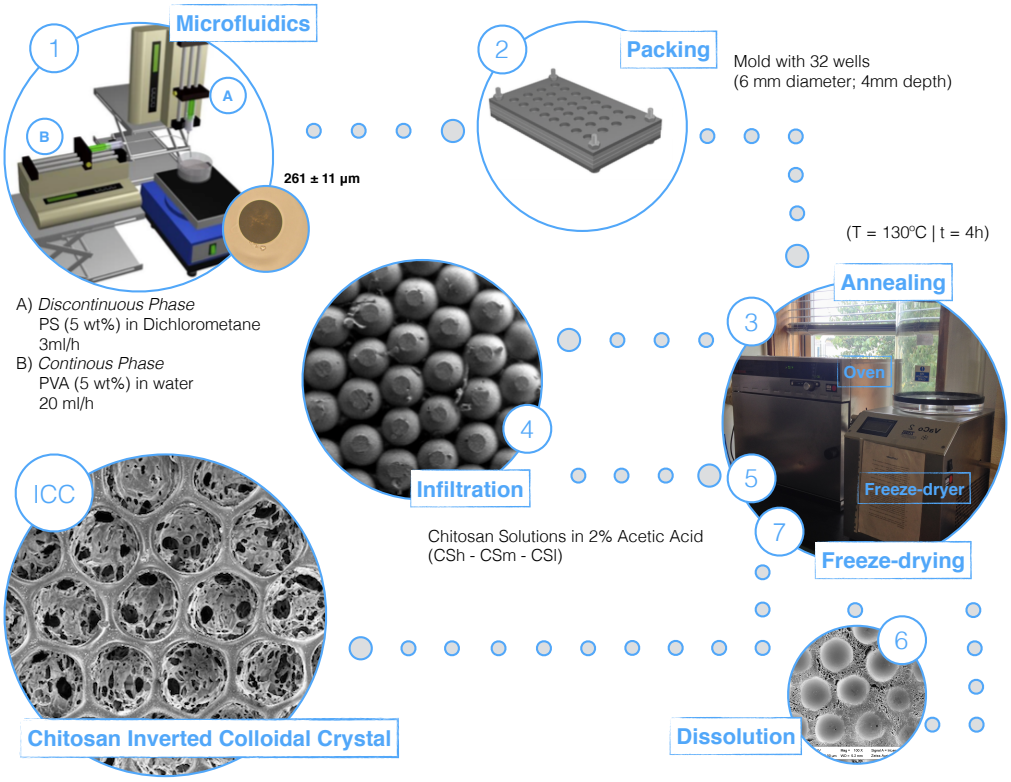

Figure 5.2: Production schematic of the chitosan based ICC scaffolds: 1) microspheres production; 2) microspheres packaging; 3) annealing into a colloidal crystal template; 4) CC infiltration with CS solution; 5) Freeze-drying of the infiltrated template; 6) template dissolution; 7) second freeze-drying and the resultant CS ICC scaffold.

After evaluation of the resultant structures and analysis of the manufacturing procedure viability, CSM and CSL were then used to prepare solutions with different concentrations but viscosity similar to the CSH 3% solution, as determined by rheological measurements (viscosity determined at the newtonian plateau and shear rate = 1.27 s^{-1}).

After sphere template infiltration with the CS solutions (CSH at 3%, CSM at 7% and CSL at 16%), the infiltrated structures are puttedput in a ultra freezing chamber at -50ºC, overnight. Then the samples are freeze-dried at -40ºC and approximately 0.07 mbar, for 24h (Vaco2 -Zirbus). The resultant structure is immersed in a sequence of solutions for sphere removal: ethanol (C_2H_6O, 99.99%, Fisher Chemical) for 1 hour, dichloromethane overnight and ethanol for 1 hour. The inverse replica is then freeze-dried a second time and stored in a thermostatic vacuum dryer (Vacuo-Temp, P-selecta).

5.2.3 ICC Degradation

In vitro degradation was carried out by immersing the scaffolds (40 samples for each Mw) in sterile phosphate buffered saline (PBS) aqueous solution at 37ºC, containing 0.02% (w/w) of sodium azide. The medium was replaced every three to four days. Ten samples of each MW were removed weekly for characterization.

5.2.4 Characterization

ICC structures were morphologically characterized by SEM. ICC pores size were measured using ImageJ™software.

Uniaxial mechanical properties of the ICC scaffolds were evaluated through compressive tests with a Rheometric Scientific (Minimat Firmware 3.1) system equipped with a 20 N load cell. Ten samples of each condition were compressed at a rate of 0.5 mm/min, in a dry state (45% relative humidity) at room temperature (23 ºC) and the compressive modulus was determined as the slope of the linear portion of the stress-strain curve.

FTIR with Attenuated Total Reflectance was used to analyze all chitosan samples produced and to determine the deacetylation degree.

The viscosity average molecular weights of chitosan were determined by capillary viscosimetry (Schott-Geräte AVS400 viscometer with a 0a capillary - 0.53±0.01 mm) and the classical Mark-Houwink-Sakurada (MHS) equation [15–17]:

$$\eta = K{M_v}^a \tag{5.1}$$

where η is the intrinsic viscosity, M_v is the viscosity-average molecular weight, and K and a are the constants for the solute-solvent system[2].

According to the data given by the supplier, the expected DD for the high MW chitosan is 75%. Following the suggestion given by Kasaai et al.[18], DD can be calculated considering the area of two of the most characteristic FTIR peaks. Thus, the DD can be determined by solving the equation:

$$DD = 1 - DA = 1 - \frac{A_{1655}}{A_{3450}} \times 115 \tag{5.2}$$

where A_{1655} and A_{3450} are the areas under the reference peaks, and 115 represents the slope of the linear curve of the absorption ratio versus the acetylation degree (DA). Software OriginPro 8.5 was used to determine the positioning, intensity and the areas under the peaks.

Solutions viscosity was determined by rheological characterization of the CSH, CSM and CSL solutions using a stress-controlled rheometer Bohlin Gemini HR nano, with a cone-plane geometry (20 mm diameter and 2º).

5.3 Results and Discussion

5.3.1 Chitosan With Different Molecular Weight

Applying the method reported by Mao et al.[13], chitosan with different molecular weight was successfully obtained with the straightforward chemical depolymerization process of

[2]In this chapter the symbol "MW" is used as an abbreviation of molecular weight. For simplicity, MW is also used to compare the various chitosan (H, M and L). M_v determined with MHS equation 5.1 and is different from M_w usually referred as weight-average molecular weight.

original CS (CSH) with $NaNO_2$. The use of CSH at concentration of 1% (wt/wt) as starting solution intended to warrant a low viscosity and low polymeric chains entanglement that allow easier sodium nitrite penetration and shortening of the depolymerization process time.

In Figure 5.3 the MWs determined from the MHS equation 5.1 and from the capillary viscosimetry experiments (see appendix A, section A.2.1) are plotted as a function of $NaNO_2$ content used in the depolymerization reaction.

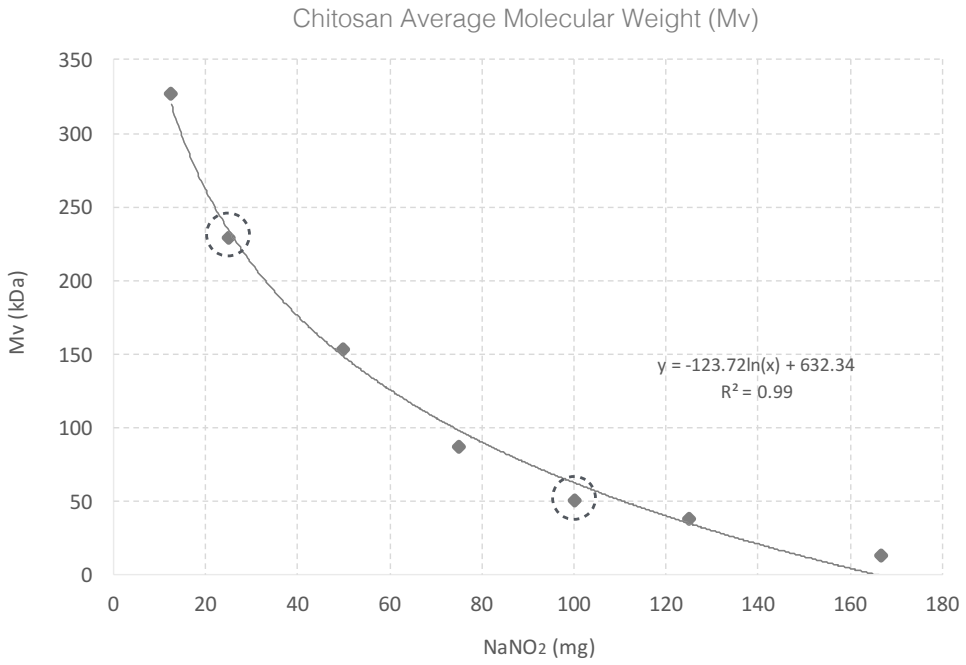

Figure 5.3: Chitosan average molecular weight. Evolution of chitosan MW with $NaNO_2$ amount used in depolymerization reaction. CS mass = 2.5g.

Within a reaction period of 1 hour, it was found a straight relation evidencing that reaction with higher amounts of $NaNO_2$ lead to the production of lower MW chitosans. However, if at the beginning the MW seems to decrease linearly with the $NaNO_2 : CS$ ratio, that relationship quickly evolves into a logarithmic function.

Chitosan with higher MW are more sensitive to depolymerization. When low MW is achieved, the continuous addition of $NaNO_2$ does not mean that further depolymerization takes place. At that point, the molecular chains are quite small and disperse easily in the aqueous medium, reducing the contact between polymer and degradation agent. Also, during the process, it was found that for lower MWs the CS extraction becomes harder and the yield decreases due mainly to the decrease of precipitation capability. This is an indication of polidispersity increase and the formation of oligochitosans that are not able to be precipitated in solvents like NaOH.

With the CS source used in this work (Cognis S) it was concluded that a 1:15 ratio (m_{NaNO_2}=166.7mg) is the maximum limit where low MW chitosans can be obtained. If further depolymerization is employed, e.g 1:10 ratio, oligochitosans are obtained through

the precipitation of the reaction solution with acetone and ethanol instead of alkaline solutions. It was also observed that with the decrease of MW, CS acquired a yellowish color, probably due to oxidation, which was intensified by the amount of $NaNO_2$ used in the reaction.

From the results obtained, 1:15 (m_{NaNO_2}=166.7mg) and 1:100 (m_{NaNO_2}=25mg) ratios were selected for CSH (MW= 538 ± 48 kDa) depolymerization into CSM (MW = 29 ± 45 kDa) and CSL (MW = 13 ± 3 kDa), respectively. The chemical analysis by FTIR measurements reveal no evidence of chemical composition modification (Figure 5.4) in the chitosan samples obtained with the depolymerization method employed.

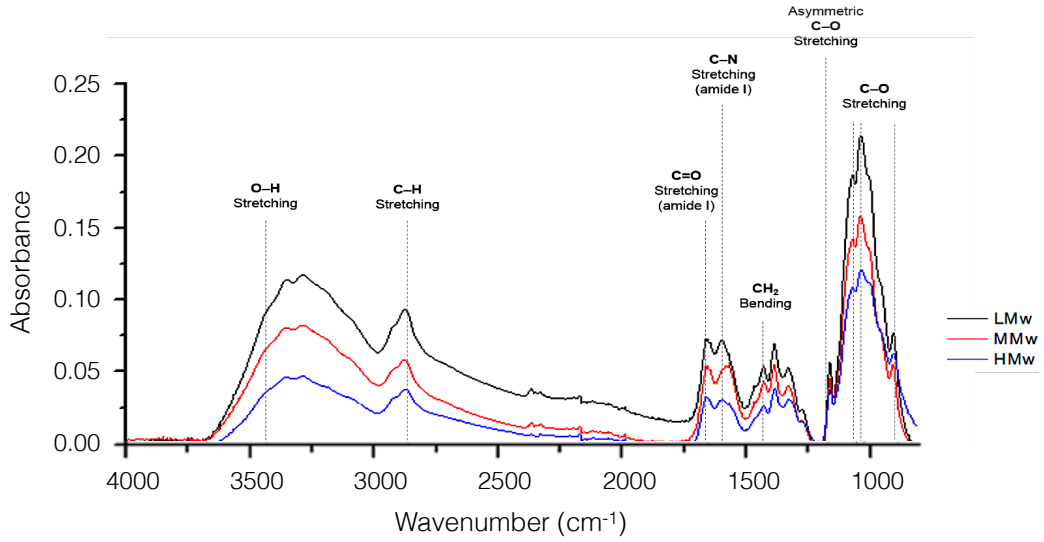

Figure 5.4: FTIR spectra of the CSH, CSM and CSL chitosan samples.

Taking into account the FTIR spectra, the amide I band (C=O stretching) at 1655 cm^{-1} and the O–H stretching band, at 3450 cm^{-1} wavenumber were considered as the most appropriate characteristic bands and are the most frequently used reference band for DD determination in the range between 59% and 100%. Solving equation 5.2, resulted in DD values of 76.7%, 73.4% and 73.5% for CSH, CSM and CSL, respectively, from which it is possible to conclude that there is no significant variation between all MW chitosans.

5.3.2 High, Medium and Low MW CS ICC scaffolds

High molecular weight polymers lead to high viscosity solutions even at low concentrations. Since viscosity plays the main and limitative role in CC template infiltration, at first 2 to 5% wt/wt CSH solutions were infiltrated and the resultant ICC were evaluated. Solutions below 2% were easily infiltrated under vacuum but due to low polymeric content, the resultant ICC was very fragile and the structures recurrently collapsed during sphere dissolution. Solutions above 4% were highly viscous and the CC infiltration required longer time periods under vacuum. Also, removing the excess solution from the template

surface became more difficult, often resulting in the formation of films that blocked the replica surface and generated misshapen scaffolds.

The 3% CSH solution showed adequate viscosity to allow penetration into the colloidal crystal voids and ensure maximization of the amount of material present, leading to the formation of well-defined walls and pores and perfect ICC geometry (Figure 5.5).

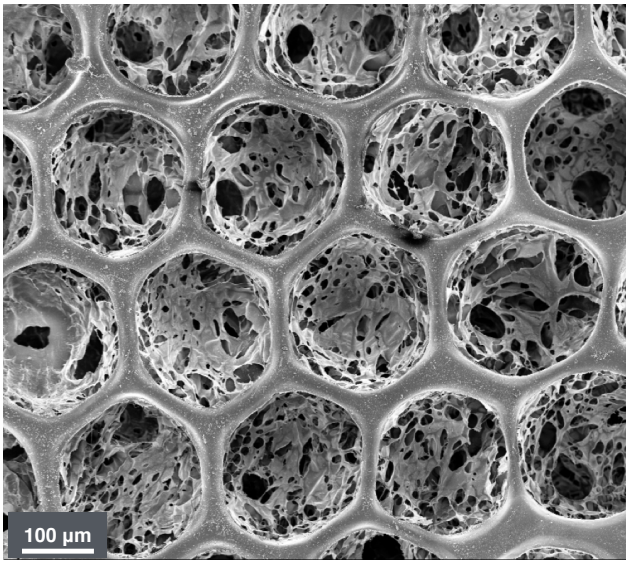

Figure 5.5: SEM image of a Chitosan Inverted Colloidal Crystal Scaffold produced with CSH 3 %(wt/wt) in 2% acetic acid aqueous solution. Pore size = 195.6 ± 12.7 μm. Interconnective window = 49.8 ± 9.6 μm

Rheology studies were conducted in order to determine optimum concentrations of CSM and CSL solutions so they would match CSH solution viscosity (μ=1.56 Pa.s). The concentrations, 7% (μ=1.63 Pa.s) CSM and 16% (μ=1.53 Pa.s) CSL, respectively, were then used as infiltrating material. After template impregnation, the freeze-drying process allowed the formation of a solid polymeric structure. Due to CS extreme absorption capability, with the addition of DCM to promote sphere removal, the polymeric structure becomes highly hydrated, the walls lose their strength and often after sphere dissolution the scaffold was also destroyed. However, introducing an ethanol bath before and after the dissolution step prevents DCM absorption while the structure is dried by the alcohol. With the second-freeze drying, CSH, CSM and CSL inverse replicas were successfully produced comprising uniform and size controlled pores with the small windows connecting adjacent pores.

In order to understand the molecular weight influence vs polymer concentration in the ICC structural stability, the different MW ICCs were degraded *in vitro* for 4 weeks and their mechanical properties were assessed through compressive tests. In Table 1, ICCs characterization regarding evolution of mechanical properties and mass loss along degradation weeks can be observed. It is known that chitosan degradation rate is inversely related to the crystallinity degree which is depended on DD [9]. Since FTIR results

Table 5.1: Chitosan ICC scaffolds characterization. Samples identified by 0 to 4 according to time (weeks) of *in vitro* degradation.

Sample		Elastic modulus kPa	Mass Loss %
CSH	H_0	240 ± 76	-
	H_1	178 ± 67	5.1
	H_2	142 ± 55	19.8
	H_3	128 ± 34	21.5
	H_4	113 ± 30	22.6
CSM	M_0	306 ± 74	-
	M_1	244 ± 60	5.3
	M_2	263 ± 42	25.5
	M_3	252 ± 58	25.9
	M_4	193 ± 21	39.5
CSL	L_0	659 ± 104	-
	L_1	184 ± 39	30.1
	L_2	199 ± 48	34.6
	L_3	195 ± 42	38.6
	L_4	152 ± 24	48.6

confirmed similar DD for all samples, this effect is excluded from the results discussion.

Initially (CSH_0, CSM_0 and CSL_0), the ICCs E increases with molecular weight decrease: the CSL ICCs elastic modulus is approximately 3 times higher than that of CSH, showing that the mass increase effect (higher concentration solution) leads to more homogeneous ICCs with higher density walls (Figure 5.6). These two aspects are determinant for the mechanical properties of cellular materials and prevail over the effect of molecular weight decrease.

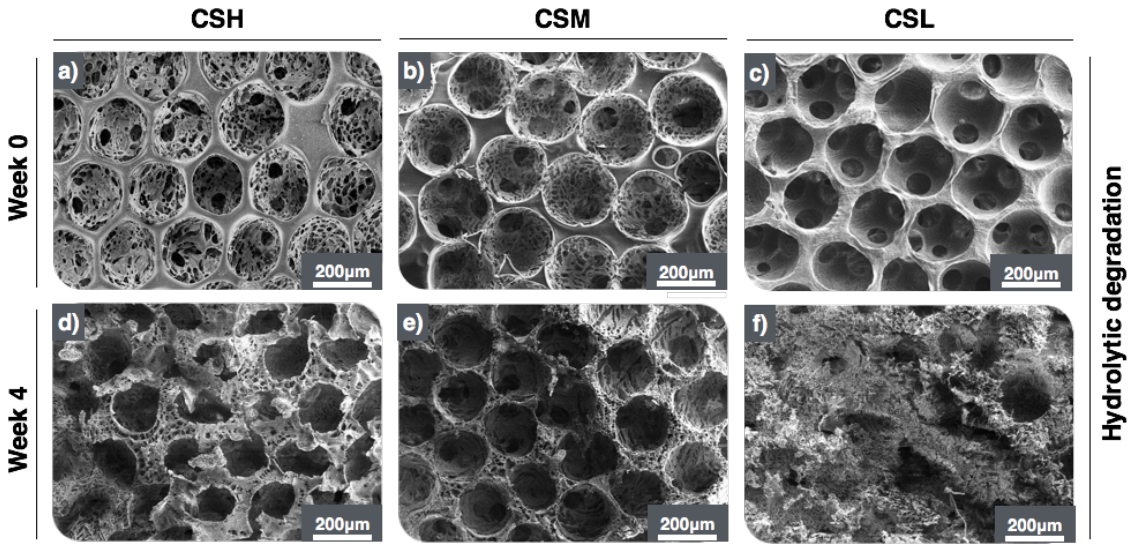

Figure 5.6: SEM images of the different chitosan ICC scaffolds produced with CSH (a,d), CSM (b,e) and CSL(c,f) before (a,b,c) and after (d,e,f) hydrolytic degradation.

For the degradation weeks 1, 2 and 3, E decreases significantly for all ICC samples. In

these steps the effect of different molecular weights and amount of impregnated chitosan are competitors and cancelled each other, i.e., although lower molecular weight samples loose mass faster, since the amount of chitosan is higher, the structure maintains its integrity for longer periods. At the end of the experiment, CSM_4 scaffolds present the highest elastic modulus of all three MW ICCs, 193 ± 21 kPa. Mass loss values are also consistent with values reported in the literature: Kuo et al.[19] have determined 25-34% degradation after 4 week cell seeding in chitin/chitosan ICCs, which is similar to values found in the present study.

Comparing samples before and after degradation, CSM_4 ICCs showed less degradation effects on morphology (Figure 5.6e). By having smaller chains than higher molecular weight samples, it becomes easier for the medium to penetrate between polymer molecules and promote degradation. However, by having a higher amount of polymer, the structure retains its integrity for a longer time, without collapsing. Degradation is visually more noticeable at week 4 in the samples with low molecular weight (Figure 5.6f). In these samples the molecular chains are already quite small and water absorption induces fragility of the structure. Therefore, even with a higher amount of polymer in the structure the morphology of the ICC was entirely lost on week 4. In this case the effect of low molecular weight supersedes the amount of chitosan in the sample.

5.4 Conclusions

The main objective of this work was to study the influence of molecular weight on the degradation behavior and mechanical properties of chitosan ICCs. For this purpose, three different molecular weights were used. High molecular weight (538 kDa) was used as received, medium (229 kDa) and low (13 kDa) were obtained through chemical depolymerization with sodium nitrite. Degradation analysis revealed that mass loss was higher in low molecular weight samples, for the same degradation time. Medium MW CS ICC scaffolds show the best performance regarding degradation rate, conservation of structural integrity and mechanical properties and because of that CSM should be considered when constructing ICCs for tissue engineering applications. This work shows how important it is to study the degradation profile of chitosan ICC scaffolds in order to choose the molecular mass that warrants an extended compliance of the scaffold.

References

[1] M Rinaudo. "Chitin and chitosan: Properties and applications". In: *Progress in polymer Science* (2006). URL: http://www.sciencedirect.com/science/article/pii/S0079670006000530.

[2] S.-K. Kim. *Chitin and Chitosan Derivatives*. English. Advances in Drug Discovery and Developments. CRC Press, Dec. 2013. ISBN: 1466566280. URL: http://books.google.pt/books?id=GIJcAgAAQBAJ&pg=PA513&dq=intitle:Chitin+and+Chitosan+Derivatives+Advances+in+Drug+Discovery+and+Developments&hl=&cd=1&source=gbs_api.

[3] S. K. L. Levengood and M. Zhang. "Chitosan-based scaffolds for bone tissue engineering". English. In: *Journal of Materials Chemistry B* 2.21 (2014), p. 3161. DOI: 10.1039/c4tb00027g. URL: http://xlink.rsc.org/?DOI=c4tb00027g.

[4] P. K. Dutta, J Dutta, and V. S. Tripathi. "Chitin and chitosan: Chemistry, properties and applications". In: *Journal of Scientific & Industrial Research* 63.1 (Jan. 2004), pp. 20–31. URL: https://www.researchgate.net/profile/Marguerite_Rinaudo/publication/223322801_Chitin_and_chitosan_Properties_and_applications/links/09e415134cc9f87fea000000.pdf.

[5] R Shelma, W Paul, and C. P. Sharma. "Chitin nanofibre reinforced thin chitosan films for Wound healing application". In: *Trends Biomater Artif Organs* (2008). URL: http://medind.nic.in/taa/t08/i2a/taat08i2p111.pdf.

[6] M Dash, F Chiellini, R. M. Ottenbrite, and E Chiellini. "Chitosan - A versatile semi-synthetic polymer in biomedical applications". In: *Progress in polymer Science* 36.8 (Aug. 2011), pp. 981–1014. DOI: 10.1016/j.progpolymsci.2011.02.001. URL: http://dx.doi.org/10.1016/j.progpolymsci.2011.02.001.

[7] C. Tangsadthakun, S. Kanokpanont, N. Sanchavanakit, R. Pichyangkura, T. Banaprasert, Y. Tabata, and S. Damrongsakkul. "The influence of molecular weight of chitosan on the physical and biological properties of collagen/chitosan scaffolds". English. In: *Journal of Biomaterials Science, Polymer Edition* 18.2 (Jan. 2007), pp. 147–163. DOI: 10.1163/156856207779116694. URL: http://www.tandfonline.com/doi/abs/10.1163/156856207779116694.

[8] A Anitha, S Sowmya, P. T. S. Kumar, S Deepthi, K. P. Chennazhi, H Ehrlich, M Tsurkan, and R Jayakumar. "Chitin and chitosan in selected biomedical applications". In: *Progress in polymer Science* (Mar. 2014), pp. 1–24. DOI: 10.1016/j.progpolymsci.2014.02.008. URL: http://dx.doi.org/10.1016/j.progpolymsci.2014.02.008.

[9] H. C. Arca and S. ŞENEL. "Chitosan based systems for tissue engineering Part 1: Hard tissues". In: *FABAD J. Pharm. Sci* 33 (2008), pp. 35–49. URL: http://www.researchgate.net/publication/229015862_Chitosan_Based_Systems_for_Tissue_Engineering_Part_1_Hard_Tissues/file/e0b49517e833a19f04.pdf.

[10] J. Venkatesan and S.-K. Kim. "Chitosan composites for bone tissue engineering–an overview." English. In: *Marine drugs* 8.8 (2010), pp. 2252–2266. DOI: 10.3390/md8082252. URL: http://www.mdpi.com/1660-3397/8/8/2252/htm.

[11] S Yang, K. F. Leong, Z Du, and C. K. Chua. "The design of scaffolds for use in tissue engineering. Part I. Traditional factors." English. In: *Tissue Engineering* 7.6 (Dec. 2001), pp. 679–689. DOI: 10.1089/107632701753337645. URL: http://eutils.ncbi.nlm.nih.gov/entrez/eutils/elink.fcgi?dbfrom=pubmed&id=11749726&retmode=ref&cmd=prlinks.

[12] S.-W. Choi, J. Xie, and Y. Xia. "Chitosan-Based Inverse Opals: Three-Dimensional Scaffolds with Uniform Pore Structures for Cell Culture." English. In: *Advanced materials (Deerfield Beach, Fla.)* 21.29 (Apr. 2009), pp. 2997–3001. DOI: 10.1002/adma.200803504. URL: http://eutils.ncbi.nlm.nih.gov/entrez/eutils/elink.fcgi?dbfrom=pubmed&id=19710950&retmode=ref&cmd=prlinks.

[13] S. Mao, X. Shuai, F. Unger, M. Simon, D. Bi, and T. Kissel. "The depolymerization of chitosan: effects on physicochemical and biological properties." English. In: *International Journal of Pharmaceutics* 281.1-2 (Aug. 2004), pp. 45–54. DOI: 10.1016/j.ijpharm.2004.05.019. URL: http://eutils.ncbi.nlm.nih.gov/entrez/eutils/elink.fcgi?dbfrom=pubmed&id=15288342&retmode=ref&cmd=prlinks.

[14] S.-W. Choi, I. W. Cheong, J.-H. Kim, and Y. Xia. "Preparation of uniform microspheres using a simple fluidic device and their crystallization into close-packed lattices." English. In: *Small (Weinheim an der Bergstrasse, Germany)* 5.4 (Apr. 2009), pp. 454–459. DOI: 10.1002/smll.200801498. URL: http://eutils.ncbi.nlm.nih.gov/entrez/eutils/elink.fcgi?dbfrom=pubmed&id=19189332&retmode=ref&cmd=prlinks.

[15] Kasaai. "Calculation of Mark-Houwink-Sakurada (MHS) equation viscometric constants for chitosan in any solvent-temperature system using experimental reported viscometric constants data". English. In: *Carbohydrate Polymers* 68.3 (Apr. 2007), pp. 12–12. DOI: 10.1016/j.carbpol.2006.11.006. URL: http://pubget.com/paper/pgtmp_7008de79031b4c9e9b42ae43ecfaa324?institution=.

[16] M. R. Kasaai, J Arul, and C Charlet. "Intrinsic viscosity-molecular weight relationship for chitosan". English. In: *Journal of Polymer Science Part B: Polymer Physics* 38.19 (2000), pp. 2591–2598. DOI: 10.1002/1099-0488(20001001)38:19<2591::AID-POLB110>3.0.CO;2-6. URL: http://onlinelibrary.wiley.com/doi/10.1002/1099-0488(20001001)38:19<2591::AID-POLB110>3.0.CO;2-6/full.

[17] M Rinaudo, M Milas, and P Le Dung. "Characterization of chitosan. Influence of ionic strength and degree of acetylation on chain expansion". English. In: *International Journal of Biological Macromolecules* 15.5 (1993), pp. 281–285. DOI: 10.1016/0141-8130(93)90027-j. URL: http://linkinghub.elsevier.com/retrieve/pii/014181309390027J.

[18] M. R. Kasaai. "A review of several reported procedures to determine the degree of N-acetylation for chitin and chitosan using infrared spectroscopy". English. In: *Carbohydrate Polymers* 71.4 (Mar. 2008), pp. 497–508. DOI: 10.1016/j.carbpol.2007.07.009. URL: http://linkinghub.elsevier.com/retrieve/pii/S0144861707003542.

[19] Y.-C. Kuo and Y.-T. Tsai. "Inverted colloidal crystal scaffolds for uniform cartilage regeneration." English. In: *Biomacromolecules* 11.3 (Mar. 2010), pp. 731–739. DOI: 10.1021/bm901312x. URL: http://eutils.ncbi.nlm.nih.gov/entrez/eutils/elink.fcgi?dbfrom=pubmed&id=20158195&retmode=ref&cmd=prlinks.

Chapter 6

Composite Chitosan/Hydroxyapatite Inverted Colloidal Crystal Scaffolds

Bone is a composite that is formed by the mineralization of an organic network with natural hydroxyapatite crystals. In this work, synthetic HAp nanorods with morphology and chemical composition similar to bone's HAp were produced. Their use in the development and characterization of composite ICC scaffolds of a biopolymer (chitosan) loaded with HAp nanorods is reported. ICC scaffolds with different CS/HAp ratios were evaluated concerning their structural morphology, mechanical properties and biological response[1].

6.1 Introduction

The development of bone scaffolds obeys not only to the need of an adequate structure with interconnected pores but also to the right choice of materials that can enhance the environment for tissue development. As noted previously, HAp is the most commonly used biomaterial in bone tissue regeneration. Since biological HAp represents the majority of the inorganic compound in vertebrates, researchers have always payed attention to its use by noting its biomineralization ability and potential to reinforce and constitute structures with sufficient mechanical properties that could match tissues in orthopedic, maxillofacial or dental fields. Complementarily, natural and renewable polysaccharides like chitin/chitosan are very interesting mostly by their excellent biostimulatory properties. Being a positively charged polymer, chitosan can establish linkages with proteins and cells triggering reconstruction and vascularization of damaged tissues. Moreover,

[1] The work described in this chapter is based on the publication: C. F. C. João, J. M. Vasconcelos, J. C. Silva, and J. P. Borges. "Chitosan based Inverse Colloidal Crystal Scaffolds". in ESB 2013 - 25^{th} European Conference on Biomaterials. Spain-Madrid, 8-12 September, 2013. ISBN: 978-84-695-7831-5. T5P015 (Poster)[1].

it can be modified towards the inclusion of medical drugs or growth factors that can contribute to treatment and enhance of the healing process.

However, CS alone does not have all the features required for mimicking bone tissue namely stifness and osteoconductivity, and what HAp based materials gain in mechanical strength they lose in flexibility. Therefore, composites with natural polymers like chitosan (or its derivatives) combined with bioactive ceramics as hydroxyapatite may prove to be more suitable for applications in the hard tissues engineering [2]. In fact, they have been gradually finding an important role due to the exhibition of tailored physical, biological and mechanical properties that allow a predictable degradation behavior while promoting bone regeneration [3]. In turn,the CS/HAp combination has been significantly explored for applications comprehending coatings, prostheses or scaffolds related with bone replacement [4–6].

Since natural bone mineral is constituted by HAp in rod/needle-like format, several authors have shown interest in exploring this particularity and reported methods like hydrothermal treatment [7], *in situ* sol-gel [8], wet chemical [9] or precipitation [10] as capable of producing HAp nanoparticles with such morphology. The importance of HAp crystals size and format and their relationship with the biological environment has also been highlighted by the role of nanorods in biomineralization and support for osteoblast attachment and proliferation [11–13].

Thus, the use of organic chitosan reinforced with inorganic hydroxyapatite nanorods in the construction of ICC scaffolds should result in excellent material properties combination. The biocompatibility, biodegradability, anti-inflammatory and anti-microbial character joined with the capability of promoting osteoblast adhesion/growth and biomineralization in an optimized structural design, gather the essential features for a scaffolds' good performance in bone tissue engineering applications.

6.2 Experimental Section

6.2.1 Hydroxyapatite Nanorods Synthesis

Hydroxyapatite powders ($Ca_{10}(PO_4)_6(OH)_2$, > 90% Sigma-Aldrich) were chemically treated according to the method reported by Chen et. al [14]. Briefly, 1 g of HAp is dispersed in 500 ml of distilled water. The suspension is magnetically stirred (Agimatic-N) and nitric acid (HNO_3, > 65%, Panreac) is added until the powder is completely dissolved. Then, pH is measured and adjusted up to pH=2, with the continuous addition of HNO_3. To promote nucleation and rod-like HAp growth, ammonia hydroxide (NH_3, 25%, Panreac) is added dropwise with constant stirring, until solution reaches pH=9.

Posteriorly, the solution is placed in an oven (Memmert) at 37 ºC during 3 days. After incubation, the solution is centrifuged during 10 min at 10,000 rpm (Heraeus, Multifuge X1R, Thermo Scientific). The supernatant is discarded and distilled water is added to the resultant pellet. This step is repeated until pH=7 is reached. Finally, the solution is

freeze-dried for 24 hours (Vaco 2, Zirbus) to remove water and extract HAp nanorods in powder form.

6.2.2 Composite Scaffolds Production

To produce the composite ICC scaffolds, simple composite mixtures of chitosan and hydroxyapatite nanorods were used as infiltration material. CS (M_w=500,000, DD 75-85%, Cognis S) was dissolved in 2% (wt/wt) aqueous acetic acid solution (CH_3COOH, 99.7%, Panreac) at a concentration of 3% (wt/wt). Then, HAp nanorods were added in order to obtain solutions of 3% CS and 3% CS + 1%, 3% and 6% HAp (wt/wt). Taking into account the densities of CS (ρ_{CS}= 1.342 g/cm^3) and HAp[2] (ρ_{HAp}= 2.734 g/cm^3), with this procedure, four solutions/suspensions were produced with the volumetric fractions (Φ):

A → 3% CS → Φ_{CS}=1.00; Φ_{HAp}=0.00

B → 3% CS+1% HAp → Φ_{CS}=0.86; Φ_{HAp}=0.14

C → 3% CS+3% HAp → Φ_{CS}=0.67; Φ_{HAp}=0.33

D → 3% CS+6% HAp → Φ_{CS}=0.50; Φ_{HAp}=0.50

The CS/HAp solutions/suspensions were poured over colloidal crystal templates with spheres of (261±11) μm diameter (see chapter 3). Then, the solutions/suspensions + template were placed in a desiccator connected to a vacuum pump and as the air was removed from the CC templates, the solution penetrates their voids. Each impregnated CC is cleaned with filter paper in order to remove excess solution. The samples are frozen and freeze-dried (Vaco 2, Zirbus) for 24 hours at approximately 0.050 mbar.

To remove the microspheres, the freeze-dried/infiltrated CCs are dipped in absolute ethanol (C_2H_6O, 99.99%, Fisher Chemical) for 1 hour, moved into a dichloromethane bath overnight to allow microspheres dissolution and the resultant structure is again immersed in an etanol bath (1 hour) before a second freeze-drying process is applied.

6.2.3 Characterization

The phase composition and crystallinity of HAp was analyzed by X-ray diffraction (XRD) using CuKα radiation generated at 45 kV and 40 mA, in the range of 20º<2θ<60º, in a X'Pert PRO (PANAlytical) X-ray diffractometer. The peaks obtained were compared with JCPDS cards: #09-0169 (β-TCP), #09-0348 (α-TCP), #09-0432 (HAp) and #37-1497 (CaO). t was calculated from X-ray diffraction patterns using the Scherrer equation 4.1 [15].

[2]HAp nanorods density was determined applying the Arquimedes' principle and using a compressed disk with known nanorods mass.

Hydroxyapatite chemical characterization was conducted through Fourier Transform Infrared (FTIR) spectroscopy. FTIR spectra of powder samples from commercial and nanorods HAp were collected using an attenuated total reflectance (ATR) sampling accessory (Smart iTR) equipped with a single-bounce diamond crystal on a Thermo Nicolet 6.700 spectrometer. The spectra were acquired in the 4.000-650 cm^{-1} range with 4 cm^{-1} resolution and 32 scans at a temperature of 20ºC.

HAp nanorods and ICC scaffolds were sputter coated with gold and morphologically characterized by scanning electronic microscopy (SEM) using a Carl Zeiss AURIGA Cross-Beam Workstation instrument equipped with an Oxford X-ray Energy Dispersive Spectrometer. HAp nanorods were also evaluated by transmission electron microscopy (TEM) by placing diluted suspensions of nanorods/ethanol in a Kevlar 25 mesh grid for further analysis by an Hitachi H8100 II microscope with thermionic emission (LaB_6).

Pore and interconnecting windows dimensions were measured from SEM images with software Image J™(version 1.46eWayne Rasband, National Institutes of Health, USA)[16].

Uniaxial mechanical properties of the ICC scaffolds were evaluated through compressive tests with a Rheometric Scientific (Minimat Firmware 3.1) system equipped with 20 N load cell. At least 10 samples of each composition were compressed at a rate of 0.5 mm/min, in a dry state (45% relative humidity) at room temperature (23 ºC) and the elastic modulus (E) was determined as the slope of the linear portion of the stress-strain curve.

ICCs biocompatibility was evaluated through cell adhesion and proliferation studies. Human osteoblasts from SaOs-2 cell line were seeded directly over the material surface. After incubation, cell activity was evaluated by measuring the absorbance of the media after metabolic reduction of resazurin into resorufin. Detailed information about the cell adhesion and proliferation essays protocols can be found in the appendix A section A.2.3.

6.3 Results and Discussion

6.3.1 Hydroxyapatite Nanorods

Hydroxyapatite nanorods were successfully obtained by the treatment of commercial HAp powders. Being able to manage the process temperature, incubation time and pH allows the production of particles with different shapes (rods, platelets, cuboids) and sizes. In our experiment, SEM and TEM images observation showed the existence of perfectly formed HAp nanocrystals with rodlike format and polydisperse dimensions (Figure 6.1). Setting temperature at 37ºC, pH=9 and incubation time of 72 h allowed the formation of particles with average length and diameter of (153.7 ± 57.3) nm and (12.2 ± 6.6) nm. This morphology is very similar to the nanorod-like HAp crystals that constitute 95% volume of enamel's surface in human teeth that have length and cross section of 100 nm to 1 μm and 33 to 65 nm, respectively [14], although it is slightly bigger than HAp

phase present in natural bone where nanorods with lengths and diameters of 40-60 nm and 20 nm are found [10].

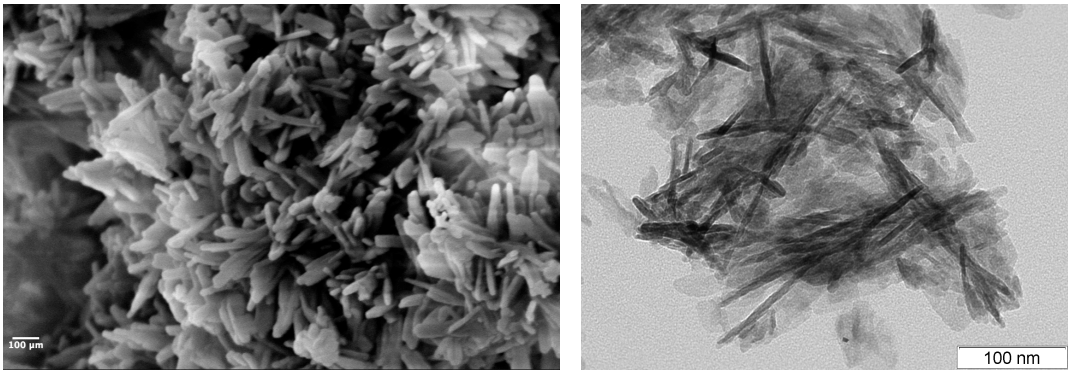

(a) (b)

Figure 6.1: Images of the hydroxyapatite nanorods produced: a) SEM; b) TEM.

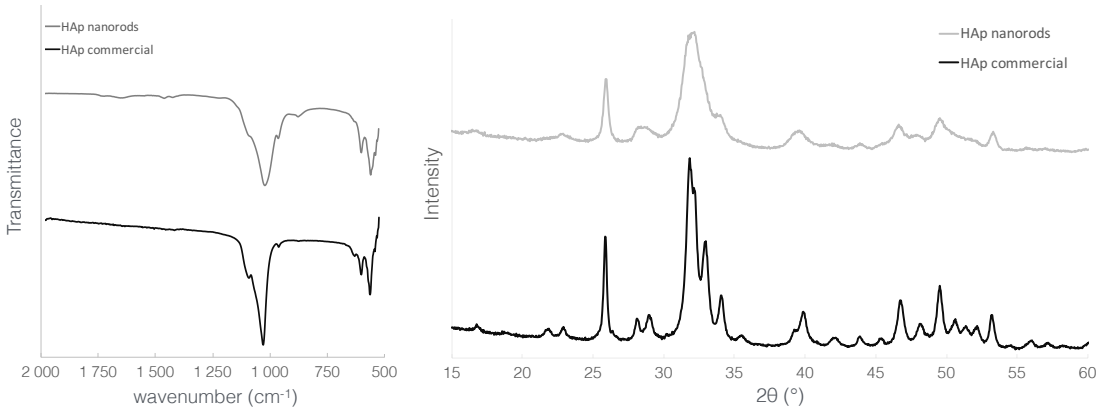

(a) FTIR spectra (b) XRD diffractogram

Figure 6.2: Comparison between the commercial and the produced HAp nanorods.

FTIR and XRD analysis confirmed the absence of modifications to HAp chemical composition and also a decrease in crystallinity due to the nanorod format, when comparing with commercial HAp. FTIR spectra (Figure 6.2(a)) evidence HAp's characteristic peaks and similarity between both samples. P-O bond of the PO_4^{3-} is noticed in the position of peaks 563 cm^{-1}, 601 cm^{-1}, 948 cm^{-1} and 1.030 cm^{-1}. Peak 862 cm^{-1} is attributed to a symmetric P-O(H) stretching vibration [9].

XRD difractograms (Figure 6.2(b)) exhibit the exclusive appearance of HAp hexagonal lattice characteristics peaks. No other phase is present as this would only happen with HAp decomposition in other CaP at very high temperature. In the proposed method, HAp is dissolved in a supersaturated solution and with continued addition of ammonia, the ceramic nucleates and grows as the pH rises. When comparing both XRD diffractograms it is perceptible the enlargement of the full width at half maximum in the HAp nanorods

sample, indicating a reduction in the crystal size. This last statement is verified by the resolution of Scherrer equation that result in crystal sizes of 7.7 nm and 4.3 nm for commercial HAp and nanorods, respectively.

6.3.2 Chitosan/Hydroxyapatite ICC Scaffolds

When considering the infiltration of CC templates, viscosity of the infiltration solution plays the key role. Full penetration within the structure must be ensured together with maximization of material in the voids between spheres. CS at concentration of 3% (wt/wt) in aqueous acetic acid solutions guarantees the necessary fluidity and viscosity for space occupation along all directions, allowing the production of homogeneous 3D structures. With the inclusion of hydroxyapatite nanorods even at low proportion, solutions viscosity augments causing an increasing difficulty in ICC fabrication. In the experimental process it was found that solutions upper limit composition for hybrid ICC development was CS+6% HAp which corresponds to species volume fraction of Φ_{CS}=0.50 and Φ_{HAp}=0.50. If the HAp content increases, the solutions become very hard to manage due to the loss of fluidity which can lead to impeded CC infiltration. Also, nanorods aggregation occurs which results in non-uniform matrices development and deficient ICC structure. In that sense, infiltration time should be taken into account since the vacuum process will take longer to force the hardly viscous composite solution to pass through the structure, after air admission.

Composite Inverted Colloidal Crystal scaffolds with composite matrix of CS/HAp nanorods were successfully developed through a process involving template infiltration and double freeze-drying (Figure 6.3). SEM images observation allow to conclude that all CC templates could be infiltrated with the proposed CS/HAp composite solutions. Scaffolds macropores (P) and interconnecting windows (Iw) diameters measurement revealed similar dimensions for all scaffolds .

3% CS $\rightarrow$ $P = (195.6 \pm 12.7)\mu$m | $Iw = (49.8 \pm 9.6)\mu$m

3%CS+1%HAp $\rightarrow$ $P = (205.3 \pm 12.1)\mu$m | $Iw = (52.6 \pm 5.9)\mu$m

3%CS+3%HAp $\rightarrow$ $P = (210.0 \pm 17.6)\mu$m | $Iw = (49.0 \pm 5.0)\mu$m

3%CS+6%HAp $\rightarrow$ $P = (194.6 \pm 12.9)\mu$m | $Iw = (57.3 \pm 4.8)\mu$m

The HAp nanorods effect is noticeable in the morphology of the ICCs. With the increase of HAp content the scaffolds walls thickness increases and the scaffolds surface seems to become roughened. The freeze-drying process induces the formation of microporosity within the surface of ICC pores and walls. However this effect loses intensity by the presence of HAp that causes matrix densification.

In CS+3%HAp scaffolds the pore sizes/shapes become more irregular and increasing the HAp content leads to further walls densification and some pores closure (CS+6%HAp).

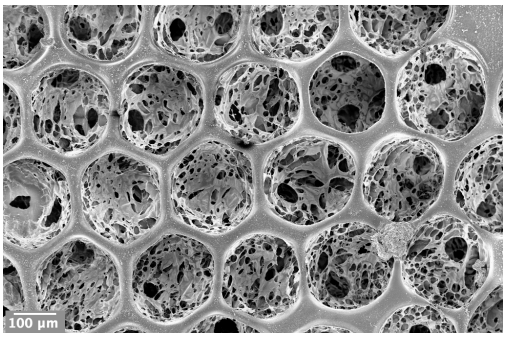

(a) Cs ICC scaffold

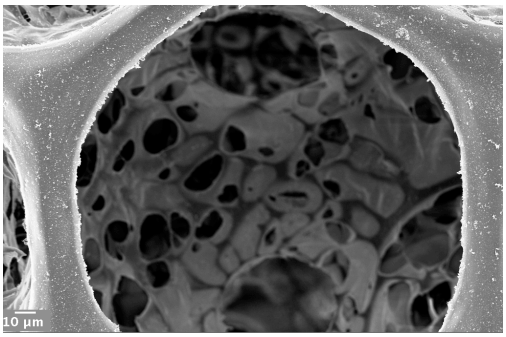

(b) CS ICC scaffold cavity

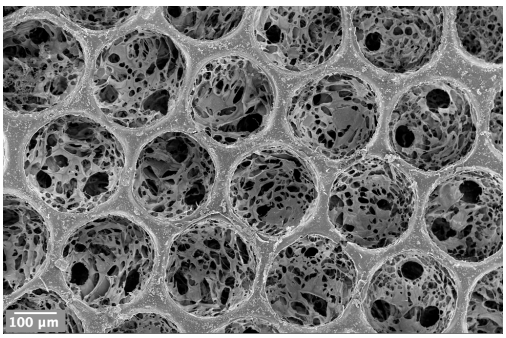

(c) CS+1%HAp ICC scaffold

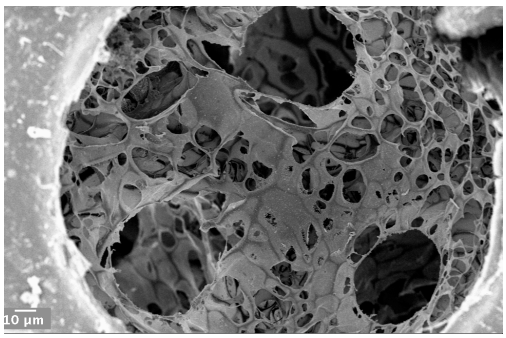

(d) CS+1%HAp ICC scaffold cavity

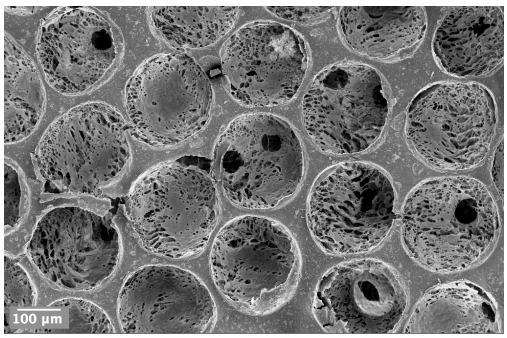

(e) CS+3%HAp ICC scaffold

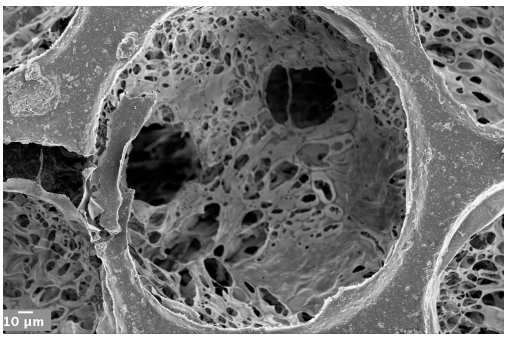

(f) CS+3%HAp ICC scaffold cavity

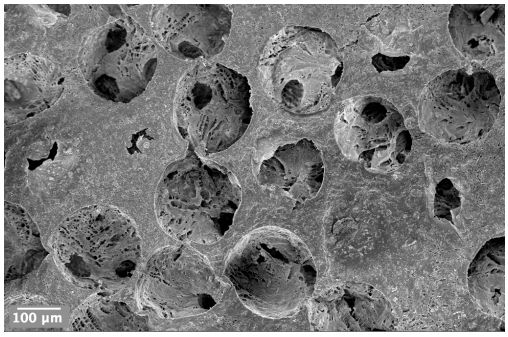

(g) CS+6%HAp ICC scaffold

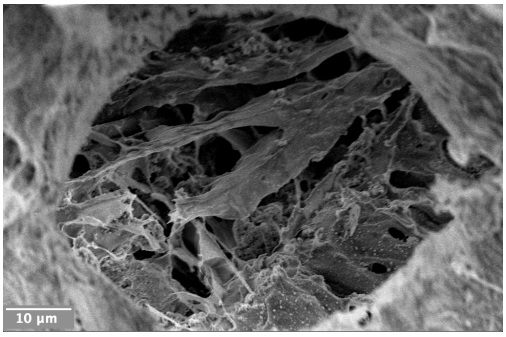

(h) CS+6%HAp ICC scaffold cavity

Figure 6.3: SEM images of ICC scaffolds with different HAp content. Left figures scale bar = 100 μm; Right figures scale bar = 10 μm.

It should be noticed that due to the higher viscosity it becomes harder to remove solution from the sphere-template surface which can lead to scaffold malformation and the morphology observed in Figure 6.3(g). Nevertheless it is visible in all scaffolds that communication between pores is ensured by the appearance of interconnective windows in the pores walls.

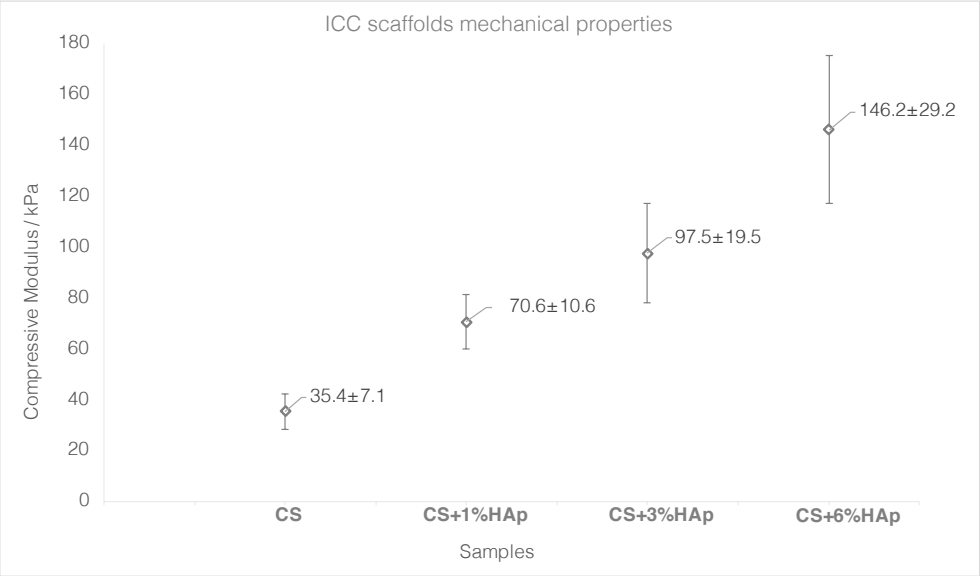

Figure 6.4: Elastic modulus of the different composite CS/HAp ICC scaffolds.

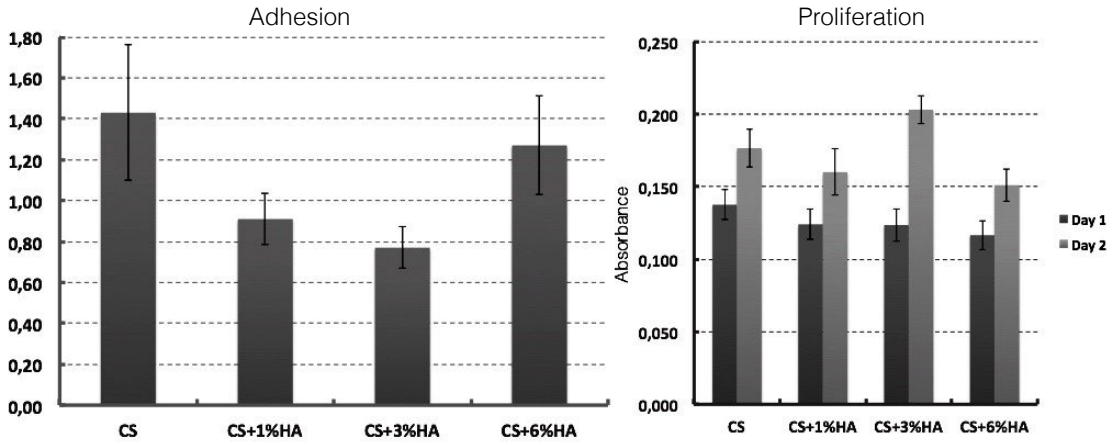

Figure 6.5: Osteoblasts SaOs-2 adhesion and proliferation in the different composite ICC scaffolds. All values were normalized to the negative control absorbance results.

Scaffolds mechanical properties were analyzed through compression tests, which show that ICC scaffolds have enhanced mechanical properties when HAp is included (Figure 6.4). E increases from 35 kPa to 146 kPa, in the CS ICC to CS+6%HAp ICC, respectively. Although there is a gradual improvement of mechanical properties from the neat CS scaffolds, the nanorods reinforcement effect is not sufficient to allow the production of

scaffolds with suitable mechanical properties for bone tissue engineering applications. In that sense further development is still needed and may involve the use of cross-linking agents that promote the formation of a stiffer polymeric network.

The scaffolds biological capability was evaluated trough adhesion and proliferation tests that confirmed the viability of these scaffolds for biomedical uses (Figure 6.5). Some researchers have pointed out that very small synthesized HAp nanocrystals (length = 40nm; width = 16nm) could be integrated by bone-forming osteoblasts with the possibility of modifying the cytoskeleton disposition, triggering higher inflammatory response and also putting in risk the cellular nuclei envelope or even leading to cell death [17]. Since bigger nanorods were applied, in this work no evidence of such risks was found and cellular adhesion evaluation revealed good interaction between osteoblasts and the scaffolds with cellular viability superior to 80%. Proliferation profiles exhibit cell growth of (128 ±13)%, (129 ± 17)%, (164 ± 17)% and (130 ± 15)% for CS, CS+1%HAp, CS+3%HAp and CS+6%HAp ICC scaffolds, respectively, which is a good indication of the scaffolds potential for bone tissue engineering applications.

6.4 Conclusions

In this work, ICC scaffolds of chitosan/hydroxyapatite were successfully produced. Hydroxyapatite with rodlike format and mean length and diameter of (153.7± 57.3) μm and (12.2±6.6) μm was used as ceramic starting material. Composite solutions allowed the production of scaffolds with CS/HAp nanorods volumetric content of Φ_{CS}=1.00 to 0.50; Φ_{HAp}=0.00 to 0.50, that exhibit homogenous porous structure with good interconnectivity. Compression tests and biological evaluation demonstrated that the mechanical properties increased with HAp content while cell adhesion and proliferation was efficient for all scaffold conditions.

References

[1] C. F. C. João, J. M. Vasconcelos, J. C. Silva, and J. P. Borges. "Chitosan based Inverse Colloidal Crystal Scaffolds". In: *European Conference on Biomaterials - ESB*. Spain, Sept. 2013, pp. 1–1. ISBN: 978-84-695-7831-5. URL: www.esb2013.org.

[2] L. Pighinelli and M. Kucharska. "Chitosan-hydroxyapatite composites." English. In: *Carbohydrate Polymers* 93.1 (Mar. 2013), pp. 256–262. DOI: 10.1016/j.carbpol.2012.06.004. URL: http://linkinghub.elsevier.com/retrieve/pii/S0144861712005644.

[3] S. K. L. Levengood and M. Zhang. "Chitosan-based scaffolds for bone tissue engineering". English. In: *Journal of Materials Chemistry B* 2.21 (2014), p. 3161. DOI: 10.1039/c4tb00027g. URL: http://xlink.rsc.org/?DOI=c4tb00027g.

[4] K. R. Mohamed, H. H. Beherei, and Z. M. El-Rashidy. "In vitro study of nano-hydroxyapatite/chitosan-gelatin composites for bio-applications." In: *Journal of Advanced Research* 5.2 (Mar. 2014), pp. 201–208. DOI: 10.1016/j.jare.2013.02.004. URL: http://linkinghub.elsevier.com/retrieve/pii/S2090123213000.

[5] J. Venkatesan and S.-K. Kim. "Chitosan composites for bone tissue engineering–an overview." English. In: *Marine drugs* 8.8 (2010), pp. 2252–2266. DOI: 10.3390/md8082252. URL: http://www.mdpi.com/1660-3397/8/8/2252/htm.

[6] S. N. Danilchenko. "Chitosan–hydroxyapatite composite biomaterials made by a one step co-precipitation method: preparation, characterization and in vivo tests". In: *Journal of Biological Physics and Chemistry* 9.3 (Sept. 2009), pp. 119–126. DOI: 10.4024/22DA09A.jbpc.09.03. URL: http://www.amsi.ge/jbpc/30909/30905.html.

[7] A. Zhu, Y. Lu, Y. Si, and S. Dai. "Frabicating hydroxyapatite nanorods using a biomacromolecule template". English. In: *Applied Surface Science* 257.8 (Feb. 2011), pp. 3174–3179. DOI: 10.1016/j.apsusc.2010.10.135. URL: http://adsabs.harvard.edu/cgi-bin/nph-data_query?bibcode=2011ApSS..257.3174Z&link_type=EJOURNAL.

[8] A. Rezaei and M. R. Mohammadi. "Development of hydroxyapatite nanorods-polycaprolactone composites and scaffolds derived from a novel in-situ sol-gel process". English. In: *Tissue Engineering and Regenerative Medicine* 9.6 (Nov. 2012), pp. 295–303. DOI: 10.1007/s13770-012-0002-z. URL: http://link.springer.com/10.1007/s13770-012-0002-z.

[9] Y. Liu, D. Hou, and G. Wang. "A simple wet chemical synthesis and characterization of hydroxyapatite nanorods". English. In: *Materials chemistry and physics* 86.1 (July 2004), pp. 69–73. DOI: 10.1016/j.matchemphys.2004.02.009. URL: http://linkinghub.elsevier.com/retrieve/pii/S0254058404001002.

[10] F. Huang, Y. Shen, A. Xie, J. Zhu, C. Zhang, S. Li, and J. Zhu. "Study on synthesis and properties of hydroxyapatite nanorods and its complex containing biopolymer". English. In: *Journal of Materials Science* 42.20 (July 2007), pp. 8599–8605. DOI: 10.1007/s10853-007-1861-x. URL: http://adsabs.harvard.edu/cgi-bin/nph-data_query?bibcode=2007JMatS..42.8599H&link_type=EJOURNAL.

[11] R. Tang, L. Wang, C. A. Orme, T. Bonstein, P. J. Bush, and G. H. Nancollas. "Dissolution at the Nanoscale: Self-Preservation of Biominerals". German. In: *Angewandte Chemie* 116.20 (May 2004), pp. 2751–2755. DOI: 10.1002/ange.200353652. URL: http://doi.wiley.com/10.1002/ange.200353652.

[12] J Huang, S. M. Best, W Bonfield, R. A. Brooks, N Rushton, S. N. Jayasinghe, and M. J. Edirisinghe. "In vitro assessment of the biological response to nano-sized hydroxyapatite". English. In: *Journal of Materials Science* 15.4 (Mar. 2004),

pp. 441–445. DOI: 10.1023/B:JMSM.0000021117.67205.cf. URL: http://link.springer.com/10.1023/B:JMSM.0000021117.67205.cf.

[13] L. Kong, Y. Gao, G. Lu, Y. Gong, N. Zhao, and X. Zhang. "A study on the bioactivity of chitosan/nano-hydroxyapatite composite scaffolds for bone tissue engineering". In: *European Polymer Journal* 42.12 (Jan. 2006), pp. 3171–3179. DOI: 10.1016/j.eurpolymj.2006.08.009. URL: http://linkinghub.elsevier.com/retrieve/pii/S0014305706002746.

[14] H. Chen, B. H. Clarkson, K. Sun, and J. F. Mansfield. "Self-assembly of synthetic hydroxyapatite nanorods into an enamel prism-like structure." In: *Journal of Colloid and Interface Science* 288.1 (July 2005), pp. 97–103. DOI: 10.1016/j.jcis.2005.02.064. URL: http://linkinghub.elsevier.com/retrieve/pii/S0021979705002092.

[15] B. D. Cullity and S. R. Stock. *Elements of X-ray diffraction; 3rd ed.* Upper Saddle River, NJ: Pearson, 2001. URL: http://cds.cern.ch/record/821266.

[16] C. A. Schneider, W. S. Rasband, and K. W. Eliceiri. "NIH Image to ImageJ: 25 years of image analysis". In: *Nature Methods* 9.7 (June 2012), pp. 671–675. DOI: 10.1038/nmeth.2089. URL: http://www.nature.com/doifinder/10.1038/nmeth.2089.

[17] X. Liu. "Cell responses to two kinds of nanohydroxyapatite with different sizes and crystallinities". English. In: *International journal of nanomedicine* Volume 7 (Mar. 2012), pp. 1239–12. DOI: 10.2147/IJN.S28098. URL: http://www.dovepress.com/cell-responses-to-two-kinds-of-nanohydroxyapatite-with-different-sizes-peer-reviewed-article-IJN.

Chapter 7

Structures with imprinted Liquid Crystalline Architecture

Inspired by chitin based hierarchical structures observed in arthropods exoskeleton, this work reports the capturing of chitin nanowhiskers' chiral nematic order into a chitosan matrix. For this purpose, highly crystalline chitin nanowhiskers (CTNW) with spindle-like morphology and average aspect ratio of 24.9 were produced by acid hydrolysis of chitin. CTNW were uniformly dispersed at different concentrations in aqueous suspensions. The suspensions LC phase domain was determined by rheological measurements and polarized optical microscopy (POM).

Chitosan (CS) was added to the CTNW isotropic, biphasic and anisotropic suspensions and the solvent was evaporated to allow the formation of films (Part 1) and 3D structures (Part 2) formation. The Films' morphologies as well as the mechanical properties were explored. The results evidence the existence of two different layered structures, one formed by chitosan layers induced by the presence of chitin and another formed by chitin nanowhiskers layers. By playing on the ratio chitin/chitosan one layered structure or the other can be obtained allowing the tunning of materials' mechanical properties. Based on the films formation procedure a similar method is proposed to the production of ICC scaffolds with imprinted liquid crystalline matrix[1].

7.1 Introduction

Nature has always delighted us with its ability to evolve highly specialized biological systems based on straightforward bottom-up self-assembly processes [2, 3]. Applying only

[1] The work described in this chapter is based on the publication: C.F.C João, C. Echeverria, A. Velhinho, J.C. Silva, M. H. Godinho, J. P. Borges. " Bio-inspired production of chitosan/chitin films from liquid crystalline suspensions". Carbohydrate Polymers. Elsevier Ltd. January 2, 2017, pp 372–381. [1].

a few basic components, the smart organization of lipids, proteins, minerals and polymers across different length scales has conducted to astonishing structural and functional materials like bones in vertebrates, exoskeletons in arthropods, nacre in mollusks and cell walls in plants. The specific design of nanostructures and their assembly into hierarchical larger macrostructures allows the unique simultaneous combination of features like high strength, low weight, fracture toughness, and stimuli-responsive adaptability that are only virtually available in natural tissues and are far more developed than those currently achieved by man-designed materials [4, 5]. In particular, biomacromolecular structural materials such as collagen, cellulose and chitin are capable of forming complex topologies that can give rise to very interesting platforms gathering lightweight and stiffness with the ability to control the direction, color and polarization of light [6–9].

As the second most abundant polymer in the world, chitin is a well-known biomaterial that possesses unique properties like biodegradability, bioactivity, non-toxicity, antibacterial, antifungal and anti-inflammatory activity [10–12] . This polysaccharide formed by poly-β-(1→4)-N-acetyl-D-glucosamine units is a fibrillar polymorphic semicrystalline polymer and the basic constituent of tissue nanostructures in different species [13, 14]. The aggregation of chitin's consecutive units leads to the formation of highly crystalline spindle-like fibrils often denominated chitin nanocrystals or chitin nanowhiskers (CTNW) that have aroused a growing interest in the scientific community due to their potential as reinforcements in nanocomposites [15]. Several methods like TEMPO-mediated oxidation [16], mechanical grinding [17, 18], ultrasonication [19] and high pressure homogenization [20] have been successfully reported as capable of producing chitin with a diverse set of widths and lengths at the nanoscale and suggested their use as structural or functional reinforcements for multiple applications [21]. Among all the methods, acid hydrolysis remains the approach capable of extract the narrow nano part of chitin - the nanowhisker – and consequently has been chosen in the present work [22, 23].

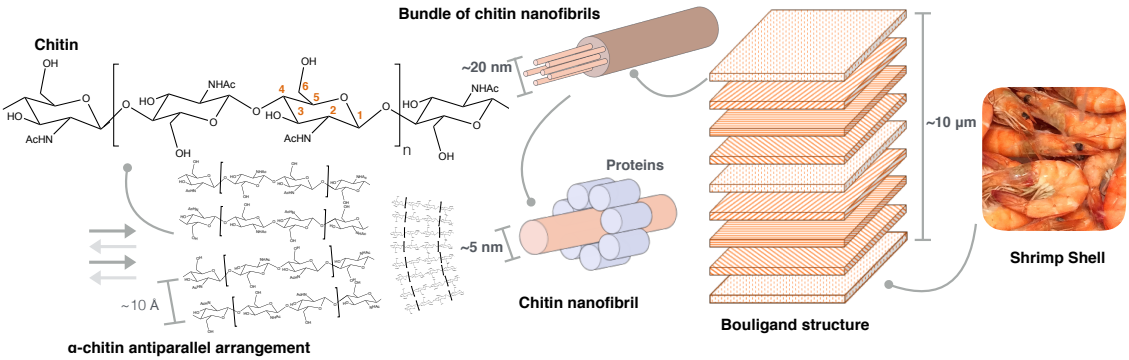

Figure 7.1: Chitin hierarchical structure within shrimp and crab shells cuticle.

From the nano to the micro levels, chitin has the ability of producing long-ranged hierarchical structures within the organic matrix of crustaceans and insects' exoskeleton

(Figure 7.1). When observing shells' cuticle under polarized optical microscopy, the matrix reveals an ensemble of regular CTNW laminae, gradually rotating around the normal direction and forming a twisted plywood system (Bouligand structure). The long range packaging of laminae leads to the formation of solid three-dimensional patterns with strong anisotropy that constitute the source of structural color and mechanical integrity [24, 25]. These structures display textures similar to the domains formed in chiral nematic liquid crystals, which has contributed to the idea that biosynthesis of living tissues must involve, during one or more steps, LC states of matter [26].

Chitosan (CS), a chitin derivative obtained when sufficient acetyl groups are removed, can be found in some fungi cell walls and although less common in nature, it is intensively explored by men. It's a well-known natural polymer that preserves the majority of chitin's properties but in opposition does not share its hydrophobicity neither its lack of swelling capability. This polysaccharide has been largely explored mainly in bioscience fields covering a wide variety of forms like films, 3D structures, microspheres etc. CS ability to be dissolved in acidic aqueous media constitutes an enormous advantage for polymer processing and chemical modification [27–29]. Moreover, since CS is a chitin derivative, the chemical similarity between both favors their compatibility and this feature has been highlighted in several applications [30, 31]. The CS/CTNW combination was used in the production of films, hydrogels, fibers and scaffolds. In addition, CTNW have also been included in multiple nanocomposites as fillers reinforcing other polymer matrices like polycaprolactone, poly(vinyl alcohol), methacrylate and natural rubber [15]. In all of those applications, the nanowhisker contribution in the improvement of composite mechanical properties has been reported. However, the reason why the reinforcement effects are lower than expected is still unknown. Small aspect ratios, lower chitin content or even whisker agglomeration has been pointed out as possible explanations [32]. Furthermore, it is clear that polymer processing methods have not accomplished the production of materials with certain functional and structural capabilities that are only available in Nature's self-templated materials [6].

The exploitation of chitin's ability to self-assemble in liquid crystalline structures is still limited and only few works regarding gelification of CTNW suspensions [33] and their biomineralization [34] were able to capture such organization. Polymer processing often leads to chiral nematic order disruption and that has been a major drawback in the production of structures with Bouligand-like architecture. Therefore, in this work we propose a different bottom-up approach to maintain chitin's chiral nematic structure in a natural polymer matrix by producing chitosan/chitin films from LC suspensions of chitin nanowhisker's. The analysis of films' mechanical properties revealed interesting features allowing to establish a tunable structure-properties relationship. Based on those results, it is also reported the transposition of films' production method into 3D structures fabrication, therefore allowing the production of ICC scaffolds with an imprinted liquid crystalline matrix. Being able to mimic chitin's native structure and to capture its liquid crystalline order may open a new path for future application in the bioscience fields.

7.2 Experimental Section

7.2.1 Preparation of Chitin Nanowhiskers

CTNW were produced following the method proposed by Revol et al. [35]. Briefly, 1g of chitin (C9213-1kg; Lot# SLBB8542V; CAS: 1398-61-4; Sigma-Aldrich. source: shrimp shell) was dissolved in 10 ml of hydrochloric acid (HCL; 37%; M= 36,46 g/mol; CAS:131020. 1212; Panreac) 3M at 110ºC during 90 minutes. After cooling to room temperature, the solution was successively centrifuged (Heraeus, Multifuge X1R, Thermo Scientific) for periods of 15 minutes at 11000 rpm, with the addition of Millipore water (Millipore Elix Advantage 3 purification system) between centrifugations and elimination of supernatant, until pH=2. At this point, the resulting supernatants were kept and dialyzed against Millipore water until neutral pH was achieved. Final CTNW suspensions were freeze-drying for 24 hours (Vaco 2, Zirbus).

7.2.2 Preparation of Chitin Nanowhiskers Suspensions

CTNW suspensions (CTNW content of 0.5, 0.62, 0.95, 1.27, 1.5, 1.9, 2.25, 2.55, 2.99, 3.7, 4.87 and 7.5% wt/wt) were produced from the dialysis retentates. The concentrations of the retentates were determined by freeze-drying a known volume of dialysed solution and measuring the mass of the freeze-dried product. CTNW suspensions were prepared either by centrifugation (higher concentration) or dilution with water (lower concentration). The suspensions were then sonicated at low intensity (20 to 30% of 750W) until a translucent suspension was achieved (max. time 30 min), indicating that nanowhiskers were well dispersed.

7.2.3 Production of Chitin Nanowhiskers/Chitosan Films

To obtain the polymeric films, 2% (v/v) acetic acid (Ac. Ac.; glacial, 99.7%, Lot#266601, M= 60.06 g/mol; CAS: 131008-1212; Panreac) solution was added dropwise to a 1.9% wt/wt CTNW suspension until pH=2.8 was achieved. Following the same procedures of centrifugation/dilution, combined solutions were prepared containing 1% wt/wt chitosan (CHITOPHARM S; M_w=500 kDa; DD=75%, CAS: 9012-76-4; Lot# UPBH8332PR; Cognis) and three different CTNW content (0.75%, 1.5% and 3.0% wt/wt). Afterwards, the solutions were placed in petri dishes and water was allowed to slowly evaporate in an oven at 37ºC for 72h, until thin films were obtained and constant weight established. The films were then stored in a vacuum desiccator.

7.2.4 Production of Chitin Nanowhiskers/Chitosan ICC Scaffolds

To prepare the hybrid scaffolds, the same solutions applied in the films production were used. The solutions were poured over the CC templates (whose production was described

in chapter 3) and then infiltrated under vacuum. When air is admitted inside the dessicator, air pressure forces the viscous solutions to penetrate the voids inside the CC template. Afterwards, the impregnated CC are cleaned with filter paper in order to remove excess solution and are placed in an oven at 37ºC for 24h. Following drying, the templates were cross-linked to prevent dissolution. The cross-linking of CS/CTNW was carried out with ephichlorodrin (ECH) under alkaline conditions following a procedure based on the one described by Zeng et al. [36] and Wei et al. [37]. CCs were immersed in solution of 0.2M ECH (C_3H_5ClO, > 99%, Lot# BCBP4230V, Fluka) 1M sodium hydroxide (NaOH, pellets, Lot#190609,EKA), and placed in a oven for 5h at 50ºC. Afterwards, CCs are again placed in the oven and dried at 37ºC for 24h. The procedure of infiltration with CS/CTNW solutions followed by cross-linking was repeated 6 times, to achieve maximum of the template voids. Then, spheres are removed by a combination of ethanol (1h), DCM (overnight) and ethanol (1h) baths. The final structure is dried at room temperature (for 12h) and stored.

7.2.5 Characterization

Rheological characterization of the CTNW suspensions was performed using a stress-controlled rheometer Bohlin Gemini HR nano, with a cone-plate geometry (20 mm diameter and 2º). Temperature during the test was kept at 25ºC. The evolution of viscosity with shear rate was recorded at room temperature for a shear rate range of 0.01–1000 $s-1$. All the measurements were obtained in steady state conditions.

Chitin crystallinity was analyzed by X-ray diffraction (XRD) using CuKα radiation generated at 45 kV and 40 mA, in the range of 5°<2θ<60°, in a X'Pert PRO (PANAlytical) X-ray diffractometer. Crystallinity index (CI) was determined following the methods reported by Cardenas et al. [38]. CI was calculated based on the equation 7.1 :

$$CI(\%) = \frac{I_{110} - I_{am}}{I_{110}} \times 100 \tag{7.1}$$

where I_{110} is the maximum intensity (arbitrary units) of the diffraction (110) at 2θ= 19° and I_{am} is the intensity of the amorphous diffraction at 2θ=15°.

Chemical characterization was conducted through Fourier Transform Infrared (FTIR) spectroscopy. FTIR spectra of powder samples from chitin and CTNW were collected using an attenuated total reflectance (ATR) sampling accessory (Smart iTR) equipped with a single-bounce diamond crystal on a Thermo Nicolet 6700 spectrometer. The spectra were acquired in the 4000-650 cm^{-1} range with 4 cm^{-1} resolution and 32 scans at a temperature of 20ºC.

CTNW suspensions of different concentration were observed by optical microscopy (Olympus Microscope Digital Camera DP73) with and without cross polarizers, at room temperature.

CTNW/CS films and CTNW were sputter coated with gold and morphologically characterized by scanning electronic microscopy (SEM) using a Carl Zeiss AURIGA CrossBeam Workstation instrument equipped with an Oxford X-ray Energy Dispersive Spectrometer.

CTNW were also evaluated by TEM by placing diluted suspensions of CTNW in a Kevlar 25 mesh grid for further analysis by an Hitachi H8100 II microscope with thermionic emission LaB6.

Mechanical properties of the CTNW/CS films were evaluated through tensile tests with a Rheometric Scientific (Minimat Firmware 3.1) system equipped with 100 N load cell. At least 25 samples (dimensions: 15 x 5 mm; gauge length: 8 mm) of each composition were drawn at a rate of 1 mm/min, in a dry state (45% relative humidity) at room temperature (23 ºC) and the modulus (E) was determined as the slope of the linear portion of the stress-strain curve. Samples thickness: CTNW – (147±21) μm ; CS – (29±9) μm; CS+0.75%CTNW – (21±5) μm; CS+1.5%CTNW – (46±5)μm; CS+3.0%CTNW – (70±10) μm.

7.3 Results and Discussion

7.3.1 Chitin Nanowhiskers and Suspensions

Although there are several approaches for polysaccharide fibril extraction from bulk material, acid hydrolysis remains the most applied method. In this work, CTNW were successfully obtained with 12% yield, after acid hydrolysis of bulk chitin with 3M HCl for 90 min. This procedure causes chitin depolymerization through the removal of amorphous content (due to faster swelling and hydrolysis) and results in the extraction of highly crystalline regions. After chemical treatment, continuous sample washing (until pH=2 is obtained) led to spontaneous appearance of colloidal suspensions with milky aspect. These suspensions were further neutralized and observed in SEM (Figure 7.2(a)) and TEM (Figure 7.2(b)) revealing chitin's typical spindle-like morphology.

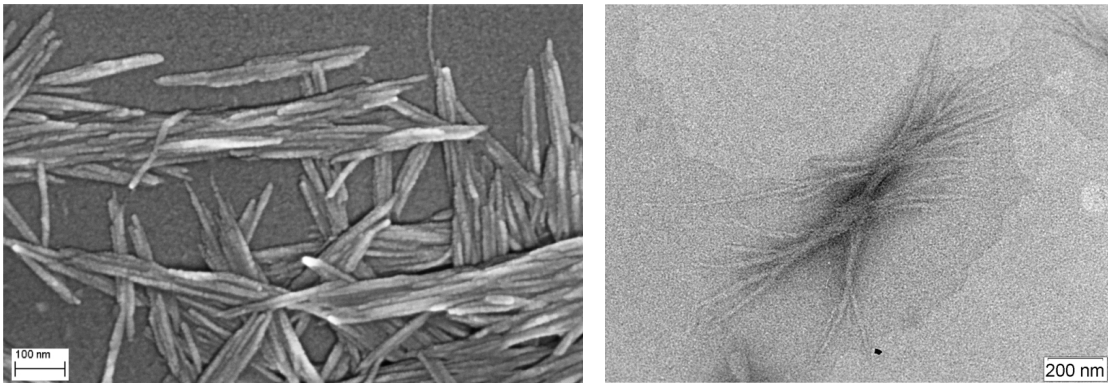

(a) (b)

Figure 7.2: Images of the produced chitin nanowhiskers: a) SEM; b) TEM.

In order to determine CTNW dimensions, images from SEM and TEM were processed with the software ImageJ [39]. A minimum of 80 measurements were considered for the determination of the nanowhiskers' dimensions and aspect ratio distributions. CTNW

have an average length (L), diameter (d) and aspect ratio (s) of (540 ± 250) nm, (24 ± 11) nm and 24.9 ± 0.7, respectively, but present high polydispersity , since both L and d have a wide range of distribution (Appendix A, Figure A.7). Acid hydrolysis causes the cleavage of amorphous content due to its differential swelling and the extraction of crystalline regions with spindle-like morphology (Figure 7.9(g)). This process is perceptible when comparing chitin XRD before and after hydrolysis (Figure 7.3(a)) where the ratio between the maximum diffraction intensity (2θ=19º) and the amorphous diffraction in the same unit (2θ=15º) increases, accounting for the increase in crystallinity.

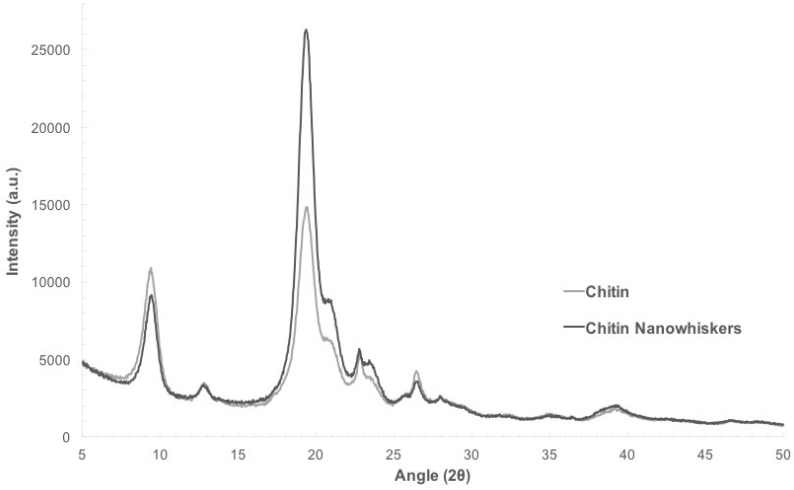

(a) XRD diffractogram

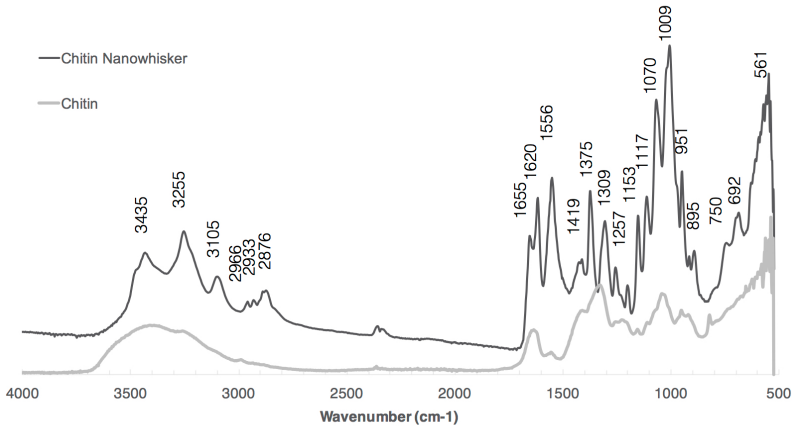

(b) FTIR spectra

Figure 7.3: X-Ray Diffractogram and FTIR spectra of chitin before (gray) and after (black) acid hydrolysis.

This fact is confirmed by the determination of CI (equation 7.1) which results in 91.4% for chitin nanowhisker, a value 6.6% higher than the one calculated for bulk chitin (CI=84.8%) (Table A.4 – Appendix A) and in accordance with values reported in the literature [40].

The chemical analysis of chitin products was conducted by FTIR measurements (Figure 7.3(b)). The spectra obtained revealed all major α-chitin characteristic bands; however chitin nanowhisker spectra also had thinner and more intense bands as a result of higher polymer crystallinity. The analysis of FTIR spectra revealed good correspondence with values reported in the literature by Cardenas et al. [38] and Goodrich et al.[40], with a slight shift of the peaks to the right (lower wavenumbers). The 3600-3000 cm^{-1} region is attributed to the OH and NH regions, with 3435 cm^{-1} corresponding to the vibration of intramolecular hydrogen bond O(3)H. . . O(5) from the ring. The NH vibrational modes are identified by the bands at 3255 cm^{-1} (intermolecular hydrogen bond C=O...H-N) and 3105 cm^{-1} (NH groups intramolecular bonded by H).

The 2966, 2876 and 951 cm^{-1} bands correspond to CH_3 and 2933, 1419 and 750 cm^{-1} to CH_2 vibration. The amide I frequency can be found in the 1655 and 1620 cm^{-1} bands, and the amide II in the 1556 cm^{-1}. Amide III and amide V absorptions are attributed to 1309 cm^{-1} and 692 cm^{-1}, respectively. C-O vibrations can be found at the 1153, 1117 and 1009 cm^{-1} bands and the vibration of the glycoside linkage C-O-C (ring) at 1153 cm^{-1}. Chitin´s anomeric center (C_1) vibration can be associated with 895 cm^{-1}, a typical band that appears in chitin from shrimp.

Further chemical analysis was conducted by ^{13}C CP/MAS NMR solid state spectroscopy (Appendix A, Figure A.8) and determination of the acetylation degree (DA). The relation between the integral of CH_3 signal and the average of glucopyranosic ring carbons integrals was used to determine DA following the equation 7.2 described by Kasaai [41]:

$$DA(\%) = \frac{I_{CH_3}}{(I_{C_1} + I_{C_2} + I_{C_3} + I_{C_4} + I_{C_5} + I_{C_6})/6} \times 100 \tag{7.2}$$

The results of NMR spectra analysis and DA determination reveal that CTNW did not suffer chemical modification when comparing with bulk chitin, maintaining their DA at 76.7%.

To investigate the liquid crystalline behavior and phase transition of CTNW systems, several CTNW suspensions (Figure 7.4(a)) were produced, comprehending concentrations between 0.5% and 7.5% (wt/wt).

Theoretical critical concentrations for phase transition were determined in order to understand what could happen when producing CTNW suspensions with different mass concentrations. Based on the work of Larson et al. [42] and applying the Onsager theory for elongated particle interaction:

$$U = 2cdL^2 \tag{7.3}$$

where U represents a dimensionless concentration, d is the rod diameter, L represents the rod length and c the number of particles per unit volume [43].

In a first approach, the anisotropy of CTNW suspensions was calculated based on the current method reported in literature, that considers chitin nanowhiskers simple

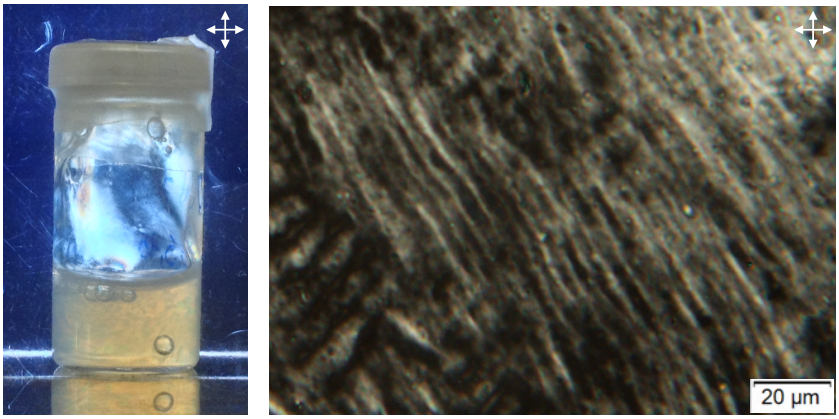

(a) Photograph (b) Optical microscopy

Figure 7.4: Images obtained with cross polarizers of CTNW aqueous suspensions:a) Photograph of 3.7% (wt/wt) suspension; b) Optical microscopy image of 7.3% (wt/wt) suspension exhibiting fingerprint texture (half-pitch of 2.6 μm).

arithmetic mean dimensions, which in this work are L=540 nm and d= 24 nm. However, polydispersity is known to affect the whisker electrical double-layer and the particle hydrodynamic volume causing variations in the liquid crystalline transitions [44]. To mitigate the effect of polydispersity and be able to determine more accurate values where the phase transitions take place, a second approach was applied considering the influence of larger particles. Applying the weighted mean of length and diameter (second moment of the distributions), the anisotropy of CTNW suspensions was calculated whereas particles with L_2= 656 nm, d_2= 29 nm and s_2= 30.9. It was theoretically found that for a generic concentration C, if C $\leq$ 2.01% (wt/wt) the system is isotropic; for 2.01%(wt/wt) < C < 2.55% (wt/wt) both isotropic and anisotropic domains coexist; and for C $\geq$ 2.55% (wt/wt) the system becomes entirely anisotropic.

The CTNW suspensions were analyzed by POM, which allowed the observation of its birefringence. As expected, when CTNW content increases the suspension birefringence becomes higher, with the appearance of typical cholesteric textures at higher concentrations. In the system proposed in this work, we registered changes in the birefringence and textures at certain and well-defined concentrations, signaling phase transitions and alterations in CTNW interaction. Acidic media can positively charge the CTNW surface, increasing the ionic strength of the suspension and influencing the particle hydrodynamic volume resulting in the modification of the LC critical limits [44]. But since low concentration acetic acid aqueous solution (2%) is used for our film production, that effect is negligible when compared with mass concentration variation.

Bellow 1.5% (wt/wt), chitin suspensions images were completely dark indicating an isotropic regime where the nanoparticles are randomly disposed. Between 1.5% and 2.5% (wt/wt) bright droplets stand out within the dark images (biphasic suspensions), indicating the formation of individualized liquid crystalline domains where rod-like

particles share the same orientation within a well-defined domain. At concentrations above 3% (wt/wt) CTNW dispersions exhibit clear birefringence with the appearance of cholesteric structures (fingerprints) at the concentration of 7.3% (wt/wt) (Figure 7.4(b)). It was also observed that for concentrations above 7.5% (wt/wt) the suspensions lose their fluidity, acquiring a gel-like appearance. This phenomenon has been reported over the years by other authors and is based on the fact that increasing the nanoparticles volume leads to the formation of a network whose structural preservation could depend upon the strength of van der Walls interactions and/or the electrostatic repulsion between the charged nanowhiskers [45].

Rheological measurements were performed for different chitin suspensions at different concentrations in order to confirm the presence of chiral nematic phases. Figure 7.5A shows the viscosity vs shear rate curve for the range of concentrations studied: 0.62-7.5% (wt/wt). As CTNW concentration increases in the suspension, the system's viscosity also increases and a simultaneous change in the shape of the curve is observed. According to the different shapes described for the different suspensions, we have separated the analysis in two different ranges of concentrations: (i) 0.62 to 2.99 % (wt/wt) and (ii) 3.7 to 7.5 % (wt/wt).

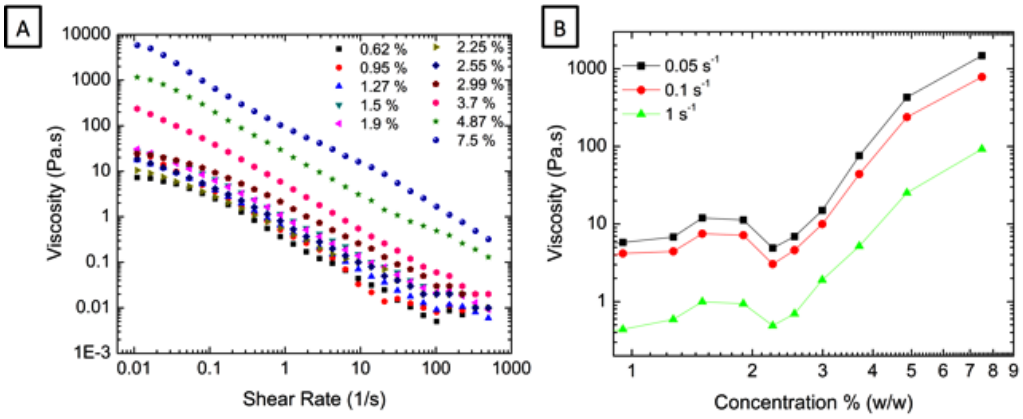

Figure 7.5: Evolution of suspensions viscosity: A) with shear rate for CTNW suspensions at different concentrations; B) with the CTNW concentrations obtained at three different shear rates.

In the first concentration range, (i) 0.62 to 2.99 % (wt/wt), the curves exhibited two Newtonian plateaus, respectively at low and high shear rates. At low shear rates, the CTNW are randomly oriented; such behavior is evidenced by the presence of the observed small or short Newtonian plateau. The plateau observed at high shear rate is an indication of the orientation of the nanowhiskers in the flow direction. When the CTNW concentration in suspension is above 3 % (wt/wt), as in the second concentration range (ii), the Newtonian plateau observed at low shear rates evolves into a shear-thinning regime. Furthermore, in the case of a CTNW suspension of 7.5 % (wt/wt) the typical "three-regime" curve is evident, which is indicative of a liquid crystalline structure as first stated by Onogi and Asada [46] and observed for cellulose nanowhiskers suspensions

[47] and chitin suspensions [44].

From the curves shown in Figure 7.5A values of viscosity at low and intermediate shear rate regions for each chitin suspension were extracted and represented as a function of CTNW concentration (Figure 7.5B). As observed from Figure 7.5B the evolution of viscosity with concentration is not monotonic, showing a maximum value, which becomes slightly more significant for low shear viscosity vs concentration curves. This deviation from a monotonic behavior is characteristic of a transition from an isotropic to an anisotropic phase as already stated in the literature [44, 48–52]. The maximum appears in the concentration range of 1.3-2.2 % (wt/wt) and indicates the co-existence of both isotropic and anisotropic phases (biphasic region); in this region CTNW are showing resistance to flow. This resistance, and therefore the viscosity, increases with concentration until a maximum viscosity value is achieved (between 1.5 and 1.9 % (wt/wt)). As the concentration increases the influence of the anisotropic fraction domains also increases, causing the viscosity to decrease due to the partial orientation of the CTNW parallel to each other, favoring the flow [50, 53, 54]. Above a CTNW critical concentration of 2.2-2.5% (wt/wt) the system becomes liquid crystalline.

The rheological behavior of the CTNW suspensions and the evolution of viscosity with concentration are in accordance with the results of the rheological measurements of chitin crystallites reported by J. Li et al. [44] and also present good correlation with the calculated theoretical concentrations where the isotropic-to-biphasic and biphasic-to-anisotropic transitions take place.

7.3.2 Part 1: Production of Chitosan/Chitin Films from Liquid Crystalline Suspensions

In order to investigate the production of CS/CTNW films retaining the chiral nematic order of CTNW suspensions, 1% (wt/wt) chitosan was dissolved in three different suspensions based on experimentally observed LC transitions: isotropic (0.75 wt/wt % CTNW), biphasic (1.5 wt/wt % CTNW) and chiral nematic (3.0 wt/wt % CTNW). Solvent evaporation gave rise to thin films that were characterized by SEM and tensile tests. For comparison, a 100% CTNW film (Appendix A, Figure A.9) was produced using a known liquid crystalline suspension of 6.4 % wt/wt CTNW. The 100% CTNW film exhibits a morphology often classified as packed sheets, as result of repeating long planes stacked into a 3D structure. Located between each layer containing a network of individualized nanowhiskers are voids formed by repulsion forces, which when seen in cross section (Figure 7.6 G,H) reflect the pitch, diminished from the precursor cholesteric liquid crystal suspension due to solvent evaporation.

The chiral nematic order of the suspensions is preserved, resulting in a geometrical Bouligand-type organization in the solid film, very similar to the reported morphologies in top-down approaches that use organisms exoskeletons directly as templates [7, 55].

When considering the different composite films (Figure 7.6), SEM images allow the

identification of different levels of nanowhisker integration and stratification within the CS matrix, which directly depends on CTNW and CS content. In CS+0.75% CTNW films, the bright protuberance scattered across the matrix indicate the presence of CNTW integrated in the CS based film and when compared with CTNW films reveal a different kind of stratification. It is possible to perceive a compact ordered structure with several layers of majorly CS. In this case the following scenario could be considered, the nanowhiskers even in low proportion are able to transfer their quirality to the CS polymeric chains, obligating them to dispose in a layered alignment responsible for film's morphology. CS+1.5% CTNW films exhibit some level of layer packing where fully merged nanowhiskers within the CS matrix can be observed. For CS+3.0%CTNW films a layer-by-layer construction is evidenced as a result of CTNW long sheets packing, similar to the morphology observed in a 100% CTNW film (Appendix A, Figure A.10).

With the increase of CTNW content the CS matrix adopts the orientation induced by the nanowhisher network, which leads to higher stratification. After a loss of fluidity caused by solvent evaporation, chitin originates films that retain the architecture of the liquid crystalline phase present in each of the CTNW suspensions, meaning that isotropic suspensions lead to the formation of films with an organized architecture of chitosan layers whereas from anisotropic suspensions films with Bouligand-like organization provided by chitin layers were obtained. Moreover CS plays a cohesive role between each consecutive layer in the composite films, mimicking protein´s behavior in living tissues. In this way it is possible to freeze the morphology resulting from CTNW self-assembly, originated by the anisotropic suspensions.

Elastic properties of the films were evaluated by tensile testing. In Figure 7.7 the results of Young's modulus are presented. CTNW and CS volume fractions, f_f and f_m respectively, where $f_f + f_m = 1$, were determined and indicated in the graphic bellow each sample. Student t test with unequal variance was used to compare E mean between each film class, accepting $P<0.05$ as statistically significant. Besides 1.5% and 3.0% CTNW films ($P>0.05$) the remaining group samples are statistically different (*$P<0.01$).

Generally, the incorporation of CTNW in the CS matrix induces the formation of stronger films when comparing with simple CS film. The cooperation between the filler (nanowhisker) and the matrix (chitosan) reaches a maximum of 5.3 GPa in CS+0.75% CTNW films. The increase between the E of CS films and that of CS+0.75%CTNW films is surely associated with the chemical compatibility and with the interaction between whiskers and matrix.

It would be expectable that with the augmentation of nanowhisker content the elastic modulus should also increase, however as seen in Figure 7.7 the reverse effect takes place. The 3.0% CTNW films show E of (2.25±0.48) GPa, a value 58% and 28% inferior to those obtained for 0.75% and 1.5% CTNW films respectively, but approximately 2% and 64% higher than for net CS and net CTNW films, respectively. In fact, when considering the films produced from the biphasic and anisotropic solutions, there is a reversion in the composite system and CNTW becomes the films matrix (E = (0.80±0.37) GPa), whereas

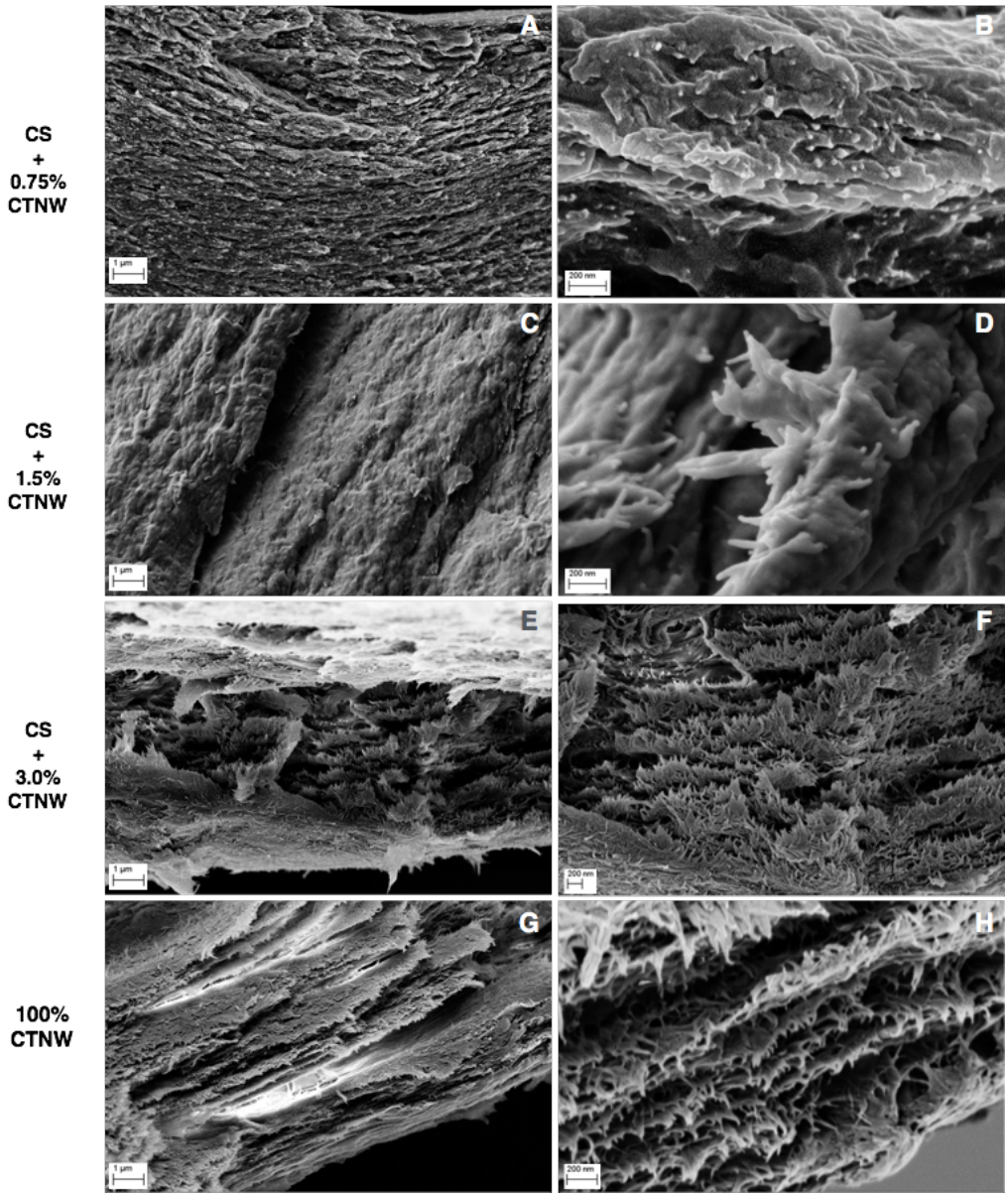

Figure 7.6: SEM images of the different CS/CTNW composite films: (A,B) - CS +0.75% CTNW; (C,D)- CS+ 1.5% CTNW; (E,F) - CS +3.0% CTNW; (G,H) - 100% CTNW.

CS becomes the reinforcing phase (E = (2.01±0.36) GPa), which explains the mechanical properties increase. As reported in the literature, Ifuku et al. [56] have found CS films with E=2.64 GPa and Shelma et al. [57] described CS+2.7%CTNW with E=(2.3±0.6) GPa, results that are remarkably close to our experimental values. Jin et al. [58] have found a similar correlation between chitin nanofibers self-assembly and the mechanical properties of composite chitin/silk films. The Young's modulus determined in our work clearly confirms the nanowhiskers' self-assembly, which is responsible for the formation of a biocomposite layered nanostructure.

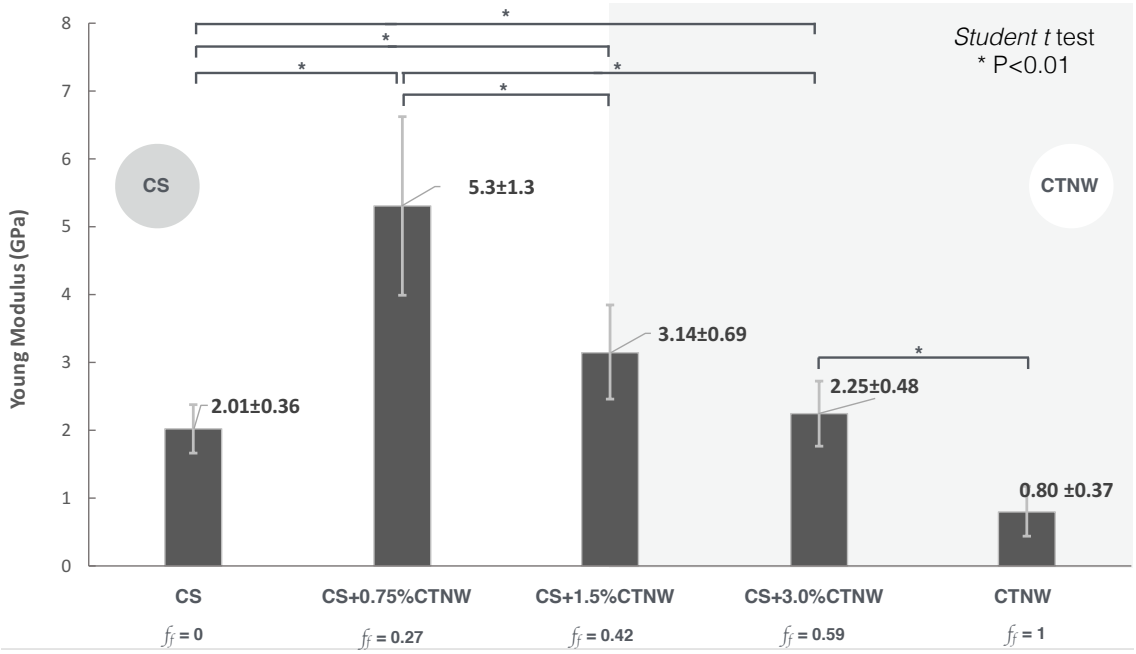

Figure 7.7: Young's modulus of CS/CTNW films. Horizontal bars indicate the comparison between two different types of films. Asterisk indicates the statistical significance (P) that arises from the *Student t* probability tests and establishes the difference between two samples means. * P<0.001.

Films' mechanical properties can be explained by the different structural organizations already observed in Figure 7.6. With the addition of CTNW, the films no longer behave as a typical matrix/reinforcement composite but instead adopt the CTNW self-assembly that leads to Bouligand-like structural formation (Appendix A, Figure A.11). Within those stratified structures two effects should be consider: intra- and inter-layer interactions. Even if the nanowhisker-matrix and nanowhisker-nanowhisker interactions were equal in all composites, which is not clear and cannot be inferred in our results, it is evident from the SEM images (Figure 7.6) that the increase of CTNW content leads to the increase of inter-layer distance and the appearance of voids resulting in the decreasing of mechanical properties.

The presence of a Bouligand-like layered structure in CS+3.0% CTNW films was also confirmed after development of mechanical properties theoretical model based on the combination of the classic shear-lag model [59] and the Halpin-Tsai model [60].

Considering the film as a 3D volume, the contained whiskers are not aligned in all the structure directions and therefore one way to approach the film's elastic behavior is to consider it as corresponding to a stack of unidirectional composite layers, each consisting of a chitosan matrix reinforced with a small amount of chitin whiskers (Figure 7.8). Summed together, the minute whisker volume fractions f_{f_k} in each of the layers must be equal to the overall reinforcement volume fraction in the film, f_f (Figure 7.8 C). Similarly, for simplicity sake, the film's thickness may be considered to be evenly divided

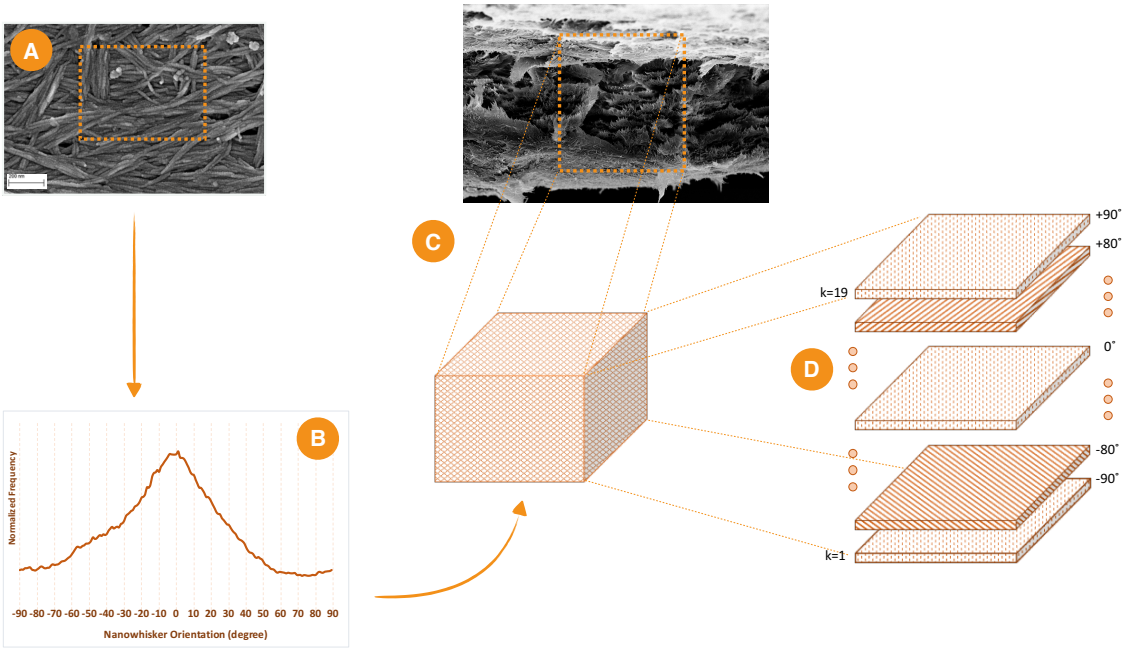

Figure 7.8: Illustrative sequence of the mechanical modeling of CS/CTNW films' Young modulus.

between all the layers.

The calculation sequence derived from this model is detailed in appendix A, section A.3.3. For the elastic constants of the film's constituent materials the values E_m=2.01 GPa (from CS film) and E_f=119 GPa were considered respectively for the CS matrix and the CTNW elastic moduli, with ν_m=0.35 and ν_f=0.29 obtained from the literature [61, 62] for the corresponding Poisson's ratios.

In both the CS and CTNW cases, the shear moduli were calculated from the above values, admitting an isotropic behavior. According to experimental results, the average whisker aspect ratio was taken to be s=30.5 and overall reinforcement volume fraction in CS+3.0% CTNW films was f_f=0.59. Since the film interior layers are not visually accessible, the reinforcement orientation distribution (Figure 7.8 B) was determined from SEM image of the film's surface (Figure 7.8 A) with the aid of ImageJ software and its OrientationJ plugin (developed in EPFL by D. Sage). This distribution was approximated by a stack of 19 unidirectional layers of different reinforcement fraction, rotated 10° from each other according to Figure 7.8 D (see Table A.5 -section A.3.3).

Applying the above considerations, the following elastic properties for the stacked composite were calculated: $(E_1)_{Film}$ = 3.57 GPa , $(E_2)_{Film}$ = 2.70 GPa, $(\nu_{12})_{Film}$ = 0.20, $(\nu_{21})_{Film}$=0.15, $(G_{12})_{Film}$ = 1.03 GPa. The values thus obtained are in good agreement with the experimental results obtained from the tensile strain tests. The observed differences may be explained by the particular values of elastic constants used in the calculations, that had to be chosen among a wide range reported in the literature. Nevertheless, when comparing the experimental and the theoretical results, two assumptions can be

formulated: 1) The model can provide useful information about the elastic behavior of a composite stack of unidirectional composite layers; 2) The hybrid CS+3.0% CTNW film elastic properties follow the mechanical properties of a Bouligand-like structure.

7.3.3 Part 2: Liquid Crystalline Inverted Colloidal Crystal

In order to produce inverted colloidal crystal scaffolds with imprinted LC matrix, a strategy that could translate the Bouligand-like structure achieved in the CS/CTNW films into the ICC scaffold was conceived. The CC templates were infiltrated with the same CS/CTNW suspensions and dried to allow film formation. Once again, viscosity of the suspensions was in evidence during impregnation and while CS and CS+0.75%CTNW suspensions were easily infiltrated by vacuum, CS+3.0%CTNW and the CTNW (6.4 wt/wt % chitin) suspensions took longer and the templates surfaces were harder to clean.

After one infiltration and drying, polymeric layers covered the spheres; however to ensure complete void volume filling, the infiltration step was repeated in order to introduce more material and produce denser ICC walls. To prevent the recently formed layers from dissolving during the second infiltration with the acidic suspension, a cross-linking step was used. ECH is recognized as less efficient than other known agents like glutaraldehyde or genipin, but was preferentially chosen over these after a previous biocompatibility study with cross-linked CS films and osteoblasts SaOs2, where ECH exhibited less toxicity. After each infiltration, the CCs were immersed in concentrated cross-linking solution which promoted the preferencial formation of covalent bonds between chitosan/chitin hydroxyl groups and ECH, therefore diminishing the matrices solubility in aqueous acids while keeping some of its swelling capability, allowed by the free amino groups [63]. Although CTNW do not dissolve in aqueous acids, they can quickly disperse in aqueous medium, so the use of a cross-linker reactive towards hydroxyl groups was intended to stiffen the organized nanofibrilar network, decreasing the fragmentation probability.

ICC scaffolds were successfully developed applying the proposed multiple infiltration and cross-linking process (Figure 7.9). SEM images observation allowed to conclude that all CC templates could be infiltrated with the CS/CTWN suspensions and were able to keep the polymeric material within the spheres voids. Despite some deterioration in the hcp geometry, the cross-linking reaction was sufficient to endow the structures with walls strong enough to be handled during the spheres dissolution. It is possible to observe the presence of pores and interconnecting windows in all scaffolds. CS (Figure 7.9(a)(b)) and CS+0.75%CTNW (Figure 7.9(c)(d)) scaffolds preserved better the typical ICC design and exhibit thick walls even though with some level of deformation. In CS+3.0%CTNW scaffolds (Figure 7.9(e)(f)), the pore walls look thinner and perfectly follow the sphere boundaries. In the CTNW scaffolds (Figure 7.9(g)(h)) the presence of pores can still be perceived but the scaffold's walls were significantly crushed during samples handling, an indication of inferior mechanical properties.

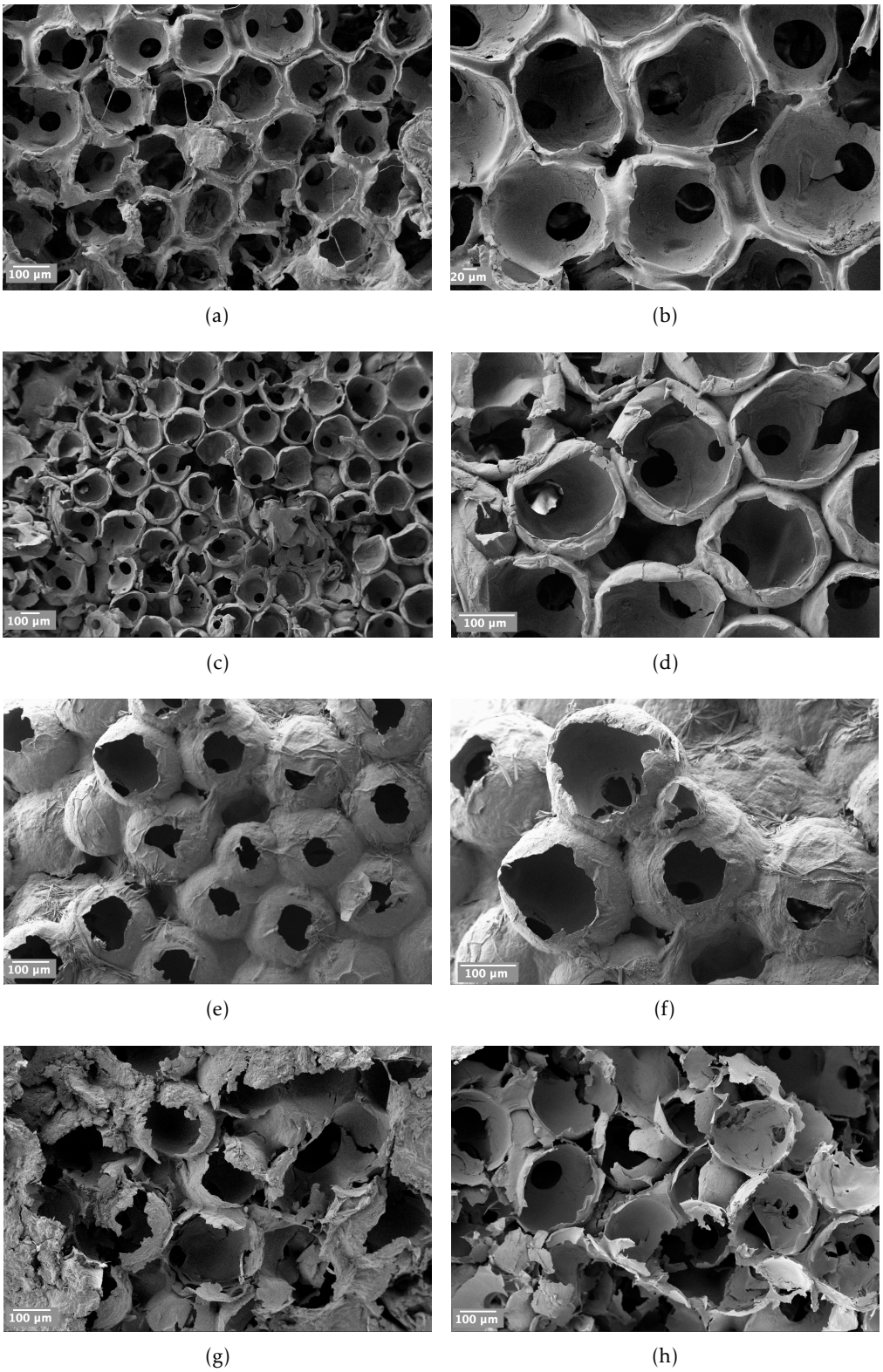

(a) (b)

(c) (d)

(e) (f)

(g) (h)

Figure 7.9: SEM images of ICC scaffolds with different CS/CTNW content: CS (a, b), CS+0.75%CTNW (c, d), CS+3.0%CTNW (e, f), CTNW (g, h).

From all scaffolds observation it is possible to conclude that some larger and smaller spheres manifested their presence by inducing local defects that destabilize the hexagonal architecture. As noticed before, suspensions viscosity effect hampered the CC surface cleaning which resulted in small layers that covered the access to pore observation. The fact that CC templates were subjected to many manipulations during the multiple infiltrations/drying procedures caused the detachment of spheres in the top and bottom template surfaces and in part justify the non-homogeneous structures observed in SEM images. Also, it can be perceived that the ICCs voids volume are not completed filled and there is room for more material penetration.

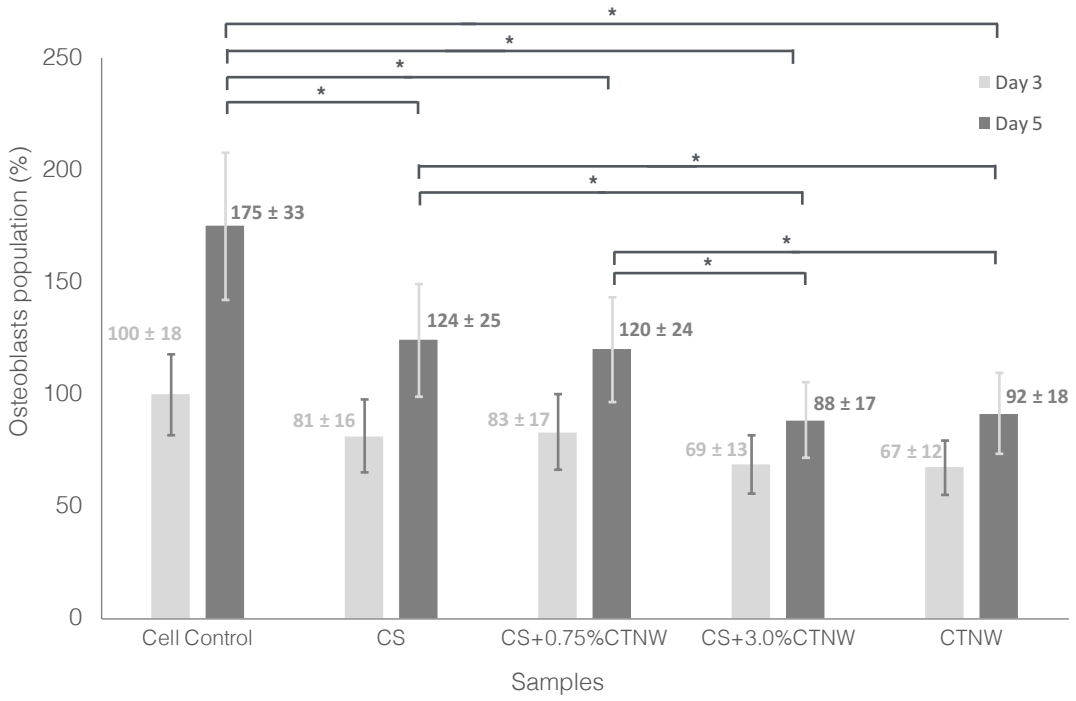

Figure 7.10: Biological evaluation of CS/CTNW composite films, as model for *in vitro* evaluation of the LC ICC surface. Osteoblasts populations determined using as reference the day 3 cell control day results. Asterisk indicates the statistical significance (P) that arises from the *Student t* probability tests and establishes the difference between two samples means. * P<0.002.

To understand the biological potential of the reported ICC scaffolds, an exploratory study was carried out concerning cell culturing of osteoblasts SaOs2 in CS/CTNW films cross-linked with ECH/NaOH. The films were used as model for *in vitro* evaluation of the ICC surfaces. In Figure 7.10 the evolution of osteoblasts populations is shown after 3 days and 5 days of cell culture. Student t test with unequal variance was used to compare cells population mean between each film class on day 5, accepting P<0.05 as statistically significant. Besides CS / CS+0.75%CTNW and CS+3.0%CTNW / CTNW comparisons, the remaining group samples are statistically different (*P<0.02).

The results evidence that cells were able to adhere and proliferate in the films surface.

From day 3 to day 5 there is a positive evolution in cell population growth of 43%, 37%, 19% and 25% for CS, CS+0.75%CTNW, CS+3.0%CTNW and CTNW films, respectively. Notwithstanding that cell population grows in all film conditions, it is also possible to conduct a different analysis dividing the results in two sub-groups that concern materials volume fraction. On day 5, CS and CS+0.75% CTNW films, where $f_m > f_f$, show 28 to 36% higher cell population number than CS+3.0%CTNW and CTNW, where $f_m < f_f$. Taking notice of the indication that SaOs2 prefer surfaces dominated by CS rather than surfaces where CTNW are the main constituent material, further studies are still needed to assess and confirm the cellular behavior in a 3D environment like the one provided by the ICC.

7.4 Conclusions

Transferring natural system principles into a synthetic application is a hard process requiring precise organization of biomaterials from the nano to the macro level. In this work, following a bottom-up approach, it was possible to capture the chiral nematic structure of chitin liquid crystalline suspensions and translate it to chitosan/chitin films. For that, highly crystalline chitin nanowhiskers with spindle-like morphology and high aspect ratio were used as starting nanomaterials for construction of chitin's Bouligand structure. Rheological and morphological evaluation of chitin nanowhiskers suspensions allowed defining liquid crystalline concentration limits where transitions between isotropic to anisotropic regimes occur. Based on LC transition, chitosan/chitin films exhibiting hierarchical architecture were successfully produced by slow evaporation of CS/CTNW suspensions. A strong correlation between chitin chiral nematic organization and the internal architecture of composite films is established, evidenced by the tunable mechanical properties. Through an adaptation of 2D films formation procedures it was possible to obtain 3D ICC scaffolds with imprinted Bouligand-like matrices, albeit with a still imperfect structure. The basis for producing scaffolds with walls resembling the films with imprinted liquid crystalline architecture was established and with further developments it is expected that homogenous ICC structures will be achieved. After that, it will be possible to upgrade the scaffolds and introduce ceramic materials which might allow the conception of matrices similar to bone mineralized fibrillar network. This type of ICCs can constitute the next evolution in the construction of applications that can better mimic tissues designed by nature.

References

[1] C. F. C. João, C. Echeverria, A. Velhinho, J. C. Silva, M. H. Godinho, and J. P. Borges. "Bio-inspired production of chitosan/chitin films from liquid crystalline suspensions". In: *Carbohydrate Polymers* 155 (Jan. 2017), pp. 372–381. DOI: 10.

1016/j.carbpol.2016.08.039. URL: http://dx.doi.org/10.1016/j.carbpol.2016.08.039.

[2] M. S. Aziz and A. Y. El sherif. "Biomimicry as an approach for bio-inspired structure with the aid of computation". In: *Alexandria Engineering Journal* (Nov. 2015), pp. 1–8. DOI: 10.1016/j.aej.2015.10.015. URL: http://dx.doi.org/10.1016/j.aej.2015.10.015.

[3] N. C. Seeman and A. M. Belcher. "Emulating biology: Building nanostructures from the bottom up". English. In: *Proceedings of the National Academy of Sciences* 99.Supplement 2 (2002), pp. 6451–6455. DOI: 10.1073/pnas.221458298. URL: http://www.pnas.org/cgi/doi/10.1073/pnas.221458298.

[4] P. Egan, R. Sinko, P. R. LeDuc, and S. Keten. "The role of mechanics in biological and bio-inspired systems". In: *Nature Communications* 6 (July 2015), pp. 7418–12. DOI: 10.1038/ncomms8418. URL: http://www.nature.com/doifinder/10.1038/ncomms8418.

[5] S Nikolov, H Fabritius, M Petrov, M Friák, L Lymperakis, C Sachs, D Raabe, and J Neugebauer. "Robustness and optimal use of design principles of arthropod exoskeletons studied by ab initio-based multiscale simulations". English. In: *Journal of the Mechanical Behavior of Biomedical Materials* 4.2 (Feb. 2011), pp. 129–145. DOI: 10.1016/j.jmbbm.2010.09.015. URL: http://linkinghub.elsevier.com/retrieve/pii/S1751616110001384.

[6] W.-J. Chung, J.-W. Oh, K. Kwak, B. Y. Lee, J. Meyer, E. Wang, A. Hexemer, and S.-W. Lee. "Biomimetic self-templating supramolecular structures." English. In: *Nature* 478.7369 (Oct. 2011), pp. 364–368. DOI: 10.1038/nature10513. URL: http://adsabs.harvard.edu/cgi-bin/nph-data_query?bibcode=2011Natur.478..364C&link_type=ABSTRACT.

[7] T.-D. Nguyen and M. J. MacLachlan. "Biomimetic Chiral Nematic Mesoporous Materials from Crab Cuticles". English. In: *Advanced Optical Materials* 2.11 (Aug. 2014), pp. 1031–1037. DOI: 10.1002/adom.201400279. URL: http://doi.wiley.com/10.1002/adom.201400279.

[8] M. I. Shams, M. Nogi, L. A. Berglund, and H. Yano. "The transparent crab: preparation and nanostructural implications for bioinspired optically transparent nanocomposites". English. In: *Soft Matter* 8.5 (2012), pp. 1369–1373. DOI: 10.1039/C1SM06785K. URL: http://pubs.rsc.org/en/Content/ArticleHTML/2012/SM/C1SM06785K.

[9] Y. Lu, Q. Sun, X. She, Y. Xia, Y. Liu, J. Li, and D. Yang. "Fabrication and characterisation of α-chitin nanofibers and highly transparent chitin films by pulsed ultrasonication". In: *Carbohydrate Polymers* 98.2 (Nov. 2013), pp. 1497–1504. DOI: 10.1016/j.carbpol.2013.07.038. URL: http://dx.doi.org/10.1016/j.carbpol.2013.07.038.

[10] R. Izumi, K. Azuma, H. Izawa, M. Morimoto, M. Nagashima, T. Osaki, T. Tsuka, T. Imagawa, N. Ito, Y. Okamoto, H. Saimoto, and S. Ifuku. "Chitin nanofibrils suppress skin inflammation in atopic dermatitis-like skin lesions in NC/Nga mice". English. In: *Carbohydrate Polymers* 146 (2016), pp. 320–327. DOI: 10.1016/j.carbpol.2016.03.068. URL: http://linkinghub.elsevier.com/retrieve/pii/S0144861716303046.

[11] E. Robles, A. M. Salaberria, R. Herrera, S. C. M. Fernandes, and J. Labidi. "Self-bonded composite films based on cellulose nanofibers and chitin nanocrystals as antifungal materials". English. In: *Carbohydrate Polymers* 144 (2016), pp. 41–49. DOI: 10.1016/j.carbpol.2016.02.024. URL: http://linkinghub.elsevier.com/retrieve/pii/S0144861716300807.

[12] Y. Qin, S. Zhang, J. Yu, J. Yang, L. Xiong, and Q. Sun. "Effects of chitin nanowhiskers on the antibacterial and physicochemical properties of maize starch films." English. In: *Carbohydrate Polymers* 147 (Aug. 2016), pp. 372–378. DOI: 10.1016/j.carbpol.2016.03.095. URL: http://linkinghub.elsevier.com/retrieve/pii/S0144861716303484.

[13] N. S. Gupta. *Chitin*. English. 1st ed. Vol. 34. Formation and Diagenesis. Springer, Nov. 2010. ISBN: 9789048196845. URL: http://books.google.pt/books?id=p99CHOFmwOEC&printsec=frontcover&dq=intitle:Chitin&hl=&cd=18&source=gbs_api.

[14] I. W. Hamley. "Liquid crystal phase formation by biopolymers". English. In: *Soft Matter* 6.9 (2010), pp. 1863–1871. DOI: 10.1039/b923942a. URL: http://xlink.rsc.org/?DOI=b923942a.

[15] C. F. C. João, J. C. Silva, and J. P. Borges. "Chitin-Based Nanocomposites: Biomedical Applications". English. In: *Eco-friendly Polymer Nanocomposites*. New Delhi: Springer India, 2015, pp. 439–457. ISBN: 978-81-322-2472-3. DOI: 10.1007/978-81-322-2473-0_14. URL: http://link.springer.com/chapter/10.1007/978-81-322-2473-0_14/fulltext.html.

[16] Y. Fan, T. Saito, and A. Isogai. "Chitin Nanocrystals Prepared by TEMPO - Mediated Oxidation of α-Chitin". English. In: *Biomacromolecules* 9.1 (Jan. 2008), pp. 192–198. DOI: 10.1021/bm700966g. URL: http://pubs.acs.org/doi/abs/10.1021/bm700966g.

[17] Y. Fan, T. Saito, and A. Isogai. "Preparation of Chitin Nanofibers from Squid Pen β-Chitin by Simple Mechanical Treatment under Acid Conditions". English. In: *Biomacromolecules* 9.7 (July 2008), pp. 1919–1923. DOI: 10.1021/bm800178b. URL: http://pubs.acs.org/doi/abs/10.1021/bm800178b.

[18] C. Chen, D. Li, Q. Hu, and R. Wang. "Properties of polymethyl methacrylate-based nanocomposites: Reinforced with ultra-long chitin nanofiber extracted from crab shells". In: *Journal of Materials & Design* 56.C (Apr. 2014), pp. 1049–1056. DOI: 10.1016/j.matdes.2013.11.057. URL: http://dx.doi.org/10.1016/j.matdes.2013.11.057.

[19] Q. Deng, J. Li, J. Yang, and D. Li. "Optical and flexible Î±-chitin nanofibers reinforced poly(vinyl alcohol) (PVA) composite film: Fabrication and property". In: *Composites Part A* 67.C (Dec. 2014), pp. 55–60. DOI: 10.1016/j.compositesa.2014.08.013. URL: http://dx.doi.org/10.1016/j.compositesa.2014.08.013.

[20] A. M. Salaberria, S. C. M. Fernandes, R. H. Diaz, and J. Labidi. "Processing of α-chitin nanofibers by dynamic high pressure homogenization: characterization and antifungal activity against A. niger." English. In: *Carbohydrate Polymers* 116 (Feb. 2015), pp. 286–291. DOI: 10.1016/j.carbpol.2014.04.047. URL: http://linkinghub.elsevier.com/retrieve/pii/S0144861714004044.

[21] C. F. C. João, A. C. Baptista, I. M. M. Ferreira, J. C. Silva, and J. P. Borges. "Natural Nanofibres for Composite Applications". In: *Fibrous and Textile Materials for Composite Applications*. Singapore: Springer Singapore, Jan. 2016, pp. 261–299. ISBN: 978-981-10-0232-8. DOI: 10.1007/978-981-10-0234-2_8. URL: http://link.springer.com/10.1007/978-981-10-0234-2_8.

[22] J. Sriupayo, P. Supaphol, J. Blackwell, and R. Rujiravanit. "Preparation and characterization of α-chitin whisker-reinforced chitosan nanocomposite films with or without heat treatment". English. In: *Carbohydrate Polymers* 62.2 (Nov. 2005), pp. 130–136. DOI: 10.1016/j.carbpol.2005.07.013. URL: http://linkinghub.elsevier.com/retrieve/pii/S0144861705003115.

[23] M. V. Tzoumaki, D. Karefyllakis, T. Moschakis, C. G. Biliaderis, and E. Scholten. "Aqueous foams stabilized by chitin nanocrystals". English. In: *Soft Matter* 11.31 (2015), pp. 6245–6253. DOI: 10.1039/c5sm00720h. URL: http://xlink.rsc.org/?DOI=C5SM00720H.

[24] M.-M. Giraud-Guille, E. Belamie, and G. Mosser. "Organic and mineral networks in carapaces, bones and biomimetic materials". English. In: *Comptes Rendus Palevol* 3.6-7 (Oct. 2004), pp. 503–513. DOI: 10.1016/j.crpv.2004.07.004. URL: http://linkinghub.elsevier.com/retrieve/pii/S1631068304001289.

[25] Y Bouligand. "Twisted fibrous arrangements in biological materials and cholesteric mesophases." English. In: *Tissue & cell* 4.2 (1972), pp. 189–217. URL: http://eutils.ncbi.nlm.nih.gov/entrez/eutils/elink.fcgi?dbfrom=pubmed&id=4600349&retmode=ref&cmd=prlinks.

[26] E Belamie, G Mosser, F Gobeaux, and M. M. Giraud-Guille. "Possible transient liquid crystal phase during the laying out of connective tissues: α-chitin and collagen as models". In: *Journal of Physics: Condensed Matter* 18.13 (Mar. 2006), S115–S129. DOI: 10.1088/0953-8984/18/13/S08. URL: http://stacks.iop.org/0953-8984/18/i=13/a=S08?key=crossref.a0b2707d2393b2c24479b3a4754c1f32.

[27] G. F. Payne and S. R. Raghavan. " Chitosan : a soft interconnect for hierarchical assembly of nano-scale components". English. In: *Soft Matter* 3.5 (2007), pp. 521–527. DOI: 10.1039/B613872A. URL: http://pubs.rsc.org/en/Content/ArticleHTML/2007/SM/B613872A.

[28] S.-K. Kim. *Chitin and Chitosan Derivatives*. English. Advances in Drug Discovery and Developments. CRC Press, Dec. 2013. ISBN: 1466566280. URL: http://books.google.pt/books?id=GIJcAgAAQBAJ&pg=PA513&dq=intitle:Chitin+and+Chitosan+Derivatives+Advances+in+Drug+Discovery+and+Developments&hl=&cd=1&source=gbs_api.

[29] J. Desbrieres and V. Babak. "Interfacial properties of chitin and chitosan based systems". English. In: *Soft Matter* 6.11 (2010), pp. 2358–2363. DOI: 10.1039/b926400k. URL: http://xlink.rsc.org/?DOI=b926400k.

[30] P. K. Dutta, J Dutta, and V. S. Tripathi. "Chitin and chitosan: Chemistry, properties and applications". In: *Journal of Scientific & Industrial Research* 63.1 (Jan. 2004), pp. 20–31. URL: https://www.researchgate.net/profile/Marguerite_Rinaudo/publication/223322801_Chitin_and_chitosan_Properties_and_applications/links/09e415134cc9f87fea000000.pdf.

[31] S. Rana and R. Fangueiro, eds. *Fibrous and Textile Materials for Composite Applications*. Textile Science and Clothing Technology. Singapore: Springer Singapore, 2016. ISBN: 978-981-10-0232-8. DOI: 10.1007/978-981-10-0234-2. URL: http://link.springer.com/10.1007/978-981-10-0234-2.

[32] N. E. Mushi, S. Utsel, and L. A. Berglund. "Nanostructured biocomposite films of high toughness based on native chitin nanofibers and chitosan". English. In: *Frontiers in Chemistry* 2 (2014). DOI: 10.3389/fchem.2014.00099. URL: http://journal.frontiersin.org/article/10.3389/fchem.2014.00099/abstract.

[33] D. X. Oh, Y. J. Cha, H.-L. Nguyen, H. H. Je, Y. S. Jho, D. S. Hwang, and D. K. Yoon. "Chiral nematic self-assembly of minimally surface damaged chitin nanofibrils and its load bearing functions". In: *Scientific Reports* (Mar. 2016), pp. 1–6. DOI: 10.1038/srep23245. URL: http://dx.doi.org/10.1038/srep23245.

[34] Y. Yamamoto, T. Nishimura, T. Saito, and T. Kato. "CaCO3/chitin-whisker hybrids: formation of CaCO3 crystals in chitin-based liquid-crystalline suspension". In: *Polymer journal* 42.7 (May 2010), pp. 583–586. DOI: 10.1038/pj.2010.32. URL: http://www.nature.com/doifinder/10.1038/pj.2010.32.

[35] J. F. Revol and R. H. Marchessault. "In vitro chiral nematic ordering of chitin crystallites". English. In: *International Journal of Biological Macromolecules* 15.6 (Dec. 1993), pp. 329–335. DOI: 10.1016/0141-8130(93)90049-R. URL: http://linkinghub.elsevier.com/retrieve/pii/014181309390049R.

[36] X Zeng and E Ruckenstein. "Control of pore sizes in macroporous chitosan and chitin membranes". English. In: *Industrial & Engineering Chemistry Research* 35.11 (1996), pp. 4169–4175. DOI: 10.1021/ie960270j. URL: http://pubs.acs.org/doi/abs/10.1021/ie960270j.

[37] Y. C. Wei, S. Hudson, J. M. Mayer, and D. L. Kaplan. "The crosslinking of chitosan fibers". English. In: *Journal of Polymer Science Part A: Polymer Chemistry* 30.10 (Sept. 1992), pp. 2187–2193. DOI: 10.1002/pola.1992.080301013. URL: http://doi.wiley.com/10.1002/pola.1992.080301013.

[38] G Cárdenas, G Cabrera, and E Taboada. "Chitin characterization by SEM, FTIR, XRD, and 13C cross polarization/mass angle spinning NMR". In: *Journal of Applied Polymer Science* 93 (2004), pp. 1876–1885. DOI: 10.1002/app.20647. URL: http://onlinelibrary.wiley.com/doi/10.1002/app.20647/full.

[39] C. A. Schneider, W. S. Rasband, and K. W. Eliceiri. "NIH Image to ImageJ: 25 years of image analysis". In: *Nature Methods* 9.7 (June 2012), pp. 671–675. DOI: 10.1038/nmeth.2089. URL: http://www.nature.com/doifinder/10.1038/nmeth.2089.

[40] J. D. Goodrich and W. T. Winter. "α-Chitin Nanocrystals Prepared from Shrimp Shells and Their Specific Surface Area Measurement". English. In: *Biomacromolecules* 8.1 (Jan. 2007), pp. 252–257. DOI: 10.1021/bm0603589. URL: http://pubs.acs.org/doi/abs/10.1021/bm0603589.

[41] Mohammad R. Kasaai. "Determination of the degree of N-acetylation for chitin and chitosan by various NMR spectroscopy techniques: A review". In: *Carbohydrate Polymers* 79.4 (Mar. 2010), pp. 801–810. DOI: 10.1016/j.carbpol.2009.10.051. URL: http://dx.doi.org/10.1016/j.carbpol.2009.10.051.

[42] R. G. Larson. *Arrested Tumbling in Shearing Flows of Liquid Crystal Polymers*. English. 1991. URL: http://books.google.pt/books?id=FhklngEACAAJ&dq=intitle:arrested+tumbling+in+shearing+flows+of+liquid+crystal+polymers&hl=&cd=1&source=gbs_api.

[43] L. Onsager. "The Effects of Shape on the Interaction of Colloidal Particles". In: *Annals of the New York Academy of Sciences* 51 (May 1949), pp. 627–659. DOI: 10.1111/j.1749-6632.1949.tb27296.x. URL: http://adsabs.harvard.edu/cgi-bin/nph-data_query?bibcode=1949NYASA..51..627O&link_type=EJOURNAL.

[44] J Li, J. Revol, and R. Marchessault. "Rheological Properties of Aqueous Suspensions of Chitin Crystallites". English. In: *Journal of Colloid and Interface Science* 183.2 (Nov. 1996), pp. 365–373. URL: http://eutils.ncbi.nlm.nih.gov/entrez/eutils/elink.fcgi?dbfrom=pubmed&id=8954679&retmode=ref&cmd=prlinks.

[45] M. V. Tzoumaki, T. Moschakis, and C. G. Biliaderis. "Metastability of Nematic Gels Made of Aqueous Chitin Nanocrystal Dispersions". English. In: *Biomacromolecules* 11.1 (Jan. 2010), pp. 175–181. DOI: 10.1021/bm901046c. URL: http://pubs.acs.org/doi/abs/10.1021/bm901046c.

[46] S. Onogi and T. Asada. "Rheology and Rheo-Optics of Polymer Liquid Crystals". English. In: *Rheology*. Boston, MA: Springer US, 1980, pp. 127–147. ISBN: 978-1-4684-3742-3. DOI: 10.1007/978-1-4684-3740-9_9. URL: http://link.springer.com/10.1007/978-1-4684-3740-9_9.

[47] M. Bercea and P. Navard. "Shear Dynamics of Aqueous Suspensions of Cellulose Whiskers". English. In: *Macromolecules* 33.16 (Aug. 2000), pp. 6011–6016. DOI: 10.1021/ma000417p. URL: http://pubs.acs.org/doi/abs/10.1021/ma000417p.

[48] R. G. Larson. *The Structure and Rheology of Complex Fluids*. Topics in Chemical Engineering. OUP USA, 1999. ISBN: 9780195121971. URL: https://books.google.de/books?id=Vt9fw_pf1LUC.

[49] G Marrucci. "Rheology of Liquid-Crystalline Polymers". In: *Pure and Applied Chemistry* 57.11 (1985), pp. 1545–1552. DOI: 10.1351/pac198557111545. URL: www.degruyter.com/view/j/pac.1985.57.issue-11/pac198557111545/pac198557111545.xml.

[50] J. Hermans. "The viscosity of concentrated solutions of rigid rodlike molecules (poly-γ-benzyl-l-glutamate in m-cresol)". In: *Journal of Colloid Science* 17.7 (1962), pp. 638–648. URL: http://www.sciencedirect.com/science/article/pii/0095852262900284.

[51] K. F. Wissbrun. "Rheology of Rod-Like Polymers in the Liquid-Crystalline State". English. In: *Journal of Rheology* 25.6 (1981), pp. 619–662. DOI: 10.1122/1.549634. URL: http://scitation.aip.org/content/sor/journal/jor2/25/6/10.1122/1.549634.

[52] A. Lu, U. Hemraz, Z. Khalili, and Y. Boluk. "Unique viscoelastic behaviors of colloidal nanocrystalline cellulose aqueous suspensions". English. In: *Cellulose* 21.3 (2014), pp. 1239–1250. DOI: 10.1007/s10570-014-0173-y. URL: http://link.springer.com/article/10.1007/s10570-014-0173-y/fulltext.html.

[53] H.-C. Lee and D. A. Brant. "Rheology of Concentrated Isotropic and Anisotropic Xanthan Solutions. 2. A Semiflexible Wormlike Intermediate Molecular Weight Sample". English. In: *Macromolecules* 35.6 (Mar. 2002), pp. 2223–2234. DOI: 10.1021/ma011527e. URL: http://pubs.acs.org/doi/abs/10.1021/ma011527e.

[54] H.-C. Lee and D. A. Brant. "Rheology of Concentrated Isotropic and Anisotropic Xanthan Solutions. 1. A Rodlike Low Molecular Weight Sample". English. In: *Macromolecules* 35.6 (Mar. 2002), pp. 2212–2222. DOI: 10.1021/ma011526m. URL: http://pubs.acs.org/doi/abs/10.1021/ma011526m.

[55] T.-D. Nguyen, B. U. Peres, R. M. Carvalho, and M. J. MacLachlan. "Photonic Hydrogels from Chiral Nematic Mesoporous Chitosan Nanofibril Assemblies". English. In: *Advanced Functional Materials* (Mar. 2016), n/a–n/a. DOI: 10.1002/adfm.201505032. URL: http://doi.wiley.com/10.1002/adfm.201505032.

[56] S. Ifuku, A. Ikuta, M. Egusa, H. Kaminaka, H. Izawa, M. Morimoto, and H. Saimoto. "Preparation of high-strength transparent chitosan film reinforced with surface-deacetylated chitin nanofibers". In: *Carbohydrate Polymers* 98.1 (Oct. 2013), pp. 1198–1202. DOI: 10.1016/j.carbpol.2013.07.033. URL: http://dx.doi.org/10.1016/j.carbpol.2013.07.033.

[57] R Shelma, W Paul, and C. P. Sharma. "Chitin nanofibre reinforced thin chitosan films for Wound healing application". In: *Trends Biomater Artif Organs* (2008). URL: http://medind.nic.in/taa/t08/i2a/taat08i2p111.pdf.

[58] J. Jin, P. Hassanzadeh, G. Perotto, W. Sun, M. A. Brenckle, D. Kaplan, F. G. Omenetto, and M. Rolandi. "A Biomimetic Composite from Solution Self-Assembly of Chitin Nanofibers in a Silk Fibroin Matrix". English. In: *Advanced materials* 25.32 (June 2013), pp. 4482–4487. DOI: 10.1002/adma.201301429. URL: http://doi.wiley.com/10.1002/adma.201301429.

[59] H. L. Cox. "The elasticity and strength of paper and other fibrous materials". English. In: *British journal of applied physics* 3.3 (Mar. 1952), pp. 72–79. DOI: 10.1088/0508-3443/3/3/302. URL: http://iopscience.iop.org/article/10.1088/0508-3443/3/3/302.

[60] J. C. Halpin and J. L. Kardos. "The Halpin-Tsai equations: A review". English. In: *Polymer Engineering & Science* 16.5 (May 1976), pp. 344–352. DOI: 10.1002/pen.760160512. URL: http://doi.wiley.com/10.1002/pen.760160512.

[61] S. Nikolov, M. Petrov, L. Lymperakis, M. Friák, C. Sachs, H.-O. Fabritius, D. Raabe, and J. Neugebauer. "Revealing the Design Principles of High-Performance Biological Composites Using Ab initio and Multiscale Simulations: The Example of Lobster Cuticle". English. In: *Advanced materials* 22.4 (Jan. 2010), pp. 519–526. ISSN: 1521-4095. DOI: 10.1002/adma.200902019. URL: http://doi.wiley.com/10.1002/adma.200902019.

[62] M. Paillet and A. Dufresne. "Chitin Whisker Reinforced Thermoplastic Nanocomposites". In: *Macromolecules* 34 (Sept. 2001), pp. 6527–6530. DOI: 10.1021/ma002049v. URL: http://adsabs.harvard.edu/cgi-bin/nph-data_query?bibcode=2001MaMol..34.6527P&link_type=EJOURNAL.

[63] V. L. Gonçalves, M. C. M. Laranjeira, V. T. Fávere, and R. C. Pedrosa. "Effect of crosslinking agents on chitosan microspheres in controlled release of diclofenac sodium". English. In: *Polímeros* 15.1 (2005), pp. 6–12. DOI: 10.1590/S0104-14282005000100005. URL: http://www.scielo.br/scielo.php?script=sci_arttext&pid=S0104-14282005000100005&lng=en&nrm=iso&tlng=en.

Chapter 8

Conclusions and Future Perspectives

Human bone is a specialized hybrid tissue that is able to gather organic and inorganic components in a symbiotic and harmonious relation. The natural design and engineering path towards the formation of this evolved composite structure allows the unique combination of desirable properties like strength and toughness while remaining lightweight that are not available from a simple sum of the constituent materials' properties but yet achievable with a multi-scale self-assembly mechanism involving a liquid crystalline environment.

During its lifetime, bone is subject to a great number of threats that can affect its performance, health and critically damage its capability to regenerate. When great volumes are lost, bone is not able to replace them and is necessary to use substitutes to fully recover or minimize damage. Current healthcare treatments focus on regaining bone volume mainly by using bone grafts from the patient himself. However, due to limitations like availability, donor site morbidity and chronic pain, there has been a strong commitment to research and develop alternatives like synthetic bone substitutes.

In the last decade, companies have greatly invested in overcoming this problem and came up with a huge portfolio of powders, granules, injectables and scaffolds that have generated financial income but not fully met the demands of tissue regeneration. Products have shown recurrent problems associated with their manufacturing technologies and for that reason the search for an optimum solution is still ongoing.

Recently, scaffolds obtained with Inverted Colloidal Crystal technology were proposed as capable of solving those problems and offer valuable solutions in tissue engineering. ICCs come from the negative replication of hexagonal close packed arrangements of monodisperse spheres and are highly organized structures with uniform pore size and improved interconnectivity. Inspired by the inverse opals developed for photonics purposes, the first ICCs scaffolds were proposed in 2004 and, from then on, different structures

comprehending applications for hard and soft tissues have been presented. Throughout the years, ICCs structures have been mainly applied as scaffolds for tissue regeneration. Nevertheless, their characteristics enable studies on cell-scaffold interaction, diffusion profiles, cell co-culture, immunotherapy models and also applications like microanalytical devices, bio-catalysts and drug or protein carriers and delivery. They have shown to excel at providing uniform cell distribution, transport of nutrients, oxygen and metabolites diffusion, favoring also vascular ingrowth and the microenvironment for cell differentiation. Those are the type of features highly valued in tissue engineering and regenerative medicine which impart ICCs as good candidates for a new line of products in healthcare.

Taking into account the above-described superior capabilities, in the present thesis the ICC architecture was projected to develop new bone scaffolds for tissue regeneration. To construct the ICCs, microspheres with uniform sizes to be used as templates were first produced. Through the development of a simple microfluidic device, PS and PCL microspheres, were obtained with sizes ranging from 150 to 400 μm depending on production parameters. PS spheres of (261 ± 11)μm were chosen to be packed into hcp templates due to their size and smooth surface. The range of diameters selected prevents the blockage of interpore windows by cells while the smooth surface allows better packaging and less defects in the pores walls.

The inverse replication of the colloidal crystal template allowed the development of a set of scaffolds with different matrix composition. Firstly, being bone a 60-70% carbonated HAp material, ceramic porous scaffolds were successfully produced applying a sol-gel route. The applied fabrication method allowed the simultaneous formation of HAp/β-TCP ordered pore structure while the polymeric CC was eliminated. The ceramic ICC exhibiting macropores sizes of 196 μm in diameter and a porosity of about 80 vol.% allowed a favorable environment for osteoblasts attachment and proliferation, presenting interesting results as bone ingrowth promoter.

Secondly, since bone also has an organic component, the production of scaffolds with full polymeric composition was also explored. Chitosan, well known by its bio-properties, was chosen as scaffold constituent material. In *in-vivo* conditions, this polymer is subjected to degradation by hydrolysis, enzymes and macrophages. In order to understand the influence of CS molecular weight (538, 229 and 13 kDa) in the degradation profile of CS ICC scaffolds, the mechanical properties of three different MW CS ICCs were assessed along four weeks of hydrolytic degradation. It was found that the molecular weight effect competed with the amount of chitosan present in the structure regarding mechanical properties evolution. In the end, medium MW CS ICC scaffolds conserved better their structural integrity evidenced by higher mechanical properties and less degraded walls.

In the third embodiment, a composite matrix was developed considering bone's hybrid nature. Hydroxyapatite with rodlike format similar to bone nanoplatelets was synthesized by treatment of commercial HAp. The nanorods with mean length and diameter of (153.7± 57.3) nm and (12.2±6.6) nm, respectively, were suspend in chitosan solutions allowing the production of scaffolds with CS/HAp nanorods volumetric content of

ϕ_{CS}=1.00 to 0.50; ϕ_{HAp}=0.00 to 0.50. The scaffolds obtained exhibited an homogenous porous structure that was efficient to promote good cell adhesion and proliferation and whose mechanical properties were enhanced with the increase of ceramic content.

Bone is much more than a simple set of organic and inorganic material. It has an hierarchical architecture depending among other things on the internal collagen fibrils organization. Chitin, like collagen, has the ability to produce long ranged hierarchical structures that are the base of different tissues in nature. So far, no synthetic application has accomplished the organization of biomaterials like nature does. Therefore, the final stage of the work proposes a bottom-up approach that allowed to come closer to that goal. First, chitin nanowhiskers with spindle-like morphology were used as nanomaterials for the construction of CS/CTNW films that exhibited a Bouligand-like structure. This experiment unraveled a strong correlation between chitin chiral nematic organization and the internal architecture of composite films and set the tone for the construction of 3D structures whose matrices share the same design. Slow-evaporation of solvent followed by crosslinking contributed to the formation of film layers between the template spheres that upon repeated infiltration resulted in dense pore walls. The procedures employed allowed the development of rudimental ICC structures whose materials respect the imprinted liquid crystalline organization obtained in the film formation.

Structures obtained by ICC technology have an impressive homogenous design but the procedures employed present some limitations mainly related to the production of uniform colloidal crystals and what happens to matrices after sphere removal. The fortuitous appearance of spheres with very small or very large dimensions causes the occurrence of local defects that tend to propagate at long-range distance and generate non-homogenous structures. Moreover there has to be a recurrent concern about applying materials that are not affected by the solvents used for sphere removal. For instance, matrices made of hydrogels can easily capture ethanol and DCM, which softens the structure that upon handling usually lead to destruction. This forces the use of combined strategies like multiple infiltrations and/or cross-linking agents that can circumvent such restrictions, however causing the introduction of more steps and more time-consuming processes.

Throughout this PhD thesis, it is possible to understand the potential associated with the use of the ICC geometry in the production of scaffolds for tissue engineering. To that extent, the results achieved and presented in the various chapters uncover the veil and leave the trails for future developments that can lead to products in the orthopedics and/or dentistry fields. The selection of materials for structures construction took into account not only the organic/inorganic bone composition, but also their biocompatibility, biomimetic and osteogenic characters as well as the availability and cost of materials that could somehow holdback researchers and companies to adopt the proposed strategies. In that sense, hydroxyapatite and chitosan have proven along the years to be good choices. Nonetheless, ICCs' versatility does not prevent other materials from being considered.

The work presented here is the beginning of a development process and there are several studies, in particular *in vitro* and *in vivo*, and room for improvement before these

scaffolds can be applied in real-life situations. In that sense further development regarding mechanical properties and biological stimulation can be done, considering for example the introduction of reinforcements or cross-linking stages that lead to stiffer materials, and the inclusion of bone morphogenic proteins that can enhance the osteogenic capability. More *in-vitro* assays are still needed to infer ICCs performance, followed by *in-vivo* experiments that will clarify what will happen when implanted in the body.

The possibility of combining ICCs with other manufacturing methods opens a new path. As seen earlier, the majority of synthetic bone grafts are made of ceramic porous structures obtained by polymeric foams replication. Thus, the method of HAp ICC production reported in this thesis shows that upon adaptation, the impregnation of CCs with ceramic slurries originates ceramic porous structures exhibiting ICC geometry with clear advantages over the existing solutions and without abruptly changing the methods used by the industry. Other improvements can involve the combination of ICC method with 3D printing. If the necessity of using microspheres is eliminated, direct printing of structures with ICC geometry will make the process easier, less time consuming and cheaper. This combination also allows the use of polymeric, composite and ceramic pastes and especially materials that are not compatible with solvents used for sphere removal.

The last chapter considers a different strategy that is inspired by organized assemblies of molecules widely seen in nature but surprisingly less explored in synthetic applications. Producing hierarchical structures like the ones found in bones or shrimp shells is a hard task that involves multiple factors. Processing technologies often cause the disruption of chiral nematic order and in that sense the translation of such organization into a 3D structure is still very limited. The method reported is able to imprint the liquid crystalline character into 2D structures (films) and be adapted to originate ICC scaffolds. Producing homogenous LC ICC scaffolds is still a challenge but seems the right approach to originate scaffolds that can mimic bone composition and organization. The inclusion of HAp nanorods or even inducing the *in-situ* biomineralization of the oriented polymeric network will certainly lead to the development of structures with unique characteristics. Such type of scaffolds will represent the next step in bone mimicking and can open the path for products that can enhance bone regeneration.

APPENDIX A

A.1 Microfluidic Working Regimes

The definition of the microfluidic working regime can be done with Cappilary (C_a) and Webber (W_e) numbers determination which characterize the continuous and discontinuous phases, respectively. In Table A.1, the values of C_a and W_e for all production condition are presented. In Figure A.1,the microfluidic system working regime is established based

Table A.1: Cappilary and Webber numbers based on the experimental data.

Phase	Needle internal diameter (d_a) (mm)	Polymer Concentration (wt/wt)	Solution Density (ρ_d) (g/cm^3)	Solution Viscosity (μ_c) (Pa.s)	Superficial Tension (γ) (mN/m)	Flow rate (v_c) (mL/h)	
							Cappilary number (C_a)
Continuous Phase (**CP**)	0.84	PVA 2%	-	5.281×10^{-3}	56.2	50	4.698×10^{-3}
						80	7.517×10^{-3}
						100	9.397×10^{-3}
						120	11.276×10^{-3}
						140	13.156×10^{-3}
		PVA 5%	-	4.9×10^{-2}	54.2	10	9.041×10^{-3}
						20	1.808×10^{-2}
						30	2.712×10^{-2}
						40	3.616×10^{-2}
						50	4.520×10^{-2}
							Webber number (W_e)
Discontinuous Phase (**DP**)	0.25	PCL 2%	1.2916	-	27.3	3	1.065×10^{-1}
		PCL 5%	1.1717		29.3		8.998×10^{-2}
		PCL 7%	1.1461		29.0		8.894×10^{-2}
		PS 5%	1.2102	-	29.5	1	1.025×10^{-2}
						3	9.230×10^{-2}
						5	2.564×10^{-1}

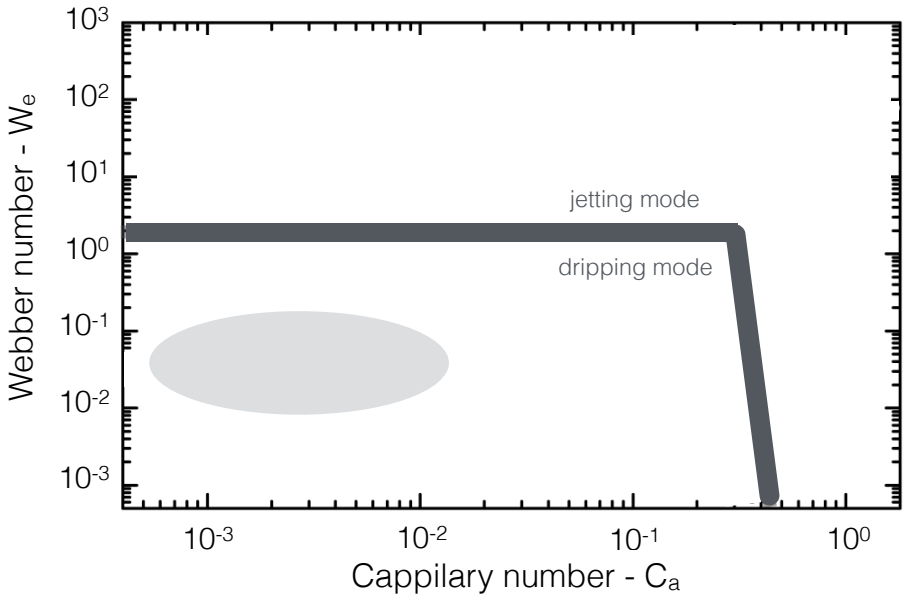

Figure A.1: Cappilary number vs Webber number. Line in dark-gray defines the microfluidic regime transition between the jetting mode and dripping mode. Spot in ligh-gray represents the experimental C_a and W_e values range determined in table A.1.

on the C_a and W_e experimental values and in the theoretical values founded in the literature[1].

A.2 Characterization

A.2.1 Viscosity-Average Molecular Weight (M_v) Determination

The viscosity average molecular weights of chitosan were determined with the combination of cappilary viscosimetry and the classical Mark-Houwink-Sakurada (MHS) equation:

$$\eta = KM_v^a \tag{A.1}$$

where η represents the intrinsic viscosity, M_v the viscosity-average molecular weight, and K and a are the constants for the solute-solvent system.

The MHS equation shows the direct relation between molecular weight and viscosity. Since higher molecular weight polymers lead to more viscous polymer solutions, determining the viscosity related to a polymer/solvent system can therefore indicate an expected molecular weight. In this work, solvent system 0.2M Acetic Acid/0.1M sodium acetate (Table A.2.1) was chosen to dissolve the different chitosan samples, determine the solutions viscosity and therefore the CS molecular weight. With this solvent, constants K and a can be determined by equations A.2, A.3 and A.4:

[1] A. S. Utada, A. Fernandez-Nieves, H. A. Stone, and D. A. Weitz. "Dripping to jetting transitions in coflowing liquid streams". doi: 10.1103/PhysRevLett.99.094502.

Table A.2: Viscosimetry parameters and constants of the solvent system used in this work.

Solvent	pH	Ionic strength μ (M)	Temperature T (ºC)	Acetylation degree (%)	x	a	$K \times 10^5$ $(dL.g^{-1})$
0.2M ac. ac./ 0.1M sod. acet.	4.38	0.1	30	24.5	0.5719	0.9691	2.2×10^5

$$a = \frac{0.6202 + 0.699x}{0.4806 + x} \tag{A.2}$$

$$x = \frac{DA}{pH\mu} \tag{A.3}$$

$$logK \times 10^{-5} = -5.7676e^a + 5.9232 \tag{A.4}$$

where DA, pH and μ represent the chitosan acetylation degree, solvent acidity and solvent ionic strength, respectively[2].

In order to determine the viscosity, a Schott-Geräte AVS400 viscometer equipped with a 0a capillary (0.53±0.01 mm) was used to measure the time that certain volume of chitosan solution took to flow a defined distance. This experiment was conducted 5 times with different concentration solutions for each chitosan sample and all results where compared with the time that the solvent system took to flow.

From these experiments, the relative viscosity (η_r) and the specific viscosity (η_{sp}) could be determined by the equations A.5 and A.6:

$$\eta_r = \frac{t}{t_0} \tag{A.5}$$

$$\eta_{sp} = \frac{t - t_0}{t_0} \tag{A.6}$$

where t and t_0 are the solution and solvent efflux time, respectively. The reduced viscosity (η_{red}) and the inherent viscosity (η_{inh}) were then obtained dividing η_{sp} and η_r with their corresponding solution concentration (c):

$$\eta_{red} = \frac{\eta_{sp}}{c} \tag{A.7}$$

$$\eta_{inh} = \frac{ln(\eta_r)}{c} \tag{A.8}$$

Since 5 concentrations were used for each sample, from the resolution of equations A.7 and A.8 it is possible to plot the evolution of those viscosities with the concentration, as represented in Figure A.2. In each of those series it is also possible to draw a tangence

[2]More information about constants determination and their comparison with theoretical/experimental results obtained in different solvent systems can be found in: Kasaai, M. R. "Calculation of Mark–Houwink–Sakurada (MHS) equation viscometric constants for chitosan in any solvent–temperature system using experimental reported viscometric constants data". doi:10.1016/j.carbpol.2006.11.006.

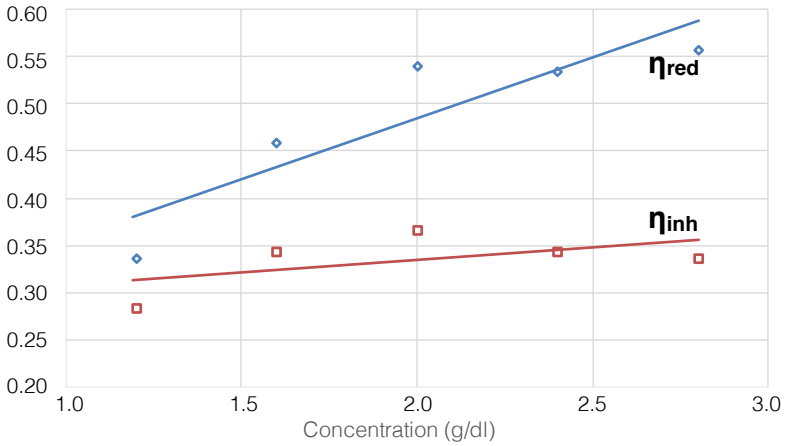

Figure A.2: Example of a plot of the reduced (blue) and inherent (red) viscosity of the chitosan sample obtained with 1:15 $NaNO_2 : CS$ ratio.

line that evidencies the viscosity/concentration proportionality. From the intersection of both tangence lines with the yy axis, two viscosity values can be obtained, $[\eta_1]$ and $[\eta_2]$. The final intrinsic viscosity η is considered the average value of the two intersections. Finally, substituting η in MHS equation A.1, the viscosity-average molecular weight can be determined[3].

A.2.2 Differential Scanning Calorimetry(DSC) and Thermogravimetry (TG)

Themal behaviour of PS, PCL, PVAc and HAp were evaluated by differential scanning calorimetry (DSC) and thermogravimetry (TG). This step had the purpose of evaluating the materials thermal behaviour to optimize the annealing temperature, sintering and degradation steps.

Table A.3: Glass transition (T_g), melting (T_m) and degradation (T_D) temperatures of PS and PVAc.

Polymer	T_g (ºC)	T_m (ºC)	T_D (ºC)
Polystyrene (PS)	97.2	307 - 415	470
Polyvynylacetate (PVAc)	45.4	302 - 360	>420

[3]More information about the cappilary viscosimetry procedures and M_v determination can be found in:

- M Rinaudo, M Milas, and P Le Dung. “Characterization of chitosan. Influence of ionic strength and degree of acetylation on chain expansion”. doi: 10.1016/0141-8130(93)90027-j.
- Kasaai, M. R.; Arul, J.; Charlet, C. "Intrinsic viscosity-molecular weight relationship for chitosan". doi: 10.1002/1099-0488(20001001)38:19<2591::AID-POLB110>3.0.CO;2-6 .
- Polymer Science Learning Center. "Dilute Solution Viscometry". Accessed 16 Ago 2016. url: http://www.pslc.ws/macrog/vis.htm.

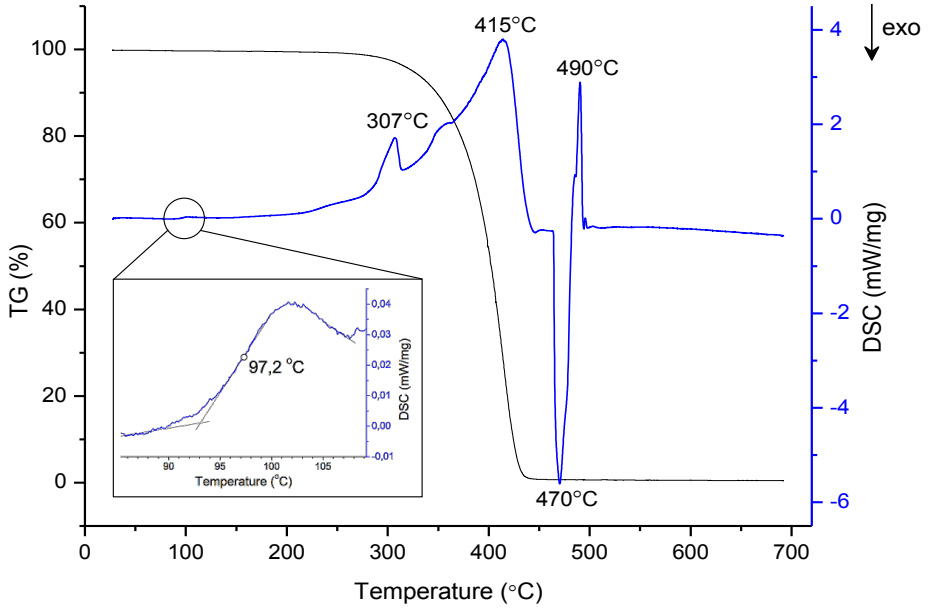

Figure A.3: TG-DSC thermogram for polystyrene with amplification of the area corresponding to the T_g peak.

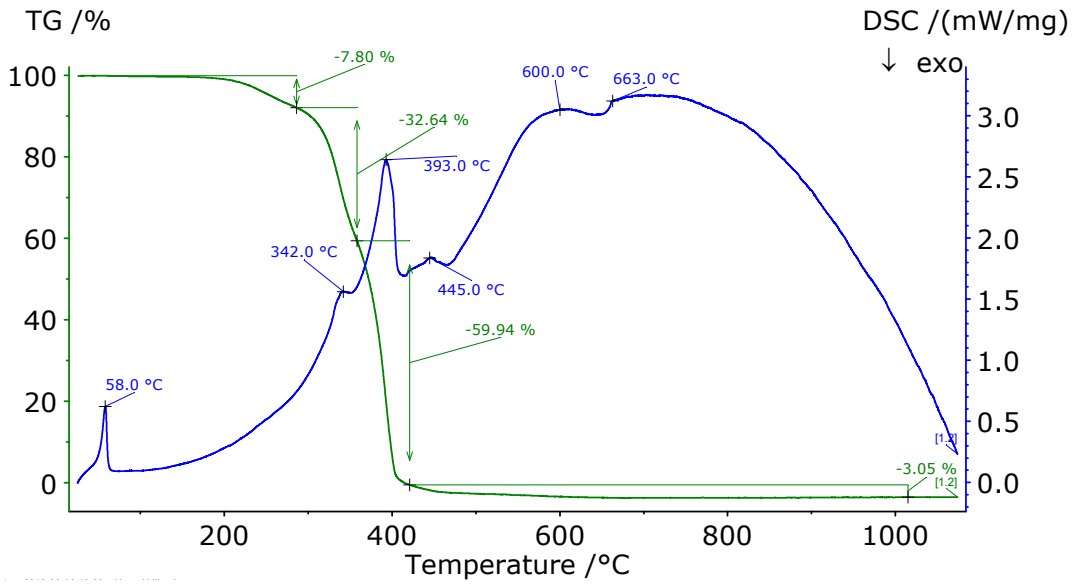

Figure A.4: TG-DSC thermogram for ϵ-polycaprolactone.

During the thermal treatment of HAp gel precursor (Fig. A.6) several decomposition reactions take place, which are evidenced by the mass losses that occur until approximately 550 °C. The first mass change of 52.67% is due to the loss of ethanol while all the others can be attributed to reactions that take place between the precursors. Crystallization probably begins at 472 °C but is accompanied by other decomposition reactions (evidenced by a mass loss of 5.18% that occurs between 400 and 550 °C) and therefore the lowest temperature chosen for sintering the samples was 600 °C (at this temperature

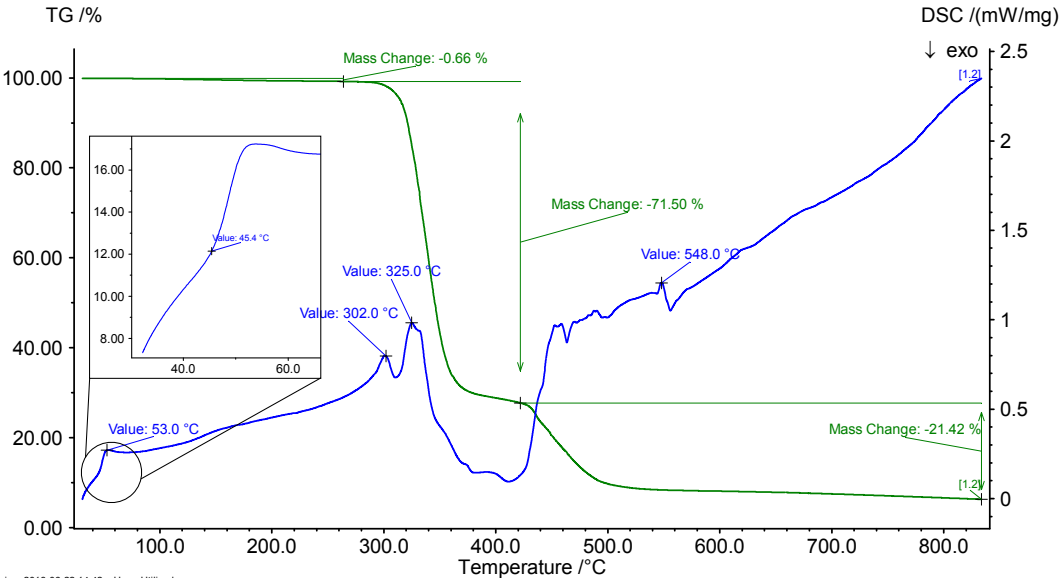

Figure A.5: TG-DSC thermogram for polyvynylacetate with amplification of the area corresponding to the T_g peak.

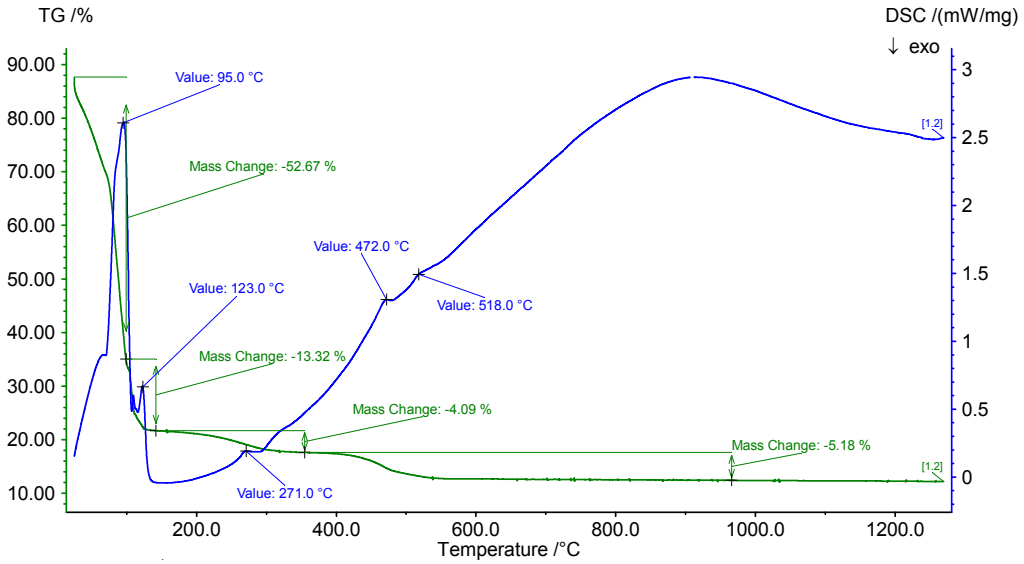

Figure A.6: TG-DSC thermogram of hydroxyapatite.

and above no more mass changes are observed). In the case of the polymers, TG-DSC thermograms (Fig. A.4 and A.5) were analyzed to determine the glass transition (T_g), melting (T_m) and degradation (T_D) temperatures. The temperatures obtained from the thermograms are summarized in Table A.3.

A.2.3 Cell Cultures: Adhesion and Proliferation Essays

ICC's biocompatibility was evaluated through cell adhesion and proliferation studies. Human osteosarcoma cells (Saos-2 cell line) were seeded directly over the material surface at a concentration of 30k cells/cm^2 using McCoy's 5A medium (Sigma-Aldrich) supplemented with 10% of fetal bovine serum (Gibco) and 1% of penicillin-streptomycin (Gibco). Adequate cell and medium controls were also set-up. ICCs were sterilized with ethanol and washed with PBS. 20h after seeding, cell adhesion rate was determined by evaluating the reduction of resazurin to resorufin by metabolically active cells. Seeding medium was substituted by new medium containing 10% of a 0.2 mg/ml resazurin solution. After 2h incubation, cell activity was evaluated by measuring the absorbance of the medium at 570 nm and 600 nm in a microplate reader (Biotek ELx 800UV). The resazurin assay was repeated at days 3, 6, 8 and 10. After 10 days, the cells were fixed with 3.7% paraformaldehyde (PFA) solution, stained with DAPI (4',6-diamidino-2-phenylindole) and observed using fluorescence microscopy.

A.2.3.1 Detailed Information

1. The ICC's were placed in a multi well plate. Four different groups were prepared:
   - Medium Control wells: containing medium without cells;
   - Medium Control wells: containing ICC's and medium without cells;
   - Cell Control wells: containing medium with cells;
   - Test wells: containing ICC's and medium with cells.

   Cells were seeded in the last two types of wells at a concentration of 30 000 cells/cm^2.
2. The multi well plate was incubated at 37°*C* for 24 hours to allow the cells to adhere.
3. The ICC's in the *Test wells* were transferred to empty wells.
4. The culture medium was removed from the wells and in its place was added a 10% vol/vol solution of resazurin (0.2 mg/mL) and culture medium.
5. After incubation for 2 hours the solution contained in the wells was transferred to a 96 well microplate.
6. The fluid absorbance was read at 570 and 600 nm in a microplate reader (Biotek ELx 800). The reading was performed in quadruplicates.

A.2.4 Chitin Nanowhiskers Characterization

A.2.4.1 CTNW Dimensions

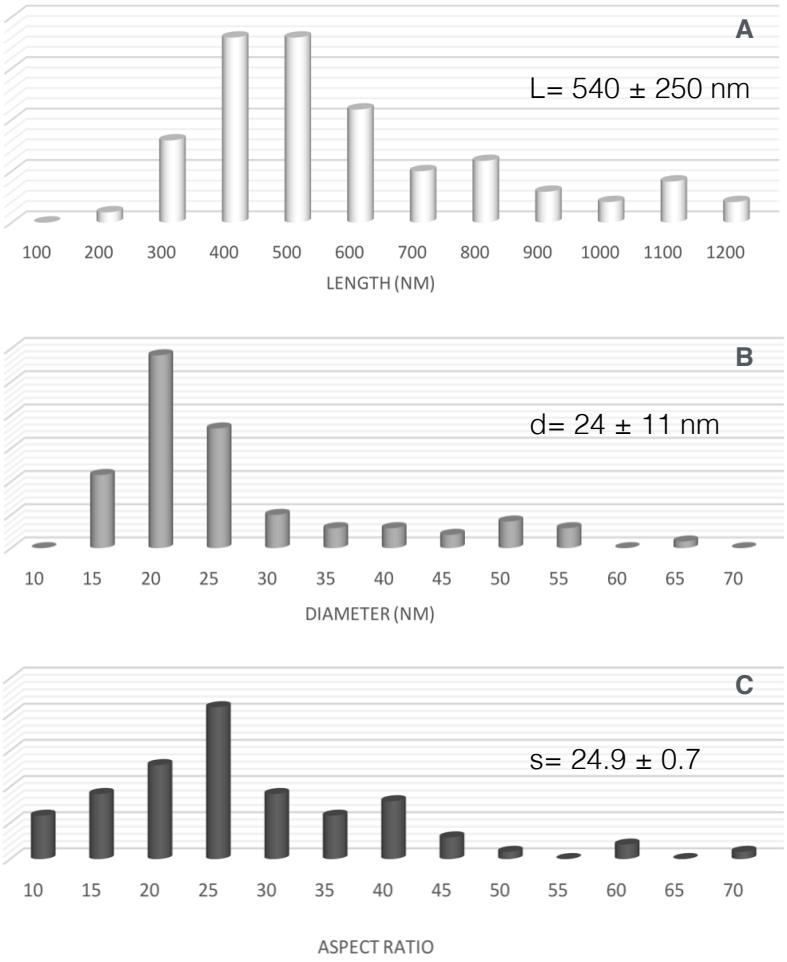

Figure A.7: Histograms of chitin nanowhisker: A) length (L); B) diameter (d); C) aspect ratio (s).

A.2.4.2 CTNW XRD Structural Parameters

Table A.4: Chitin and chitin nanowhiskers structural parameters obtained from X-Ray Diffraction.

Sample	Plane	Position (2θ)	D-spacing (Å)	FWHM (2θ)	CI (%)
Chitin	(020)	9.37	9.42	0.95	84.8
	(101)	12.82	6.89	0.71	
	(040)(110)	19.40	4.57	1.03	
	(130)	22.79	3.89	0.31	
	(013))	26.40	3.37	0.40	
CTNW	(020)	9.44	9.36	0.87	91.4
	(101)	12.71	6.95	0.63	
	(040)(110)	19.40	3.57	1.11	
	(130)	22.75	3.90	0.32	
	(013)	26.43	3.37	0.40	

A.2.4.3 CTNW NMR Analysis

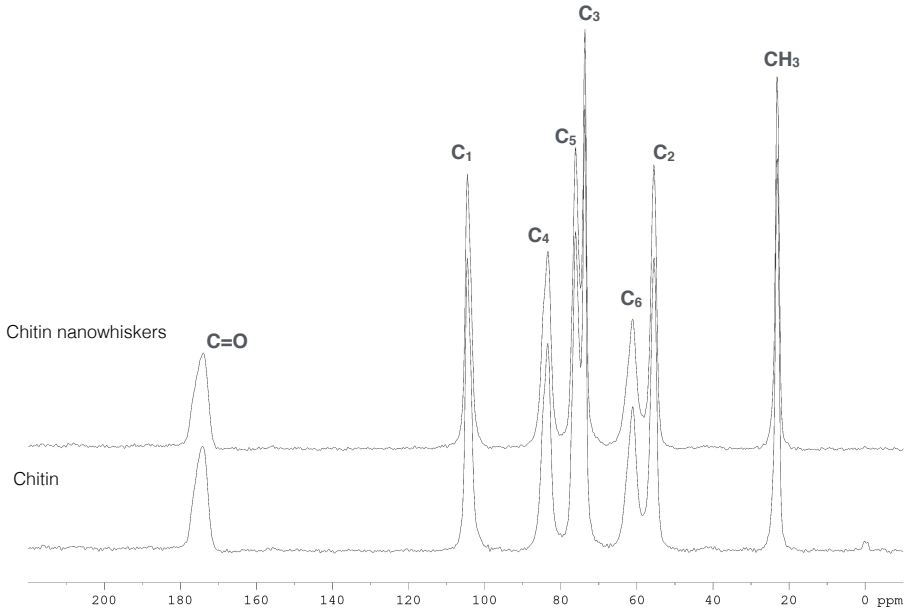

Figure A.8: NMR spectra of chitin (bulk) and chitin nanowhiskers. Carbon numbering with correspondence with chitin's molecular structure of Figure 7.1.

A.3 Chitin Nanowhiskers Films

A.3.1 CTNW Films SEM Images

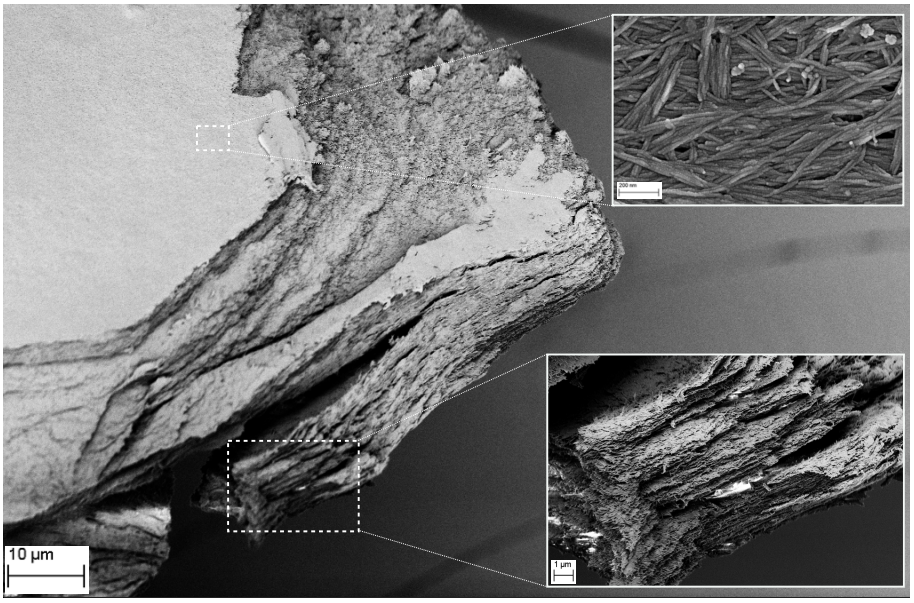

Figure A.9: SEM image of chitin nanowhisker film with magnification of film's surface and cross section.

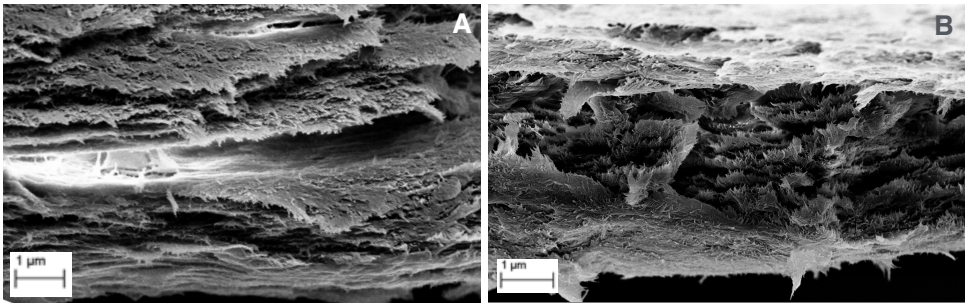

Figure A.10: SEM image of: A) CTNW film; B) CS+3.0%CTNW film.

A.3.2 CTNW Based Films Internal Organization

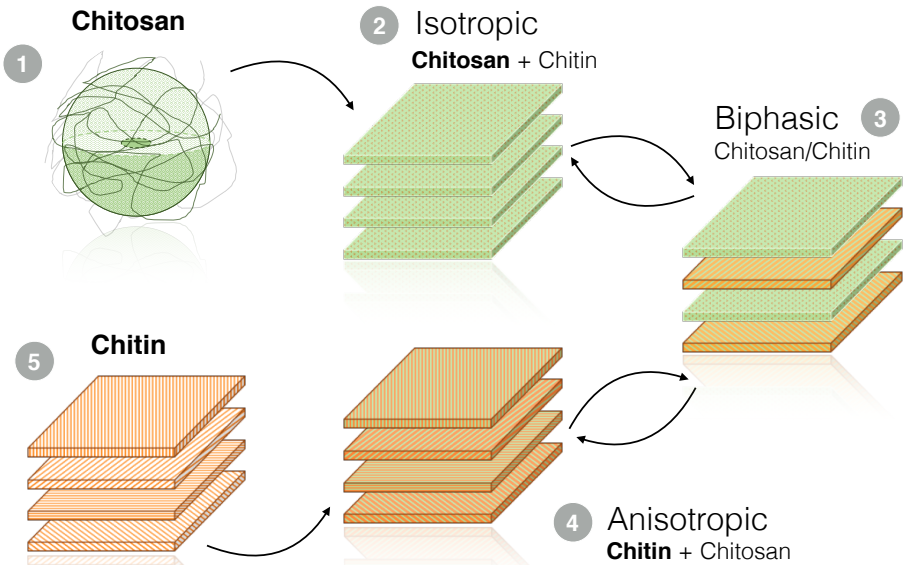

Figure A.11: Shematic representation of the internal organization transition of composite films. Green - chitosan; Orange - chitin nanowhiskers.

A.3.3 CTNW Based Films Mechanical Properties Modeling

Table A.5: Elastic constants considered for the chitosan matrix and the chitin reinforcements

Orientation range	Representative angle ϕ_K	Reinforcement volume fraction f_{f_k}
$\phi \leq$-85°	-90°	0.00925
-85°< $\phi \leq$ -75°	-80°	0.01564
-75°< $\phi \leq$ -65°	-70°	0.02354
-65°< $\phi \leq$ -55°	-60°	0.02948
-55°< $\phi \leq$ -45°	-50°	0.02948
-45°< $\phi \leq$ -35°	-40°	0.03444
-35°< $\phi \leq$ -25°	-30°	0.04109
-25°< $\phi \leq$ -15°	-20°	0.05231
-15°< $\phi \leq$ -5°	-10°	0.06723
-5°< $\phi \leq$ +5°	0°	0.07315
+5°< $\phi \leq$ +15°	+10°	0.06162
+15°< $\phi \leq$ +25°	+20°	0.04839
+25°< $\phi \leq$ +35°	+30°	0.03669
+35°< $\phi \leq$ +45°	+40°	0.02611
+45°< $\phi \leq$ +55°	+50°	0.01845
+55°< $\phi \leq$ +65°	+60°	0.01371
+65°< $\phi \leq$ +75°	+70°	0.01250
+75°< $\phi \leq$ +85°	+80°	0.01295
$\phi >$ +85°	+90°	0.00576

A.3.3.1 Elastic Behavior Modelling

The classic shear-lag model[4] can be used to determine the longitudinal elastic modulus $(E_1)_k$ for a layer given layer k:

$$(E_1)_k = \left[f_{f_k} E_f \frac{1 - tanh(ns)}{ns} + (1 - f_{f_k}) E_m \right] \tag{A.9}$$

In the above equation, E_f and E_m are the elastic moduli respectively of the chitin fibres and the chitosan matrix; s is the fibres' aspect ratio, while n is given by:

$$n = \left[\frac{2E_m}{E_f(1+\nu_m) ln(\frac{1}{f_{f_k}})} \right]^{1/2} \tag{A.10}$$

with ν_m referring to chitosan's Poisson ratio. For the same layer, the transverse modulus $(E_2)_k$, as well as the in-plane shear modulus $(G_{12})_k$ may be computed from the Halpin-Tsai model[5] :

$$(E_2)_k = \frac{E_m(1 + \xi_E \eta_E f_{f_k})}{1 - \eta_E f_{f_k}} \tag{A.11}$$

$$(G_{12})_k = \frac{G_m(1 + \xi_G \eta_G f_{f_k})}{1 - \eta_G f_{f_k}} \tag{A.12}$$

In the preceding equations, ξ_E and ξ_G are parameters close to unity, whereas η_E and η_G correspond to:

$$\eta_E = \frac{\frac{E_f}{E_m - 1}}{\frac{E_f}{E_m + \xi_E}} \tag{A.13}$$

$$\eta_G = \frac{\frac{G_f}{G_m - 1}}{\frac{G_f}{G_m + \xi_G}} \tag{A.14}$$

with G_f and G_m being the shear moduli of the chitin fibres and the chitosan matrix, respectively. By knowing the Poisson ratios ν_f and ν_m of the constituent materials, it is then possible to compute the values of both in-plane Poisson ratios of the composite layer:

$$(\nu_{12})_k = f_{f_k} \nu_f + (1 - f_{f_k}) \nu_m \tag{A.15}$$

$$(\nu_{21})_k = \left[f_{f_k} \nu_f + (1 - f_{f_k}) \nu_m \right] \frac{(E_2)_k}{(E_1)_k} \tag{A.16}$$

[4] Cox, H. L. The elasticity and strength of paper and other fibrous materials. British journal of applied physics. IOP Publishing March 1, 1952, pp 72–79.

[5] Halpin, J. C.; Kardos, J. L. The Halpin-Tsai equations: A review. Polymer Engineering and Science. Society of Plastics Engineers, Inc. May 1, 1976, pp 344–352.

In possession of the various engineering constants, one may determine the relevant values of the layer's stiffness matrix:

$$(C_{11})_k = \frac{(E_1)_k}{1-(\nu_{12})_k(\nu_{21})_k} \tag{A.17}$$

$$(C_{22})_k = \frac{(E_2)_k}{1-(\nu_{12})_k(\nu_{21})_k} \tag{A.18}$$

$$(C_{12})_k = \frac{(\nu_{12})_k(E_2)_k}{1-(\nu_{12})_k(\nu_{21})_k)} = (C_{21})_k = \frac{(\nu_{21})_k(E_1)_k}{1-(\nu_{12})_k(\nu_{21})_k} \tag{A.19}$$

$$(C_{66})_k = (G_{12})_k \tag{A.20}$$

The above calculations may be repeated for each layer in the stack. However, if the resulting values are to be used in conjunction in order to predict the properties of the stacked structure, a common referential must be used. Thus, for each layer, it becomes necessary to transform the terms of its stiffness matrix, so as to obtain the equivalent terms written under the common referential. If this is taken as corresponding to the orthogonal directions of a particular layer (henceforth designated the 0-layer), and if a generic k layer's longitudinal axis differs from that of the 0-layer by an angle ϕ_k , the terms of its transformed stiffness terms matrix are:

$$(\bar{C}_{11})_k = (C_{11})_k cos^4\phi_k + (C_{22})_k sin^4\phi_k + [2(C_{12})_k + 4(C_{66})_k]cos^2\phi_k sin^2\phi_k \tag{A.21}$$

$$(\bar{C}_{22})_k = (C_{11})_k sin^4\phi_k + (C_{22})_k cos^4\phi_k + [2(C_{12})_k + 4(C_{66})_k]cos^2\phi_k sin^2\phi_k \tag{A.22}$$

$$(\bar{C}_{66})_k = [(C_{11})_k + (C_{22})_k - 2((C_{12})_k + 4(C_{66})_k)]cos^2\phi_k sin^2\phi_k + (C_{66})_k[cos^4\phi_k sin^4\phi_k] \tag{A.23}$$

$$(\bar{C}_{12})_k = (\bar{C}_{21})_k = (C_{12})_k[cos^4\phi_k sin^4\phi_k] + [(C_{11})_k + (C_{22})_k - 4(C_{66})_k]cos^2\phi_k sin^2\phi_k \tag{A.24}$$

Two further terms must be considered through this transformation, which relate to the possibility of interaction between normal and shear behaviour during off-axis loading of the layer:

$$(\bar{C}_{16})_k = [(C_{11})_k - (C_{12})_k - 2(C_{66})_k]cos^3\phi_k sin\phi_k - [(C_{22})_k - (C_{12})_k - 2(C_{66})_k]sin^3\phi_k cos\phi_k \tag{A.25}$$

$$(\bar{C}_{26})_k = [(C_{11})_k - (C_{12})_k - 2(C_{66})_k]sin^3\phi_k cos\phi_k - [(C_{22})_k - (C_{12})_k - 2(C_{66})_k]cos^3\phi_k sin\phi_k \tag{A.26}$$

The resulting behaviour of the film may then be obtained by averaging the results for the n stacked layers:

$$(\bar{C}_{ij})_{Film} = \frac{\sum_{k=1}^{n}(\bar{C}_{ij})_k}{n} \tag{A.27}$$

Inverting the film's stiffness matrix $[\bar{C}_{ij}]_{Film}$ provides the terms of its compliance matrix $[\bar{S}_{ij}]_{Film}$, which in turn can be used to determine the films elastic properties:

$$(E_1)_{Film} = \frac{1}{(\bar{S}_{11})_{Film}} \tag{A.28}$$

$$(E_2)_{Film} = \frac{1}{(\bar{S}_{22})_{Film}} \tag{A.29}$$

$$(\nu_{12})_{Film} = -(E_1)_{Film}(\bar{S}_{21})_{Film} \tag{A.30}$$

$$(\nu_{21})_{Film} = -(E_2)_{Film}(\bar{S}_{12})_{Film} \tag{A.31}$$

$$(G_{12})_{Film} = \frac{1}{(\bar{S}_{66})_{Film}} \tag{A.32}$$